Caractérisation expérimentale et modélisation de l'OAPS en tant que précurseur de membranes polyOAPS-imides

Saman Salimi

UNIVERSITÉ SAVOIE MONT BLANC

THÈSE

Pour obtenir le grade de

DOCTEUR DE L'UNIVERSITÉ SAVOIE MONT BLANC

Spécialité : **Matériaux, Mécanique, Génie civil, Électrochimie**

Arrêté ministériel : 25 Mai 2016

Présentée par

Saman SALIMI

Thèse dirigée par **Sylvie NEYERTZ**, Maîtresse de Conférences, USMB

Préparée au sein du Laboratoire d'Électrochimie et Physico-chimie des Matériaux et des Interfaces dans l'École Doctorale I-MEP2 – Ingénierie – Matériaux, Mécanique, Environnement, Énergétique, Procédés, Production.

Caractérisation expérimentale et modélisation de l'OAPS en tant que précurseur de membranes polyOAPS-imides

Thèse soutenue publiquement le **29 Mars 2022**,
devant le jury composé de :

Monsieur José SANCHEZ MARCANO
Directeur de Recherche, Institut Européen des Membranes, Rapporteur
Madame Catherine MARESTIN
Chargée de Recherche, Université Claude Bernard Lyon 1, Rapporteur
Monsieur Lionel FLANDIN
Professeur des Universités, USMB, Examinateur
Madame Sylvie NEYERTZ
Maîtresse de Conférences, USMB, Directrice de thèse
Monsieur David BROWN
Professeur des Universités, USMB, Invité

AGENCE NATIONALE DE LA RECHERCHE ANR

Experimental characterization and modelling of OAPS as a precursor for polyOAPS-imide membranes

Table of contents

Abbreviation list

2D-NMR	Two-dimensional nuclear magnetic resonance spectroscopy
6FDA	4,4'-(Hexafluoroisopropylidene)diphthalic anhydride
6FPPr	2,6-bis(trifluoromethylphenylene) pyridine
6FPT	2,5-bis(3-trifluoromethylphenylene)
APS	aminophenylsilsesquioxane
BMI	Bismaliemide
BPADA	4,4'-(4,4'-isopropylidenediphenoxy)bis(phtalic anhydride)
BTDA	Benzophenone-3,3',4,4'-tetracarboxylic dianhydride
BTFDA-DAB	2,2'-bis (p -trimethoxyphenyl) hexafluoropropane dianhydride-3,3'- diaminobenzidine
CUT	Continuous use temperature
DFT	Density functional theory
DMAC	Dimethylacetamide
DMF	Dimethylformamide
EDS	Energy dispersive spectroscopy
FBP-6FPT	2,5-bis(3-trifluoromethylphenylene) thiophene
FE-SEM	Field emission scanning electron microscope
FFV	Fractional free volume
EB	Electron beam
GC	Gradient corrected
GIAO	Gauge-including atomic orbital
GPC	Gel permeation chromatography
GS	Gas separation
HDT	Heat distortion temperature
HETCOR	Heteronuclear correlation spectroscopy
HOSE	Hierarchical Organisation of Spherical Environments
IGA	Isothermal gravimetric analysis
IE	Ion exchange
LDA	Local density approximation
MAE	Mean absolute error
MBR	Membrane bioreactors
MD	Molecular dynamics
meta-APS	*meta*-aminophenylsilsesquioxane
MF	Micro-filtration
MMMs	Mixed matrix membranes
MWD	Molecular weight distribution

NF	Nano-filtration
NMP	N-Methyl-2-pyrrolidone
NMR	Nuclear magnetic resonance
OAPS	Octa(aminophenyl)silsesquioxane
ODA	4,4'-Oxydianiline
ODPA	4,4'-Oxydiphthalic anhydride
ONPS	Octa(nitrophenyl)silsesquioxane
OPS	Octa(phenyl)silsesquioxane
Ortho-OAPS	*ortho*-aminophenylsilsesquioxane
PA	Polyamide
Para-OAPS	*para*-aminophenylsilsesquioxane
PBI	Polybenzimidazole
PC	Polycarbonate
PCM	Polarizable Continuum Model
PEEK	Polyetheretherketone
PEI	Polyetherimide
PI	Polyimide
PMDA	Pyromellitic dianhydride
POPs	Poly[organophasphazenes]
POSS	Polyhedral oligomeric silsesquixanes
PSA	Pressure swing adsorption
PSF	Polysulfone
PTFE	Polytetrafluoroethylene
QM	Quantum mechanical
RMSE	Root mean square error
RO	Reverse osmosis
RTI	Relative Temperature Index
SCRF	Self-Consistent Reaction Field
TAP	2,4,6-triaminopyrimidine
T_g	Glass temperature
TGA	Thermal gravimetric analysis
T_m	Melting temperature
VDW	Van der Waals
VOL	Volatile Organic Liquids
VSA	Vacuum swing adsorption
XRD	X-ray diffraction

ZIF	Zeolitic imidazolate frameworks

Abstract

Gas separation by dense polymer membranes is a promising alternative to the cryogenic distillation or adsorption separation processes due to its much lower energy costs. Unfortunately, polymers tend to lose their structural integrity at high temperatures. To improve the thermomechanical resistance while maintaining the gas-sieving properties, hybrid ultrathin membranes based on inorganic POSS (polyhedral oligosilsesquioxanes) cross-linked with organic imides have recently been developed using interfacial polymerization. These polyPOSS-imide membranes were indeed found to perform under tougher operating conditions than conventional polymers. However, the aliphatic arms of the inorganic POSS precursors used so far were too flexible and prone to thermal degradation.

This work aims to attain more stable hybrid membranes using a new inorganic POSS precursor, the octa(aminophenyl)silsesquioxane (OAPS). This siloxane-based cage has three different isomers depending on the *meta*, *ortho* and *para* position of the amine with respect to the phenyl group. An extensive literature search showed that the isomer ratios were not clearly defined and that several synthesis routes gave different results. This is problematic as the nature of the isomer will strongly affect the resistance and gas selectivities of the resulting membranes. Experimental characterizations including picnometry, infrared spectroscopy (IR), 1-dimensional and 2-dimensional nuclear magnetic resonance (NMR) have been performed for a commercial OAPS containing all three isomers and a controlled OAPS containing only the *para* and *me*ta isomers. To better identify the isomers, the experimental results were compared to predictions of the IR and NMR spectra by quantum mechanical methods such as Density Functional Theory and by machine-learning methods such as MestreNova. OAPS was then used as a precursor to make new hybrid membranes with increased thermoresistance. These polyOAPS-imide membranes were characterized using IR, thermal gravimetric analysis (TGA), scanning electron microscopy (SEM), energy dispersive spectroscopy (EDS) and permeability measurements. They were found to degrade well over 400°C and to preserve gas selectivities of ~10 for H_2/CH_4 and H_2/N_2 at 250°C. In parallel, a force-field was developed to carry out molecular dynamics simulations of the three OAPS isomers in order to characterize their differences at the atomic level.

Résumé en français

La séparation des gaz par les membranes polymères denses est une alternative prometteuse aux procédés de séparation par distillation cryogénique ou par adsorption en raison de ses coûts énergétiques beaucoup plus faibles. Malheureusement, les polymères ont tendance à perdre leur intégrité structurale à hautes températures. Afin d'améliorer leur résistance thermomécanique tout en conservant leurs propriétés de séparation des gaz, des membranes hybrides ultrafines à base de POSS (polyhedral oligosilsesquioxanes) inorganiques réticulés avec des imides organiques ont récemment été développées par polymérisation interfaciale. Ces membranes polyPOSS-imides se sont effectivement montrées plus performantes dans des conditions difficiles que les polymères conventionnels. Par contre, les motifs aliphatiques des précurseurs POSS utilisés initialement étaient trop flexibles et sujets à la dégradation thermique.

L'objectif de ce travail est de développer des membranes hybrides plus stables à partir d'un nouveau précurseur POSS inorganique, l'octa(aminophenyl)silsesquioxane (OAPS). Cette cage siloxane possède trois isomères différents selon la position en *meta*, en *ortho* ou en *para* du groupement amine par rapport au groupement phényle. Une recherche de littérature a montré que les proportions des isomères étaient mal définies et que plusieurs voies de synthèse donnaient des résultats différents. Cela pose problème car la résistance et la sélectivité des membranes vont fortement dépendre de la nature des isomères. Un OAPS commercial contenant les trois isomères et un OAPS contrôlé contenant uniquement les isomères *para* et *meta* ont été caractérisés expérimentalement par picnométrie, spectroscopie infrarouge (IR), ainsi que par résonance magnétique nucléaire (RMN) unidimensionnelle et bidimensionnelle. Afin de mieux identifier les isomères, les résultats expérimentaux ont été comparés aux prédictions des spectres IR et RMN par des méthodes de mécanique quantique telles que la Density Functional Theory et par des méthodes d'apprentissage automatique telles que MestreNova. Le précurseur OAPS a ensuite été utilisé pour fabriquer de nouvelles membranes hybrides à thermorésistance élevée. Ces membranes polyOAPS-imides ont été caractérisées par IR, analyse thermogravimétrique (ATG), microscopie électronique à balayage (MEB), spectroscopie à dispersion d'énergie (EDS) et mesures de perméabilités. Elles ont pu conserver leur stabilité bien au-delà de 400°C et une sélectivité de ~10 pour les séparations H_2/CH_4 et H_2/N_2 à 250°C. En parallèle, un champ de force a été développé pour

effectuer des simulations de dynamique moléculaire des trois isomères OAPS afin de caractériser leurs différences au niveau atomique.

I. Introduction

Due to the fast increase in population and the growth in energy consumption and industry, it is predicted that energy-related CO_2 emissions will increase by ~50% from 36 Gigatons in 2019 to 55 Gigatons in 2030 with the current and planned policies.[1-2] The combustion of fossil fuels causes environmental issues and global problems, including greenhouse gases and air toxics, with the main contributor being coal.[3] Over the past decades, there has been a growing interest in the development of membrane-based gas separation technologies to overcome the aforementioned environmental challenges and for specific applications such as O_2 enrichment, H_2 recovery and sweetening of natural gas. A growing interest in inorganic and polymer membranes for use in various industrial sectors has emerged. New fairly advanced polymers and copolymers such as polybenzimidazoles, thermally rearranged poly(benzoxazole)s and poly(benzoxazole-co-imides) have been produced.[4-8]

A membrane is generally defined as a selective barrier between two phases.[9] The separation of gases can refer to any technique that may have multiple products or may be used to purify only one product. As shown in Figure 1, the feed is divided into two streams by the membrane, including the permeate, which is the part of the feed passing through the membrane, and the retentate, which is the part of the feed that cannot pass through the membrane. Depending on the purpose of the separation, the product will either be the permeate or the retentate.

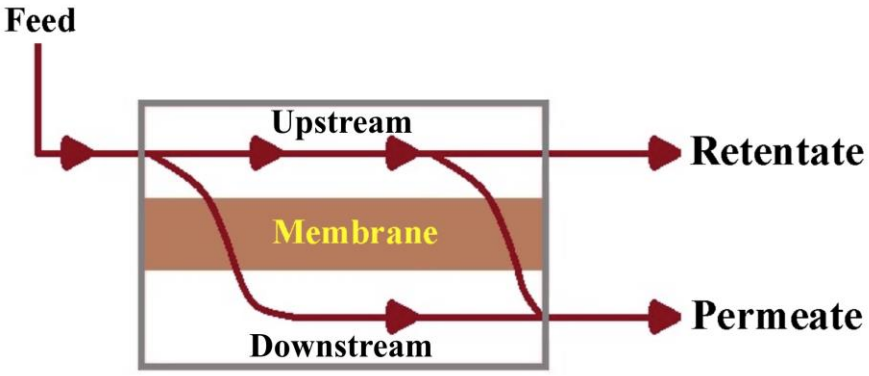

Figure 1. Separation of the components in a mixture by a membrane.

A gas takes the shape of its container and reaches a uniform density inside the container even in the presence of other objects. If gases are not confined to the container, they

are known as vapours that circulate in space. Atoms or molecules of matter move freely in the gaseous state and are less compact than in the solid and liquid states.[9]

The most important properties of gases include:

1. High compressibility: external forces can compress the gas and reduce its volume; when removing the external forces, the gas volume increases again.
2. Thermal expansion: when a gas sample is heated, its volume increases, and when it is cooled, its volume decreases.
3. Low viscosity: gases flow more easily than liquids.
4. Low density: the density of gases is in grams per cubic decimeter, while the density of liquids and solids is in grams per cubic centimetre.
5. Infinite miscibility: gases can be mixed in any proportion.

Important variables that describe a gas are its pressure *P*, temperature *T* and volume *V*. In a gas mixture, the behaviour of the gas depends on its number of molecules,[9] unless the interactions of the gas-gas molecules are strong such as in the case of water vapour.

For the separation of gases, the most important membrane parameters are permeability and selectivity. Permeability is a volume current that passes through the unit of the membrane surface area for a known membrane thickness and at a given pressure difference (Equation 1):[9-10]

$$P = J\frac{l}{\Delta p} \tag{1}$$

where J is the gas flux through a membrane of thickness l, and Δp indicates the pressure difference across the membrane. J is defined by Fick's first law (Equation 2)[10] as:

$$J = -D\frac{\partial C}{\partial x} \tag{2}$$

where D is the diffusion coefficient and $\left(\frac{\partial C}{\partial x}\right)$ is the penetrant concentration as a function of the distance x across the membrane.

By combining Equations 1 and 2 while assuming that the downstream pressure is negligible, one obtains Equation 3:

$$P = DS \tag{3}$$

where S is the solubility coefficient.

The separation factor $\alpha_{A/B}$, which refers to a mixture of gases, is defined as the ability of a membrane to separate gas A from gas B (Equation 4):[10]

$$\alpha^{*}_{A/B} = \frac{y_A / y_B}{x_A / x_B} \tag{4}$$

where x and y are the upstream and downstream mole fractions of A and B respectively. Equation 5 shows the ideal permselectivity $\alpha_{A/B}$ of the membrane, which is the ratio of the permeabilities or permeances of the individual gases:

$$\alpha_{A/B} = \frac{P_A}{P_B} \tag{5}$$

In other words, the difference in the permeation of the penetrants measured individually determines the selectivity of the membrane. Equation 5 is often a good approximation for the true separation factor (Equation 4), providing that there are no specific effects due to the mixture. For example, in the case of oxygen purification, $\alpha_{O2/N2}$ is the extent to which the membrane can separate oxygen from nitrogen with oxygen being the desired penetrant.[11]

The membrane separation technology selectively separates mixtures through pores and/or fine gaps in a continuous molecular structure. It is based on the physical or chemical interactions of the mixture's components with the membrane material. Membrane separations are often categorized by the size of the pores and the separation driving force. This includes microfiltration (MF), Ultrafiltration (UF), Nanofiltration (NF), Ion exchange (IE), Reverse osmosis (RO), and gas separation membranes, which have either the smallest pores or no pores.[9] According to the IUPAC notation,[12-14] microporous membranes have pore diameters of less than 2 nm (20 Å) and macroporous membranes have pore diameters greater than 50 nm (500 Å); the mesoporous category thus lies in the middle with pore diameters between 2

and 50 nm (20-500 Å). Nonporous membranes do not have any clearly-defined pores. Figure 2 shows different mechanisms of separation depending on the pore diameters, from the smallest to the largest:[9, 14-15]

- Solution-Diffusion: this mechanism is generally considered to have a three-step process. Firstly, the gas molecules are adsorbed at the membrane surface on the upstream side. This is followed by the diffusion of the gas molecules through the matrix. Finally, the gas molecules desorb on the downstream side. This mechanism occurs for nonporous membranes, i.e. those based on polymers.
- Molecular Sieving: this mechanism happens when the pore sizes are sufficiently small (3.0–5.2 Å), leading to the separation of gas molecules that differ in kinetic diameter. The pore sizes of the membrane are so small that only the smaller gas molecules can permeate.
- Knudsen Diffusion: Knudsen separation can be obtained with mesoporous membranes having pore sizes smaller than 50 nm. It gives relatively low separation selectivities. In this mechanism, the gas molecules are separated according to their mean free path.
- Convection flow: when the pore diameters are longer than the mean free path of the gas molecules, the convection flow occurs, and no efficient separation can be achieved.

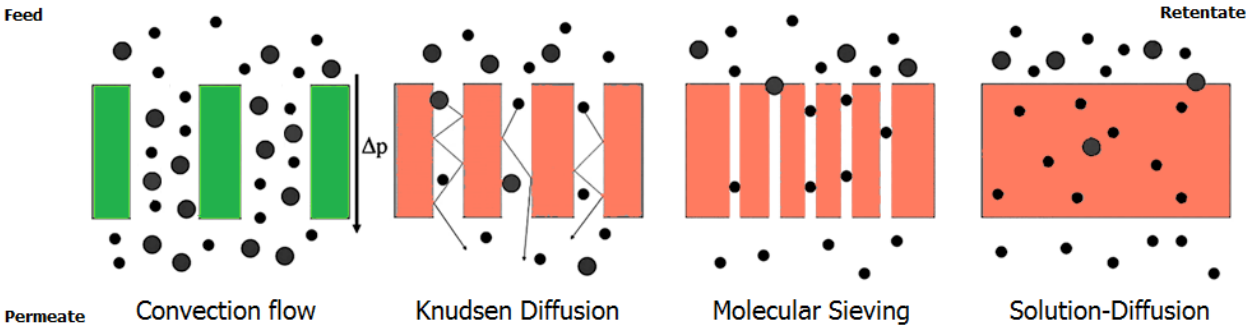

Figure 2. Convection flow and the three other possible mechanisms for membrane gas diffusion depending on the pore sizes.

Compared to alternative separation methods, the advantages of the membrane processes are the reduced power consumption, the low volume and the lack of need for a large space, the various possibilities in shapes, sizes and design, the low-pressure drop and

the high mass transfer. Its disadvantages are the short membrane lifespan, the relatively low selectivities and permeabilities, the plasticization phenomena, the limited mechanical properties, the defects, the ageing and the high manufacturing costs.[16] Within this context, inorganic nanomaterials have been used to provide higher permeabilities, selectivities and resistances in the new generation of mixed-matrix membranes (MMMs) and hybrid membranes. MMMs are polymer matrices in which inorganic fillers are dispersed at the nanometer level. They combine the resistance benefits of the inorganic particles and the economical processing capabilities of the polymers.[17] Hybrid membranes refer to the polymeric and the inorganic phases being connected by covalent bonds.[18]

Membrane processes have now reached the first stage of maturity in many important processes such as:[9]

- Nitrogen or oxygen separation from the air;
- Separation of hydrogen from other gases such as nitrogen and methane;
- Hydrogen recovery from vapours in ammonia plants;
- Hydrogen recovery in oil refining processes;
- Methane separation from the other biogas compounds;
- Water vapour extraction from natural gas and other gases;
- CO_2 separation from natural gas;
- H_2S withdrawal from natural gas;
- Volatile Organic Liquids (VOL) removal from vapour atmospheres.

An example is the use of membranes for partial air separation, which was developed as a promising alternative to adsorption and cryogenics.[19] Cryogenic distillation is a large-scale process producing very pure gas and liquid products.[20] The basic choice between cryogeny or non-cryogeny mostly depends on the number of products that must be prepared (e.g. oxygen or nitrogen or both), the required production rates of each gas and/or liquid product and the required purities of the products.[9] Compared to a membrane process, cryogenic air separation produces highly-purified gases or liquids. However, cryogenic distillation may be complicated in practice. Initially, pre-cooled air is compressed to 650 kPa in a multistage process. It is then throttled to cool to very low temperatures (below around -180ºC) and liquefy. Nitrogen and oxygen are subsequently separated in a fractional distillation column. While liquid oxygen settles to the bottom of the column, nitrogen boils

and can be removed through the top of the column. The remaining contents then move to a low-pressure distillation column to enhance the oxygen purity. The nitrogen stream is condensed to generate the reflux stream and liquid nitrogen is produced as well.[21] The final result is oxygen with a purity of more than 99%. The cryogenic distillation process is illustrated in Figure 3.[22]

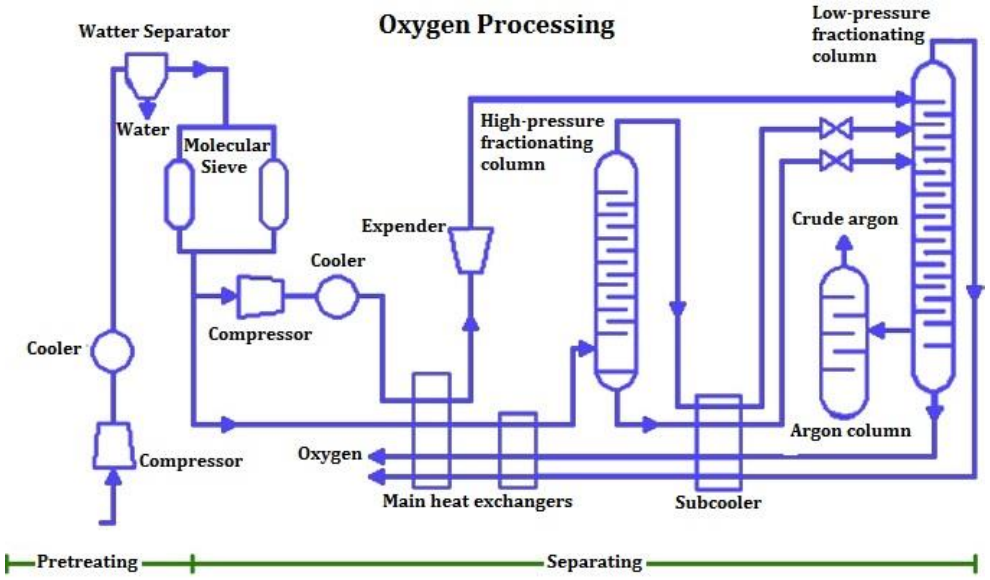

Figure 3. A cryogenic distillation system.[22]

Adsorption separation (pressure swing adsorption or PSA) is another process in which gases tend to be adsorbed to solid surfaces under pressure. A gas is adsorbed under high pressures to a surface such as a carbon molecular sieve, and reducing the pressure then desorbs the gas. PSA can be used to separate a mixture of gases because different gases are adsorbed more or less strongly to different solid surfaces. Vacuum swing adsorption (VSA) is another technique that operates at near-ambient temperatures and pressures.[9]

The current polymeric membranes can compete with these traditional technologies in specific energy consumptions when the required product mole fraction is low. In air separation, an optimized membrane module with a selectivity of more than 8 can replace a large-scale cryogenic distillation if the required molar fraction of oxygen is 50%.[23] Table 1 presents a cost comparison of the three technologies for the removal of 8% N_2 from natural gas. The total capital cost and the processing cost of the membrane technology are much lower than for the other conventional techniques.

Table 1. Cost comparison of the technologies for the removal of 8% N_2 from natural gas.[24-25]

Technology	Total capital cost (US$/Mscfd)	Processing cost (US$/Mscf)
Cryogenic distillation	11200	1.30
Pressure swing adsorption	1300	1.65
Membranes	280	0.30

Mscfd: million standard cubic feet per day; Mscf: million standard cubic feet

Unfortunately, dense polymers are not very adapted to harsh conditions. Indeed, the gas separation performance of highly-thermostable polymers such as e.g. polyimides declines above 200°C, and by now, only a few high-temperature applications have been reported for such membranes.[4] Table 2 illustrates the highest testing temperatures for gas separations by thermoresistant polymer-based membranes. T_g is the glass transition temperature, above which the polymer becomes too flexible and its mechanical performances severely decline. In addition, selectivity can decrease at high pressures of certain gases such as CO_2 because of plasticization effects.[26-27]

Table 2. The highest testing temperatures for gas separations (GS) in thermoresistant dense membranes.[28]

Heat-resistant polymeric membranes	Membrane material	Maximum GS test temperature (°C)	Maximum reported T_g (°C)
Fluorinated polymeric membranes	FBP-6FPT	75	253
Inorganic polymeric membranes	POPs	100	91
Carbocyclic polymeric membranes	PEEK	260	230
Heterocyclic polymeric membranes	PBI	400	436
Ladder polymeric membranes	BTFDA-DAB	90	> 400
Polymer blends membranes	BMI/PEI	35	> 400
Mixed matrix membranes	PBI/ZIF-90	400	> 400

Within this context, the Films in Fluids group at the University of Twente (The Netherlands) recently prepared a series of novel hyper-crosslinked inorganic-organic ultrathin membranes using interfacial polycondensation. The idea was to combine the high thermoresistance of inorganic materials with the efficient separation properties of organic materials. These so-called polyPOSS-imides consist of a large molecular network of alternating polyhedral oligomeric silsesquioxanes (POSS), i.e. silicon oxide cages with the basic formula $R_nSi_nO_{1.5n}$ (n = 6, 8, 10, 12), and organic precursors at the basis of aromatic

imides.[4] These hybrid membranes were indeed found to preserve their gas separations characteristics at elevated temperatures and pressures, i.e. up to 300°C and 60 bar[4, 29] and as such, it can become a key-enabling technology for industrial-scale gas separations under harsh conditions.[4]

In collaboration with the University of Twente, molecular modelling studies were performed for these initial hybrid membranes at University Savoie Mont Blanc (USMB, France).[30-31] They pointed to a weak link in the structures, which is the aliphatic chain linker between the inorganic and the organic moieties. The present work aims to attain more stable hybrid ultrathin membranes by using a new POSS precursor, the octa(aminophenyl)silsesquioxane (OAPS), which has three isomers depending on the *meta*, *para* and *ortho* position of the amines on the phenyl groups.

- In the first stage, an extensive literature search was carried out on thermoresistant polymers and the POSS family.

- In a second stage, experimental investigations including density, infrared (IR), and nuclear magnetic resonance (NMR) characterizations were performed for both a commercial OAPS containing all three isomers and for a controlled OAPS containing only the *para* and *meta* isomers. To better identify the nature of the isomers, the experimental results were compared to predictions of the IR and NMR spectra by quantum mechanical and machine-learning methods.

- In a third stage, the commercial OAPS was used as a precursor to make novel hybrid polyOAPS-imide membranes with increased thermoresistance. These were characterized using IR, thermal gravimetric analysis (TGA), scanning electron microscopy (SEM), energy dispersive spectroscopy (EDS) and permeability measurements.

- In a fourth stage, a force-field was developed for OAPS to be used in subsequent molecular dynamics (MD) simulations, which provide direct structural and dynamical information at the atomic level as a function of time[32] by integrating the classical equations of motion.[33]

II. Thermoresistant polymers

The main impetus for the development of thermoresistant polymers initially came from the aerospace field.[34] During the late fifties and early sixties, synthetic activity was at its pinnacle. But it declined because of the decrease in aerospace expenses, the difficulties in manufacturing the required materials, and the cost of these materials.[34] Indeed, thermal stability and processability are two opposite requirements in the production of thermoresistant polymers. As a result, few polymers have achieved commercial exploitation.

The strength of chemical bonds affects the thermal stability,[34] and the primary bond energy between the atoms in the polymer chain is considered as being the source of thermal resistance.[35,28] Table 3 shows a list of typical bond strengths.

Table 3. Bond strengths (kJ/mole).[34, 36]

C-S	273	C-N	307	C-H	416	P-O	528	C=C	609
		Si-H	319	C-F	428	P-C	580	C=N	617
		Si-C	328	Si-N	437				
		C-Cl	340	Si-O	445				
		C-C	349						
		C-O	361						

The emphasis on bond strength resulted in the development of inorganic polymers. For example, in Table 3, the Si-O bond energy in polysiloxanes is almost 450 kJ/mole. The vibrational energy increases with heat, so the energy of bond dissociation is decisive in the thermostability.[37] To achieve thermoresistant polymers:[34]

(a) The most powerful chemical bonds should be used
(b) Rearrangement reactions should not be made easy
(c) Maximum resonance stabilization should be used
(d) All the bond angles in the ring structures should be under the same tensions
(e) There should be polybinding as much as possible.

The condition (a) is not often the limiting one, because most bonds are strong enough to be stable. Almost all the systems degrade because of condition (b) because the rearrangement reactions tend to increase with high temperatures. Since more energy is needed to break the bonds that have resonance stabilization, condition (c) is an advantage.

Condition (d) refers to the angles keeping the atoms in close proximity when a bond is broken, so bond healing is possible upon dissipating the excess energy through the molecule. To meet condition (e), there should be more than one link for a skeletal atom in the polymer chain. These conditions relate to an ideal case, but in practice, a polymer has rarely a perfect structure.[34]

Table 4 shows the relative ranking of the linking groups in polymers according to the temperature at which a 25% weight loss happens in a period of 2 hours in the presence or the absence of oxygen. The amide and carbonyl links show the highest thermal stability.

Table 4. Thermal and thermal-oxidative stability of some simple flexible linking groups. These are the temperatures in ºC for a 25% weight loss in 2h without and with oxygen, respectively.[28, 38-39]

Linking group	Thermal stability (ºC)	Thermal-oxidative stability (ºC)
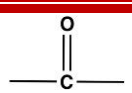	500	389
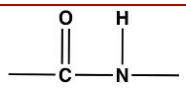	500	431
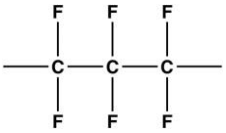	469	N/A
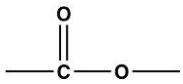	457	447
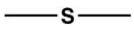	436	418
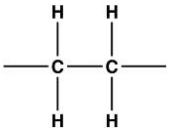	429	383
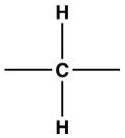	408	N/A
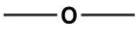	N/A	368

Secondary forces such as hydrogen bonding and dipole-dipole interactions are another important factor since the sum of these forces determines the cohesion between neighbouring chains. These forces have a crucial influence on the T_g and the melting point T_m. As such, it is

usually possible to improve the polymer resistance by increasing the number of polar side groups or by making the arrangements of the chains more regular.

The most common polymers are non-crosslinked and are called thermoplastics. The chains can also be chemically crosslinked, thus leading to the thermosets, which are produced by the curing of prepolymers or polymers.[28] Curing is a chemical process by which the prepolymer or polymer in a viscous or solid-state is converted to a material with a higher molecular mass. This can be performed by chemical reactions induced by thermal curing, electron-beam irradiation (EB curing), photo-irradiation (photo-curing) or via mixing with a chemical crosslinking agent.[35, 40] Molding or casting can be performed during curing by heating usually up to more than 200ºC. Thermosets are often more brittle, more rigid, less soluble and harder than thermoplastics.[28] Low-crosslinked thermosets with long chains (between the crosslinks) are flexible while highly-crosslinked ones with shorter chains are rigid.[28]

Degradation and thermal decomposition happen through pyrolysis or thermolysis of the polymers. As explained above, to overcome decomposition and degradation, the polymer should preferably include aromatic and/or heterocyclic backbones (not aliphatic backbones), resonance structures and strong chemical bonds with high bond enthalpies. As such, thermoresistant polymers are often made up of alternate moieties of aromatic rings and heterocyclic units, which is the case for e.g. polyimides (PIs) (Figure 4) and their derivatives.

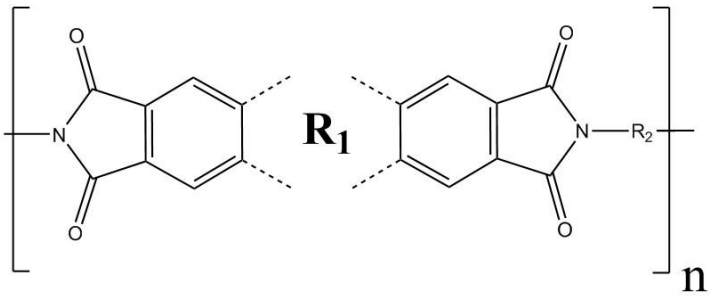

Figure 4. The general structure of a polyimide, R_1 and R_2 are usually aromatic and/or heterocyclic groups.

Durability in the range of 250-350ºC is now well established for the PIs.[41] Hydrogen bonding has also an important role in other highly polar polymers such as polyurethanes and polyamides.[28, 37] As for the PIs, the resonance stabilization of the aromatic structures supplies further bond strength and thermoresistance.[35] Indeed, thermosets such as phenolic resins

present a high thermostability due to their high aromatic content, making them suitable for use under harsh conditions.[42]

When polymers are exposed to heat, thermoplastic and thermoset polymers show different behaviours. Thermoplastic polymers are melted or softened and return to their solid-state by heating and cooling. In this repeatable process, the covalent structure of the thermoplastic polymer does not change,[43] and weak forces such as Van der Waals forces, dipole-dipole interactions or hydrogen bonding allow for these materials to be recycled.[40] On the other hand, due to the existence of crosslinks between the molecules, thermosets do not melt or soften but break down at elevated temperatures.[40] However, it should be noted that for highly-thermoresistant thermoplastic polymers, the molten temperature can be quite close to the degradation temperature too.

There is no standard definition for the thermal stability of polymers. For the user, the criterion is that the features of interest should be kept under the desired range of temperatures.[34] However, P. E. Cassidy [20] has defined the thermoresistance of a polymer as:

- Maintenance of the polymer chemical features above 300ºC in air measured by Thermogravimetric Analysis (TGA).
  or
- Maintenance of the polymer physical characteristics for a long time at 280ºC in air evaluated by Isothermal Gravimetric Analysis (IGA).

TGA is a popular technique to study the deterioration of the polymers because of its wide range of applications and reliability:[34]

1- Easy measurements
2- Wide choice of commercial instrumentation
3- Small samples (milligrams or less)
4- Can be accomplished under any atmosphere
5- No specific fabrication procedure is needed. Infusible and insoluble materials can also be tested
6- No limitations in heat and mass transfer at low heating rates.[44]

IGA is a similar thermogravimetric technique, but it measures the weight change with time at a specified temperature, giving information on the material stability and composition. It is routinely used in industry.[45-46] IGA is closer to the real conditions, but TGA is easier to use in an academic laboratory since it analyses the samples in a shorter time.[47]

Since the mechanisms for loss of the thermal properties are not exactly addressed, other researchers have interpreted differently the definition of thermoresistant polymers. Indeed, terms such as "high" or "good" have been frequently used to describe thermoresistance without addressing quantification.[28] Some questions have been raised, such as the environment for studying thermoresistance, the stability of the material at a specific temperature, etc.[37]

There are six categories of thermoresistant polymers:[28]

1- Fluorinated polymers such as polytetrafluoroethylene (PTFE), which have high C-F bond energies and shielding of the carbon chains
2- Ladder polymers such as polypyrrone, which have polybondings, stiff chains and high T_g
3- Inorganic polymers such as polyphosphazenes and siloxanes, which have strong bonds
4- Carbocyclic polymers such as polysulfones (PSFs) and polyamides (PAs), which have stiff chains, resonance stability and high T_g
5- Heterocyclic polymers such as PIs and polybenzimidazoles (PBIs), which have the same features as carbocyclic polymers.

There are also three other ways to boost the chain stiffness by incorporating inorganic or polymeric additives or by introducing crosslinks into the target polymer:

6- Hybrid inorganic/polymers;
7- Polymer blends;
8- Thermosets.

Figure 5 shows a spectrum of low to high-performance thermoplastics polymers in comparison to their cost. In this Figure, thermoplastics are divided into three main types according to their thermal, chemical, and mechanical stabilities. Some highly thermoresistant

thermoplastics are listed in Table 5.[28] The Continuous Use Temperature (CUT), also called the Relative Temperature Index (RTI), is the temperature at which 50% of the features (such as mechanical strength) are maintained after 100000 hours. It characterizes durability. The Heat Distortion Temperature (HDT) is the temperature at which a material distorts under a certain stress. The typical stress is 1.82 MPa but values between 0.45 and 8 MPa have also been used.[48]

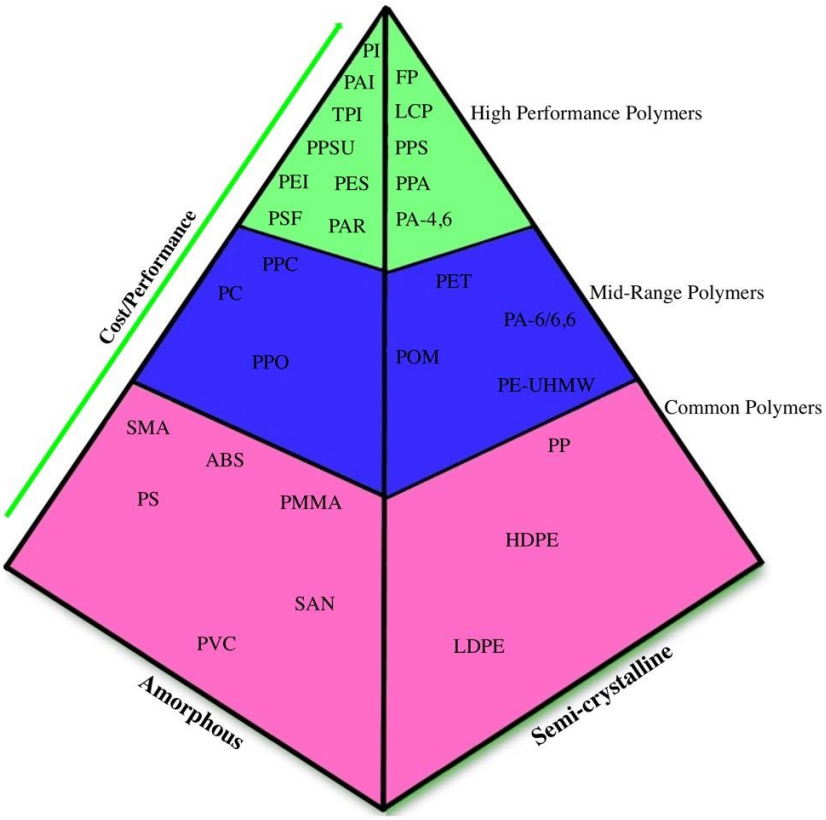

Figure 5. The pyramidal scheme of typical thermoplastic materials.[28]

Table 5. Some highly thermoresistant thermoplastic polymers.[28, 49-55]

Abbreviation	Polymer	T_g (°C)	CUT[a] (°C)	HDT[b] (°C)/Stress (MPa)
PAI	Polyamide-Imide	275	250	279/1.82
PI	Polyimide	250	288	246/1.8
PEE	Polyethersulfone	224	177-204	204-238/1.82
PEI	Polyetherimide	213	177-204	199-216/1.8
PSF	Polysulfone	190	149-171	171-182/1.82
PEEK	Polyetheretherketone	143	204-232	177-321/1.8
PPA	Polyphthalamide	134	204-232	117-260/1.8
PPS	Polyphenylene Sulfide	92	204-232	149-288/1.8

[a] Continuous Use Temperature.

[b] Heat Deflection Temperature.

From a practical point of view, the processability of the membrane is another factor that affects thermoresistance in addition to stability and durability. Figure 6 shows that these three factors have to be unified.

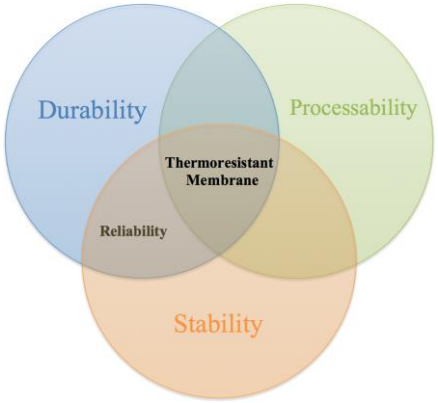

Figure 6. The three important factors to prepare thermoresistant membranes.[28]

The processing difficulties (green in Figure 6) mainly result from the low solubility of thermoresistant polymers in the common solvents.[28] Some approaches to improve the situation are:

1- The use of the aprotic polar solvents such as DMAC, DMF, and NMP.[56-57]

2- Adding inorganic salts such as LiCl or $CaCl_2$ to the aforementioned solvents.[58-59]

3- The use of acids, such as HF, CHF_3, H_2SO_4 and sulfonic acid.[60]

4- Thermal phase inversion, in which the polymer is dissolved at a high temperature in a solvent and the solution is cooled to precipitate the polymer.[60]

As mentioned above, polyimides (PIs) are well suited to thermoresistant applications due to their remarkable thermo-oxidative durability and mechanical features.[61-62] Besides, they exhibit high CO_2/CH_4, H_2/CO_2, H_2/N_2, and CO_2/N_2 selectivities. They are thus very good candidates for gas separation applications.[63] PIs are heterocyclic and can be aliphatic or aromatic. To overcome the difficulties of synthesis and processing caused by their limited solubility and infusibility, noticeable efforts have been done to incorporate bulky substituents, alkyl side chains, biphenylene, and twisty units into the polymer backbones.[41, 62, 64-67 68-71] Besides, it is known that polymers having $-CF_3$ exhibit boosted solubility and that the strong C-F bond further improves the chemical and thermal stability. Consequently, a lot

of studies have been carried out to explore the structural properties of $–CF_3$ substituted monomers in PIs. The $–CF_3$ group improves the fractional free volume (FFV) and disrupts the chain packing, which leads to increased permeability.[28] The PIs based on the 4,4'-(hexafluoroisopropylidene)diphthalic anhydride (6FDA) monomer (Figure 7) present indeed very high CO_2 permeabilities and CO_2/CH_4 selectivities:[28, 72]

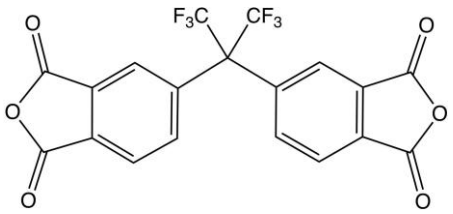

Figure 7. The 6FDA dianhydride.

Table 6 reports studies performed on the gas separation applications of 6FDA-based PIs:

Table 6. 6FDA-based polyimide gas permeability data in Barrer at 35°C and pressures up to 20 atm.[28]

Membrane	Full Name	P (atm)	H_2	O_2	N_2	CO	CH_4
6FDA-ODA[73]	2,2-bis(3.4-dicarboxyphenyl) hexafluoropropane dianhydride and oxydianiline	1-10	-	4.3	0.83	23	0.38
6FDA-MDA[73]	2,2-bis(3.4-dicarboxyphenyl) hexafluoropropane dianhydride and methylenedianiline	1-20	-	4.6	0.81	19	0.42
6FDA-IPDA[73]	2,2-bis(3.4-dicarboxyphenyl) hexafluoropropane dianhydride and isopropylidenedianiline	1-10	-	7.5	1.34	30	0.70
6FDA-6FpDA[74]	2,2-bis(3.4-dicarboxyphenyl) hexafluoropropane dianhydride and 4.4' (hexafluoroisopropylidene)-dianiline	10	-	16	3.40	64	1.60
6FDA-m-PDA[75]	2,2-bis(3.4-dicarboxyphenyl) hexafluoropropane dianhydride and *meta*-phenylenediamine	1.4-8.2	20.3	2.6	0.36	8.2	0.14
6FDA-2,4-DATr[75]	2,2-bis(3.4-dicarboxyphenyl) hexafluoropropane dianhydride and 2,4-diaminotoluene	1.4-8.2	87.2	7.4	1.31	28.6	0.71
6FDA-3,5-DBTF[75]	2,2-bis(3.4-dicarboxyphenyl) hexafluoropropane dianhydride and 3.5-diaminobenzotrifluoride	1.4-8.2	58.6	6.4	1.17	21.6	0.45
6FDA-4BDAF[76]	2,2-bis(3.4-dicarboxyphenyl) hexafluoropropane dianhydride and 4.4'-bis(aminophenoxyphenyl) hexafluoropropane	3-8.8	46	5.4	0.98	19	0.51
6FDA-3,3'-ODA[76]	2,2-bis(3.4-dicarboxyphenyl) hexafluoropropane dianhydride and 3,3' -oxydianiline	3-10	14	0.68	0.10	2.1	0.03
6FDA-3BDAF[76]	2,2-bis(3.4-dicarboxyphenyl) hexafluoropropane dianhydride and 3,3'-bis-(aminophenoxyphenyl) hexafluoropropane	3-8.8	21	1.3	0.24	6.3	0.13
6FDA-p-PDA[76]	2,2-bis(3.4-dicarboxyphenyl) hexafluoropropane dianhydride and paraphenylenediamine	2.8-6.8	23	2.1	0.38	11.8	0.18
6FDA-mp'ODA[77]	2,2-bis(3.4-dicarboxyphenyl) hexafluoropropane dianhydride and 3,4'-oxydianiline	10	23.7	1.6	0.26	6.1	0.12
6FDA-APAP[77]	2,2-bis(3.4-dicarboxyphenyl) hexafluoropropane dianhydride and 2-(3-amino-(4-phenyl)-2-amino- phenyl)propane	10	38.2	2.89	0.47	10.7	0.22

6FDA-BATPHF[77]	2,2-bis(3.4-dicarboxyphenyl) hexafluoropropane dianhydride and 2,2-bis(4-(4-amino-2-trifluoropropane dianhydride and 2,2-bis(4,4.-amino-2-trifluoromethylphenoxy) phenyl) hezafluoropropane	10	55.4	6.5	1.30	22.8	0.70
6FDA-DAF[78]	2,2-bis(3.4-dicarboxyphenyl) hexafluoropropane dianhydride and 2,7-diaminofluorene	10	-	7.85	1.27	32.2	0.63

The studies of Sen and Banerjee[79] on other types of dianhydrides such as 4,4'-oxydiphthalic anhydride (ODPA), 2,2-Bis[4-(3,4-dicarboxyphenoxy) phenyl]propane dianhydride (BPADA), 3,3',4,4'-benzophenone tetracarboxylic dianhydride (BTDA) and pyromellitic dianhydride (PMDA) (Figure 8) also showed dramatically higher permeabilities and selectivities than the typical PSF, cellulose acetate (CA) and polycarbonate (PC) membranes.

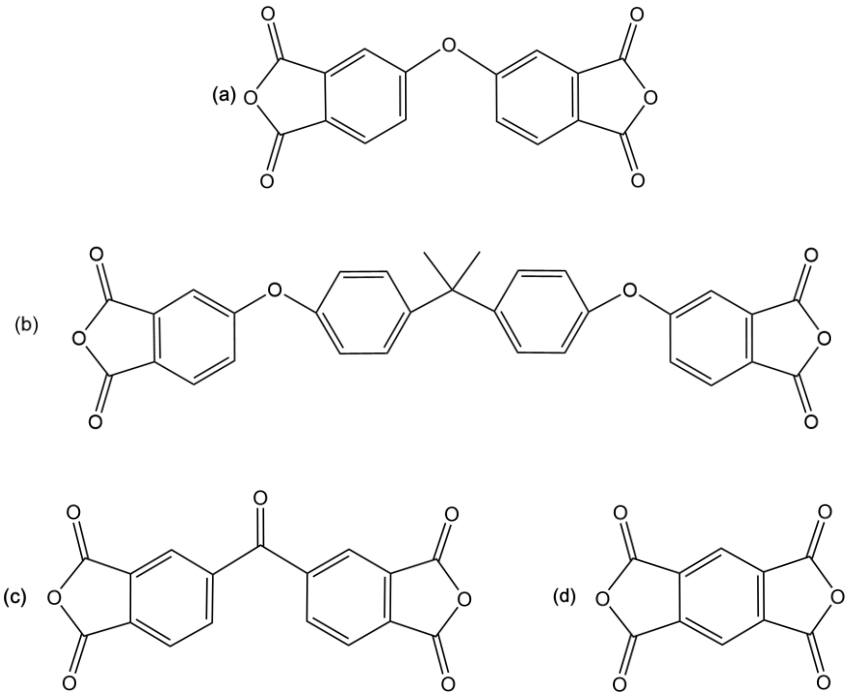

Figure 8. (a) ODPA, (b) BPADA, (c) BTDA and (d) PMDA.

Al-Masri et al.[80] synthesized dense 6FDA-based PIs membranes with methyl substituents at high yields (Figure 9), which were easily soluble in typical high boiling point aprotic solvents such as NMP, DMF, and DMSO, and also in low boiling point solvents such as THF, CH_2Cl_2, and $CHCl_3$. Increasing the ratio of the methyl to imide nitrogen content resulted in higher permeabilities, diffusivities, and solubilities, as well as T_g being higher than 300°C (Table 7).[80]

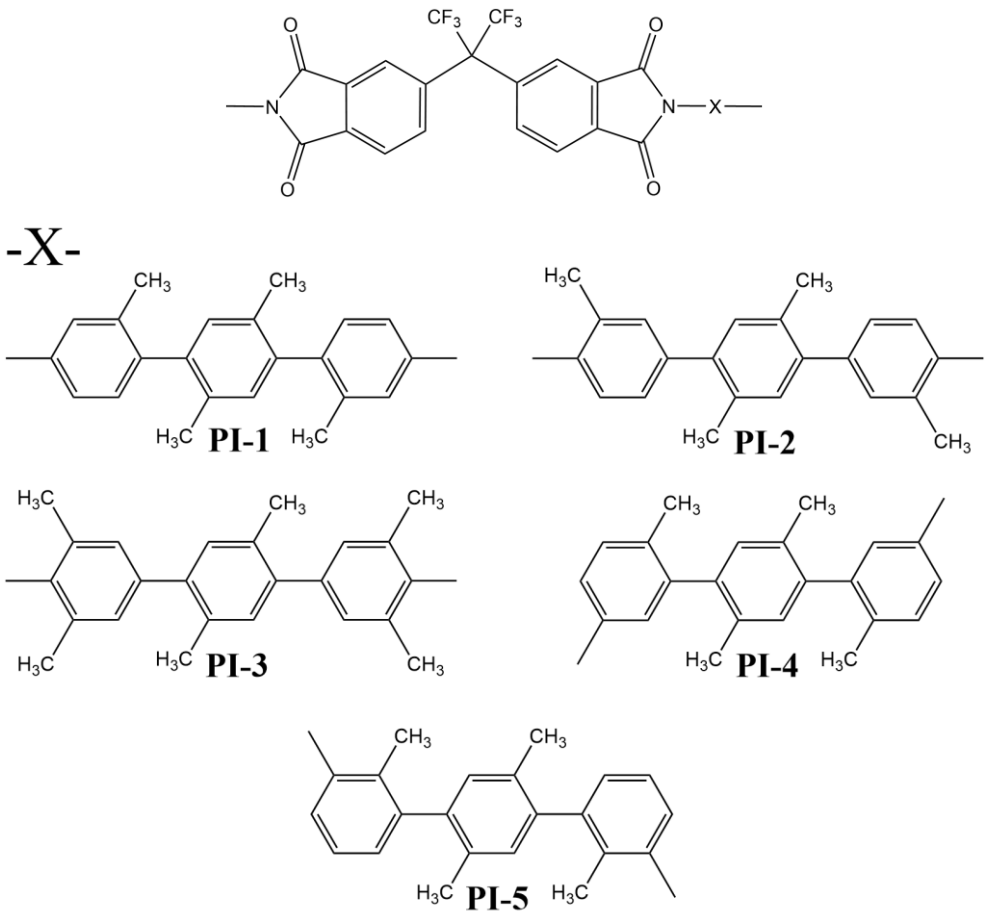

Figure 9. Different 6FDA-based PIs synthesized by Al-Masri et al.[80] Note that PI-3 has two methyl substituents on the first and third rings.

Table 7. Single-gas permeabilities in Barrer for the different PIs of Al-Masri presented in descending order as compared to a polysulfone (PSF-1) membrane.[80]

PI	P_{He}	P_{H_2}	P_{CO_2}	P_{O_2}	P_{N_2}	P_{CH_4}
PI-3	230	350	360	67.0	16.5	15.0
PI-5	160	210	190	32.0	7.3	5.6
PI-4	84	100	62	12.0	2.4	1.9
PI-2	47	51	not measured	8.6	1.6	1.1
PSF-1	71	72	32	7.2	1.4	0.9

It is clear that isomerism makes a difference. A report on different PIs isomers[81] indicated that the PMDA-4,4'-ODA polyimide has higher permeability and a lower selectivity toward He, CO_2, CH_4, O_2, and N_2 than its PMDA-3,3'-ODA isomer. The authors attributed the differences to the intrasegmental (rotational) mobility of the *para* PMDA-4,4'-ODA as compared to the *meta* PMDA-3,3'-ODA isomer. The phenyl rings in the *para*-isomer can rotate around their principal axis whereas no rotation is possible in the *meta*-isomer. Dynamic

mechanical analyses, as well as measurements of CO_2 diffusivity in both isomers, support this hypothesis. Similarly, a series of hyperbranched copolyimides (HBPI)s based on the commercially-available monomers ODPA (Figure 8), ODA, and 2,4,6-triaminopyrimidine (TAP) (Figure 10)[82] show a considerably lower permeability for all gases than a linear ODPA-ODA polyimide. The permeabilities improved with increasing content of the ODA amine. However, low permeabilities are not always only a drawback. Compared to other polyimides, the HBPIs presented very high selectivities, which indicates that these materials can be used in gas separation applications such as CO_2/N_2, O_2/N_2, CO_2/CH_4, H_2/CH_4, etc.

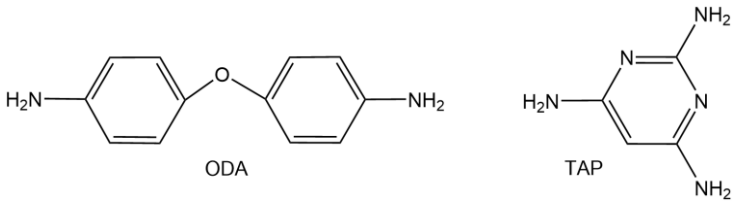

Figure 10. The ODA and TAP monomers.

In addition to the influence of the chemical structures and the high-temperature issues, the performance of the PIs membranes decreases when they are exposed to high pressures of penetrants such as CO_2. This phenomenon, which is called plasticization, reduces the T_g and the thermal stability while the permeability increases along with a loss in selectivity.[83]

To further improve the thermostability of PI membranes, many methods such as polymer-polymer blending,[84] inorganic-polymer blendings[85], and crosslinking[86] have been employed. The latter is at the basis of the hypercrosslinked polyPOSS-imides networks designed by the University of Twente. For the current project, the 6FDA, PMDA, and ODPA dianhydrides (Figure 8) have been selected as possible organic precursors for the imides.

III. POSS and OAPS in the literature

Compounds containing Si-O have been studied for many years.[87] In the last 2 decades, the new field of silsesquioxane chemistry, based on the $RSiO_{3/2}$ repeat units with R being an organic fragment, has gained interest. These materials between organic silicon polymers and inorganic compounds display versatile hybrid features, which are due both to their potentially-reactive and easily-modified R-Si part and to their thermally-stable and chemically-inert inorganic Si-O-Si part. Various structures from ladder polymers to highly ordered species with the common formula $(RSiO_{3/2})_n$, where n is usually 6, 8 or 10, have been synthesized.[88]

POSS (Figure 11)[89] is the abbreviation of polyhedral oligosilsesquioxanes, i.e. n = 8. These chemically-cubic siloxane cages have nanoscale dimensions in the range of 1-3 nm depending on the organic substituent R along with a very robust inorganic framework.[87]

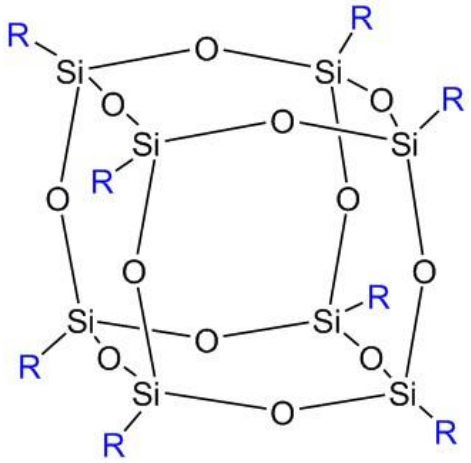

Figure 11. Polyhedral oligosilsesquioxanes (POSS)[89] - T_8R_8 structures.

The full nomenclature of POSS is complicated, so the nomenclature used for siloxane polymers is employed. A silicon atom connected to three oxygen atoms then connected to another silicon is defined by "T", and if R = H as in Figure 11, the abbreviation of the structure is T_8H_8. In T_8R_8, R can also be alkyl, aryl, alkoxy, siloxy, phenyl, aminophenyl, etc.[87] Many routes have been reported to synthesize POSS, but all of them can be listed in two reaction types:

a) Preparing POSS derivatives by making a T_n core from a precursor having fewer than *n* silicon atoms,

b) Chemically modifying the functional groups of an existing T_n core to get a new POSS derivative.[87]

In recent years, the incorporation of POSS into polymer matrices has attracted attention in order to create nanocomposites with enhanced mechanical and thermal properties.[90] Their rigid cage-like structure, nanoscale size and ability to tailor properties by introducing different functional groups make POSS effective candidates for high-performance membranes.[91] They can be introduced by physical blending, chemical polymerization, and crosslinking.[92-94] The thermal stability of the POSS-based membranes depends on the amount of POSS in the polymer matrix, the POSS-polymer interface interactions and the amount of crosslinking. In addition, the local polymer topology, interactions and mobility can be changed and as a result, macroscopic features such as the T_g, thermal and mechanical stability can be improved. Indeed, the preparation of hybrid membranes by incorporating inorganic fillers into high-performance polymers is aimed at overcoming the weaknesses of both types of materials, e.g. the poor processability of the inorganic fillers and the low thermal and mechanical stabilities of the polymers. However, the preparation of defect-free and robust nanocomposite membranes still remains a challenge.[28]

As far as gas separation properties are concerned, POSS has been shown to affect the permeability characteristics in mixed-matrix membranes (MMM). Incorporation of a commercial poly(ethylene glycol)-functionalized POSS (PEG-POSS) in two grades of poly(ether block-amide), PEBAX® MH 1657 and PEBAX® 2533, showed a higher permeability for both MMMs and a higher selectivity for PEG-POSS/PEBAX® 2533.[95] A MMM comprising of octa(aminophenyl)silsesquioxane (OAPS) in 6FDA-methylenedianiline (6FDA-MDA) up to 20% wt displayed a decrease in the permeabilities for all the gases tested, except for CO_2 with increasing OAPS loading.[96] Another report showed improved selectivities for CO_2 over H_2 in POSS/PEBAX® MMMs.[97] The authors attributed this observation to stronger interactions between the polymer and CO_2 and reduced transport channels for H_2. As far as hybrid membranes are concerned, Dasgupta et al.[98] synthetized polyimide-POSS (PI-POSS) membranes with the POSS being attached at both ends of the polyimide chains. The permeability of CO_2, N_2, O_2 and CH_4 increased, while the selectivities for gas pairs such as CO_2/CH_4 and O_2/N_2 were comparable to those in the pure PI membranes.

Nieck E. Benes, Michiel J. Raaijmakers and colleagues at the University of Twente have recently synthesized hybrid hypercrosslinked polyPOSS-imide membranes, where the inorganic POSS is linked through an extensive periodic network by organic aromatic imide bridges.[4, 99-100] As shown in Figure 12, an organic solvent containing the organic monomer and an aqueous phase comprising an octa(aminopropyl)silsesquioxane POSS are contacted. A polycondensation reaction occurs at the interface and this results in a polyPOSS-(amic acid) intermediate. The subsequent step is a heat treatment to convert the amic acids to cyclic imides (imidization). The chemical structures involved in the polycondensation and imidization steps are provided in Figure 13. In the following part of this work, the name "POSS" will be used either for the entire family or for this specific octa(aminopropyl)silsesquioxane when referring to the work of the University of Twente.

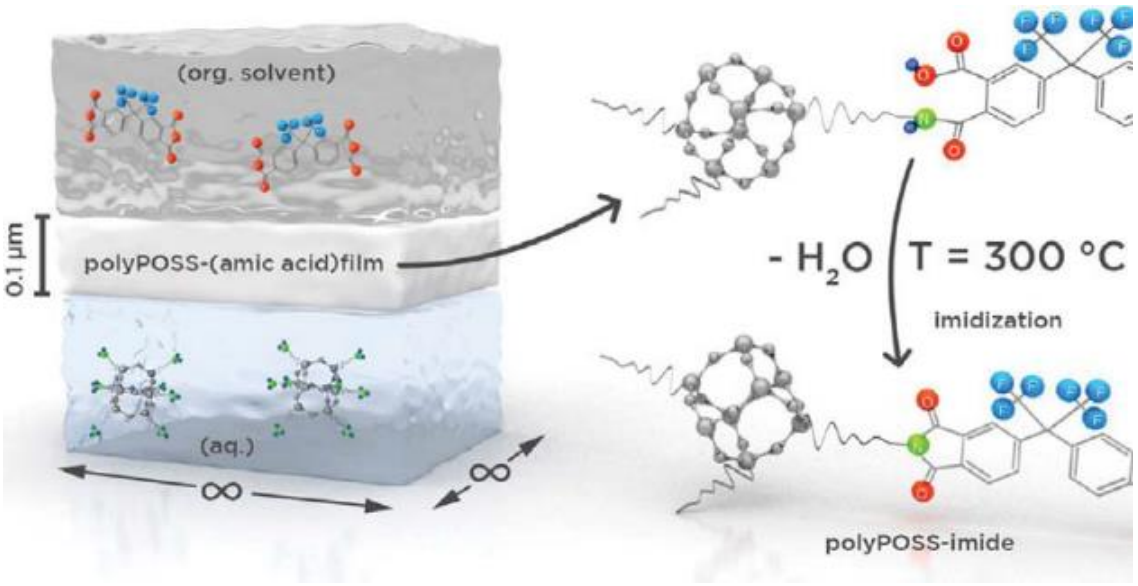

Figure 12. Interfacial polycondensation reaction of 6FDA in toluene and octa(aminopropyl)silsesquioxane POSS in water and the subsequent conversion of the amic acid to the cyclic imide (imidization) by a heat treatment up to 300°C.[4]

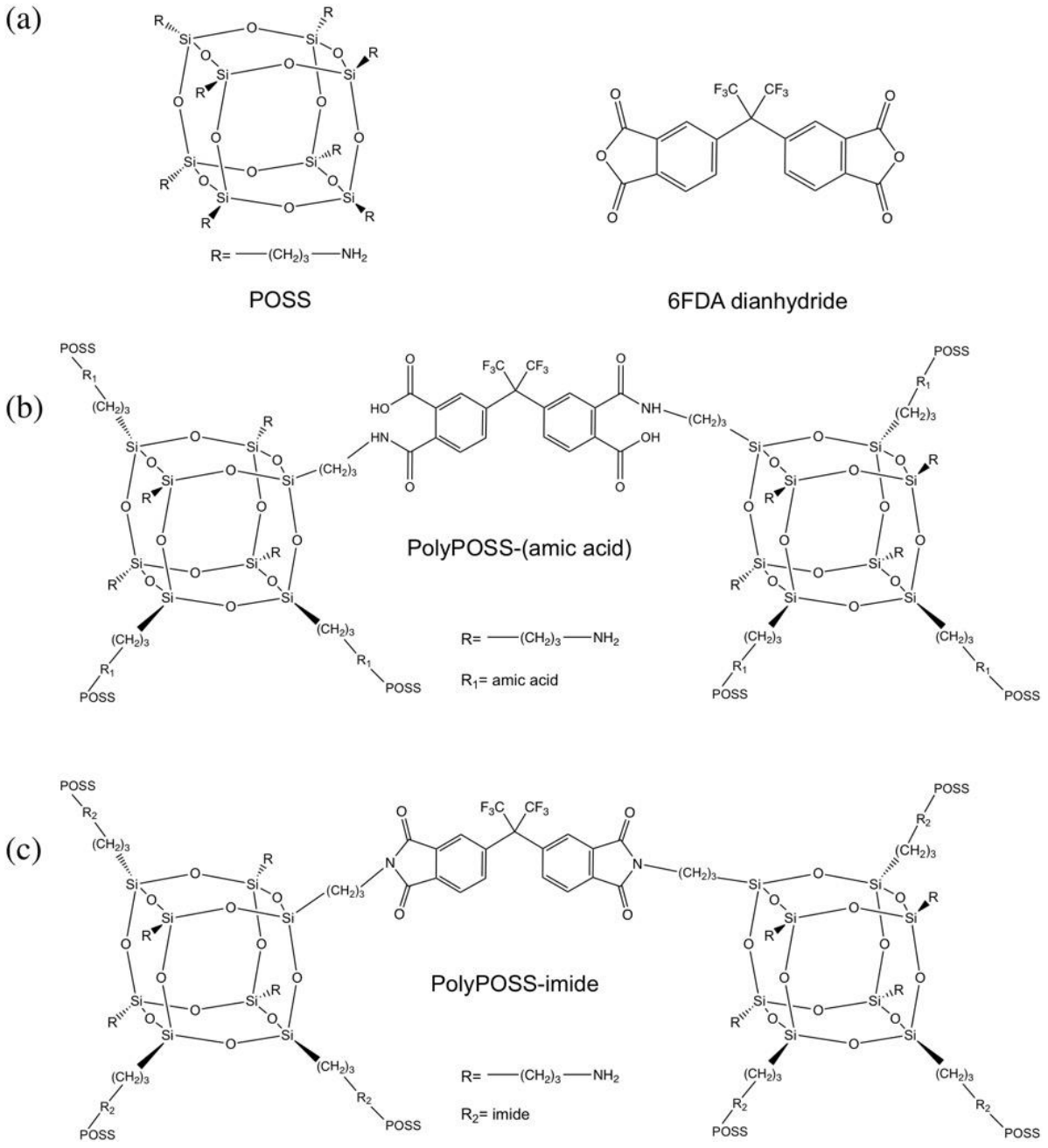

Figure 13. Chemical structures of (a) the POSS and 6FDA dianhydride monomers, (b) the interfacial polycondensation leading to the polyPOSS-(amic acid), and (c) the imidization leading to the 6FDA polyPOSS-imide network.[31]

As can be seen in Figure 14, the polyPOSS-imide thin films present various gas separation and permeabilities at a trans-membrane pressure of 2 bar and over a large range of temperatures, which arise from the rigid POSS and the nature of the mobile organic moieties (here, BPDA and BPADA, chemical structures provided on the right side of Figure 14).[99-100]

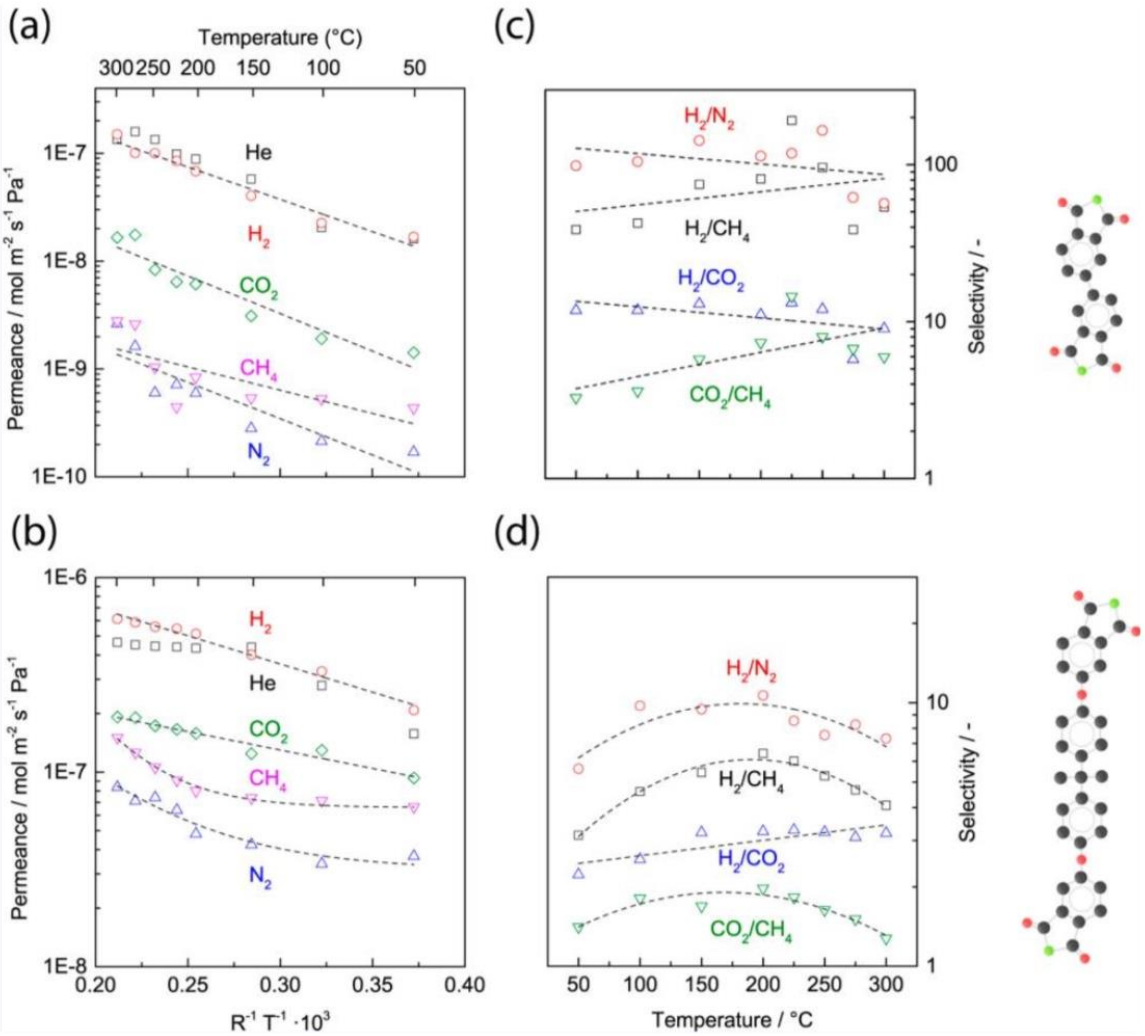

Figure 14. Left side: Arrhenius plot of the logarithm of the single-gas permeance as a function of 1/T for polyPOSS-imides derived from (a) BPDA and (b) BPADA. Right side: the corresponding ideal gas selectivities for H_2/N_2, H_2/CH_4, H_2/CO_2 and CO_2/CH_4 as a function of T.[100]

Raaijmakers et al. reported the polyPOSS-imide activation energies for gas permeation as being 5−7 higher than those in conventional polyimides.[4] They attributed these relatively high activation energies to the high-energy barriers for gas diffusion in the rigid networks. Some of these membranes could maintain the selectivity for H_2/CH_4 and H_2/N_2 and even increase the selectivity for H_2/CO_2 up to 300°C. A TGA analysis confirmed that no degradation happened below 300ºC.[100] The impact of elevated pressures of plasticizing gases on the sorption, dilation and swelling of the polyPOSS-imide membranes was also investigated. Compared with conventional polyimides such as Matrimid® (3,3',4,4'-benzophenone tetracarboxylic dianhydride and diaminophenylindane), the sorption and swelling of polyPOSS-imide membranes were found to be much higher after exposure to CO_2

and CH_4 under pressures up to 50 bar. It was attributed to the large quantity of open space in the hybrid networks and the flexible responses of the networks.[29]

Studying polyPOSS-imide networks via molecular dynamics (MD) simulations confirmed their remarkable abilities for gas separations up to 300ºC.[26] A comparison of uncrosslinked PMDA and POSS mixtures, the amic-acid intermediates, and the final PMDA polyPOSS-imide networks indicated that the volume shrinkage during imidization was less than the quantity of water removal, thus leading to a large void space and an improved gas solubility in the polyPOSS-imides. The model membranes also showed solid-like elastic moduli at room temperature and at 300ºC when subjected to uniaxial tension.[30] In another study, new molecular models were obtained for the flexible 6FDA precursor and compared to those with the shorter and rigid PMDA. Crosslinking 6FDA with POSS led to a larger thermally-induced dilation of the networks and more volume loss per H_2O over imidization than for PMDA.[31] Figure 15 shows the isotropic dilation for the 6FDA and PMDA polyPOSS-imide networks at 300ºC. As can be observed, the PMDA polyPOSS-imide is more resistant but only at high dilations. The -$(CH_2)_3$- linker was found to play the main role in the first part of the deformation for both samples and as such to be a "weak link".

POSSs with stronger R substituents such as phenyl groups should offer a higher thermostability than the aliphatic groups. However, the new POSS precursor should also have NH_2 functional groups, as the polycondensation requires them to react with the dianhydrides and produce the links between organic and inorganic fragments. Since the imide part proved its reliability in thermoresistant membranes,[4, 99] the dianhydride precursors can be conserved.

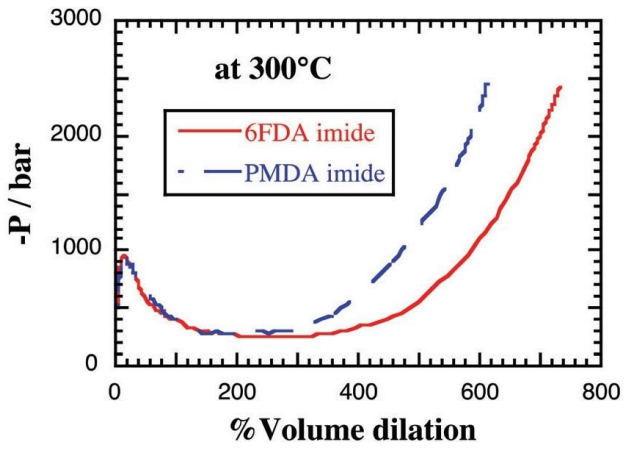

Figure 15. Isotropic dilation for model 6FDA and PMDA polyPOSS-imide networks at 300ºC.[31]

Although the phenyl derivatives of POSS offer high thermal stability (> 400ºC/air), they have not attracted as much attention as the other types of POSS, because the most typical phenyl POSS, i.e. $[PhSiO_{1.5}]_8$ referred to as octa(phenyl)silsesquioxane (OPS), presents a low solubility (less than 200 mg in 1 litre of boiling CH_2Cl_2). Therefore, the isolation of this compound is difficult and it can only be prepared in amounts of hundred milligrams. A better yield can be obtained via base-catalyzed synthesis.[101-104] Figure 16 shows the reaction pathway for the synthesis of OPS by Brown et al.[102]

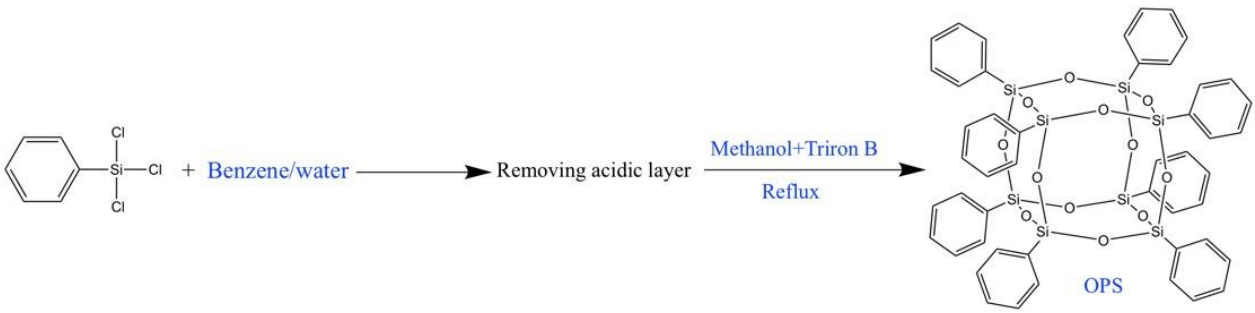

Figure 16. Octa(phenyl)silsesquioxane (OPS).[101]

However, as noted above, our new POSS precursor will require $-NH_2$ groups to carry out polycondensation. Nitration of OPS was the first electrophilic substitution reported by Olssen and Gronwall in 1961.[105] The authors described the NO_2 nitro groups of the resulting octa(nitrophenyl)silsesquioxane (ONPS) as inert since they could not reduce them to amines, and consequently, no new effort was reported for 38 years.[101] Tamaki, Laine et al.[106] revisited the reaction and realized that these nitro groups can be easily reduced using formic acid/Et_3N as the reducing agent with Pd/C as the catalyst. This produced octa(aminophenyl)silsesquioxane (OAPS).

Figure 17 shows the three possible pure isomers for OAPS depending on the position of the amine substituents, i.e. the *meta*, *ortho* and *para* forms. However, in practice, these are ideal structures. In reality, the synthesis route summarized in Figure 18 leads to a mixture of OAPS cages with the different groups on the same cage being probably in different forms. For example, a cage can have five $-NH_2$ groups in the *meta* position, two in the *ortho* position, one in the *para* position, and so on.

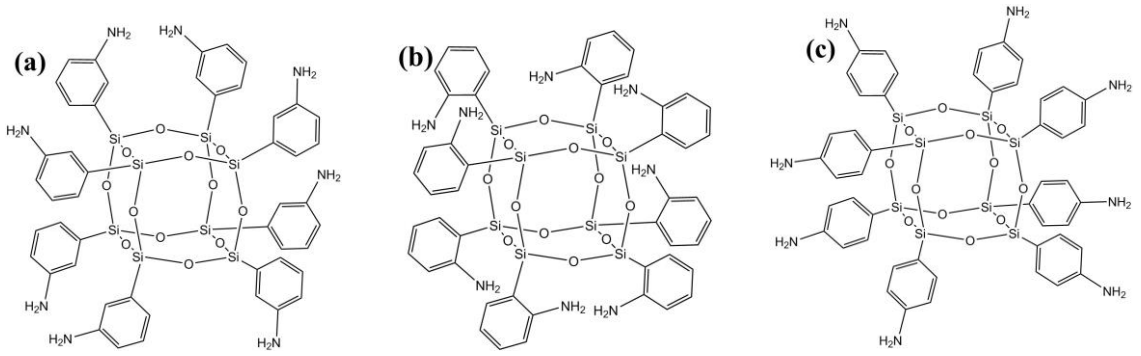

Figure 17. The pure (a) *meta* (b) *ortho* and (c) *para* isomers of OAPS.

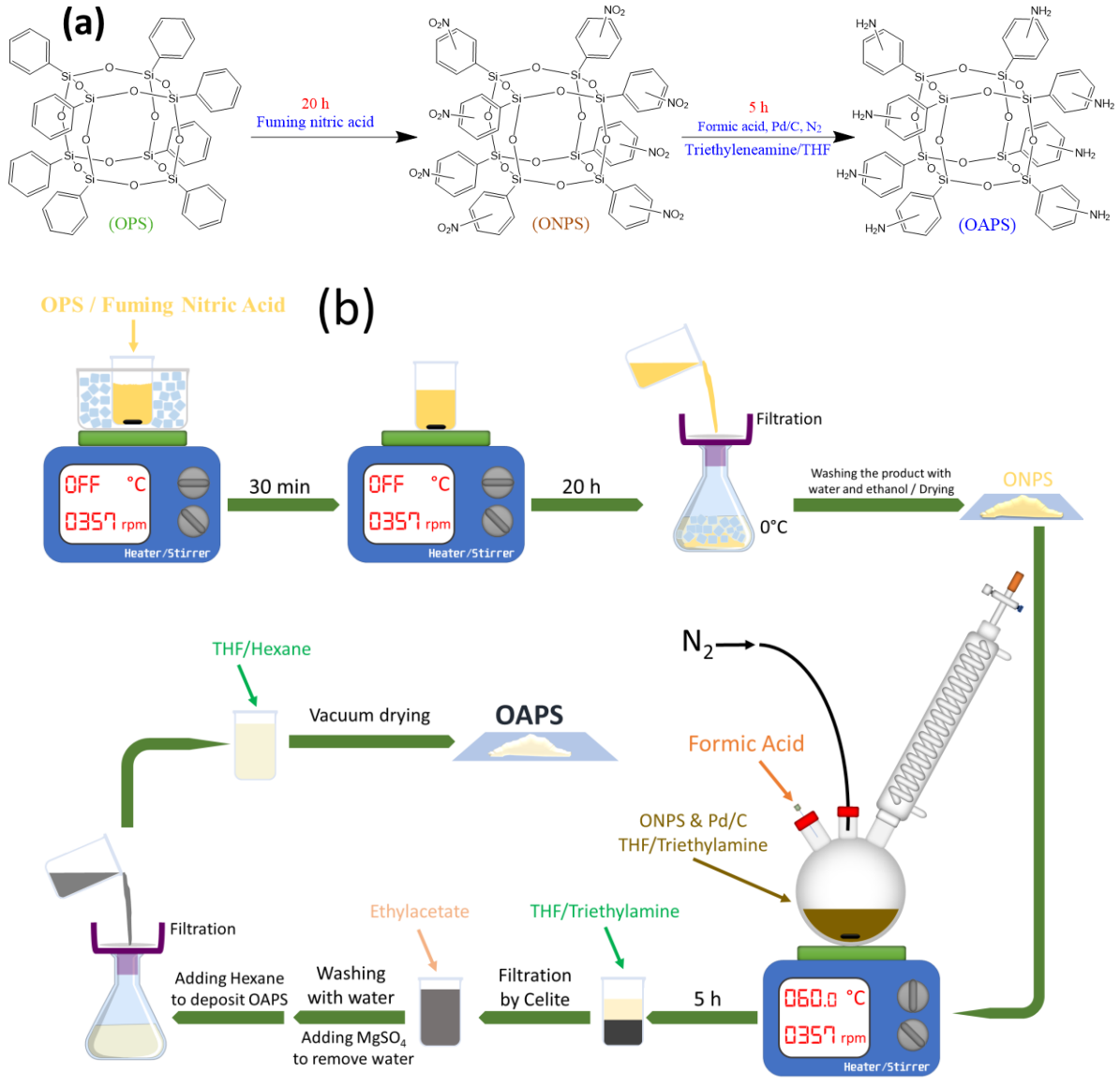

Figure 18. (a) The summary and (b) the details of the synthesis of ONPS (octa(nitrophenyl)silsesquioxane) and OAPS (octa(aminophenyl)silsesquioxane) from OPS (octa(phenyl)silsesquioxane) by Laine's method.[106]

Rather than modifying the OPS structure, another less-used route is to start directly from aminophenyltrimethoxysilane (APTMS) precursors for the aminophenylsilsesquioxane

(APS) structures. This was done by Lee et al.,[107] by using the *meta* and *para* isomers of APTMS shown in Figures 19(a-b). The *ortho* isomer was not included. Both *meta*-aminophenylsilsesquioxane (*meta*-APS) and *para*-aminophenylsilsesquioxane (*para*-APS) isomers were synthesized in the same way (Figure 19(c)): their *meta*-APTMS and *para*-APTMS precursors reacted individually with tetrabutylammonium hydroxide and were then quenched with glacial acetic acid. The separate products (pure *meta*-APS and pure *para*-APS) each led to a mixture of cage sizes ranging from 8 to 14 silicon units with the dodecamer being predominant. This alternative approach allows for better control of the isomer proportions, but its downside is that the cage sizes are less well-controlled than with Laine's nitration/reduction of OPS (Figure 18).

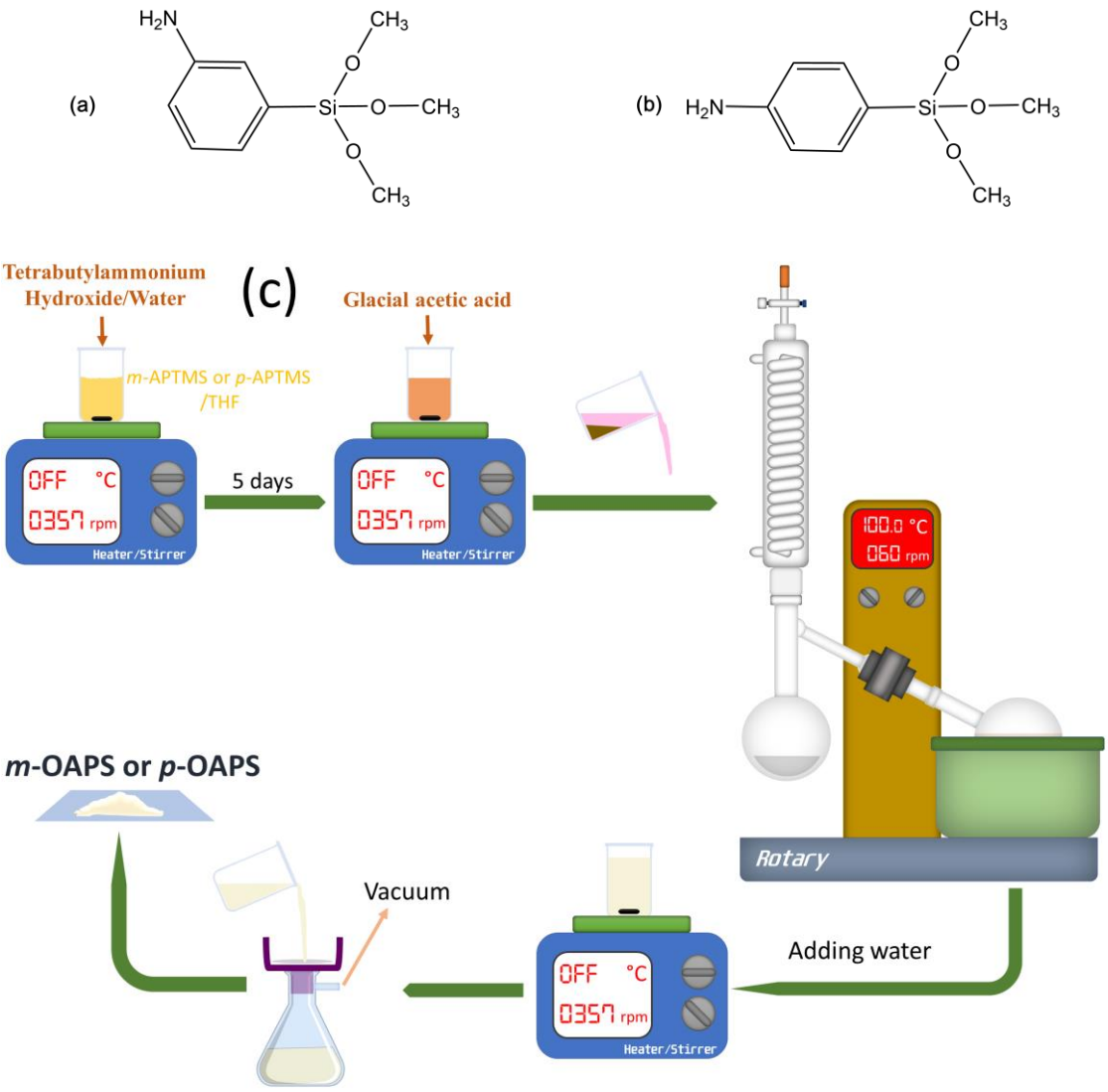

Figure 19. The (a) *meta* and (b) *para* isomers of APTMS (small precursors for isomer-specific OAPS) along with (c) the details of the synthesis of OAPS from APTMS by Lee's method.[107]

More recently, the Norwegian SINTEF research organization,[108] which is a partner of the University of Twente, used a controlled sol-gel conversion upon hydrolysis and condensation of the *meta* (30-40%) and *para* (60-70%) APTMS precursors bought from Gelest.[109] The final product is a 21% w/w solution of *para* and *meta* isomers of OAPS in DMSO. Although Gelest can produce the APTMS isomers individually, the mixture of *meta* (30-40%) and *para* (60-70%) isomers of APTMS is less expensive.[109]

As a precursor for hybrid structures, OAPS has already been used in blends[94, 96, 110] or in covalent-bond reactions.[90, 98] An example is the polyOAPS-PMDA structure (Figure 20),[111] which was built from both monomers reacting directly in NMP (and not through interfacial polymerization). It was able to show a thermal stability up to 500ºC with a 5% mass loss.

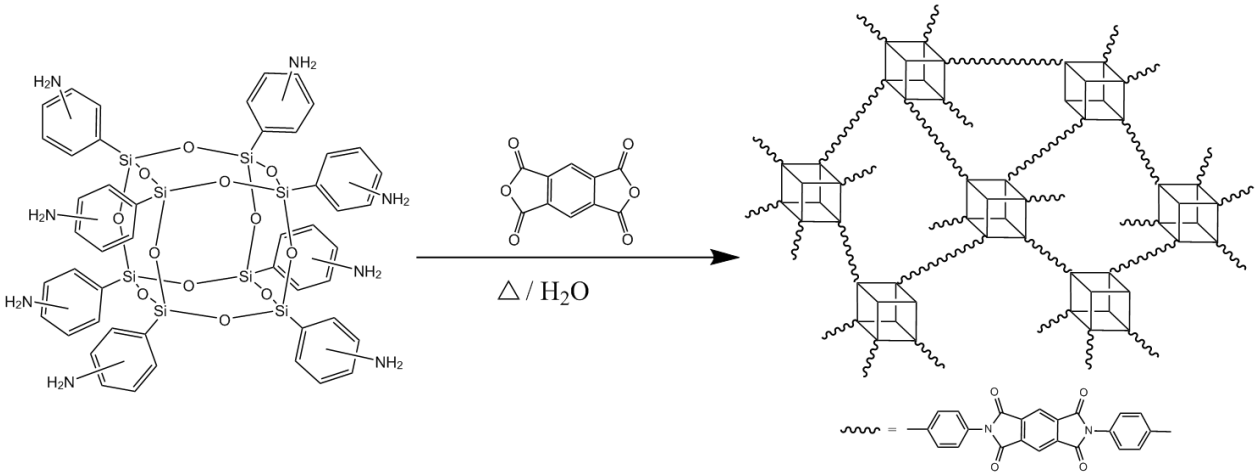

Figure 20. PolyOAPS-PMDA synthesized in NMP.[111]

Unfortunately, this polyOAPS-PMDA was also found to be brittle and efforts were made to employ more flexible and longer dianhydrides such as ODPA (Figure 21).[101] Networks built from OAPS/ODPA/ODA (4,4'-oxydianiline)[112] and OAPS/ODA/BMI (bismaleimide)[113] have been reported as well.

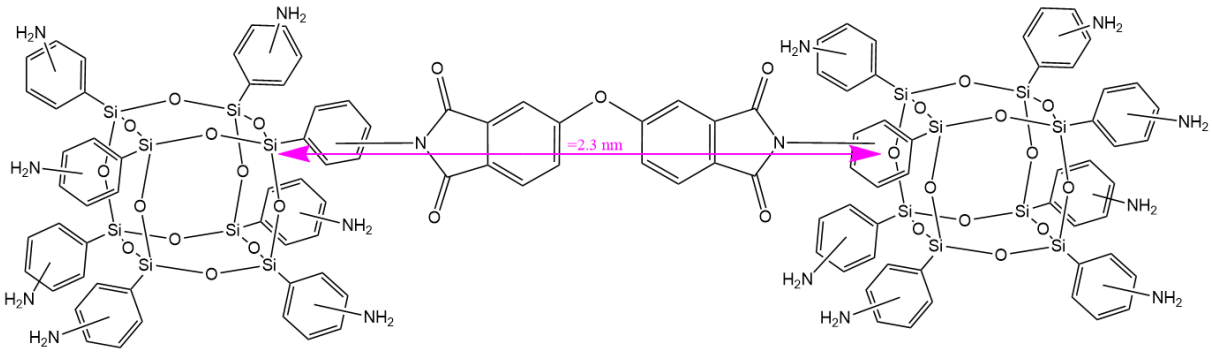

Figure 21. PolyOAPS-ODPA synthesized in NMP. [101]

The problem with mixing the monomers in the same solvent is that a shapeless product appears, whereas it would be preferable to produce a defect-free, uniform and thin layer to operate as a gas separation membrane. This is the main reason for attempting to use the interfacial polymerization route, as was done by the University of Twente (Figure 12). The difficulty of this approach is that it requires two immiscible solvents, one for the OAPS precursor and one for the dianhydride precursor, in order to create an interface where the thin layer can be generated.

The off-white OAPS powder is soluble in THF, DMF, 1,4-dioxane, acetone, DMSO and ethyl acetate but it is insoluble in water, benzene, ethanol and petroleum ether.[113] The dianhydrides are soluble in DMF, NMP, DMAc, THF, toluene, and so on.[114] For making polyOAPS-imide thin layers, two immiscible solvents should be chosen. Table 8 shows different solvents and their miscibility.[115]

Table 8. Solvents miscibility.[115]

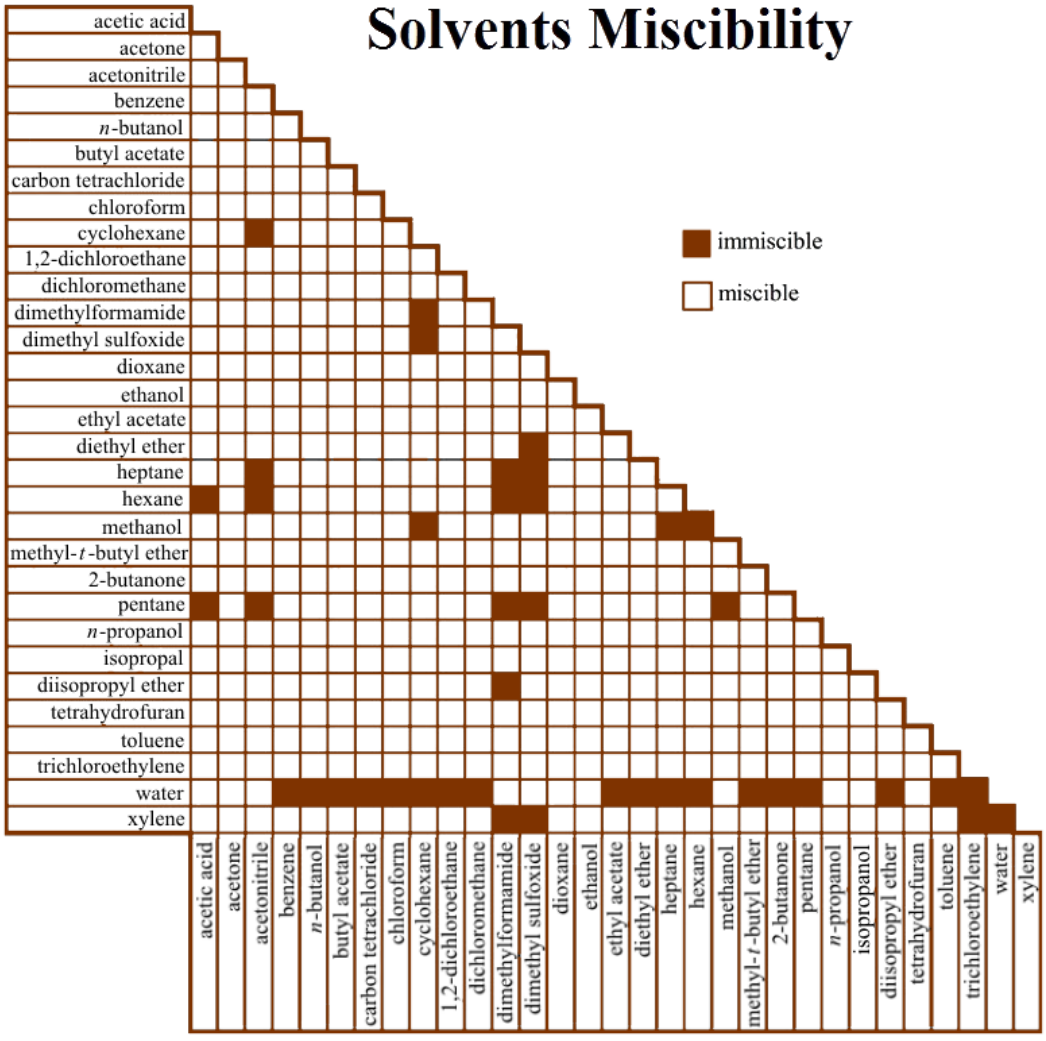

Although there are different possibilities, the typical solvents used at the University Twente are toluene for the dianhydride, water for the octa(aminopropyl)silsesquioxane POSS and DMSO/water for OAPS. Since DMSO (the solvent for OAPS) and toluene (the solvent for the dianhydride) are miscible, a certain amount of water (which is immiscible with toluene) must be added to the DMSO in order to have two immiscible phases.

As far as the structure of the new inorganic precursor is concerned, several experimental techniques were used to characterize OPS, ONPS and OAPS, i.e. the intermediate and final products in Laine's nitration/reduction approach (Figure 18) as well as those obtained by Lee et al. from the APTMS precursors (Figure 19). Many efforts focused on elucidating the ratios of the different *para*, *meta* and *ortho* isomers of OAPS.

1) Infrared spectroscopy (IR)

Almost any compound containing covalent bonds absorbs radiation frequencies in the infrared region of the electromagnetic spectrum. This region lies at approximately 700 nm to 1 mm in terms of wavelengths. An important use of IR spectroscopy is to obtain structural information since the absorption of each bond type (N-H, C-H, O-H, C-X, C=O, C-O, C-C, C=C, C-N, and so on) is only found in specific portions of the vibrational infrared region.[116] This is typically 400 to 4000 cm^{-1} in terms of wavenumbers.

Figure 22 displays the comparative IR spectra of OPS, ONPS and OAPS, i.e. the route towards the functionalization of amine groups in the nitration/reduction approach (Figure 18).[117] The peak at 1115 cm^{-1} corresponds to the Si-O-Si stretching in the cages,[117] and is present in all three compounds. The two peaks at 1350 and 1530 cm^{-1} in the IR spectra of ONPS disappear after reduction to OAPS. The two peaks at 3220 and 3380 cm^{-1} can be attributed to the -NH bond in OAPS. These comparative IR spectra show that the OPS phenyl rings have indeed been functionalized by $-NH_2$ in the final OAPS product.

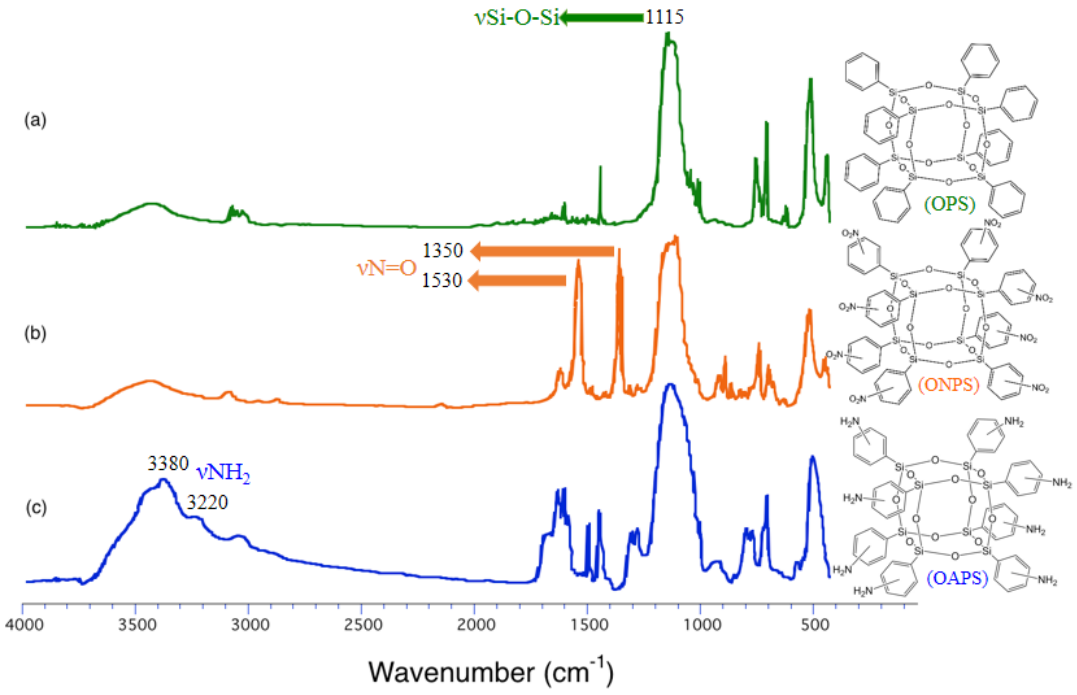

Figure 22. IR spectra of (a) OPS, (b) ONPS and (c) OAPS.[117]

2) Nuclear magnetic resonance (NMR)

Nuclear magnetic resonance (NMR) provides information on magnetically distinct atoms. For instance, when hydrogen nuclei are studied, one can determine the number of each distinct type of H and information about their immediate environment. Resonance of the ^{1}H hydrogen in a molecule can be detected since this isotope is magnetically active, has a spin of ½ and can be found in most organic compounds. Similar information can be achieved for the carbon nuclei (the ^{13}C nucleus also has a spin 1/2 but has a natural abundance of only 1%)[118] and for some other atoms such as silicon, nitrogen, oxygen, fluorine, etc.[116] For the OAPS and related structures, hydrogen nuclear magnetic resonance (^{1}H-NMR), carbon-13 nuclear magnetic resonance (^{13}C-NMR) and silicon-29 nuclear magnetic resonance (^{29}Si-NMR) characterizations were all attempted on ONPS and OAPS obtained by the nitration/reduction route (Figure 18). Only the ^{29}Si-NMR spectra for OAPS have been reported following the synthesis route by Lee et al. (Figure 19).[107]

Since the ^{1}H-NMR spectrum of ONPS is sharper and clearer than that of OAPS, Tamaki et al.[106] measured the isomer ratios by using both ^{1}H-NMR and ^{13}C-NMR on ONPS (Figure 23). The assumption was that the isomer ratios of OAPS (which has amines) should be the same as those of ONPS (which has nitro groups) since, based on the reduction

reaction, each -NO_2 should be displaced by one -NH_2.[106] Steric hindrance and electron-withdrawing effects of the POSS core were expected to prevent the formation of the *ortho* isomer. As such, the authors interpreted the ten peaks of the ONPS ^{13}C-NMR spectrum (Figure 23(a)) as ten different carbon environments for the *meta* and *para* isomers. There were three small extra peaks at 123, 137, and 159 ppm, but they were described as "insignificant". The triplet peak appearing at 8.73 ppm in the ^{1}H-NMR spectra (Figure 23(b)) was assigned to the most positively charged hydrogen placed between the nitro group and the siloxy group for the *meta* isomer, which the authors used to calculate the *meta*-isomer ratio. The surface area of the shift at 8.73 ppm was assumed to be equal to the unit, and the total surface area of the phenyl hydrogens shifts from 7.5 ppm to 8.8 ppm was found to be 7.76. The surface area of the shift at 8.73 ppm multiplied by the 4 *meta* phenyl hydrogens with respect to the total surface area of all phenyl hydrogens is (4 /7.76) ≈ 0.52. The ratio of the *meta* isomer was thus found to be 52%.

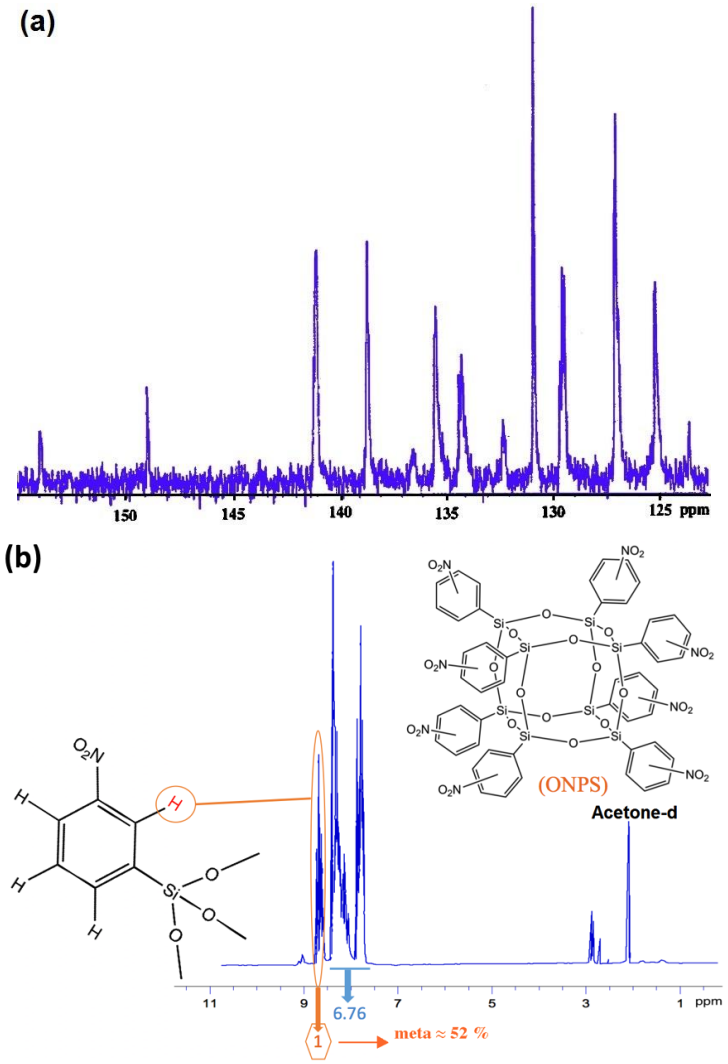

Figure 23. The experimental (a) ^{13}C-NMR and (b) ^{1}H-NMR spectra of ONPS in acetone-*d6*.[106]

By assuming that the *ortho* isomer was negligible, the ratio of *meta* to *para* could then be calculated as being 52% to 48%.[106] By using TGA analysis, the authors revealed that the decomposition of both ONPS and OAPS begins at the earliest at 350ºC.

Kim et al.[119] produced OAPS in a similar way to Tamaki et al.[106] (Figure 18) but with some modifications on the conversion of ONPS to OAPS. They achieved a higher yield of OAPS by using a lower concentration of the reagents over a longer time (20 h) and at a lower temperature (40ºC). As can be seen in Figure 24, the authors used the cleavage of the Si-C bond in two different ways (peroxidation and D_2O/F^-) to detach the rings from the ONPS corners and isolate the organic substituents. The ^{1}H-NMR spectra of nitrophenol and deuterated nitrobenzene were then used to re-measure the isomer ratio of ONPS. Although the ^{1}H-NMR spectra were not provided in the paper, the ratios were reported as being 70%, 25% and 5% for *meta*, *ortho* and *para* respectively for both cleavage methods. Takahashi et al.[120] redid the Si-C cleavage using peroxidation and obtained 76%, 21% and 3%, whereas Sulaiman et al.[121] reported 65%, 10% and 25% for *meta*, *ortho* and *para* respectively, which likewise indicated the presence of the three isomers. It should be noted that the corresponding author of the papers by Tamaki et al.,[106] Kim et al.,[119] Takahashi et al.,[120] and Sulaiman et al.[121] is Prof. Richard Laine, so these results originate from the same group using slightly modified routes.

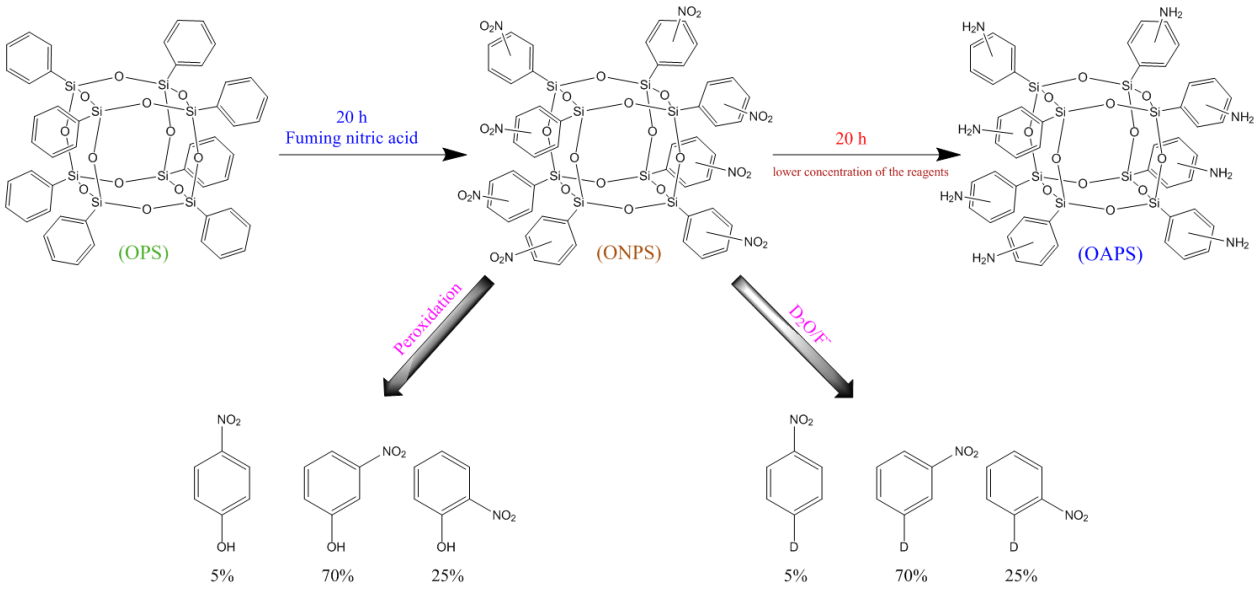

Figure 24. Laine's modified method at the ONPS step, Si-C cleavage of ONPS and the resulting isomer ratios.[119]

In another modification of Laine's method, Zhang et al. shortened the time of nitrifying OPS to 6 hours and used hydrazine as well as $FeCl_3$ instead of the expensive Pd/C catalyst to reduce ONPS to OAPS.[113] The yields of the yellow ONPS and the off-white OAPS were 92% and 86% respectively. But there were no attempts to calculate the isomer ratios.

Although Tamaki et al.[106] had written that the formation of *ortho* isomer was unlikely, Kim et al.[119] claimed that 25% of the isomers were *ortho* and that there was very little *para*.[119] Due to the electron-withdrawing nature of the cage and the steric hindrance, Tamaki et al.[106] expected to have a majority of *meta*, then *para* and then *ortho* at last (or no *ortho* at all). These conflicting observations, which have not been resolved yet, are definitely a problem when OAPS is obtained by the nitration/reduction approach.

However, the assumption that the isomer ratios are the same in ONPS and OAPS was confirmed by the ^{1}H-NMR spectrum of OAPS (Figure 25).[122] Tamaki et al.[106] and Huang et al.[117] calculated the integration ratio of the peaks for the amine groups with respect to the aromatic groups to obtain the amount of quantitative reduction of the nitro to amine groups. This ratio is 2:1 for aromatic to amine H, which indicates that there is one amine per phenyl ring and that the nitro groups are completely displaced with amine groups.

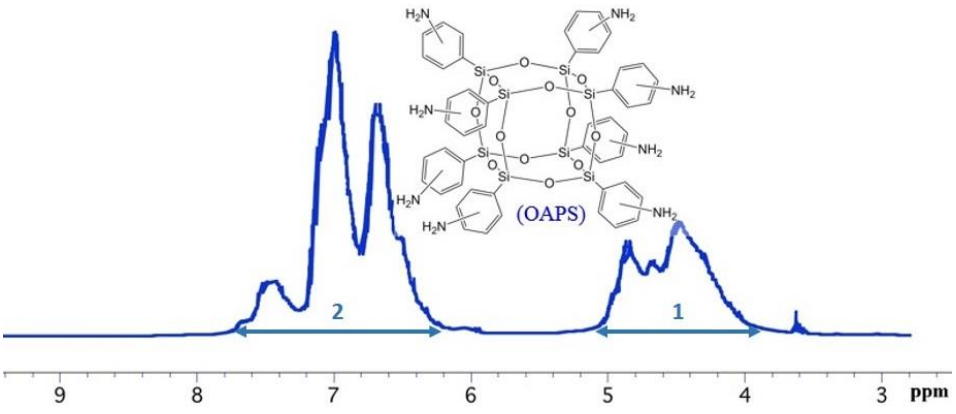

Figure 25. The ^{1}H-NMR spectrum of OAPS in acetone-d_6 and the ratio of aromatic H (6.2 to 7.8 ppm) to amine H (3.9 to 5 ppm).[106]

The ^{13}C-NMR spectrum of OAPS in Figure 26 apparently shows ten peaks. Tamaki et al.[106] interpreted the same number of the peaks in the ONPS (Figure 23(a)) and the OAPS ^{13}C-NMR spectra as the presence of ten different carbons for the *meta* and *para* isomers. But by assuming that the results of Kim et al.[119] are correct, there should be 16 peaks: 4 for *para*,

6 for *meta*, and 6 for *ortho*. Since the peaks overlap and some peaks are too small, it is not clear how many individual peaks appear. That may be the reason why Tamaki et al.[106] used the description "insignificant peaks" for the three smallest peaks in the ^{13}C-NMR spectrum of ONPS, without attempting to provide an explanation for their presence.

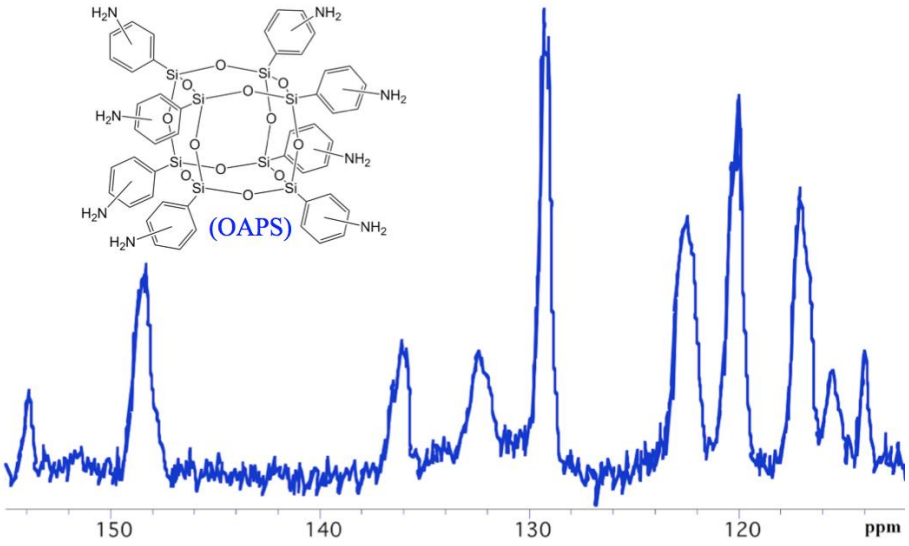

Figure 26. ^{13}C-NMR spectra of OAPS in acetone-d_6.[122]

The solid-state ^{29}Si-NMR spectra of ONPS and OAPS show two overlapping peaks (Figure 27).[113, 122-123] These studies were published before the work of Kim et al.[119] determining the isomer ratios via the Si-C cleavage of ONPS. Zhang et al.[113] concluded that these peaks were related to the *meta* and *para* isomers, but as explained before, it was not known at the time that the *ortho* should also be present. This remains again unresolved. The peak is much more narrow in the ^{29}Si-NMR spectra of the simpler OPS, which suggests that all Si atoms feel the same environment there.

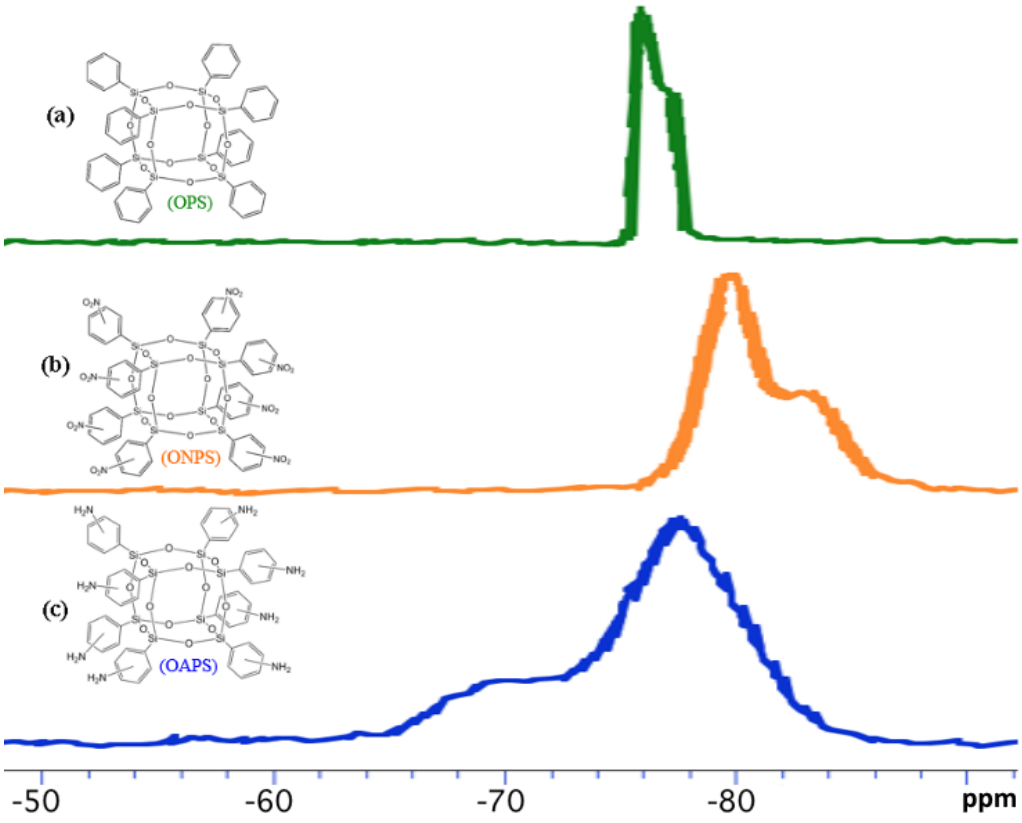

Figure 27. Solid-state ^{29}Si-NMR spectra of OPS (a), ONPS (b) and OAPS (c).[113, 123]

To assess their alternative synthesis approach based on aminophenyltrimethoxysilanes (Figure 19), Lee et al.[107] purchased a commercial OAPS prepared through nitration/reduction by Mayaterials Inc., and compared its ^{29}Si-NMR spectra with that of the pure *para*-APS and *meta*-APS obtained from the APTMS precursors. We refer to APS (aminophenyl silsesquioxane) when the cages can have different sizes, i.e. they are not necessarily octamers as in OAPS. As can be seen in Figure 28, the commercial OAPS in (c) shows broad resonances in the ^{29}Si-NMR spectrum while the *para*-APS (a) and *meta*-APS (b) exhibit much more narrow spectra. The authors suspected that the nitration/reduction of OPS did not fully preserve the integrity of the Si-O cage structures and that OAPS was converted into an ill-defined resin when using Laine's approach. They attributed the many narrow peaks in Figures 28 (a) and (b) to the presence of cages with different numbers of Si and identified the dodecamer as being probably predominant. Indeed, the main orange peak of *meta*-APS matches the sharpest peak of the commercial OAPS, but the main purple peak of *para*-APS corresponds to a region where there are smaller peaks.

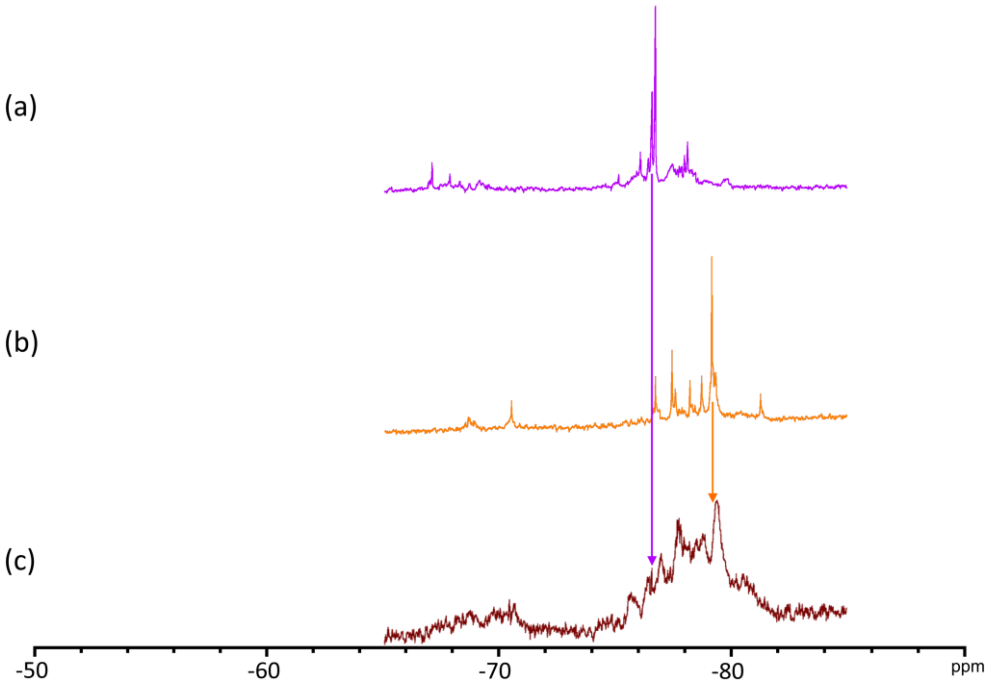

Figure 28. The ^{29}Si-NMR spectra of APS (with the dodecamer being supposed to be predominant) obtained either from (a) *para*-APTMS, (b) *meta*-APTMS along with that of (c) OAPS produced through nitration/reduction of OPS.[107] All spectra were measured in DMSO-*d6*.

3) X-ray diffraction (XRD)

XRD crystallography is widely used to obtain information on the atomic-scale structure.[124] Figure 29 presents the XRD pattern of OAPS obtained by nitration/reduction.[113] The sharper peak at 2θ=8º shows the long-range order in OAPS (d = 1.1 nm), which corresponds to the diameter of the OAPS cage. The broad halo centred at 2θ =19º, which usually appears in the XRD pattern of amorphous materials, is the result of random packing at the molecular level caused by the amine-substituted isomers.[113]

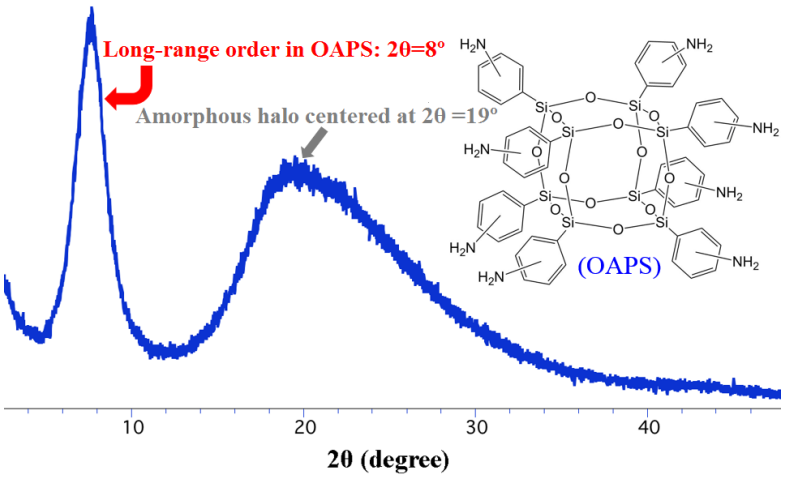

Figure 29. The XRD pattern of OAPS.[113]

Lee et al.[107] also used XRD to assess the differences between their synthesis from aminophenyltrimethoxysilanes and the nitration/reduction approach (Figure 30). All three OAPS showed the same reflection peak at 2θ = 7.8° (attributed to a d-spacing of 1.126 Å) which corresponds to the peak at 8° reported in Figure 29. However, the intensity varied in the order pure *para*-APS > pure *meta*-APS > OAPS by nitration/reduction. The authors concluded that the lower intensity of the latter was probably due to its ill-defined resin-like structure. They also suggested that since *para*-APS contains only one possible site for its NH_2 substituent, it displays more order than *meta*-OAPS having two possible sites. However, it remains unclear why the XRD pattern for the pure *meta*-OAPS (intact cages according to Lee et al.) looks closer to that of the nitration/reduction OAPS (ill-defined cages according to Lee et al.), whereas their NMR spectra are much more different (Figure 28). It should also be remembered that there is a mixture of cage sizes in the Lee approach, whereas all of them should be eight-cornered in the Laine approach.

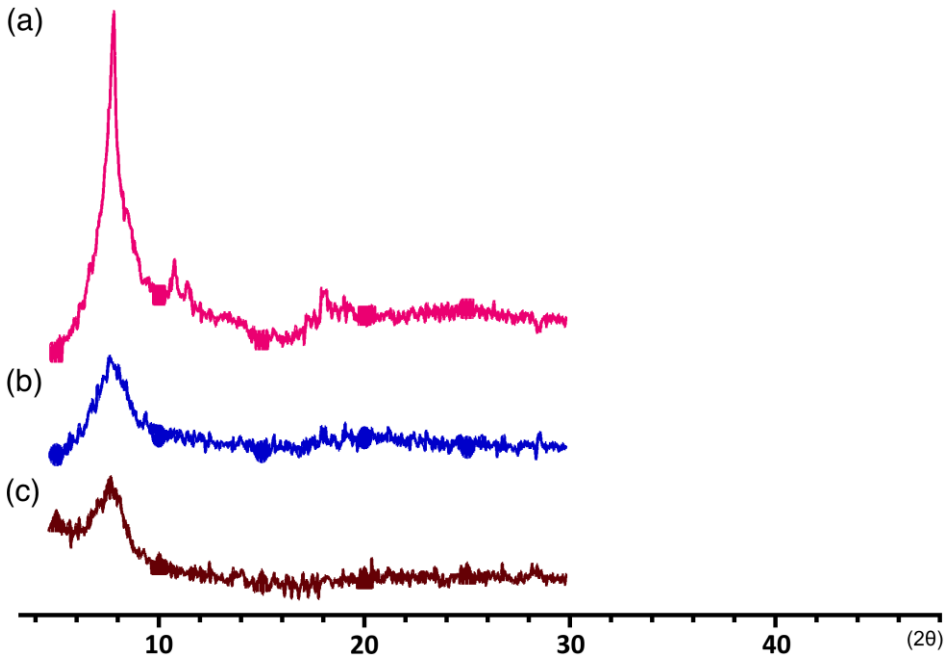

Figure 30. XRD patterns of (a) *para*-APS cage mixtures $(p\text{-}NH_2C_6H_5[SiO1.5])_n$, (b) *meta*-APS cage mixtures $(m\text{-}NH_2C_6H_5[SiO1.5])_n$ where n=8,10,12; and (c) OAPS prepared by nitration/reduction. Curves are vertically shifted for clarity.[107]

4) Gel permeation chromatography (GPC)

Gel permeation chromatography or GPC is a technique used for the determination of molecular weight distributions (MWD).[125] The GPC curves of the nitration/reduction OAPS

prepared using three different temperatures for the reduction of ONPS (Figure 31) were accompanied by shoulders at 50ºC and 60ºC probably representing some oligomeric species (10-20%). On the other hand, the oligomerization did not appear at 40 ºC. It was suggested that a lower temperature could thus result in a more uniform product. However, the authors did not provide the corresponding molecular weights.

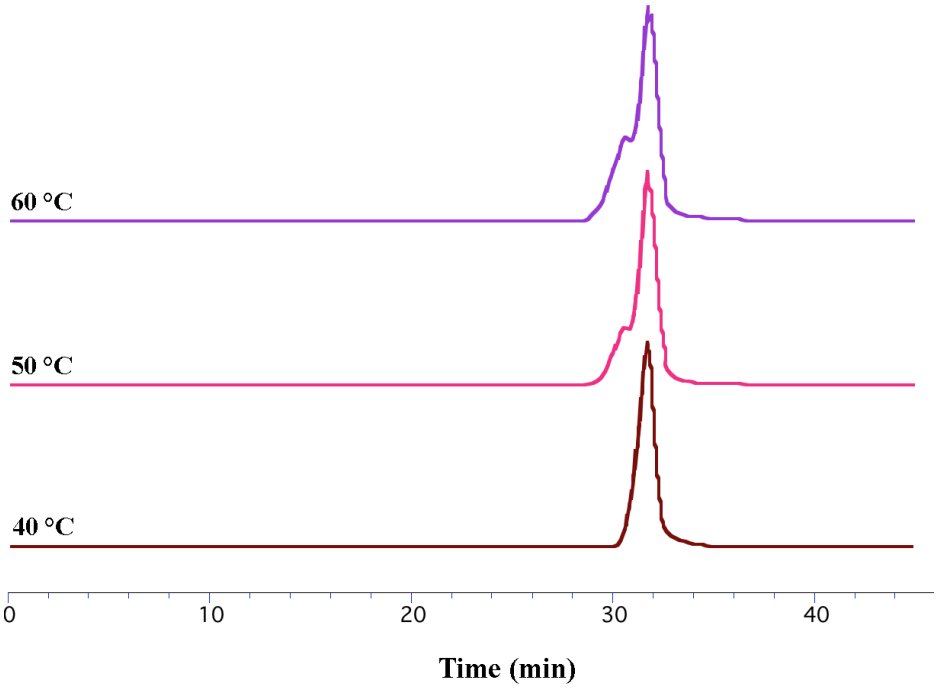

Figure 31. GPC curves of OAPS produced by the reduction of ONPS at three different temperatures.[119]

It should be noted that there are other phenyl-derived silsesquioxanes than OPS, ONPS and OAPS. These include for example the structures shown in Figure 32, i.e. hexadeca(aminophenyl)silsesquioxane (HDAPS) and its hexadeca(nitrophenyl)silsesquioxane (HDNPS) precursor as well as even more complex structures such as octa(maleimidophenyl)silsesquioxane (OMIPS).[101, 111, 113, 120] Nagendiran et al.[126] synthesized crosslinked polyaspartimides by polymerizing OMIPS with three different diamines. However, all these structures introduce a very high degree of complexity and they are difficult to get commercially. As such, it was decided to keep OAPS as the most interesting candidate.

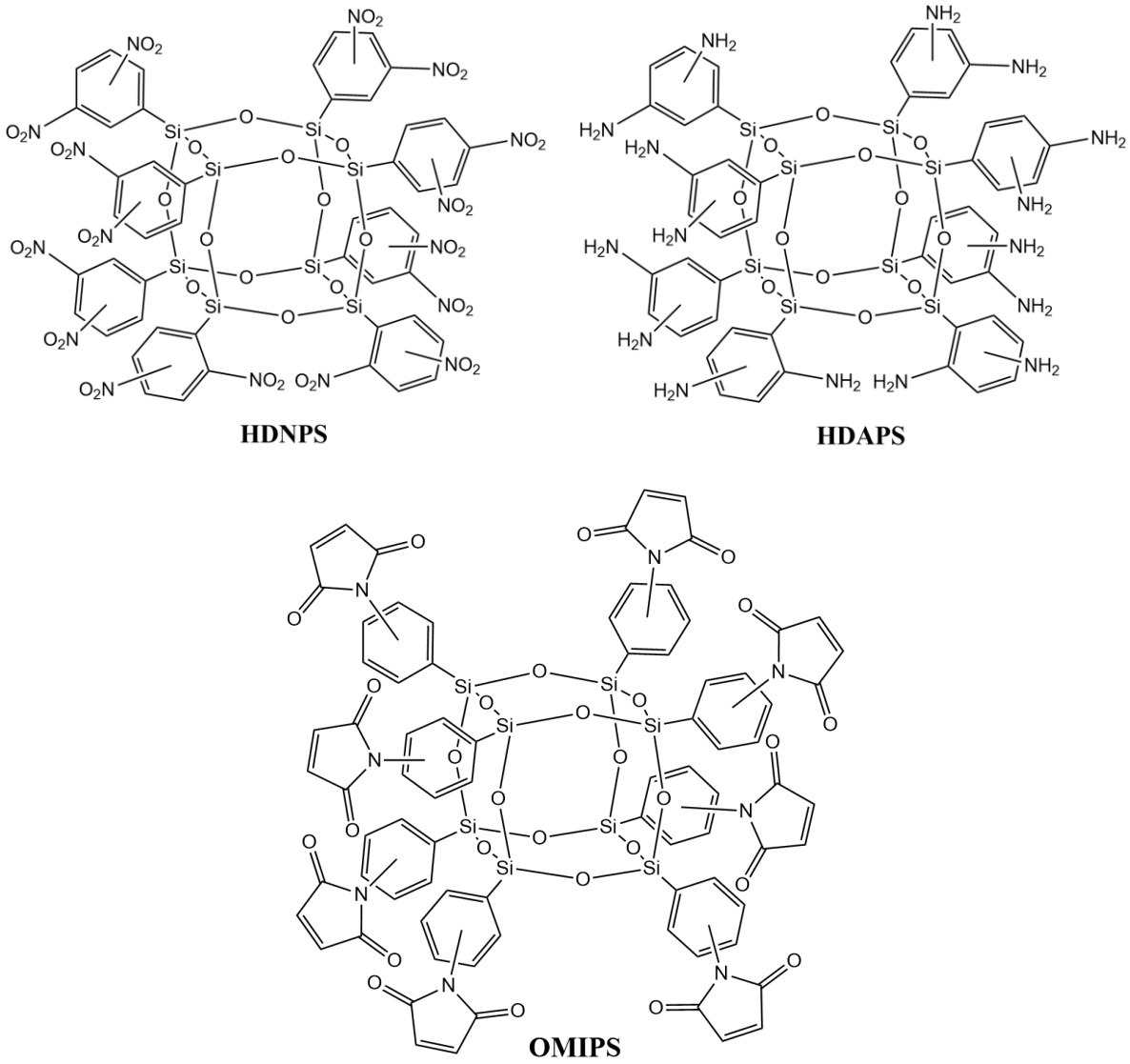

Figure 32. Other examples of phenyl-derived silsesquioxanes.

IV. Characterization of a commercial and a controlled OAPS

The experimental part of the research was mostly performed in the *Films in Fluids* research group directed by Prof. Nieck Benes at the University of Twente. After selecting OAPS as a suitable candidate precursor to make new hybrid polyOAPS-imide membranes, it was first purchased from Gelest Inc.[109] Based on the information presented by Gelest, this "commercial OAPS", which came as a powder, was synthesized using the Laine nitration/reduction route. In agreement with Choi et al.[112] and Kim et al.,[119] Gelest[109] claimed that their product is a mixture of *meta*:*ortho*:*para* with a 60:30:10 ratio and typically contains 20% of dimer.

Later in the work, a (60%*para*/40%*meta*) OAPS was synthesized using the Lee aminophenyltrimethoxysilane route. As mentioned before, this synthesis was carried out by SINTEF, a Norwegian partner of the University of Twente. They used an inexpensive mixture of the *meta* (30-40%) and *para* (60-70%) APTMS isomers also provided by Gelest as the initial reactants. This "controlled OAPS" was dissolved in DMSO before being provided to the University of Twente.

The main structural differences between the so-called commercial and controlled OAPS can be summarized as follows:

- the commercial OAPS should contain all three isomers while the controlled OAPS does not have any *ortho* isomer.

- the controlled OAPS contains a lot more of the *para* isomer than the commercial OAPS.

- the commercial OAPS is based solely on eight-cornered Si siloxane cages, while there could be larger siloxane cage structures too in the controlled OAPS.

Both types of OAPS were characterized experimentally using picnometry as well as IR and NMR spectroscopies. In addition, IR and NMR predictions were performed by different softwares (machine-learning approaches such as MestreNova and quantum mechanical approaches such as DFT with Gaussian) in order to better understand the experimental results.[127-128]

1) Density of the commercial OAPS

Figure 33 shows (a) the dark yellow commercial OAPS powder from Gelest[109] and (b) the controlled OAPS solution in DMSO. The latter can be obtained as a powder following the evaporation of the solvent.

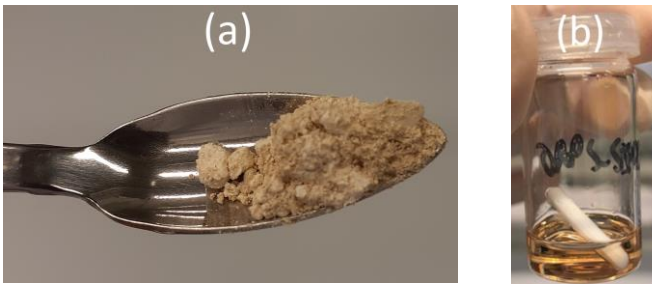

Figure 33. The OAPS samples: (a) commercial powder and (b) controlled solution.

Since the OAPS are in the form of powders, the AccuPyc II 1340 pycnometer (Figure 34) was used to measure their densities. However, the technique first had to be tested on NaCl and on a spherical metallic standard. As can be observed in Figure 34, an inert gas (such as helium or nitrogen) flows into a chamber of known volume (valve "a" opens then closes), and the sample is sealed in the instrument chamber. Then the gas expands into another precise internal volume (valve "b" opens). The pressure drops upon filling the sample chamber and then discharging it into the second empty compartment allows for the measure of the sample volume. The gas molecules rapidly fill the pores and only the solid phase of the sample displaces the introduced gas. Dividing the measured volume by the weight of the sample gives the gas displacement density. The pressure then vents off by opening valve "c".[129]

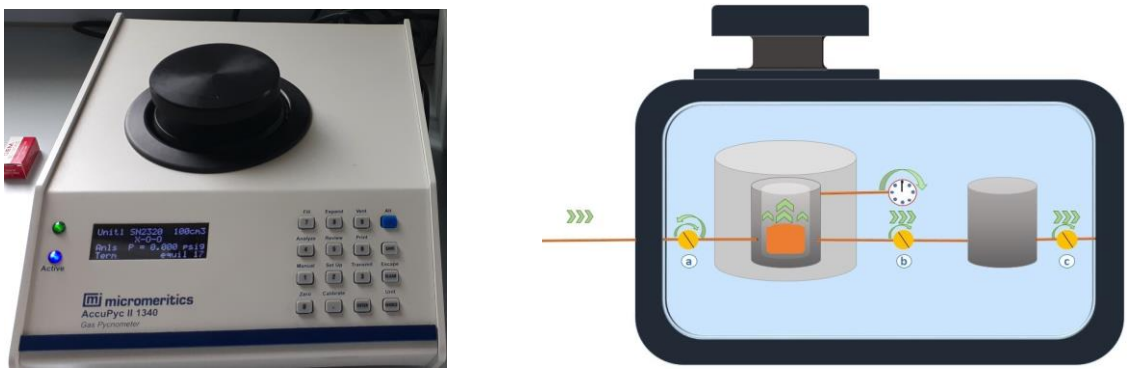

Figure 34. A photo (left) and a schematic diagram (right) of the AccuPyc II 1340 pycnometer; a, b and c are the valves.[129]

This technique is non-destructive as it uses the gas displacement method to measure the volume. Furthermore, it generates much more precise and reproducible densities than the traditional Archimedes water displacement method,[129] since the small gas molecules can diffuse in the pores, cavities, and any open space. The reproducibility (precision) is guaranteed within +/- 0.02% of the nominal full-scale cell chamber volume.[89] Since the full-scale cell chamber volume of the AccuPyc II 1340 pycnometer used is 74.051 cm^3, the nominally guaranteed precision should be ± 0.015 cm^3.

The pycnometer calculates the volume of the sample by using Equation 6:[89]

$$V_{sample} = V_{cell} - \frac{V_{expansion}}{\frac{P_1}{P_2} - 1} \tag{6}$$

where P_1 is the gauge pressure after filling by the inert gas (helium) and P_2 is the gauge pressure after expansion. V_{cell} and $V_{expansion}$ are already known via a calibration procedure, whereas P_1 and P_2 are measured by the gauge included inside the pycnometer. The weight of the sample should be measured by a precise balance and inserted into the memory of the pycnometer.

Before beginning each test, the pycnometer performs purges to sweep the compartments. The default number of the purges and P_1 were set to 10 and 1.5 bar respectively. Although P_1 fluctuates cycle-by-cycle, it is recorded at each cycle to calculate the volume in the most precise way. The number of cycles for each analysis was set to 30, with the steady-state being reached for each cycle. The pycnometer calculated the average volume and density by averaging 30 measurements for each test. The average temperature was also obtained by averaging 30 recorded temperatures for the 30 measurements. The standard deviations were measured for the volumes, densities and temperatures.

To test the accuracy of the pycnometer, a NaCl sample with a specific density of 2,17 g/cm^3 was first analyzed. Although the purge process sweeps the compartments, the water absorption for a material such as NaCl should also be considered. It was thus put in a vacuum oven to ensure that there was no water absorbed. The pycnometer applied 10 purges before starting each test to remove the moisture probably absorbed by the NaCl sample during its displacement from the oven into the cell (sample holder) of the pycnometer. The volumes and

densities of NaCl were found to fluctuate with the changes in ambient temperature during the day. Figure 35(a) shows the changes in volume and temperature as a function of the test number. Figure 35(b) shows the inverse correlation between temperature and density.

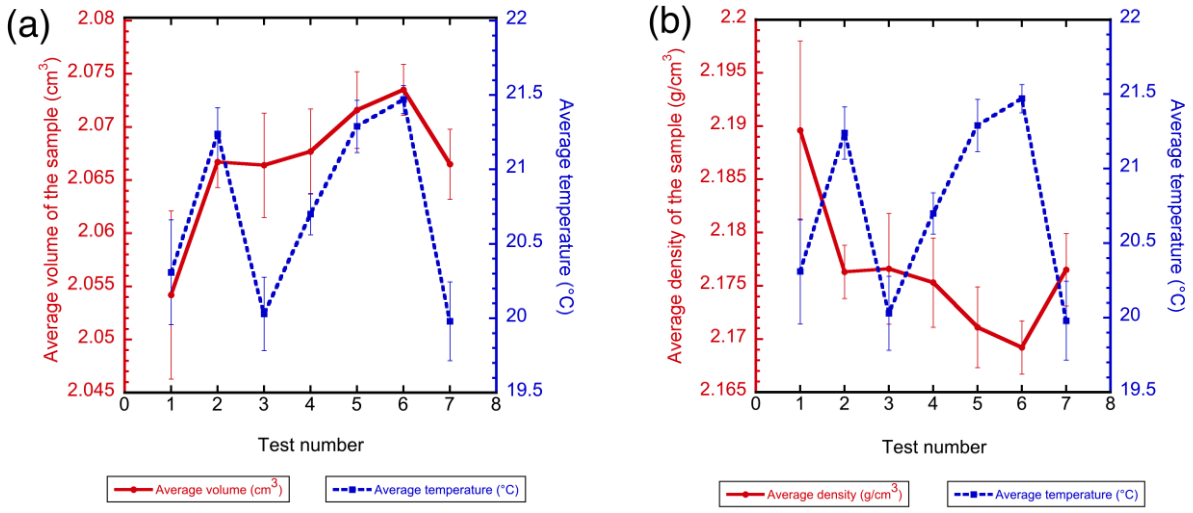

Figure 35. The average temperature along with (a) the average volume and (b) the average density of NaCl as a function of the test number.

The differences between the highest and lowest volumes and densities are 0.0193 cm^3 and 0.0204 g/cm^3 respectively, while the difference between the temperatures is 1.16°C. The volume and density of NaCl change by 0.0166 cm^3 and 0.0176 g/cm^3 per °C, respectively. Obviously, the density is inversely proportional to the temperature.

The compartments and internal components of the pycnometer are made of a metal alloy, so the fluctuations in temperature can also affect the volumes of the compartments (Equation 6), in addition to the sample volume. To study the effect of each factor, two different experiments were performed. Initially, the empty cell was tested and then a spherical metallic standard in steel with an accurately known volume (accessory of the pycnometer) was placed inside the cell to compare its nominal volume with the measured volume.

Figure 36 illustrates the impact of temperature on the volumes measured by the pycnometer when using a blank cell. Ideally, all measured volumes (V_{sample}) should be zero. But the V_{sample} values are positive, even though they remain in the ± 0.015 cm^3 guaranteed error range. This is because the V_{cell} parameter is recorded with the last calibration and remains constant until the next calibration. The calibration process is done with standard

metal samples. All measured volumes are positive, and the average temperature at which the calibration was performed is probably different from the temperature at which the volume of the blank cell is measured. Indeed, the calibration process of the pycnometer takes almost 2 hours (the same as a complete test), but the average temperature of the calibration over the 2 hours cannot be obtained and only the temperature of the final cycle is presented. On the other hand, in a complete test, the pycnometer averages 30 recorded temperatures for the 30 measurements. In the present case, the recorded temperature for the calibration process was 21.2°C. According to Figure 36, the difference between the highest and lowest volumes is 0.0084 cm^3 while the difference between the temperatures is 1.162°C. The volume of the sample in the blank cell changes by 0.0072 cm^3 per °C. This was 0.0166 cm^3/°C for NaCl, which is more than twice the volume variation of the blank cell. It can be a result of the cooperative impact of NaCl and the cell volume variations resulting from the changes in the ambient temperature.

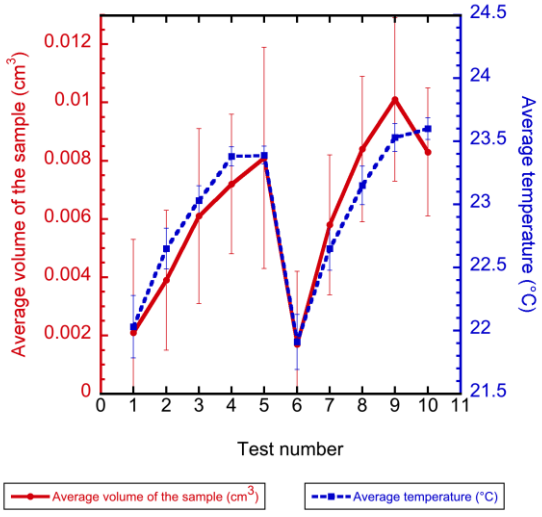

Figure 36. The average volume of the sample and the average temperature of the blank cell as a function of the test number.

To further investigate, a spherical metallic standard with a nominal volume of 6.3714 cm^3 and a mass of 95.1566 g was tested. Figure 37 shows how the volumes and densities change with respect to the average temperatures. As before, there is a direct correlation between volume and temperature (Figure 37(a)) while Figure 37(b) shows the inverse correlation with the density. The differences between the highest and lowest volumes and densities are 0.0097 cm^3 and 0.0227 g/cm^3, respectively, while the difference between the temperatures is 1.99°C. The volume and density of the standard change by 0.0049 cm^3 and

0.0114 g/cm^3 per °C, respectively. The volume change is less than that of NaCl but the limitation of the precision should also be considered.

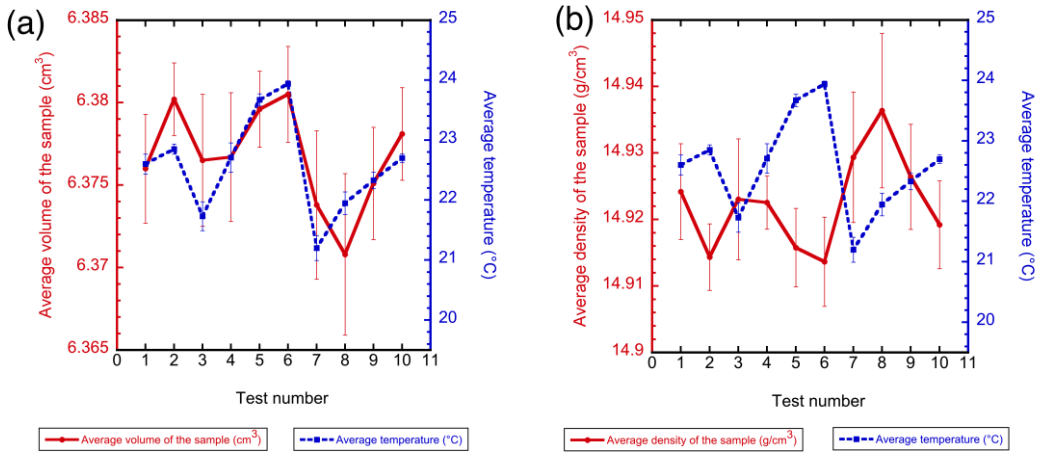

Figure 37. The average temperature along with (a) the average volume and (b) the average density of the spherical metallic standard, as a function of the test number.

Following these preliminary tests, 0.9087 g of the commercial OAPS was put in a vacuum oven to evaporate any moisture. It was then immediately weighed and transferred rapidly into the pycnometer to limit as much as possible the absorption of humidity. The same number of purges (10) and cycles (30) were set for each test. Figures 38(a) and 38(b) show the volumes and densities measured for that commercial OAPS. The differences between the highest and lowest volumes and densities are 0.0084 cm^3 and 0.0179 g/cm^3, respectively, while the difference between the temperatures is 2.58°C. The volume and density of the commercial OAPS change by 0.0032 cm^3 and 0.0069 g/cm^3 per °C, respectively. The density of the commercial OAPS sample averaged over the ten tests and was found to be 1.39 g/cm^3 with a standard deviation of 0.01 g/cm^3.

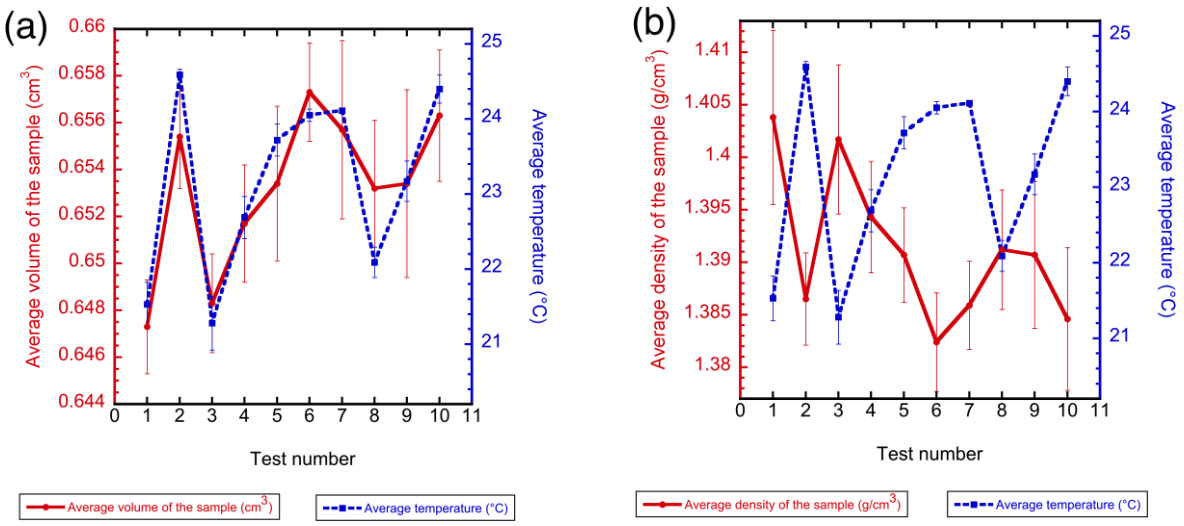

Figure 38. The average temperature along with (a) the average volume and (b) the average density of the commercial OAPS, as a function of the test number.

According to the results presented above for NaCl, the blank cell, the sphere and the commercial OAPS, it is clear that the temperature affects the measurements. To remove the impact of this factor, the pycnometer does a pressure calibration before each cycle. Thirty pressure calibrations are automatically performed with each test, but during each cycle (2 to 4 minutes), the ambient pressure is assumed to remain constant. As mentioned before, the nominally guaranteed precision is ± 0.015 cm^3 and it is compatible with the error bars presented in the graphs. But it would be better to actually maintain the temperature constant during the calibrations and the tests. Micromeritics Instrument Corpcompany[89] proposes a thermoelectric device for the accurate control of the temperature from 15–36 °C (±0.1 °C), which is adjustable in 0.1 °C increments. This could be an option for use with temperature-sensitive samples when the ambient temperature cannot be adequately controlled.

Following the evaporation of its solvent, the density of the controlled OAPS was measured with the pycnometer in the same way as for the commercial OAPS. It was found to be 1.37 g/cm^3 with a standard deviation of 0.01 g/cm^3. Both values are reasonably close and thus provide confidence in the results presented above.

2) IR spectroscopy of OAPS

As noted before, almost all inorganic or organic compounds containing covalent bonds absorb frequencies in the infrared region of the electromagnetic spectrum. Its wavelengths *l* are shorter than those associated with microwaves but longer than those associated with visible light.[116] Table 9 shows the energy transitions in the different regions of the electromagnetic spectrum. The vibrational transitions of the infrared region are especially interesting for chemical purposes and are referred to in terms of wavenumbers $\bar{\upsilon}$ expressed in cm^{-1} by taking the reciprocal of the wavelengths. IR wavenumbers typically cover the 400 to 4000 cm^{-1} range.[116]

Table 9. Energy transitions in different regions of the electromagnetic spectrum.[116]

Region of Spectrum	Energy Transitions
X-rays	Bond breaking
Ultraviolet/visible	Electronic
Infrared	Vibrational
Microwave	Rotational
Radio frequencies	Nuclear spin (nuclear magnetic resonance) Electron spin (electron spin resonance)

In order to further compare the commercial and controlled OAPS samples, experimental IR spectra were obtained for both of them at the University of Twente using a Perkin Elmer ATR-IR spectrometer. Only a small amount of OAPS powder was used directly and the samples needed no specific preparation process. As for the density, since the controlled OAPS was initially dissolved in DMSO, its solvent was first evaporated by heating before performing the IR analysis.

In parallel, Density Functional Theory (DFT)[130] calculations were carried out on separate model structures of the pure *para*, *meta* and *ortho* isomers of OAPS (Figure 17) with the Gaussian software.[128] The Avogadro software[131-132] was used to analyze the Gaussian outputs as described in Annexe 1. There are several quantum mechanical methods available to calculate the vibrational frequencies starting from model molecular structures. The *ab initio* methods, such as Hartree-Fock (HF), which investigate all the details of the electron movements are very computationally expensive. However it was shown that many properties of a molecule can be derived from its electron density distribution only,[133-134] and this gave

rise to DFT approaches. Depending on the level of theory used, this allows for lower computational requirements than the *ab initio* methods.[134]

The basis of quantum mechanics is the Schrödinger Equation.[134] Due to complex interactions between the electrons, an analytical solution for the Schrödinger equation is only possible for a few nuclei and electrons. Thus, it needs to be solved numerically by different approximations.[134] HF is an approximation named after its developers D. R. Hartree and W. A. Fock. It is based on the so-called Slater-determinant, which is an asymmetrized product of *n* one-electron wave functions, instead of using one wave function depending on *n* electrons.[134] On the other hand, as mentioned above, DFT exploits the properties of the target molecule based on its electron density. There are three categories of Density Functional methods: (i) Local Density Approximation (LDA), which assumes the uniformity of the electron density throughout the molecule,[135-136] (ii) Gradient Corrected (GC) methods which account for the non-uniformity of the electron density,[137] (iii) Hybrid methods which use interesting features of the *ab initio* methods, particularly the Hartree-Fock theory, to improve the functionals used in DFT.[138-140] Electronic correlation means that the electrons cannot be considered "independent" in a many-electron system such as a molecule. They are surrounded by an effective potential that accounts for all interactions with the other electrons, and which influences the excited-state features.[141] In addition to the correlations, there are exchanges, which means that, due to their quantum nature, different electrons cannot be discerned from each other when their wave functions overlap. This has a direct consequence on the symmetry of the many-body wavefunctions and the Hartree-Fock method is able to discern correlation effects from exchanges.

The B3LYP (Becke, 3-parameter, Lee-Yang-Parr) level of theory is a hybrid exchange-correlation functional that linearly combines the Hartree-Fock exact exchange functional and the GGA (Generalized Gradient Approximation) corrections with the LDA electron-electron and electron-nuclei energies. GGA uses the density gradient to correct for the deviation from uniform densities.[140]

A very important factor that must be considered in the DFT calculations is the basis set for expanding the molecular orbitals.[140] A basis set is a set of functions (called the basis functions) used to provide the electronic wave functions in the Hartree-Fock method or DFT theory in order to turn the partial differential equations of the model into algebraic equations suitable for efficient implementation on a computer. A large basis set is expected to present

accurate results but also requires a large computational cost. On the other hand, a small basis set is computationally efficient but can produce inaccurate results. It is therefore desirable to have the accuracy and at the same time use basis sets that are as compact as possible.[140]

The minimal basis set is the minimum number of basis functions required to describe the ground state of atoms in a molecule. For example, the minimal basis for O ($1s^2$, $2s^2$, $2p^4$) contains five basis functions:1s, 2s, $2p_x$, $2p_y$, $2p_z$. In addition to the minimum number of basis functions, extra basis functions can be added to define the expanded basis sets. There are various kinds of extended basis sets including multiple-zeta (double, triple, etc), split-valence, polarization and/or diffuse functions:[140]

- In double-zeta basis sets, each orbital in the minimal basis set is replaced by two basis functions, for instance, the double-zeta basis set for O contains ten functions instead of five. The same principle applies to other multiples.
- Split-valence basis sets simplify the computational efforts by using the double (or more)-zeta description only for the valence orbitals, while the inner-shell electrons are described by the minimal basis assumption.
- Polarization functions are shown between two parentheses and are characterized by an orbital quantum number *l* larger than the largest *l* in the minimal basis set approximation, *i.e.* they provide more room space for the electrons to get away from each other and minimize electron-electron repulsions. As an example, for O: $1s^2$, $2s^2$, $2p^4$, the “d, f ...” orbitals (l = 2, 3…) are polarization functions, whereas for H: $1s^1$, the “p” (l = 1) orbitals are polarization functions.
- Diffuse functions such as the very shallow Gaussian basis functions more accurately display the "tail" parts of the atomic orbitals, which are far from the atomic nuclei.[142] Diffuse functions are indicated by + and can be important for describing anions, large soft molecular structures and long-range interactions such as Van der Waals forces, as well as for accomplishing electronic excited-state and electric field property calculations.[128, 140]

In the present work, we use split-valence basis sets. Their notation comes from the group of John Pople and is typically expressed as X-YZWG.[143-144] Here, X shows the number of primitive Gaussians including each core atomic orbital basis function. The Y, Z and W indicate that the valence orbitals consist of three basis functions each, the first one

comprising a linear combination of Y primitive Gaussian functions, the second one comprising Z primitive Gaussian functions and the third one comprising W primitive Gaussian functions. G is an initial for Gaussian. For example, 6-311G means that the inner shell atomic orbital (1s orbital) is a linear combination of six primitives and each valence shell atomic orbital is split into three parts (triple zeta) using three, one and one primitive Gaussians respectively.[140, 144-145] As explained above, "G" means Gaussian.[128] Another example, which is less expensive but still accurate enough in some cases, is the 6-31G(d,p) basis set, which means that, as in the previous example, the inner shell atomic orbital (1s orbital) is a linear combination of six primitive Gaussians, but in that case, each valence shell atomic orbital is split into an inner and outer part (double zeta) using three and one primitive Gaussians, respectively. In addition, (d,p) polarization functions are used for heavy atoms and hydrogens respectively.[144] It was chosen here to perform the geometry optimizations and predict the vibrational frequencies for the three isomers of OAPS along with B3LYP, which is the most widely-used functional due to its superior quality in the energy evaluation of small molecules.[142] B3LYP also reproduces very well the geometries of molecules.[146-149] Hence, all calculations in this Section were carried out using B3LYP as the hybrid density functional with the polarization functions added to a double zeta basis set 6-31G(d,p).[147-151]

Since the IR spectra arise from changes in dipole moments during the analyses, different isomers with different amounts of symmetry may present different spectra, i.e. the change in the dipole moment may diminish in a more symmetrical structure such as the *para* isomer. Indeed, Figure 39 shows that there are differences between the experimental bands of (a) the commercial OAPS and those of (b) the controlled OAPS, whereas they only differ by the nature and proportions of the isomers. Interestingly, there are no signs of large peaks around 3500 cm^{-1}, which would be characteristic of -OH groups and thus of open siloxane cages. This suggests that most or all of the cages are intact.

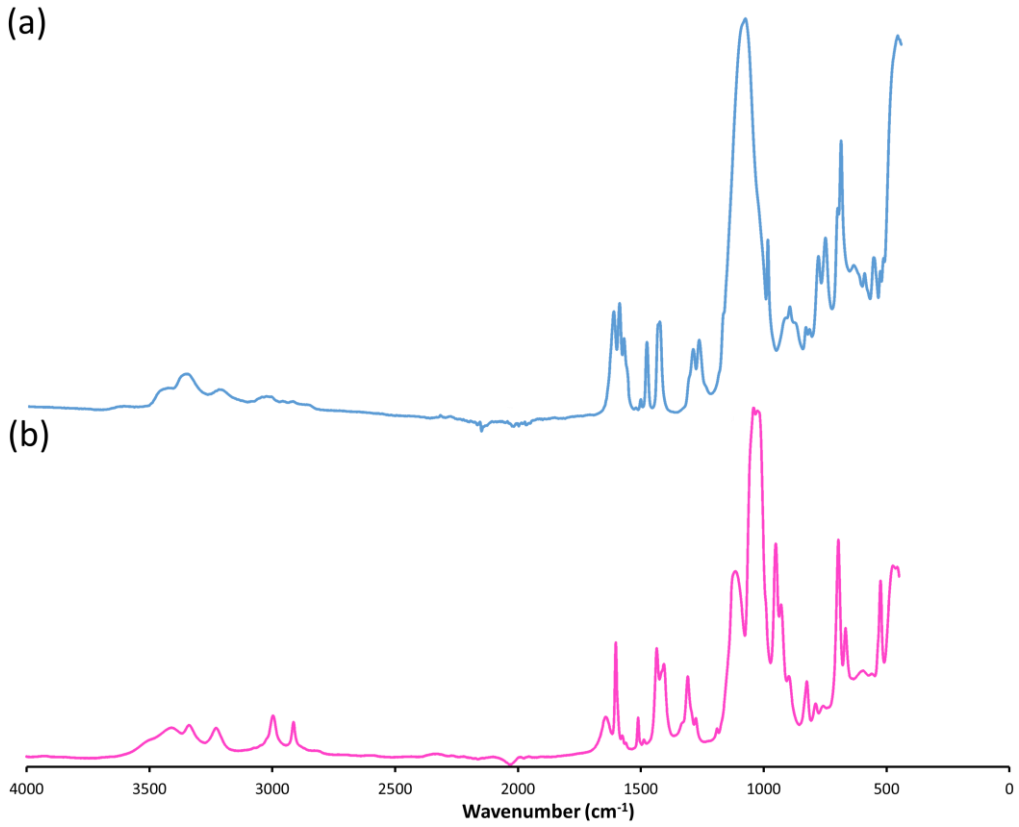

Figure 39. A comparison of the experimental IR spectrum for (a) the commercial and (b) the controlled OAPS.

Figure 40 compares separately the predicted IR spectra for each of the three isomers, i.e. in (a) *meta*, in (b) *ortho* and in (c) *para*, with the experimental IR spectra of the commercial OAPS (Figure 39(a)). The different vibrational modes were identified using the Avogadro software (Annexe 1). The predicted spectra are obviously restricted to specific optimized structures while the experimental spectrum takes into account a very large number of possible structures, hence its much broader peaks. However, Figure 40(a) for the *meta* isomer still indicates a good compatibility between the experimental and the predicted spectra for wavenumbers below 1700 cm^{-1}. The predicted bands for the *ortho* isomer (Figure 40(b)) are broader, especially for the Si-O-Si stretching vibrations. Figure 40(c) for the *para* isomer indicates lower intensities for most of the predicted bands due to its more symmetrical structure. This may prove that there are indeed higher proportions of the *ortho* and *meta* isomers in the commercial OAPS. All three predicted spectra show slightly overestimated bands for wavenumbers beyond 3000 cm^{-1}, but such overestimations for the N-H vibrations have already been observed in other reports,[152-156] and this is a part of the spectrum which has very low intensities.

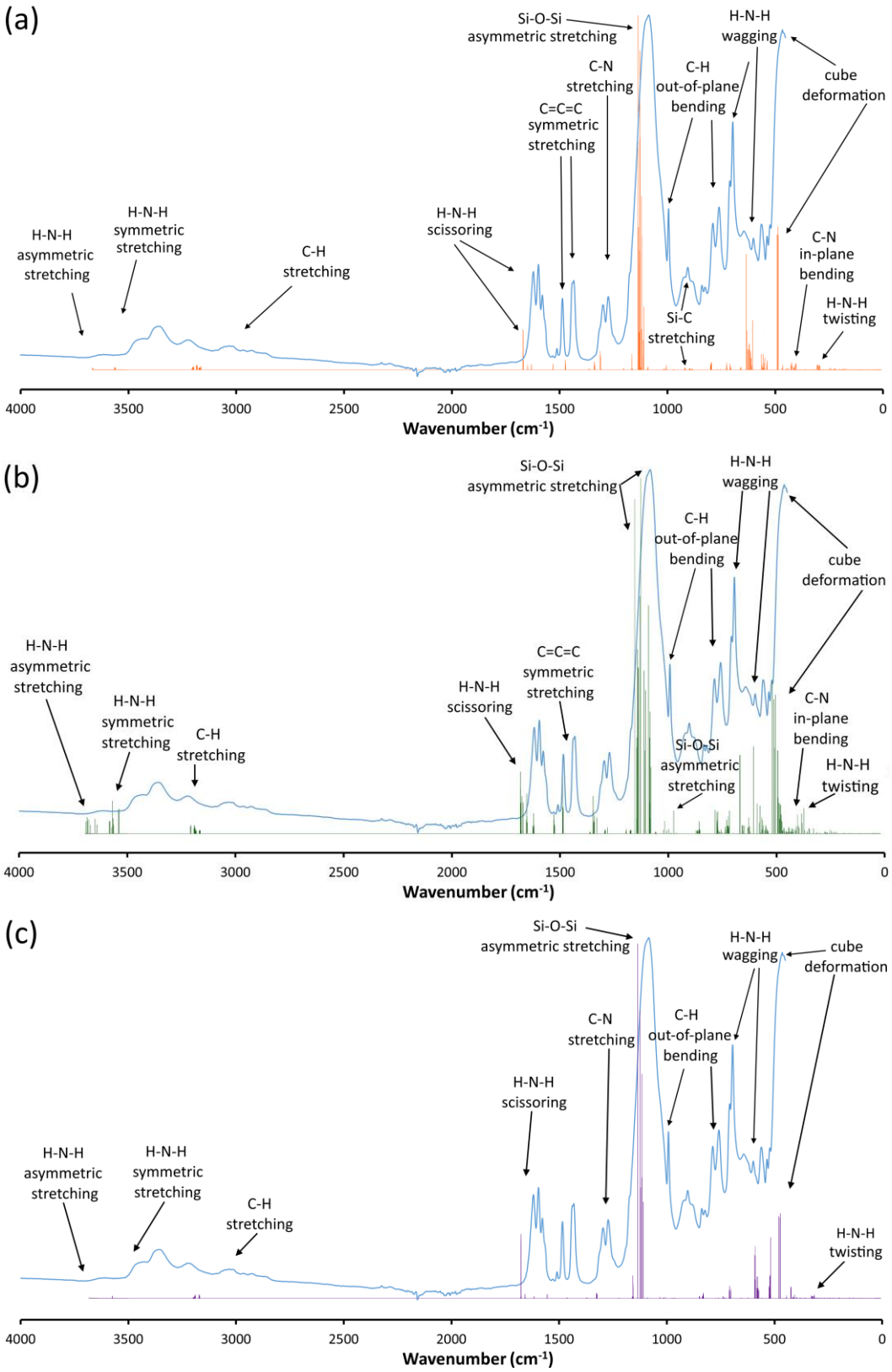

Figure 40. A comparison of the experimental IR spectrum for the commercial OAPS (blue) with the predicted IR spectra for model (a) *meta* (orange), (b) *ortho* (green), and (c) *para* (purple) pure isomers of OAPS obtained from DFT calculations at the B3LYP/6-31G(d,p) level.

Figure 41 compares the experimental spectra of both (a) the commercial and (b) the controlled OAPS with the three predicted IR spectra assembled. A lot of information can be obtained:

- As shown in Figure 40, the compatibility between the experimental and the three predicted spectra assembled is rather good for the commercial OAPS, which seems to agree with the presence of the *ortho* isomer, despite what has been reported by Tamaki et al.[118]

- A sharp peak of H-N-H wagging at 520 cm^{-1} (yellow rectangle) is observed for the controlled OAPS while there is only a small trace of it for the commercial one. Unlike for the other isomers, this rather strong peak was predicted for the *para*-OAPS, which could confirm its high proportion in the controlled OAPS.

- Two strong peaks for the out-of-plane vibrations of C-H appear at 756 cm^{-1} and 784 cm^{-1} (red rectangle) for the commercial OAPS, whereas they almost disappear for the controlled OAPS. Both of them correspond to predicted bands for the *ortho* isomer.

- The strong peak at 1115 cm^{-1} (dark blue rectangle) in the commercial OAPS illustrates the Si-O-Si stretching vibrations which are common to the three isomers because of the silicon oxide cages.[117] In the controlled OAPS, this broad peak is split into two peaks (light blue rectangles), with only one overlapping with the predicted peaks. It is not easy to assign these peaks to the specific *para* and *meta* isomers but it is clear that the *ortho* isomer leads to broader predicted bands in this region.

- The sharp peak at 1485 cm^{-1} for the commercial OAPS (brown rectangle) corresponds to a predicted band for the *ortho*-OAPS and does not appear in the controlled OAPS.

- The predicted bands for the *ortho*-OAPS from 1280 cm^{-1} to 1690 cm^{-1} are stronger than for the other two isomers (see Figure 40(b)). This agrees with the experimental spectrum of the commercial OAPS showing stronger peaks in the same region than the controlled one.

- Other peaks could be specific to one isomer, although many of them overlap in the experimental spectra. For example, the peak appearing at 670 cm^{-1} (pink rectangle) in the commercial OAPS seems to correspond to the *ortho* isomer. The peak at 710 cm^{-1} (green rectangle), which is sharp in the controlled OAPS matches with a predicted peak for the *para*-OAPS.

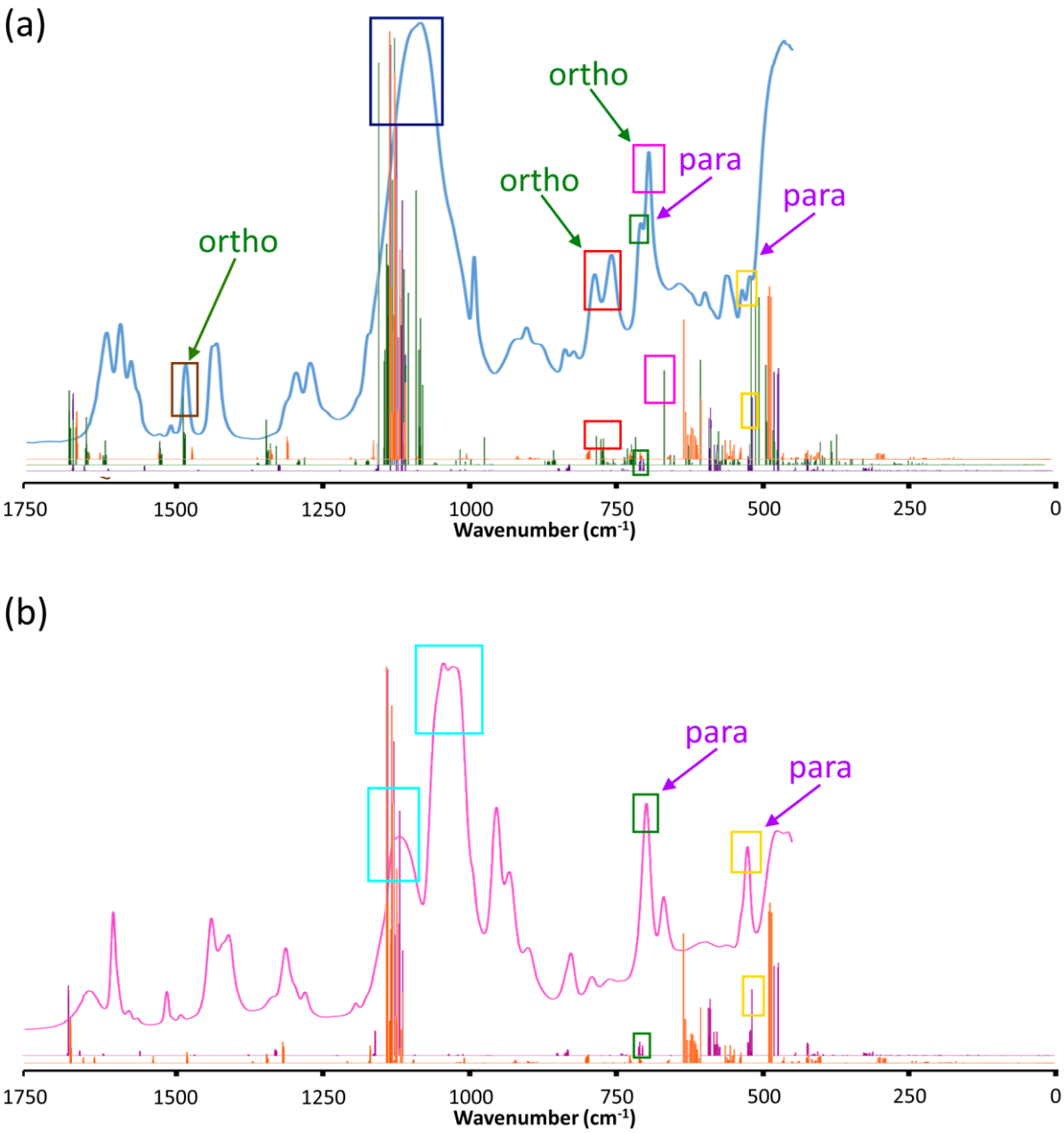

Figure 41. A comparison of (a) the commercial (blue) and (b) the controlled (pink) OAPS experimental spectra with the predicted IR spectra for the *meta* (orange), *ortho* (green), and *para* (purple) OAPS isomers up to 1750 cm^{-1}.

These compared analyses seem to confirm the different natures of both OAPS samples in terms of isomers and show how DFT predictions on a limited number of model structures can be a useful tool to help the interpretation of the experimental spectra.

3) NMR spectroscopy of OAPS

a) The experimental NMR spectra

The NMR spectrum is associated with the emission of electromagnetic radiation by a nucleus at a given frequency of radiation. The ^{29}Si-NMR, ^{13}C-NMR, and ^{1}H-NMR spectra of the commercial and controlled OAPS were recorded at the University of Twente using the Bruker AVANCE III 600 MHz NMR spectrometer. DMSO-d6 was used as the solvent of the samples.

Figure 42 shows the ^{29}Si-NMR spectra of the commercial (blue line) and controlled (pink line) OAPS compared to the OAPS purchased by Lee et al. (brown line).[107] As for our commercial OAPS, Lee's purchased OAPS was obtained by nitration/reduction of OPS. A good compatibility can be observed between the three spectra in Figure 42. However, there are differences between the controlled OAPS spectrum in (b) and both OAPS spectra obtained from nitration/reduction in (a)-(c). Indeed, the intensities of the main shifts at -77.8 ppm and -79.4 ppm (violet and orange rectangles) in the controlled OAPS are in reverse order compared to those of the nitration/reduction OAPS. The increase in intensity at -77.8 ppm in Figure 42(b) can be attributed to the higher portion of the *para* isomer while the decrease at -79.4 ppm is probably due to the lower portion of the *meta* isomer in the controlled OAPS. On the other hand, there are no clearly defined signatures of the *ortho* isomer in the ^{29}Si-NMR spectra, whereas it should be present in the nitration/reduction OAPS samples.

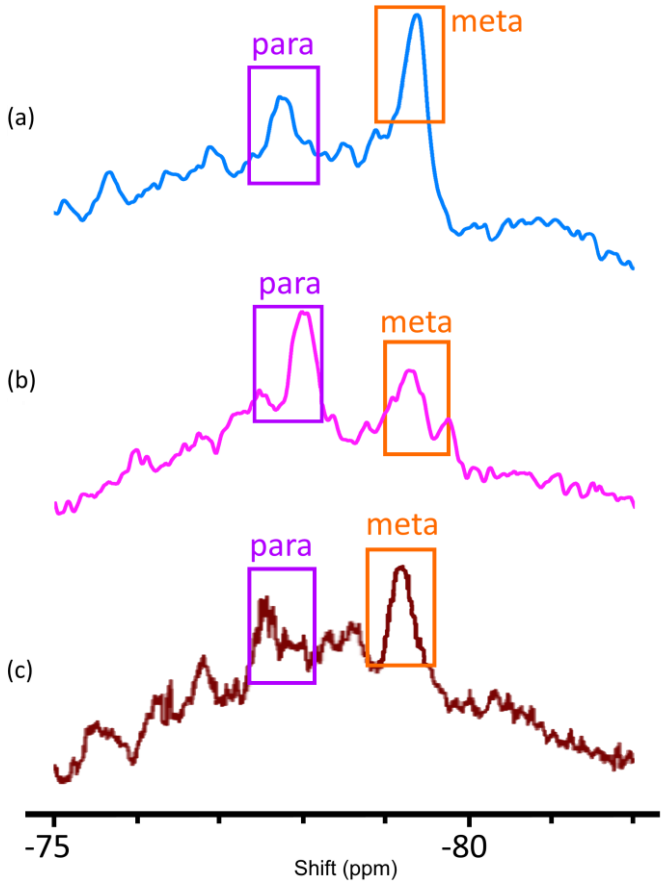

Figure 42. A comparison of the experimental ^{29}Si-NMR spectra for (a) the commercial OAPS, (b) the controlled OAPS, and (c) the OAPS purchased by Lee et al.,[107] all of them in DMSO-d6, along with a proposed isomer assignment for the main peaks.

Similarly, Figure 43 shows the good compatibility of the ^{13}C-NMR spectrum for the commercial OAPS (light blue line) with that of OAPS produced through nitration/reduction by Krishnan et al. (dark blue line).[157] There are at least two peaks at 132 ppm and 154 ppm in the nitration/reduction samples (green rectangles in (a)-(c)), that do not have any equivalent peaks in the (b) controlled OAPS spectrum. These two peaks should again be related to the presence of the *ortho* isomer. The controlled OAPS spectrum also shows weaker peaks in comparison to the other two spectra. Surprisingly, there is a peak in (b) (red rectangle) that shows such a small trace that it cannot be easily revealed in the nitration/reduction samples. That may be why Tamaki et al.[106] reported only ten observable peaks for their ^{13}C-NMR spectrum and concluded that this reflected the presence of the *meta* and *para* isomers only. However, as explained in this work, there are definitely indications of the presence of the *ortho* isomer too in the nitration/reduction samples.

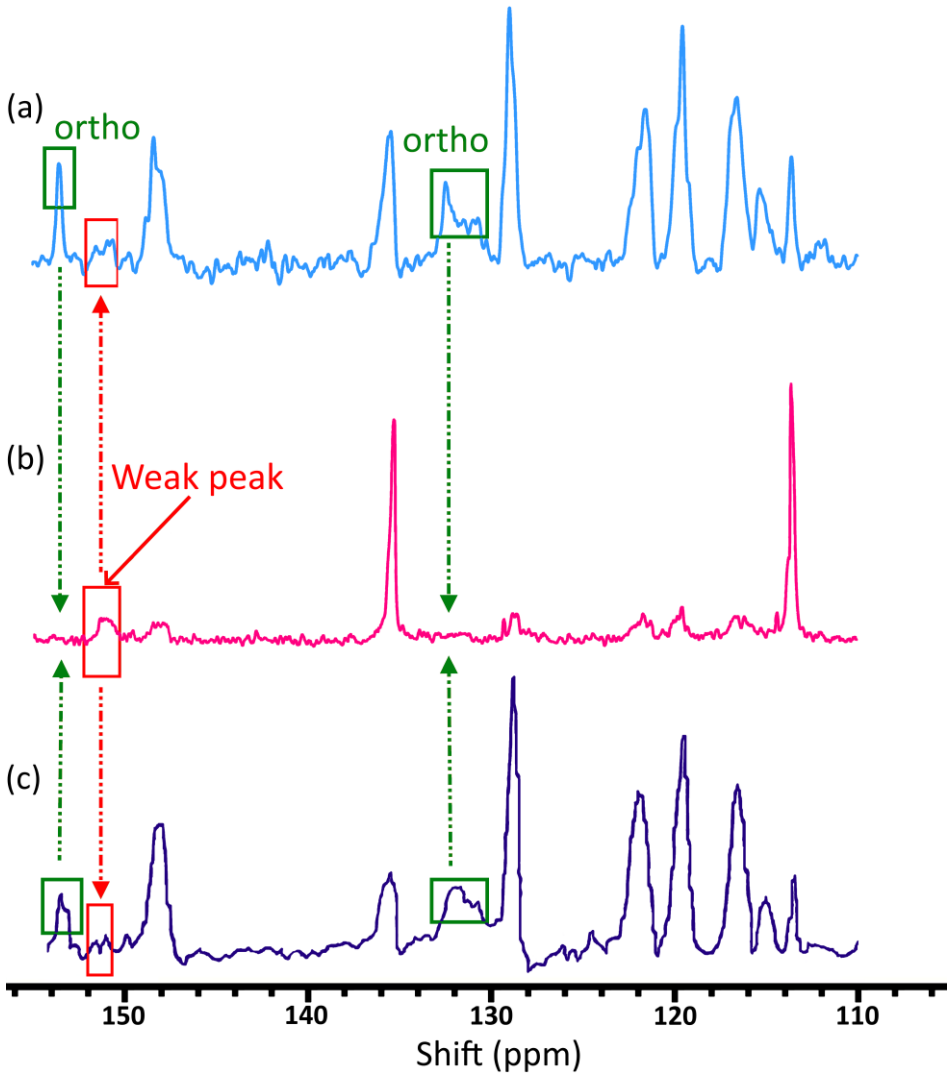

Figure 43. A comparison of the experimental ^{13}C-NMR spectra for (a) the commercial OAPS, (b) the controlled OAPS and (c) the OAPS prepared by Krishnan et al.,[157] all of them in DMSO-d6, along with a proposed assignment for *ortho*-specific peaks.

The ^{1}H-NMR spectra of the commercial and controlled OAPS are compared to that obtained by nitration/reduction by Zhang et al.[113] in Figure 44. Both commercial (light blue line) and Zhang (dark blue line) OAPS spectra are again quite similar but different from the controlled OAPS spectrum (pink line). They are also compatible with the ^{1}H-NMR spectra published by Tamaki et al.[106] and Huang et al.[117] Two broad regions can be distinguished: one from 4.2 ppm to 5.4 ppm, which corresponds to the amine hydrogens, and the other one from 6.2 ppm to 7.8 ppm, which is related to the four aromatic hydrogens of the OAPS phenyl arms. The latter appears in a slightly more narrow range, i.e. 6 ppm to 7.3 ppm, for the controlled OAPS.

The main differences between the three spectra are:

- The yellow rectangles at 5.3 ppm, red rectangles at 6.6 ppm and green rectangles at 7.3 ppm show peaks that do not appear in the (b) controlled OAPS spectrum and can thus be linked to the *ortho* isomer.

- The orange rectangles at 5.15 ppm indicate small peaks in both (a) the commercial and (c) Zhang OAPS, which become stronger for the (b) controlled OAPS with a higher proportion of *para* isomer. Similarly, the sharp peak at 6.25 ppm in the controlled OAPS (brown rectangle) is probably also related to the aromatic *para* hydrogens.

As mentioned before (Figure 25), the number of amine functional groups on each arm or ring connected to the core can be obtained by dividing the integration of the peaks. This ratio is equal to 2 for all OAPS understudy, which means that there are two amine hydrogens along with four aromatic hydrogens, i.e. one -NH_2 per ring for all three samples. However, it is difficult to distinguish the aromatic hydrogens of the different OAPS isomers. This is the reason why Tamaki et al.[106] tried to use the ^{1}H-NMR spectrum of ONPS with its sharper peaks (Figure 23) to calculate the isomer ratio.

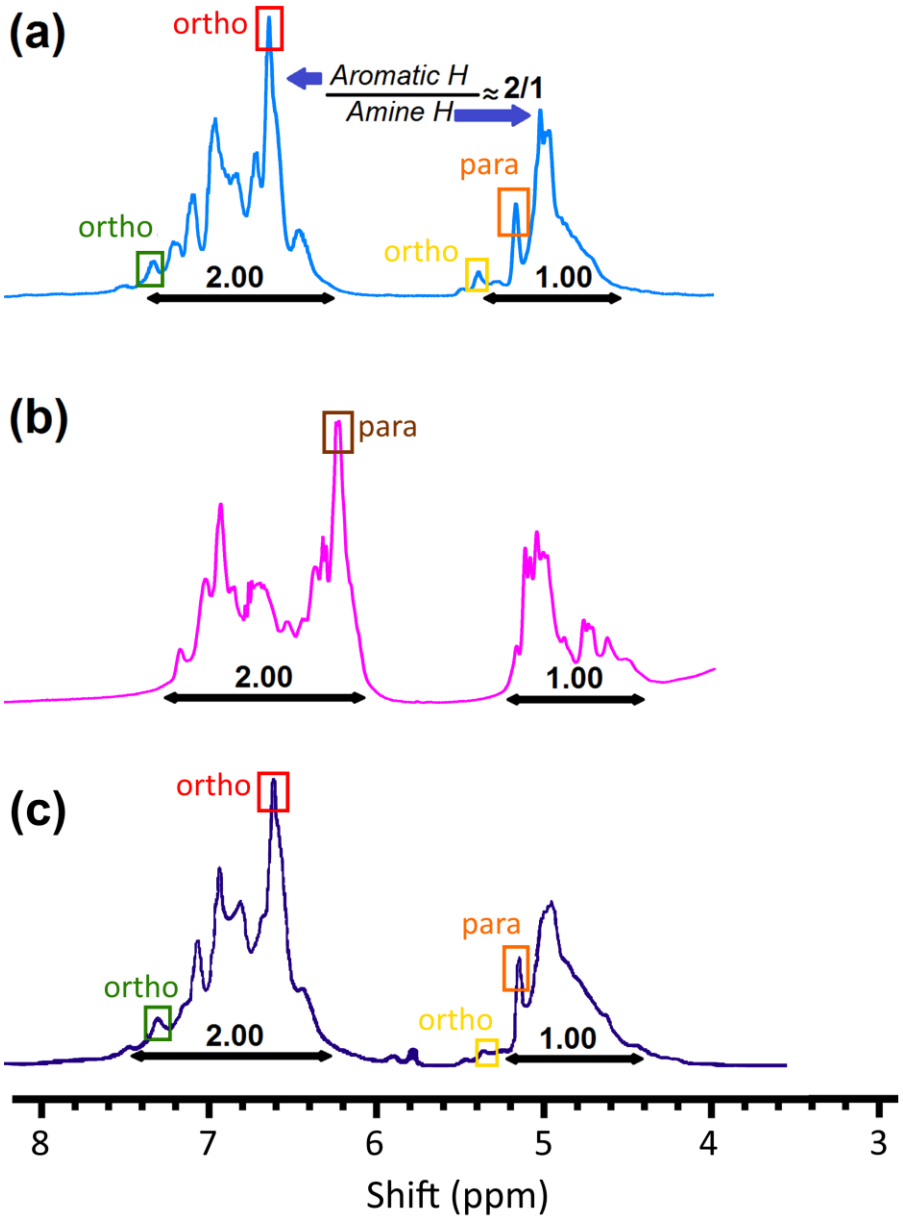

Figure 44. A comparison of the experimental ^{1}H-NMR spectra and surface areas of (a) the commercial OAPS, (b) the controlled OAPS, and (c) the OAPS prepared by Zhang et al.,[113] all of them in DMSO-d6, along with a proposed isomer assignment for the main peaks.

In addition to conventional one-dimensional NMR (1D-NMR) methods, two-dimensional NMR spectroscopy (2D-NMR), which has been developed since the 1980s, analyses the samples with two frequency axes rather than with one.[158-160] It is aimed at facilitating the interpretation of NMR spectra for complex molecules.[160] 2D-NMR techniques can be divided into three main categories, each of which is based on several techniques (Table 10).[161] In homonuclear correlation spectroscopy, both axes of a correlation spectrum display shifts for a single isotope, commonly hydrogen (^{1}H). Heteronuclear correlation

spectroscopy (HETCOR) is linked to two different isotopes such as carbons and hydrogens. Through-space correlation spectroscopy studies nuclei that are physically close to each other, irrespective of the presence of a bond between them.

Table 10. 2D-NMR techniques.[161]

Homonuclear 2D-NMR	Heteronuclear 2D-NMR	Through-space correlation 2D-NMR
Correlation spectroscopy (COSY)	Heteronuclear single-quantum correlation spectroscopy (HSQC)	Nuclear Overhauser effect spectroscopy (NOESY)
Exclusive correlation spectroscopy (ECOSY)		
Total correlation spectroscopy (TOCSY)	Heteronuclear multiple-bond correlation spectroscopy (HMBC)	Rotating-frame nuclear Overhauser effect spectroscopy (ROESY)
Incredible natural-abundance double-quantum transfer experiment (INADEQUATE)		

In a heteronuclear single-quantum correlation (HSQC) spectrum, the 1D-NMR of one nucleus is plotted versus the 1D-NMR of another type of nucleus.[161] In our particular case, the HSQC spectrum correlates the carbon nuclei with the hydrogens directly connected to them, i.e. one-bond couplings. The ^{13}C spectrum is presented on the *y*-axis and the ^{1}H spectrum on the *x*-axis. To interpret such a spectrum, each ^{13}C shift is selected on the *y*-axis and a line is drawn horizontally, i.e. parallel to the ^{1}H-NMR *x*-axis, until a cross-peak is encountered. Similarly, each ^{1}H shift is selected on the *x*-axis and a line is drawn vertically until a cross-peak is encountered. These cross-peaks identify which hydrogens are connected to which carbons and vice versa. When a line encounters no cross-peak, it implies that this carbon has no connected hydrogen.

Figure 45(a) shows the HSQC spectrum obtained for the commercial OAPS. Ten cross-peaks can be observed, indicating ten different carbons connected each to one hydrogen. It confirms that the ^{1}H-NMR shifts from 6.2 ppm to 7.8 ppm refer to the aromatic hydrogens. The three isomers of the commercial OAPS possess sixteen different environments for carbon atoms, ten of which are connected to the hydrogens and the six others to either silicon or nitrogen. The black rectangle shows the ^{1}H-NMR signals presenting no connections to the carbon atoms. These peaks between ~4.5 ppm to ~5.5 ppm are the amine hydrogens, as reported by Tamaki et al.[106] The brown rectangle indicates a ^{1}H-NMR shift specific of the *ortho* amine hydrogens (Figure 44). The orange and purple rectangles show the ^{13}C-NMR signals displaying no connections to the hydrogens. The yellow

rectangles for ^{1}H and red rectangles for ^{13}C give examples of overlapping peaks. The blue rectangles indicate points, which are probably related to incomplete or open cages as their intensities are low. The green rectangles indicate the ^{13}C-NMR shifts related to the *ortho* isomer (Figure 43). Such an HSQC spectrum clearly confirms the presence of the three isomers and the report of Kim et al.[119] is thus more accurate than that of Tamaki et al.[106]

Figure 45(b) shows the HSQC spectrum of the controlled OAPS. Six cross-peaks corresponding to six different carbons connected each to one hydrogen can be observed, as expected from the presence of the *meta* and *para* isomers only. The four remaining carbons are those connected to either silicon or nitrogen. The purple rectangle shows again the ^{13}C-NMR signals having no connections to the hydrogens. The ^{1}H-NMR peaks between ~4.5 ppm to ~5.5 ppm are the amine hydrogens as indicated by the black rectangle. The *ortho* amine shifts between 5.2 ppm and 5.5 ppm (yellow rectangles in Figure 44 and brown rectangle in Figure 45(a)) are absent from Figure 45(b). The pink rectangles display expanded cross-points, which could be related to the different sizes of the OAPS cages in the controlled sample. Indeed, different cages sizes possess different numbers of oxygens and as such, they probably have slightly different electron-withdrawing tendencies. The ^{13}C-NMR peaks specific to the *ortho* isomer (green rectangles in Figure 45(a)) disappear in Figure 45(b), thus confirming its absence. Such an HSQC spectrum shows that there are indeed only two isomers out of the possible three in the controlled OAPS sample.

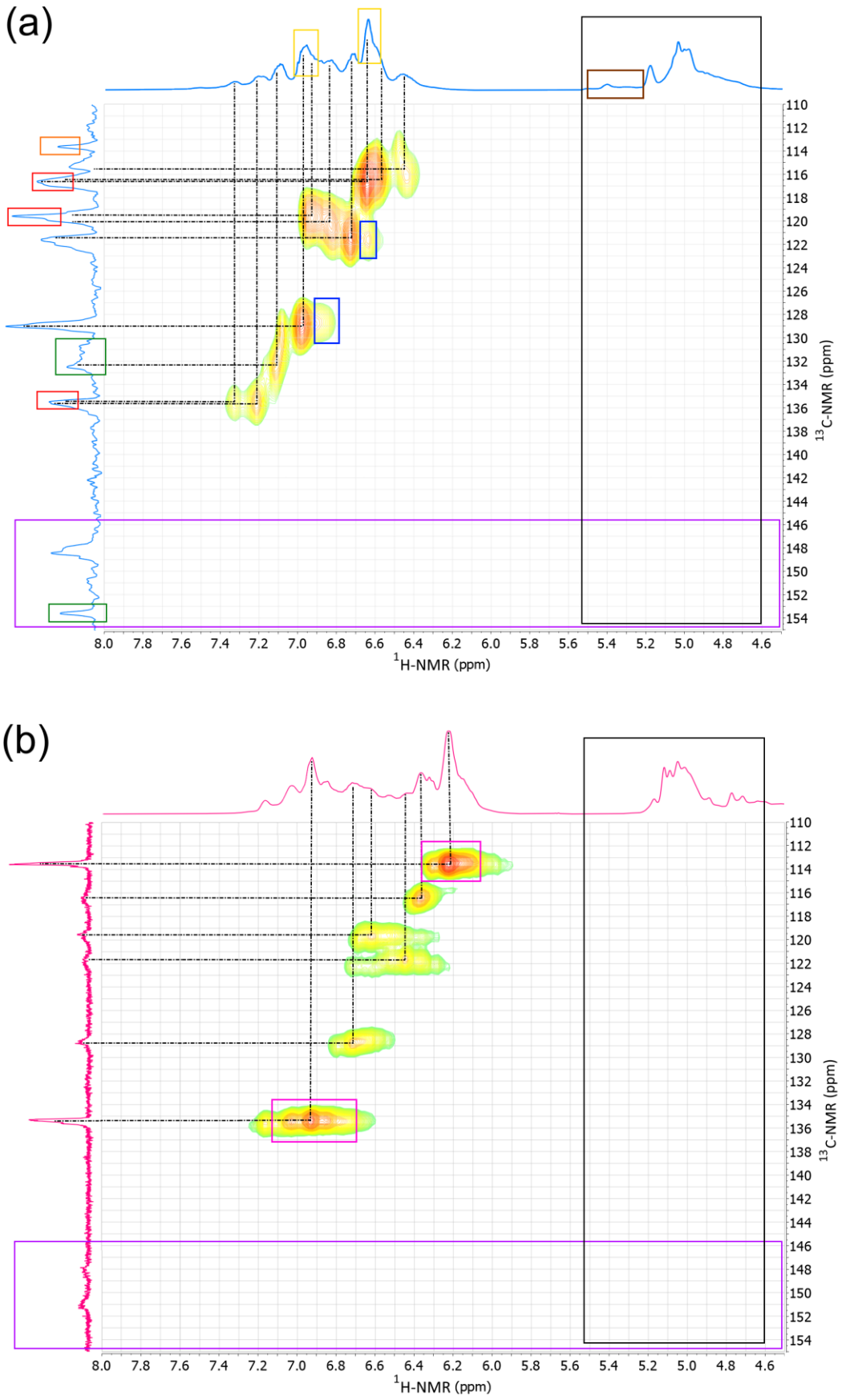

Figure 45. The HSQC spectra of (a) the commercial OAPS and (b) the controlled OAPS.

b) Predictions of the NMR spectra

b.1) Description of the methods

There are both fast and slow computational methods to predict NMR spectra. All fast NMR prediction methods use databases of assigned data. In a nutshell, these approaches can be summarized as:[127]

- Increments methods (from tables of fragments)
- Machine Learning methods
- HOSE-code methods

The most common algorithms for NMR prediction use reference databases where a large number of spectra and their assigned 2D or 3D chemical structures are the source knowledge. The MestreNova software[127] uses both machine learning and the HOSE (Hierarchical Organization of Spherical Environments) code prediction, which was first described by Bremser.[127, 162] The HOSE code starts at the carbon atom whose shift is to be predicted, looks one bond away from the carbon, and tries to find this environment in its database. If it is successful, it moves two bonds away and tries again and so on until it either comes across something which is not represented in the database or it reaches the boundary of the molecule (Figure 46). The HOSE code approach works very well for structures, which are represented in the reference collection.

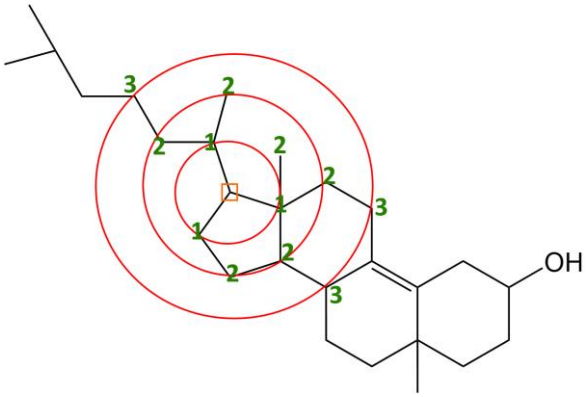

Figure 46. The prediction path for ^{13}C-NMR by HOSE.[127]

"NMRPredict" is the name of the prediction module in MestreNova. If the environment of an atom can be predicted to be three neighbouring atoms or more (NMRPredict goes to a maximum of five neighbouring atoms), the prediction can be

considered very reliable. However, if the query structure is not well represented in the database and the atom environment can only be predicted to one or two neighbouring atoms, the prediction cannot be relied upon. To improve the situation, NMRPredict also uses a unique Neural Network algorithm,[127] which is more general and error-tolerant than the HOSE code and is more accurate at predicting shifts for atoms whose environments are not in its database. It should be noted that even a quality reference database of 10000 compounds and the best software may deliver poor prediction accuracy due to specific conformational features.[127] MestreNova includes a module for minimization of the input structures, which tries to find the optimized geometries according to specific parameters fed to the software by the developer (no details on the techniques and parameters used for minimization are provided). Another factor is the chemical environment. MestreNova calculates the NMR spectrum of a single-point structure at the moment, which is not the case for a molecule dissolved in a solvent. Although there is an option to select a common solvent in the software in order to carry out more accurate calculations, the prediction depends on the database and the machine learning feature ability. In the present case, DMSO was chosen as the solvent for the calculations as it was used for the experimental NMR spectrometry.

In addition to the MestreNova approach, it is also possible to predict an NMR spectrum with much slower quantum mechanical (QM) calculations such as the DFT calculations carried out by Gaussian (Annexe 2). As explained in the previous section, it did give good results at the B3LYP/6-31G(d,p) level for the IR spectra. However, in the case of the NMR spectra, results can be very dependent on the level of theory used. As such, different levels of theory with a solvent correction, i.e. here SCRF=(solvent=DMSO) and the GIAO formulation first had to be tested,[163-165] in order to perform both the optimization and calculation of the NMR chemical shifts for the different OAPS isomers. The SCRF (Self-Consistent Reaction Field) keyword[166] accounts for the presence of the solvent (here DMSO) by locating the solute in a cavity within the solvent reaction field using the Polarizable Continuum Model (PCM).[167] This method, which represents the solute cavity through a set of overlapping spheres was initially introduced by Tomasi et al.[168-169] and Pascual-Ahuir et al.,[170] and it has been further improved by Tomasi, Barone, Mennucci et al.[171-179] and other researchers.[128] The GIAO (Gauge-Including Atomic Orbital) formulation results in all matrix elements involving the basis functions being independent of the origin.[118] Since Gaussian calculates the absolute shieldings, the same level of theory has to be used for tetramethylsilane (TMS) as the reference for the chemical shifts.

To do an in-depth research, different DFT functionals used in the literature for NMR predictions,[180-183] *i.e.* B3LYP, B3PW91, and HCTH407 were used along with 6-311+G(2d,p) as the main basis set and PCM as the default SCRF method in order to predict the chemical shielding values. Here, the 2d term in the basis set adds two sets of d functions on the heavy atoms, and p adds one set of p functions on the hydrogens.[184] The molecules were previously all optimized at the B3LYP/6-31G(d,p) level as it is a good compromise between time and accurate energy minimisation.[149] As far as the functionals are concerned, the first one, B3LYP, has already been presented in the previous Section about the IR predictions. The second one, B3PW91, is a hybrid functional representing Becke's three parameters and combining Perdew and Wang's gradient-corrected exchange (published in 1991) with the correlation functions and Hartree-Fock exchanges.[185-186] The third one, HCTH407, which is a GGA approach,[187] refers to Hamprecht, Cohen, Tozer, and Handy,[188] who fitted their parameters by using 407 atomic and molecular training systems. Contrary to the hybrid B3LYP and B3PW91, there are no HF functions for HCTH407.[188] In addition, the B3LYP/6-31G(d,p) level of theory used for the IR spectra was attempted for NMR prediction and its results will also be presented. These different combinations of DFT functionals and basis sets, which were tested for all three types of NMR spectra (^{29}Si, ^{13}C and ^{1}H), are summarized in Table 11.

While they have been shown to be appropriate for ^{13}C-NMR and ^{1}H-NMR, conventional DFT approaches are not always able to produce as good predictions for the less common ^{29}Si-NMR spectra.[183, 189-198] As such, in that specific case, the B3PW91 and HCTH407 functionals were also tested with a more extended basis set, i.e. 6-311++G(2df,2pd). The 2df term adds two d along with one f function for the heavy atoms, and the 2pd term adds two p and one d functions for the hydrogens. In addition, even more powerful Hartree-Fock calculations were attempted with the main 6-311+G(2d,p) and the extended 6-311++G(2df,2pd) basis sets. In the HF model, each electron is described by an orbital and the total wave function is presented as a product of orbitals,[199] thus making it a lot more computationally expensive than DFT. These approaches are thus also mentioned in Table 11, but as noted above, the predictions with the extended 6-311++G(2df,2pd) basis set and the heavy HF approach were restricted to ^{29}Si-NMR. Indeed, it will be shown that for ^{13}C-NMR and ^{1}H-NMR, a sufficient degree of accuracy can be obtained using more manageable (i.e. lower) basis sets and DFT methods.

Table 11. The different combinations of methods and basis sets used to calculate the chemical shifts using the Gaussian software.

	B3LYP	B3PW91	HCTH407	HF
6-31G(d,p)	*	-	-	-
6-311+G(2d,p)	*	*	*	*
6-311++G(2df,2pd)	-	*	*	*

The procedure to get chemical shifts from the calculations by Gaussian is detailed in Annexe 2. As noted above, Gaussian is in general very heavy in terms of calculations (for a specific OAPS isomer, DFT and HF calculations take typically 10 and 20 days respectively, to complete both optimization and NMR prediction), whereas MestreNova produces the results in a few minutes. As such, it is interesting to attempt and compare both approaches.

b.2.) Case study: the *meta*-OAPS isomer

Due to the highly time-consuming DFT calculations, a siloxane cage with one *meta* ring and seven hydrogens linked to the Si (Figure 47(a)) was first fed to both MestRenova and Gaussian in order to calculate the chemical shifts for the various combinations of Table 11. In a second stage, one method was discarded and the other calculations were repeated on an 8-ring *meta*-OAPS (Figure 47(b)) since it is expected that the presence of the rings connected to the silicons will somewhat displace the shifts. Note that, in the following Figures, the 8-ring *meta*-OAPS is simply shortened to *meta*-OAPS.

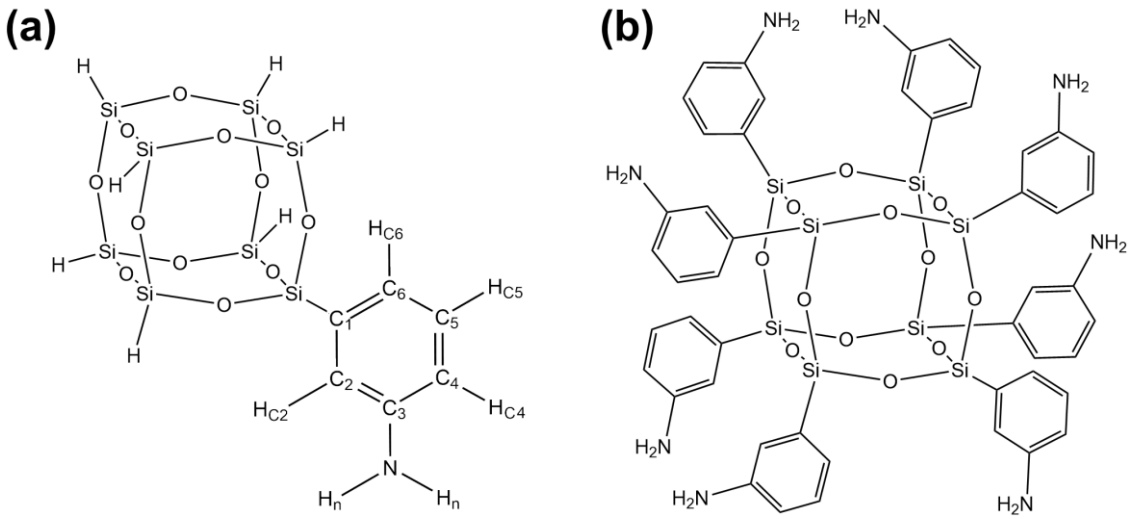

Figure 47. The molecular structures of a) the 1-ring *meta*-OAPS and b) the 8-ring *meta*-OAPS. The phenyl ring carbons are named C_1, C_2, C_3, C_4, C_5 and C_6. H_{C2}, H_{C4}, H_{C5} and H_{C6} are the aromatic hydrogens connected to C_2, C_4, C_5 and C_6 respectively. H_n indicates both amine hydrogens.

b.2.1.) The ^{29}Si-NMR predicted spectra for the 1-ring meta-OAPS

Figure 48 shows the ^{29}Si-NMR shifts predicted by Gaussian[128] using the combinations presented in Table 11 (dashed lines) and MestreNova[127] (line) for the 1-ring *meta*-OAPS along with two experimental spectra in the range from -50 to -90 ppm. In the predicted spectra, only the shift of the silicon connected to the aminophenyl ring was taken into account. The blue experimental spectrum corresponds as before to the commercial OAPS obtained by nitration/reduction (all three isomers present, same as in Figure 42) and displays clear chemical shifts at -79.4 ppm, -77.8 ppm, -76.9 ppm, and -75.7 ppm along with a smaller one at -69 ppm. The orange experimental spectrum is that of the pure *meta* isomer obtained from the condensation of APTMS precursors by Lee et al.[107] It shows a distinct peak at -79.1 ppm, which is close to the sharpest peak of the blue spectrum at -79.4 ppm and could indicate that this belongs to the *meta* isomer.

As far as MestreNova is concerned, the predicted chemical shift for the Si connected to the single *meta*-ring appears at -59.3 ppm which differs from the experimental spectra by 20 ppm. The shift predicted by Gaussian at the B3LYP/6-31G(d,p) level of theory is at -61.9 ppm, which is also very distant from the main experimental peaks around -79.4 ppm. On the other hand, the Gaussian predictions with the 6-311+G(2d,p) and 6-311++G(2df,2pd) basis sets are closer to the experiment. For the former, the Si shift is underestimated by ~10 ppm for B3LYP and HCTH407 and by ~3 ppm for B3PW91, while it is overestimated by ~2 ppm by HF. The situation is further improved for HF by using the more extended 6-311+G(2d,p) basis set since it predicts the Si shift at -80 ppm, i.e. very close to the sharpest experimental peak. This is not the case for both B3PW91 and HCTH407 whose predicted shifts with 6-311++G(2df,2pd) are even further from the experiment than when associated with the lower 6-311+G(2d,p) basis set. It clearly shows that both the methods and the basis sets significantly affect the final accuracy of the prediction.

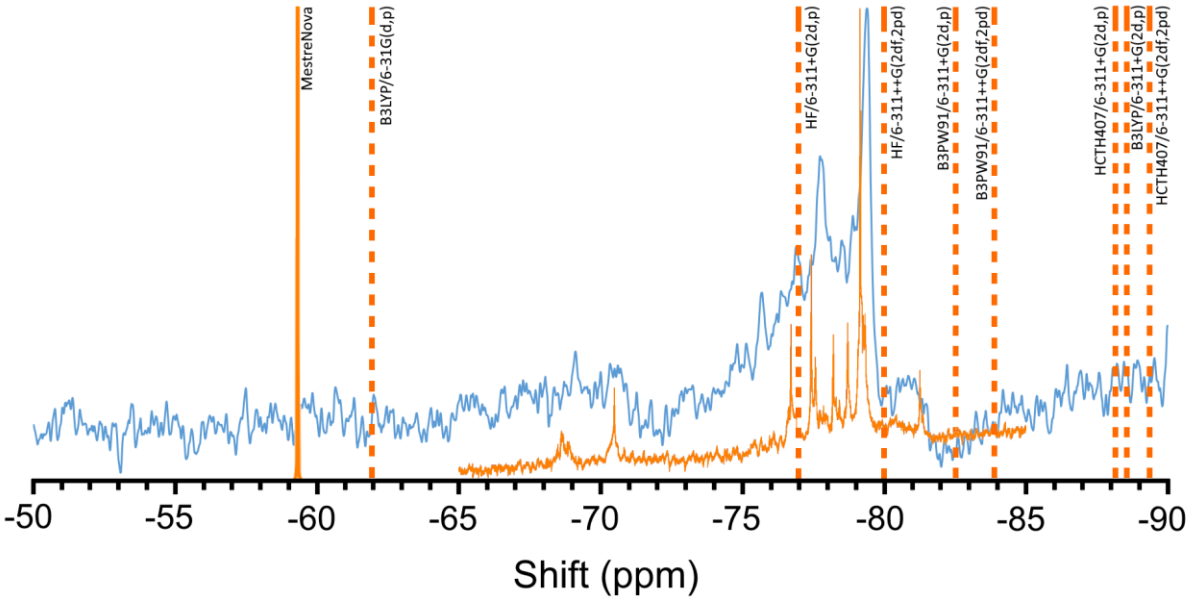

Figure 48. The experimental ^{29}Si-NMR spectra of the commercial OAPS (blue line) and the pure *meta* isomer of Lee et al. (orange line)[107] compared with the predicted chemical shifts by Gaussian (dashed lines) and MestreNova (lines) for the 1-ring *meta*-OAPS. Note that in the following NMR Figures, the same colour code and representations will systematically be used: Gaussian will be represented by dashed lines, MestreNova by lines, the experimental commercial OAPS by a blue line and the experimental pure *meta* and *para* spectra of Lee et al. by an orange and a purple line respectively.

b.2.2.) The ^{13}C-NMR predicted spectra for the 1-ring meta-OAPS

Figure 49 shows separately several predicted ^{13}C-NMR spectra for the 1-ring *meta*-isomer along with the experimental ^{13}C-NMR spectrum for the commercial OAPS (blue line). Lee et al.[107] did not report any ^{13}C-NMR spectra for their pure *meta*-OAPS and *para*-OAPS structures.

There again, the predicted peaks appear at different chemical shifts to the experimental ones, although they are in general much closer for the lower basis sets than for the ^{29}Si-NMR spectra. One overlap is predicted at ~125 ppm by MestreNova (red rectangle in (a)). In the Gaussian predictions, some shifts are found within less than 2 ppm and could also be possible overlaps. This is the case for B3LYP when associated with 6-31G(d,p) at ~125 ppm (purple rectangle in (b)) and when associated with 6-311+G(2d,p) at ~136 ppm (green rectangle in (c)). Both B3PW91 and HCTH407 indicate overlaps at 134.5 ppm (pink rectangle in (d)) and 127.9 ppm (brown rectangle in (e)), respectively. As noted before, the existence of overlaps (which do not allow to see the peaks separately) can explain why

Tamaki et al.[106] observed ten peaks and excluded the *ortho* isomer in their nitration/reduction OAPS.

Each predicted shift in Figure 49 can be assigned to one specific aromatic carbon according to the definition of Figure 47(a). The carbon shifts are in the order $C_4 < C_2 < C_6 < C_5 < C_1 < C_3$ for the Gaussian predictions. The order is similar for MestreNova, except for the C_1 shift which is predicted between C_4 and C_6 rather than close to C_5. However, it should be remembered that the MestreNova predictions are carried out on directly-inbuilt and optimized structures within that code, and as such, they can slightly differ from the Gaussian-inbuilt and optimized structures.

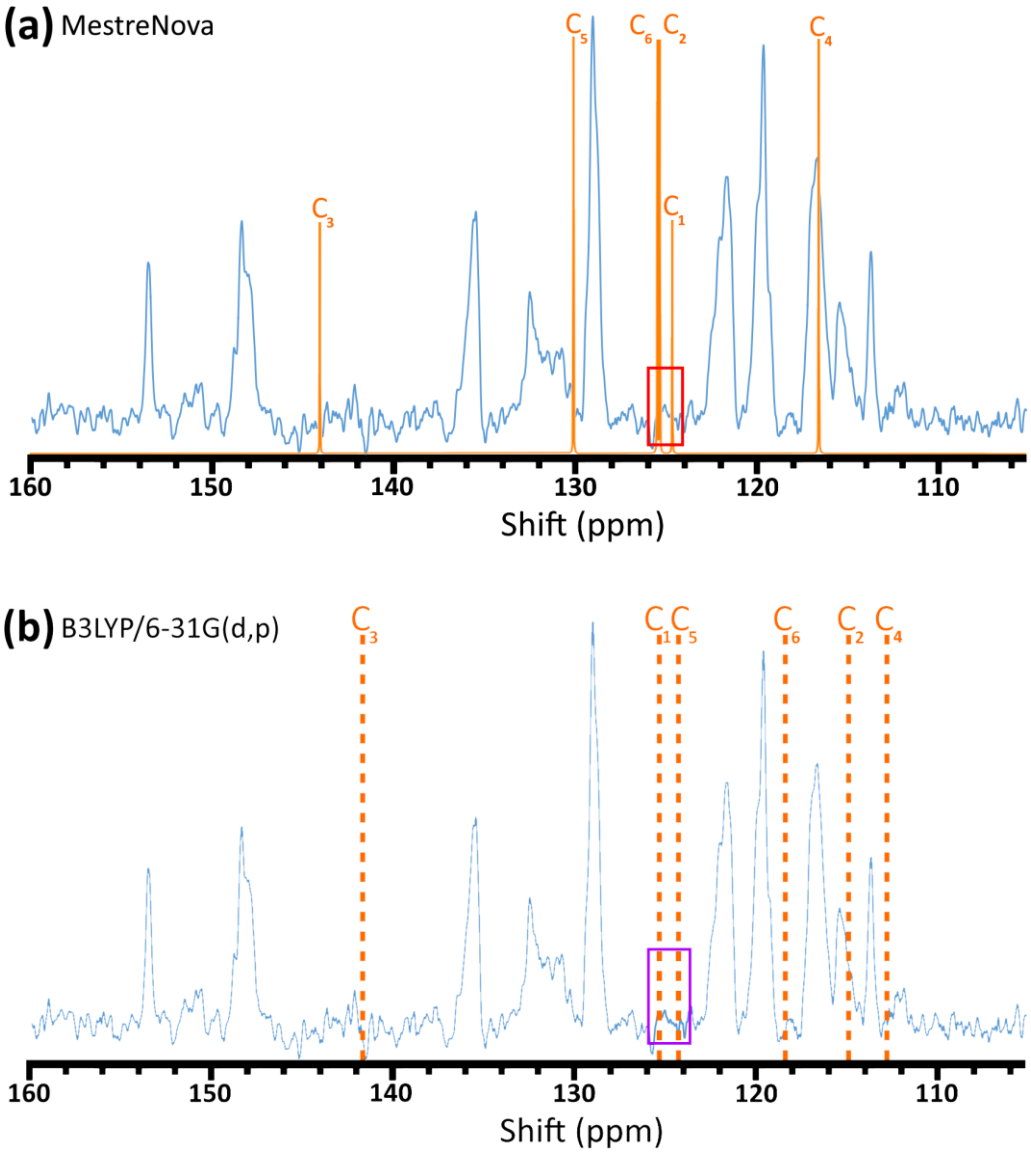

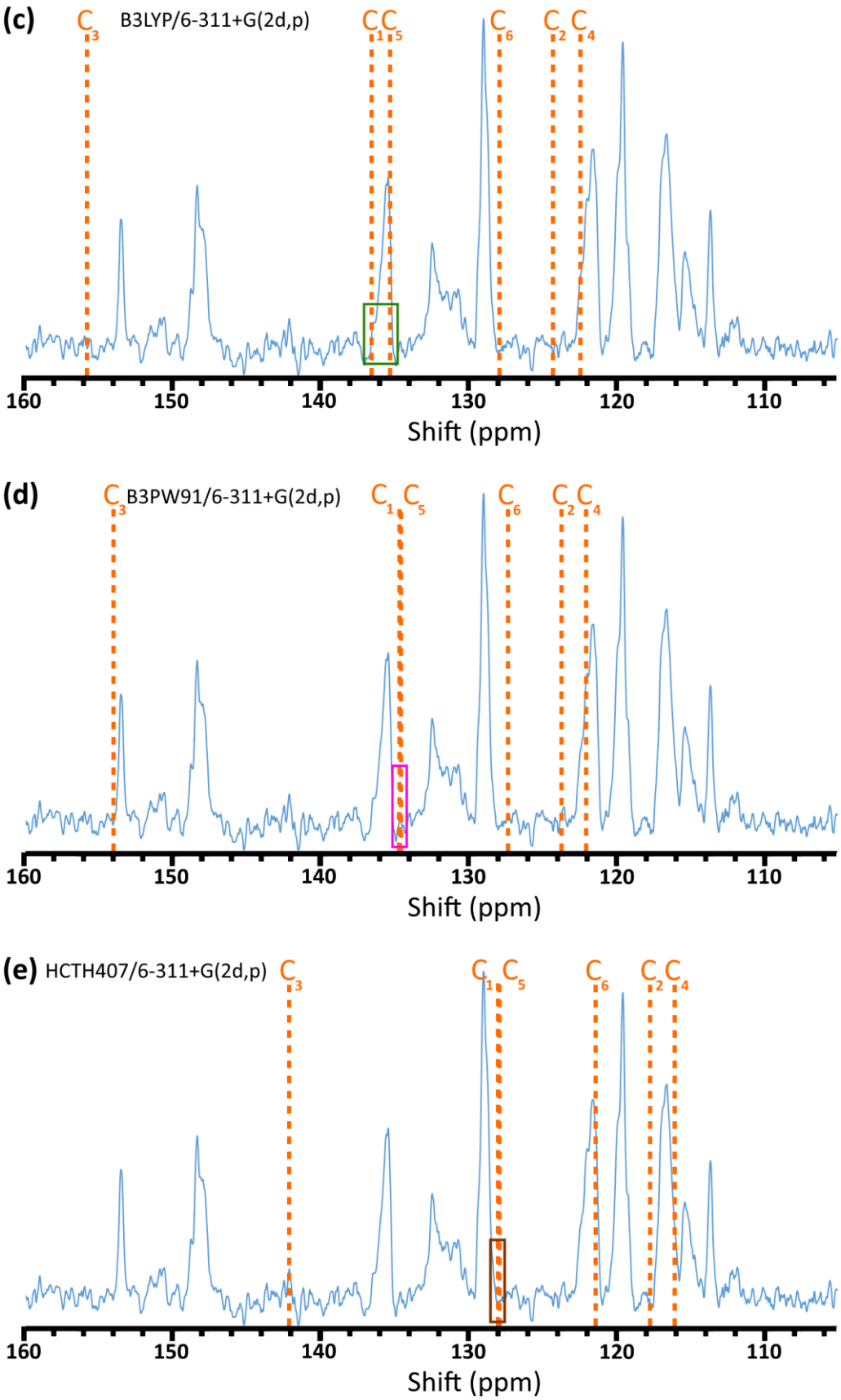

Figure 49. A comparison of the OAPS ^{13}C-NMR experimental spectrum (blue line) with the chemical shifts predicted for the aromatic carbons of the 1-ring *meta*-OAPS by Gaussian (dashed lines) and MestreNova (lines).

As the five predicted spectra are not easy to distinguish, the quality of the prediction was assessed by calculating the differences between all predicted peaks and their closest experimental peaks according to Equation 7. To eliminate the background, only the experimental peaks whose intensity was at least 25% of the main peak at 129 ppm were selected. Although this is somewhat subjective, this allows for the comparison of all predicted spectra under the same conditions.

$$Difference = \sqrt{\sum (\text{predicted shifts - closest experimental shifts})^2} \qquad (7)$$

The differences in ppm are reported in Table 12 and show that Gaussian at the B3PW91/6-311+G(2d,p) level of theory gives the best prediction for the 1-ring *meta*-OAPS.

Table 12. The differences between the experimental and the predicted ^{13}C-NMR peaks for the 1-ring *meta*-OAPS according to Equation 7.

Method	MestRenova	B3LYP 6-31G(d,p)	B3LYP 6-311+G(2d,p)	B3PW91 6-311+G(2d,p)	HCTH407 6-311+G(2d,p)
Difference / ppm	7.4	7.8	4.0	3.3	6.5

b.2.3.) The ^{1}H-NMR predicted spectra for the 1-ring meta-OAPS

Figure 50 shows the predicted ^{1}H-NMR spectra for the 1-ring *meta*-isomer along with the experimental ^{1}H-NMR spectrum for the commercial OAPS (blue line). Lee et al.[107] did not report any ^{1}H-NMR spectra for their pure *meta*-OAPS and *para*-OAPS structures. In the predictions, the ^{1}H-NMR shifts of the hydrogens directly connected to the Si were omitted. As for the aromatic carbons in Figure 49, each predicted shift can be assigned to a specific hydrogen as defined in Figure 47(a).

The (a) MestreNova spectrum matches rather well the experimental spectrum for both aromatic (left part of the spectrum) and amine (right part of the spectrum) hydrogens. The Gaussian-predicted shifts for the aromatic hydrogens at the (b) lower B3LYP/6-31G(d,p) level of theory are also fairly good consistent with the experimental spectrum, while the shifts obtained from the larger (c-e) 6-311+G(2d,p) basis set appear to be slightly overestimated. In

addition, they predict possible overlaps as indicated by the pink rectangles. The hydrogen shifts are in the order $H_{C4} < H_{C2} < H_{C6} < H_{C5}$ for all predictions, i.e. they follow the same order as the Gaussian predictions of their attached carbons. However, unlike MestreNova, all Gaussian-predicted peaks appear to be strongly underestimated for the amine hydrogens. The same problem was reported in other studies,[200-201] and was attributed to the NH_2 groups forming hydrogen bonds with the solvent, which is not properly taken into account by the PCM formalism.[201-202]

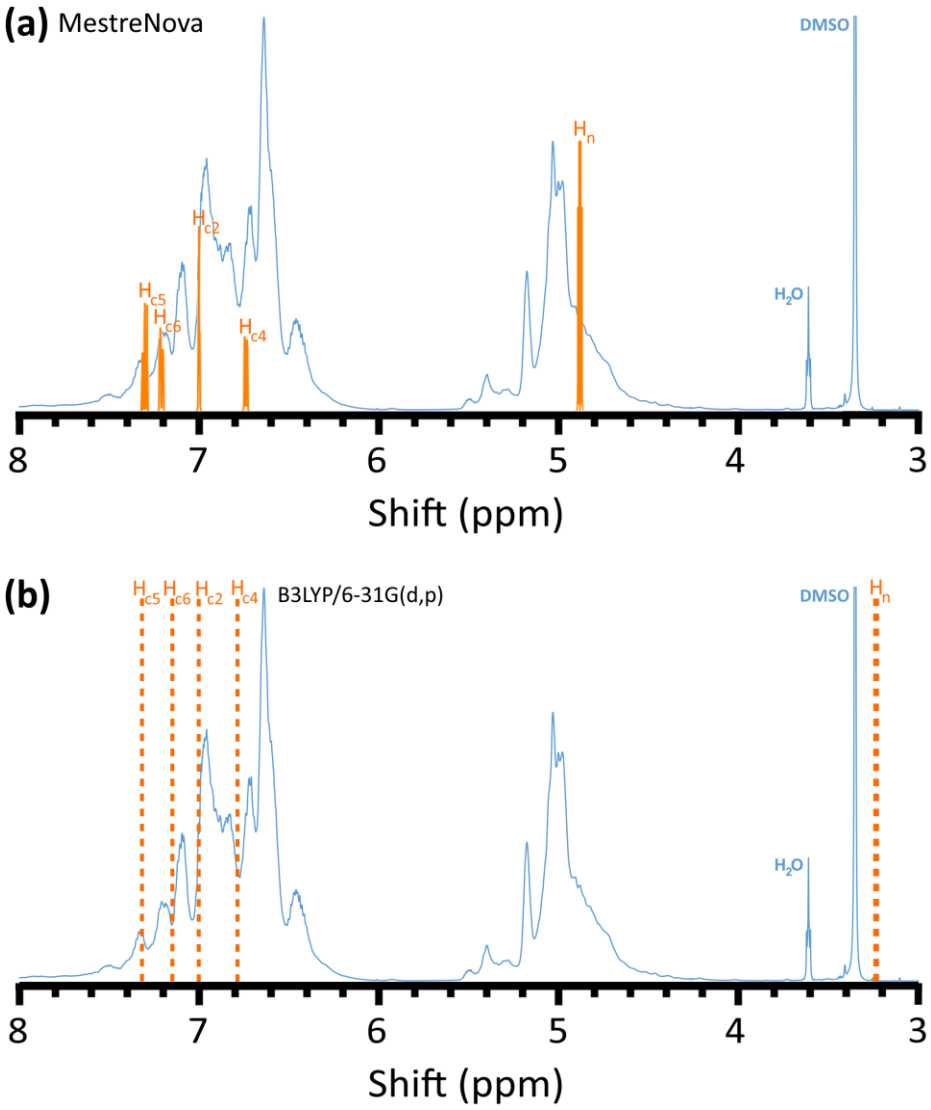

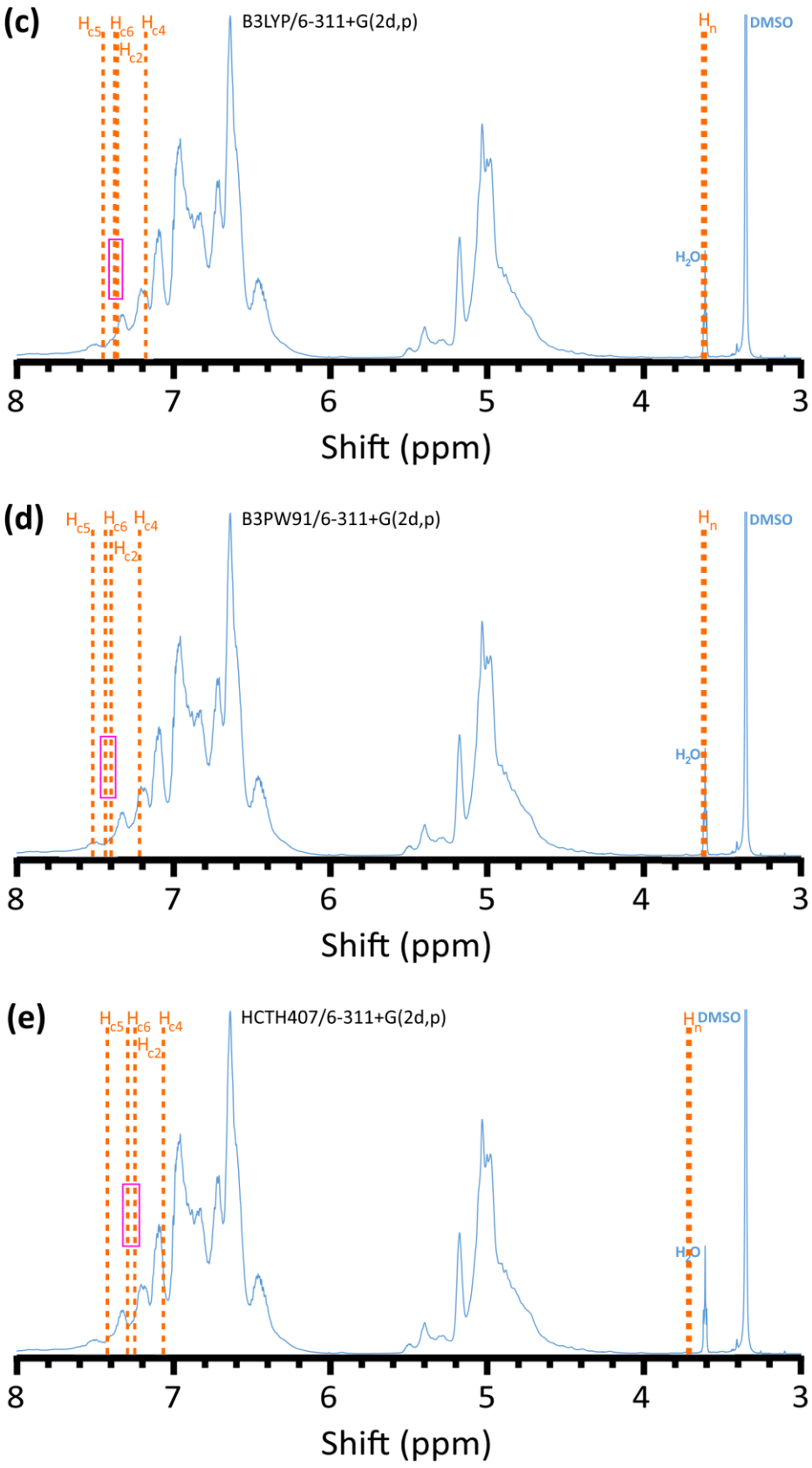

Figure 50. A comparison of the OAPS ^{1}H-NMR experimental spectrum (blue line) with the chemical shifts predicted for the aromatic and amine hydrogens of the 1-ring *meta*-OAPS by Gaussian (dashed lines) and MestreNova (lines).

Since it is more difficult to assign each ^{1}H-NMR predicted shift to a specific experimental one than for the ^{13}C-NMR spectra (Equation 7 and Table 12), the methods were here compared based on the distance between the lowest shift for the aromatic H and the sharpest experimental peak at 6.64 ppm (Table 13).

Table 13. The differences between the main experimental and the closest predicted ^{1}H-NMR peaks for the aromatic hydrogens of the 1-ring *meta*-OAPS.

Method	MestRenova	B3LYP 6-31G(d,p)	B3LYP 6-311+G(2d,p)	B3PW91 6-311+G(2d,p)	HCTH407 6-311+G(2d,p)
Difference / ppm	0.10	0.10	0.60	0.66	0.49

Although MestreNova could not produce results close to the experimental ^{29}Si-NMR spectrum (Figure 48), it shows matchable shifts for the ^{13}C-NMR and especially for the ^{1}H-NMR spectra (Table 13). So it was used again to evaluate the NMR shifts of the 8-ring isomers. DFT at the lower 6-31G(d,p) level of theory also performed quite well for the aromatic hydrogens in the ^{1}H-NMR spectrum (Table 13), but it was much further from the experiment for both the ^{29}Si-NMR and the ^{13}C-NMR spectra. Consequently, it was discarded and only B3LYP, HCTH407, and B3PW91 at the main 6-311+G(2d,p) level of theory were further tested with Gaussian for the 8-ring structures.

b.2.4.) The ^{29}Si-NMR predicted spectra for the 8-ring meta-OAPS

Figure 51 shows the predicted ^{29}Si-NMR shifts for the 8-ring *meta*-OAPS along with the same two experimental spectra as in Figure 48. All Gaussian-predicted shifts are moved to the left in comparison to the 1-ring *meta*-OAPS, which confirms that the presence of the eight aminophenyl rings displaces the shifts. On the other hand, the MestreNova results do not depend on the structure being a 1-ring or an 8-ring *meta*-OAPS, which is a drawback of this approach. They remain also clearly too far from the experimental ^{29}Si-NMR peaks.

At the main 6-311+G(2d,p) level of theory, the DFT shifts predicted by B3LYP and HCTH407 move to -86.8 ppm and -85.7 ppm, respectively. The B3PW91-predicted shift is displaced by 3.7 ppm to -78.8 ppm, which now falls within the experimental range, whereas the HF-predicted peak at -74.9 ppm is further away. With the extended 6-311++G(2df,2dp)

basis set, B3PW91 and HF predict peaks at -80.3 ppm and -78.0 ppm, which are also within the experimental range, unlike the HCTH407-predicted shift at -85 ppm.

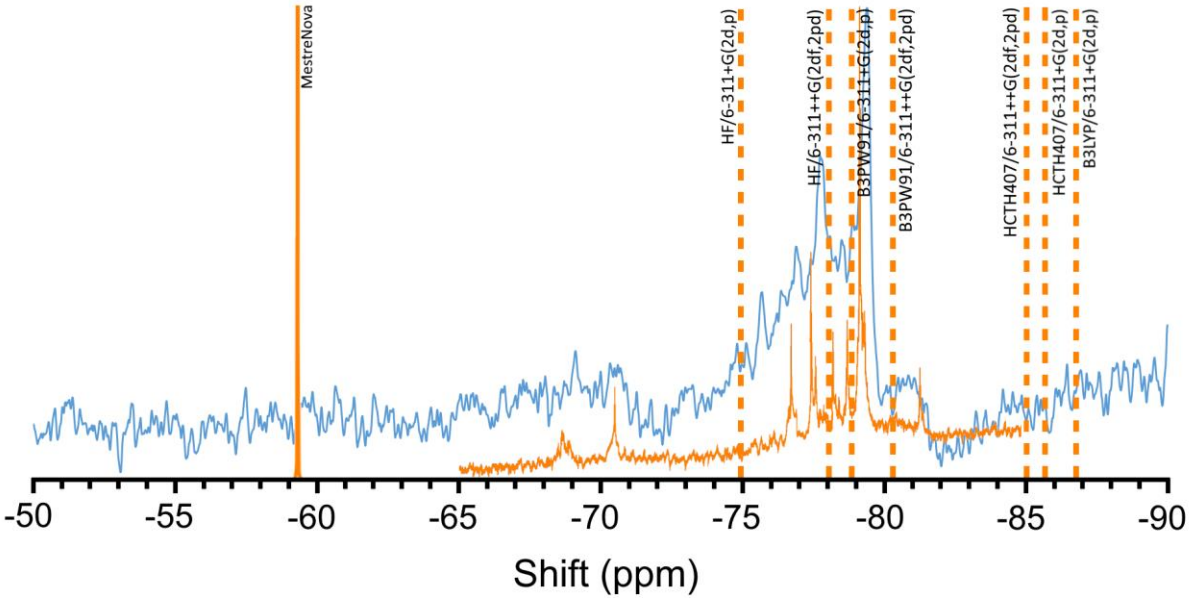

Figure 51. The experimental ^{29}Si-NMR spectra of the commercial OAPS (blue line) and the pure *meta* isomer of Lee et al. (orange line)[107] compared with the predicted chemical shifts by Gaussian (dashed lines) and MestreNova (lines) for the 8-ring *meta*-OAPS.

As for the one-ring OAPS (Figure 48), the Gaussian approaches with B3PW91/6-311+G(2d,p) and HF/6-311++G(2df,2pd) predict the closest ^{29}Si-NMR shifts to the experimental peaks of the pure *meta* isomer. Consequently, these will be the methods tested to predict the ^{29}Si-NMR shifts for the *ortho* and *para* isomers.

b.2.5.) The ^{13}C-NMR predicted spectra for the 8-ring meta-OAPS

Figure 52 shows the predicted ^{13}C-NMR shifts for the 8-ring *meta*-OAPS along with the commercial OAPS experimental spectrum. Unlike for the 1-ring *meta*-OAPS (Figure 49), no overlaps are predicted by neither MestRenova nor Gaussian. The pink rectangles in Figure 52 indicate the few predicted shifts which are the same as for the 1-ring *meta*-OAPS. All other shifts were found to differ, indicating how the presence of the aminophenyl rings affects the results. The displacements of the predicted chemical shifts from the 1-ring to the 8-ring *meta*-OAPS are shown by arrows (← for MestreNova and ← for Gaussian), whose lengths are proportional to the changes. As shown in (a), the largest change is found

for MestreNova with the 1-ring shift at ~124 ppm being displaced by ~10 ppm to the left in the 8-ring structure. This results in the ^{13}C-NMR MestreNova predicted shifts associated with specific carbons being now in the same order as for Gaussian, which is also identical to that in the one-ring *meta* structure.

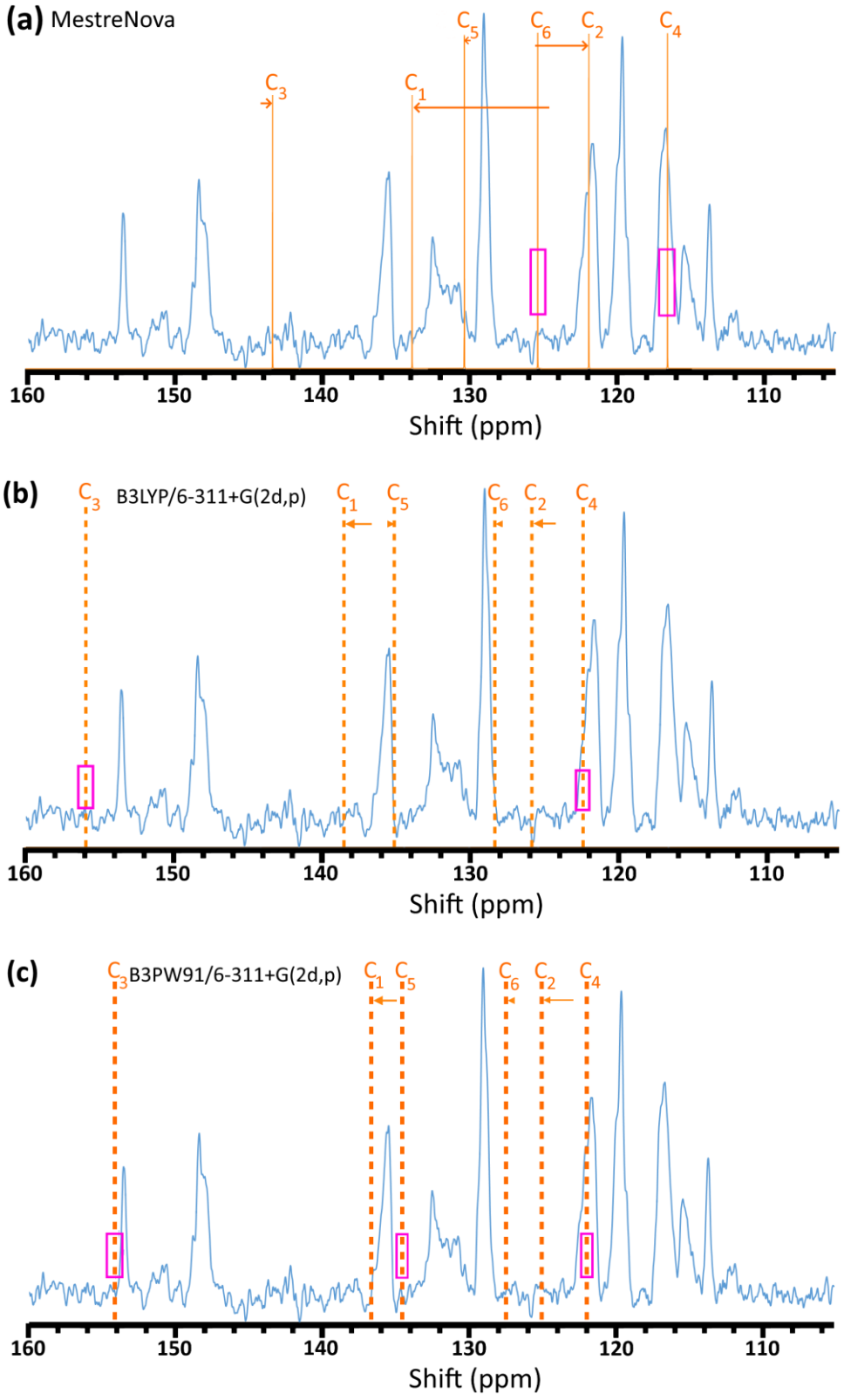

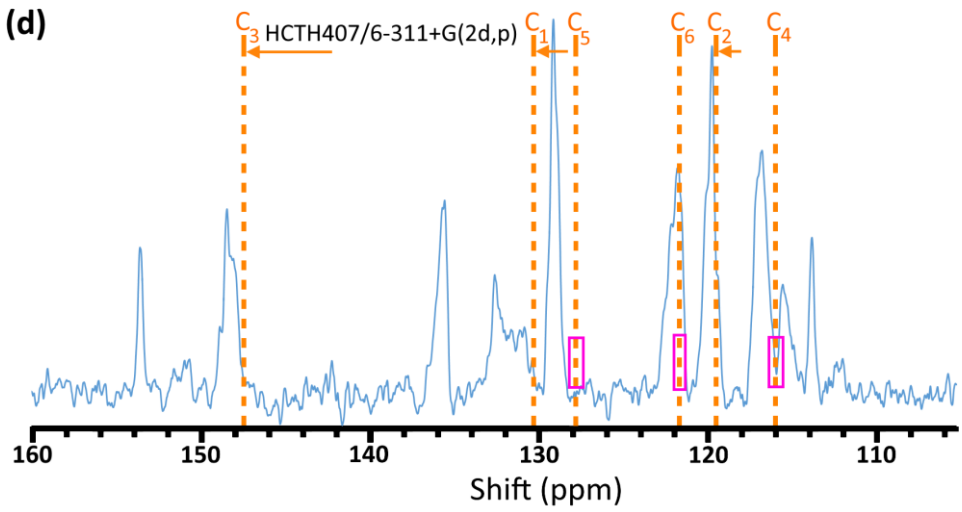

Figure 52. A comparison of the commercial OAPS ^{13}C-NMR experimental spectrum (blue line) with the chemical shifts predicted for the aromatic carbons of the 8-ring *meta*-OAPS by Gaussian (dashed lines) and MestreNova (lines). The arrows ← and ← indicate the differences in shifts with respect to the 1-ring *meta*-OAPS generated by Gaussian and MestRenova respectively.

There again, the quality of the prediction was assessed according to the difference between the predicted peaks and their closest experimental peaks (Equation 7). As for the 1-ring analyses (Table 12), only the experimental peaks whose intensity was at least 25% of the main peak at 129 ppm were selected to eliminate the background. These differences in ppm are reported in Table 14 for the various methods tested and show that HCTH407/6-311+G(2d,p) now gives the best prediction.

Table 14. The differences between the experimental and the predicted ^{13}C-NMR peaks for the 8-ring *meta*-OAPS according to Equation 7.

Method	MestRenova	B3LYP 6-311+G(2d,p)	B3PW91 6-311+G(2d,p)	HCTH407 6-311+G(2d,p)
Difference / ppm	2.5	2.3	2.1	1.4

Compared to the 1-ring *meta*-OAPS, the HCTH407 method at the 6-311+G(2d,p) level of theory seems to be better than B3PW91, although the latter provides the second-best prediction. This change in order is due to the three HCTH407-predicted shifts at 116.2 ppm (C_4), 119.7 ppm (C_2), and 121.8 ppm (C_6) being very close to their respective experimental peaks. As such, Gaussian with HCTH407/6-311+G(2d,p) will be the method used to predict the ^{13}C-NMR shifts for the *ortho* and *para* isomers.

b.2.6) The ^{1}H-NMR predicted spectra for the 8-ring meta-OAPS

Figure 53 shows the predicted ^{1}H-NMR spectra for the 8-ring *meta*-isomer along with the commercial OAPS experimental spectrum. The red rectangles indicate the chemical shifts predicted by (a) MestreNova, which are somewhat displaced to the right in comparison to the 1-ring *meta*-OAPS (Figure 50). As a whole, they match even better with the experimental data, thus suggesting that MestreNova is well adapted to ^{1}H-NMR prediction. On the contrary, the three Gaussian methods (b-d) still overestimate the chemical shifts for the aromatic hydrogens (with the pink rectangles showing possible overlaps) and underestimate the chemical shifts for the amine hydrogens. The displacements of the predicted chemical shifts from the 1-ring to the 8-ring *meta*-OAPS are again shown by arrows, but they remain very small. Consequently, the relative order for the specific ^{1}H-NMR shifts remains the same as for the 1-ring structure.

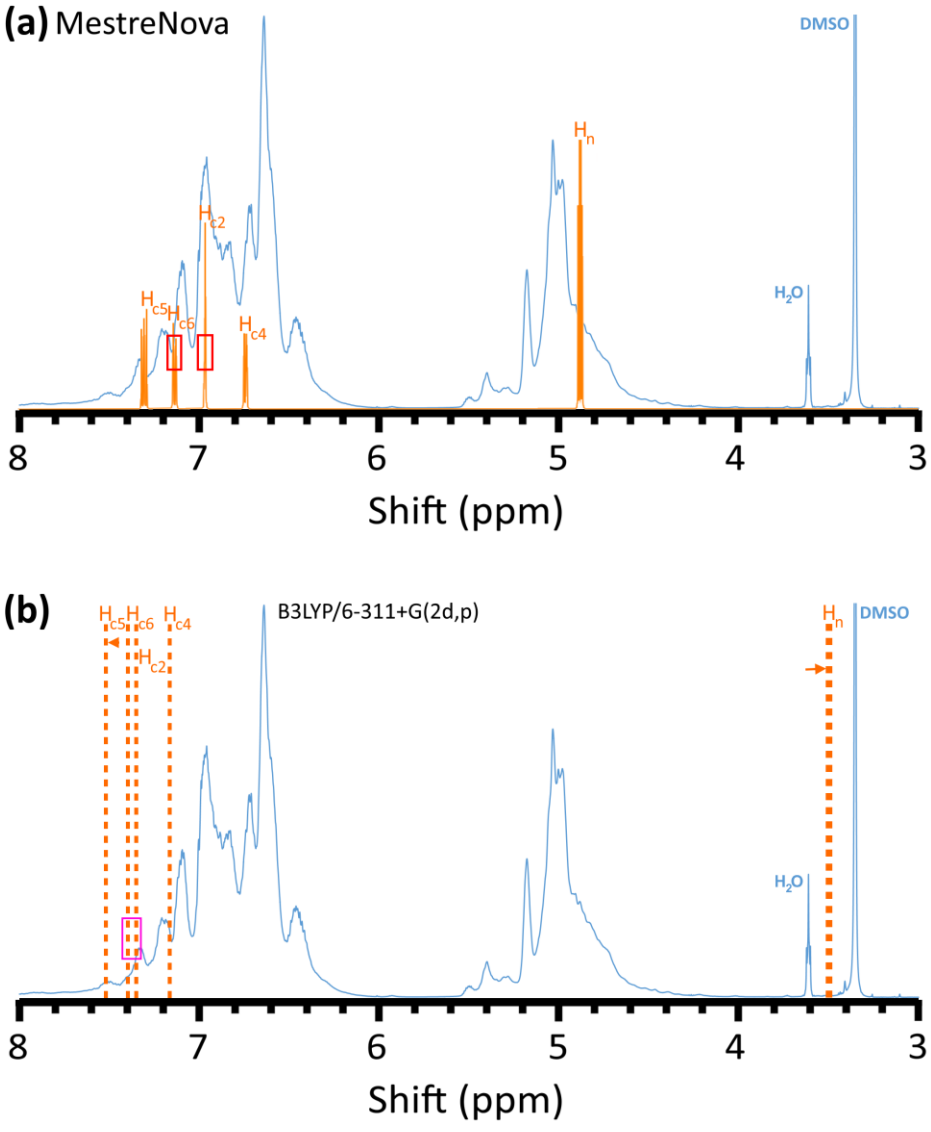

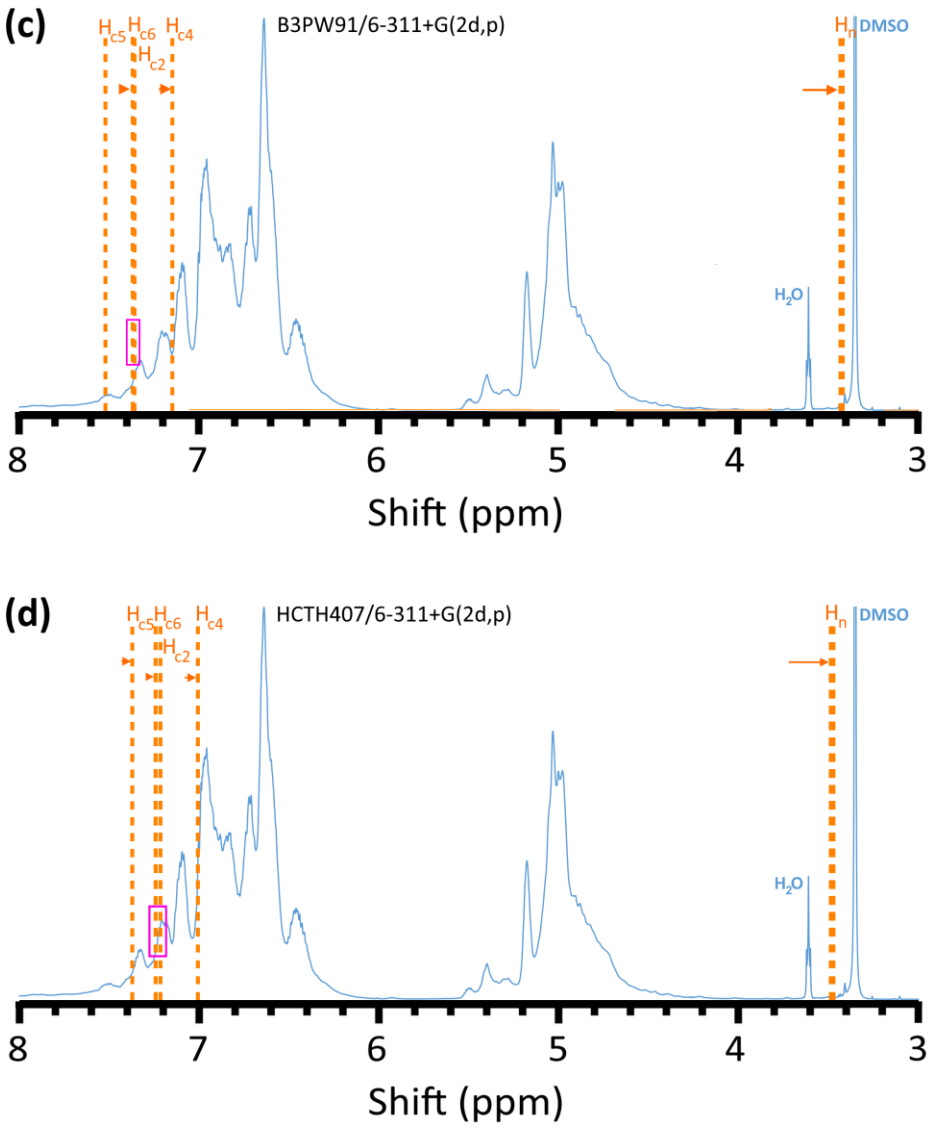

Figure 53. A comparison of the commercial OAPS ^{1}H-NMR experimental spectrum (blue line) with the chemical shifts predicted for the aromatic and amine hydrogens of the 8-ring *meta*-OAPS by Gaussian (dashed lines) and MestreNova (lines). The arrows ← indicate the differences in predicted shifts for the 8-ring *meta*-OAPS with respect to the 1-ring *meta*-OAPS by Gaussian.

As for the 1-ring *meta*-OAPS (Table 13), the methods were compared by calculating the distance between the lowest shift of the aromatic H and the sharpest experimental peak at 6.64 ppm. They are reported in Table 15 for the 8-ring *meta*-OAPS. If MestreNova still gives the best prediction, the HCTH407 method at the 6-311+G(2d,p) level of theory is now the most appropriate Gaussian approach. This is interesting as this method was selected as the optimal one for ^{13}C-NMR.

Table 15. The differences between the main experimental and the closest predicted ^{1}H-NMR peaks for the aromatic hydrogens of the 8-ring *meta*-OAPS.

Method	MestRenova	B3LYP 6-311+G(2d,p)	B3PW91 6-311+G(2d,p)	HCTH407 6-311+G(2d,p)
Difference / ppm	0.01	0.51	0.50	0.17

MestreNova clearly produces more compatible ^{1}H-NMR chemical shifts for *meta*-OAPS than the time-consuming Gaussian DFT calculations but its major downside is that it performs very poorly for both ^{13}C-NMR and ^{29}Si-NMR spectra. As it would be better to be able to predict all types of spectra with similar approaches, it was decided to further prospect the ^{1}H-NMR OAPS spectra using both MestreNova and the best DFT approach, *i.e.* HCTH407/6-311+G(2d,p). As such, both methods were tested in parallel to predict the *ortho* and *para* ^{1}H-NMR spectra in addition to that of the *meta* isomer.

b.2.7) Reproducibility: ^{29}Si-NMR, ^{13}C-NMR, and ^{1}H-NMR for meta-OAPS

Before studying both other isomers, Figure 54 assesses the reproducibility of the optimized methods for the prediction of the *meta*-OAPS ^{29}Si-NMR, ^{13}C-NMR, and ^{1}H-NMR spectra. For this purpose, three more structures of the 8-ring *meta*-OAPS were prepared from scratch as before, *i.e.* first by Hyperchem[203] and then optimized by Gaussian at the B3LYP/6-31G(d,p) level. Three new 8-ring *meta*-OAPS structures were also drawn and optimized by MestRenova. The NMR-predicted shifts were obtained using:

* both B3PW91/6-311+G(2d,p) and HF/6-311++G(2df,2pd) for ^{29}Si-NMR

* HCTH407/6-311+G(2d,p) for ^{13}C-NMR,

* both MestreNova and HCTH407/6-311+G(2d,p) for ^{1}H-NMR

in order to test the reproducibility of the predictions initially carried out on a single 8-ring *meta*-OAPS structure (Figures 51-53).

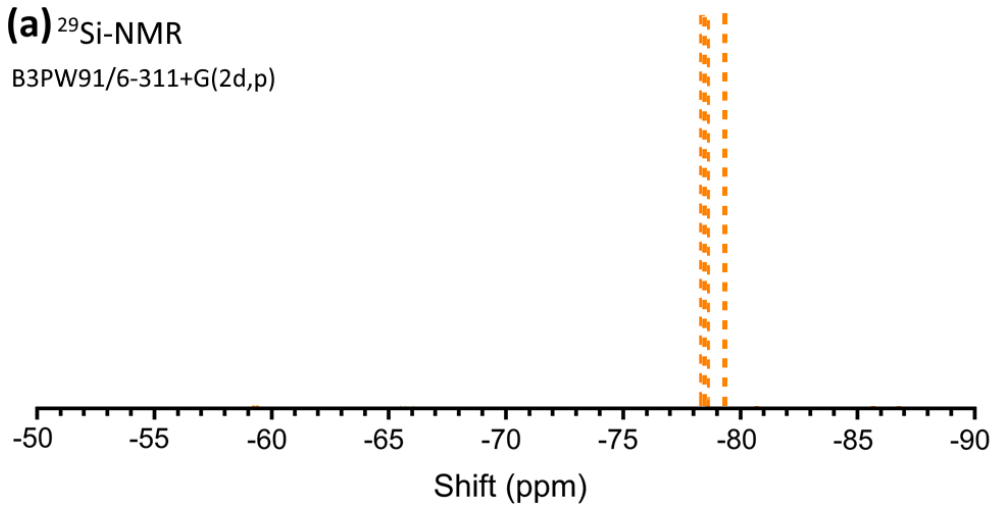
(a) 29Si-NMR
B3PW91/6-311+G(2d,p)
-50
-55
-60
-65
-70
-75
-80
-85
-90
Shift (ppm)

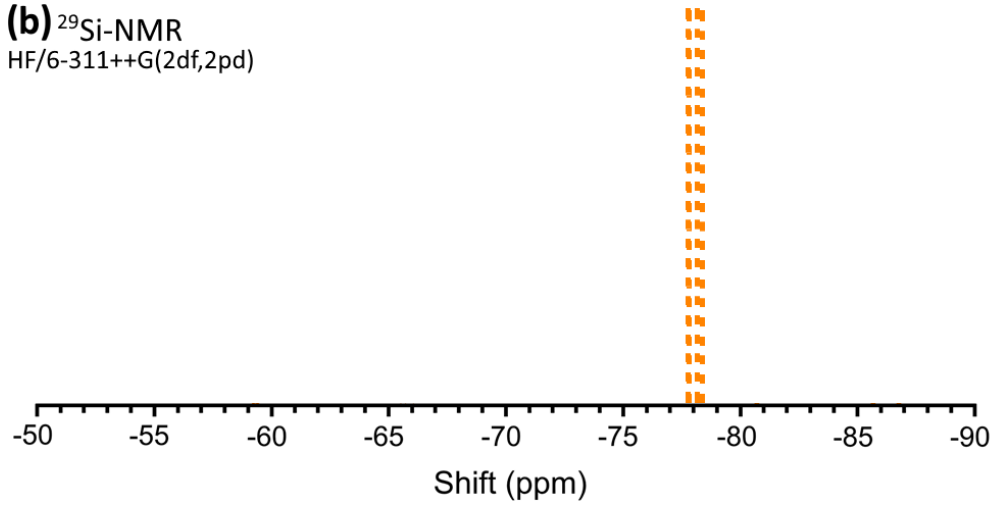
(b) 29Si-NMR
HF/6-311++G(2df,2pd)
-50
-55
-60
-65
-70
-75
-80
-85
-90
Shift (ppm)

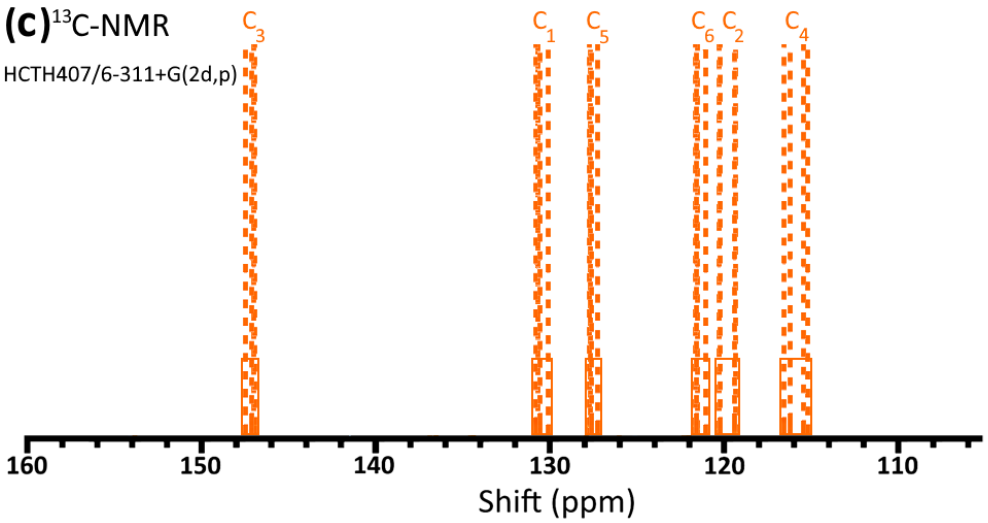
(c) 13C-NMR
HCTH407/6-311+G(2d,p)
C3
C1
C5
C6
C2
C4
160
150
140
130
120
110
Shift (ppm)

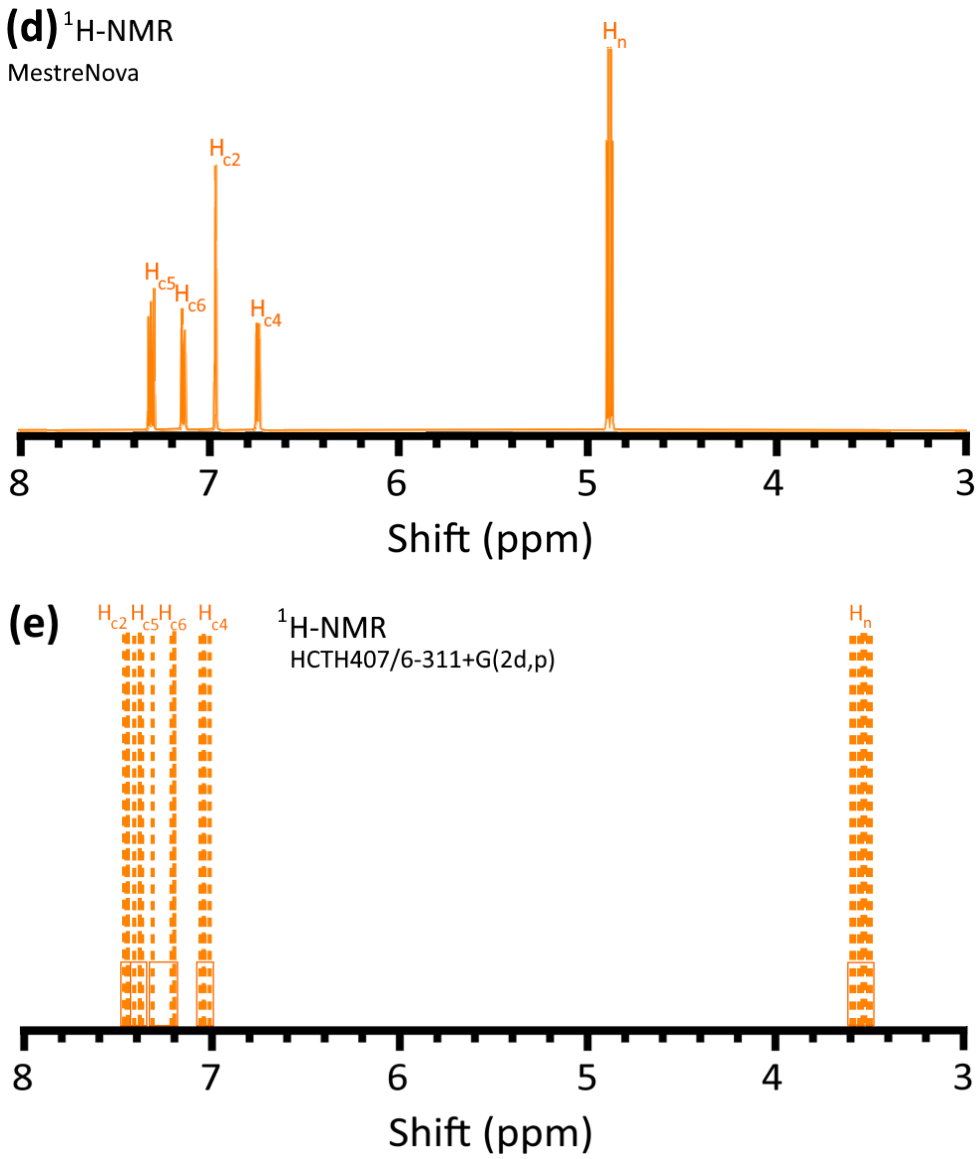

Figure 54. Reproducibility of the predicted spectra for (a-b) ^{29}Si-NMR (c) ^{13}C-NMR and (d-e) ^{1}H-NMR using the optimized methods described above for four different 8-ring *meta*-OAPS structures

For the ^{29}Si-NMR shifts, four different structures predict results within a difference of less than 1 ppm at the same level of theory. For the ^{13}C-NMR shifts, the differences are less than 2 ppm as indicated by the width of the orange rectangles. For the ^{1}H-NMR shifts, no differences are observed between the four different structures with MestreNova. It should be mentioned that this code calculates the spin-spin coupling along with the shifts, thus splitting each peak into a few smaller peaks. For example, the peak at 7.3 ppm for H_{c5} is split into three smaller peaks because of its adjacents H_{c4} and H_{c6} on the aromatic ring. For the ^{1}H-NMR shifts calculated with Gaussian, the differences are less than 0.2 ppm as indicated by the width of the orange rectangles. The reproducibility is thus rather good for all cases tested.

b.3) The *ortho* and *para* isomers

Figures 55(a) and 55(b) show the different chemical environments for the carbons and hydrogens of the *ortho* and *para* isomers of OAPS, respectively. Due to the symmetry in the *para* isomer, there are only four carbon types and three hydrogen types with different chemical environments. On the other hand, as for the *meta* isomer, each carbon and each hydrogen in the *ortho* isomer presents a different chemical environment.

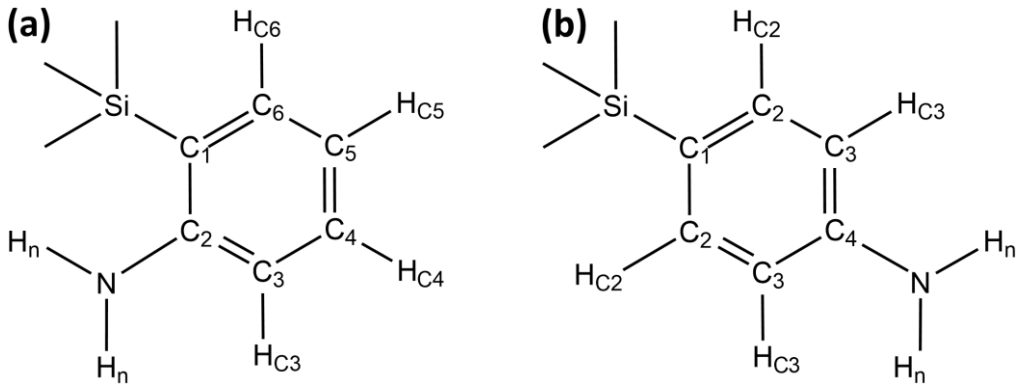

Figure 55. The molecular structures of a) the *ortho* and b) the *para* isomers connected to OAPS.

Figures 56 and 57 display the spectra predicted by the optimized methods for the ^{29}Si-NMR, ^{13}C-NMR, and ^{1}H-NMR shifts of the 8-ring *ortho*-OAPS and *para*-OAPS isomers, respectively. As for Figure 54, they were calculated on four different structures each in order to directly assess their reproducibility. The predicted shifts associated with specific aromatic carbons and hydrogens are indicated in the ^{13}C-NMR and ^{1}H-NMR analyses.

The reproducibility of the predictions for the *ortho* isomer (Figure 56) is very good. The predicted ^{29}Si-NMR shifts by (a) B3PW91/6-311+G(2d,p) are within less than 0.5 ppm for the four different structures whereas those predicted by (b) the HF methods are within less than 1 ppm. The ^{13}C-NMR predictions all fall within less than 1 ppm (c). The ^{1}H-NMR shifts predicted by MestreNova are identical for the four structures (d), while those predicted by HCTH407/6-311+G(2d,p) (e) also show a very good reproducibility within a range smaller than 0.1 ppm for each specific hydrogen.

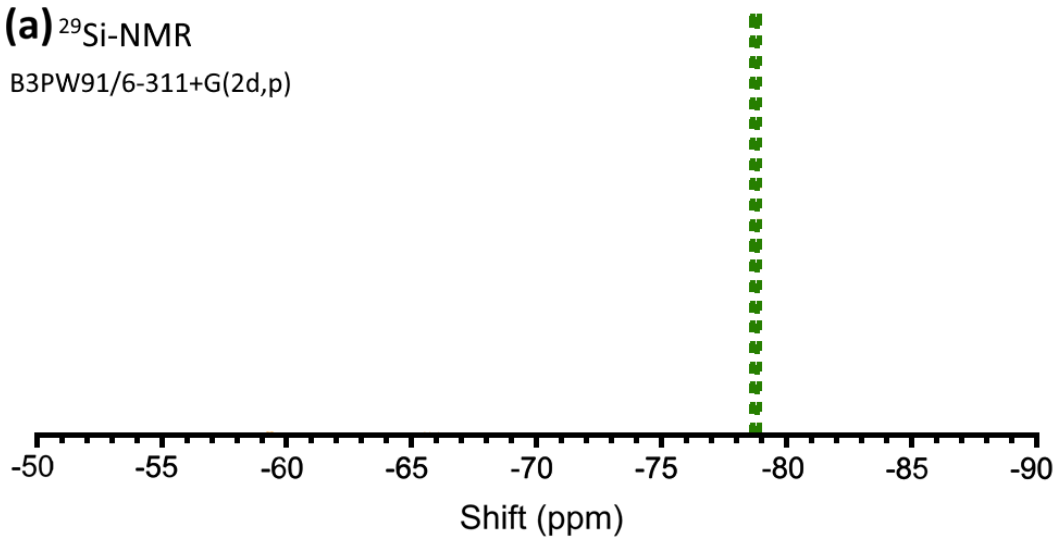
(a) 29Si-NMR
B3PW91/6-311+G(2d,p)
-50
-55
-60
-65
-70
-75
-80
-85
-90
Shift (ppm)

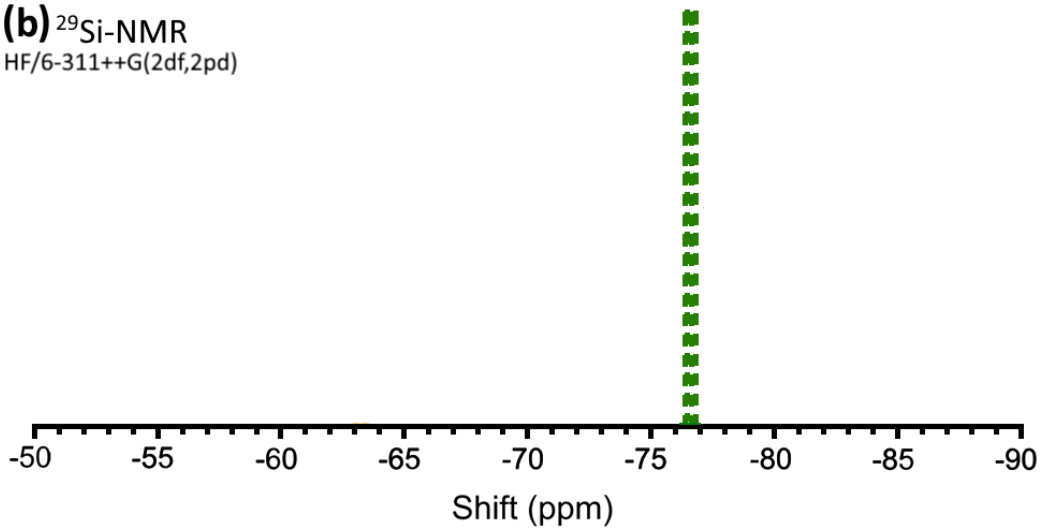
(b) 29Si-NMR
HF/6-311++G(2df,2pd)
-50
-55
-60
-65
-70
-75
-80
-85
-90
Shift (ppm)

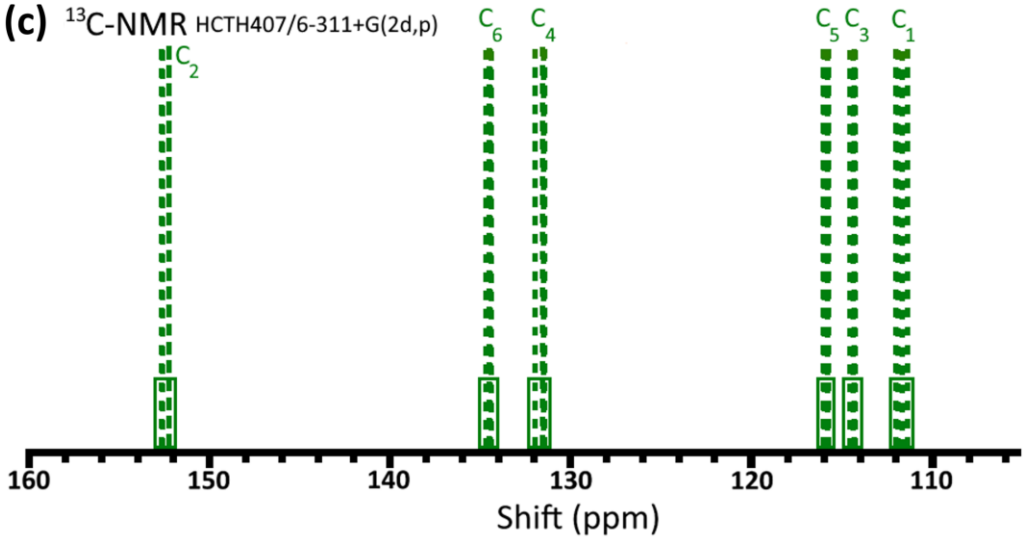
(c) 13C-NMR HCTH407/6-311+G(2d,p)
C2
C6
C4
C5
C3
C1
160
150
140
130
120
110
Shift (ppm)

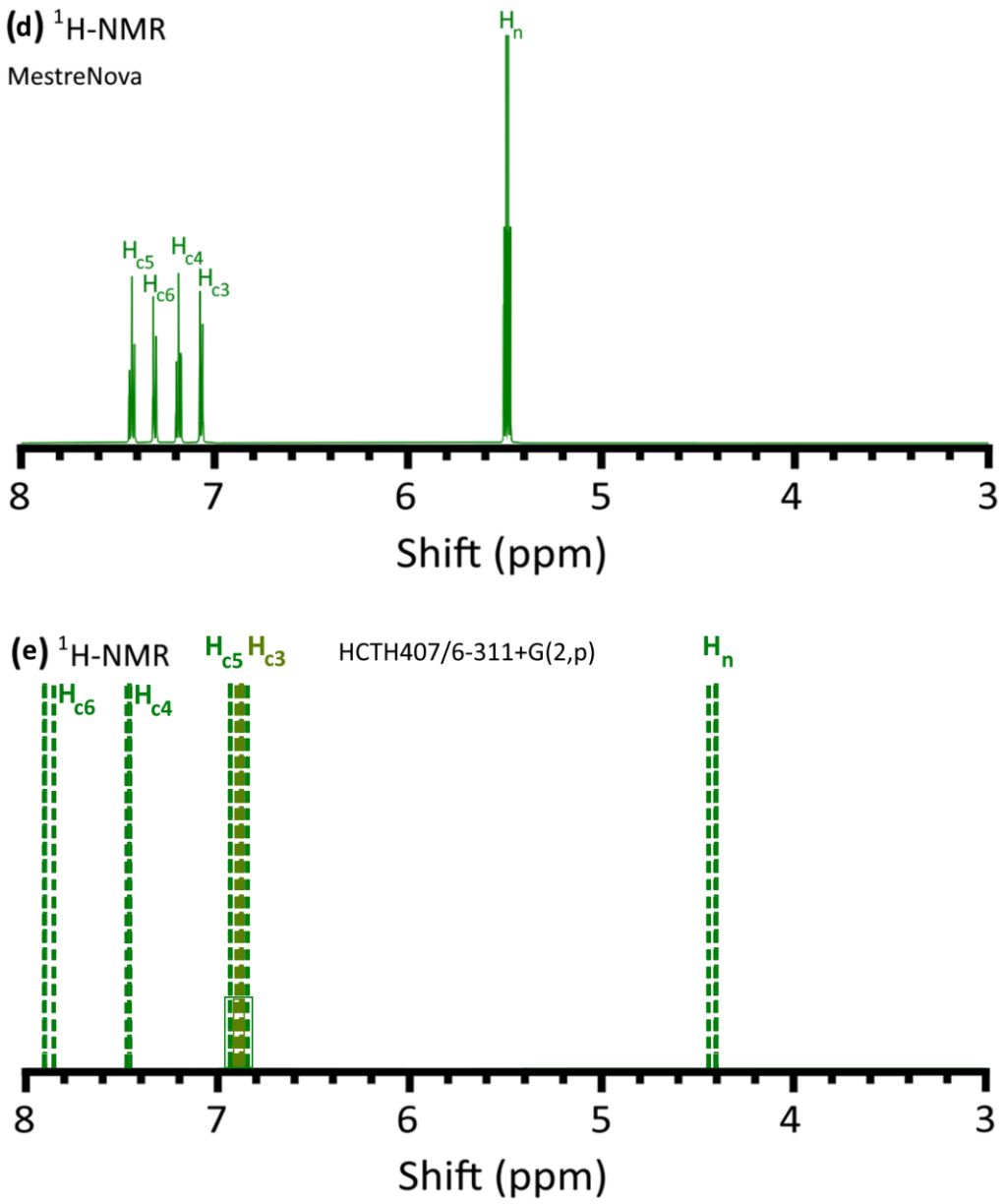

Figure 56. Reproducibility of the predicted spectra for (a-b) ^{29}Si-NMR (c) ^{13}C-NMR and (d-e) ^{1}H-NMR using the optimized methods for four different 8-ring *ortho*-OAPS structures

For the *para* isomer (Figure 57), the predicted ^{29}Si-NMR shifts at (a) B3PW91/6-311+G(2d,p) cover a wider range for the four different structures than for the *ortho* isomer, but they still fall within only 2 ppm. On the other hand, HF/6-311++G(2df,2pd) predicts more centralized data (b). The range for the predicted specific ^{13}C-NMR shifts (c) is less than 1 ppm and as expected, there are only four different carbon types in the *para* isomer. Similarly, MestreNova (d) predicts three ^{1}H-NMR shifts and the HCTH407/6-311+G(2d,p) level of theory (e) displays a range of less than 0.2 ppm for the amine shifts and less than 0.1 ppm for the aromatic shifts (e). The surface areas of the three peaks in MestreNova (d) are equal

because there are two hydrogens in each chemical environment (one set of two amine hydrogens and two sets of two aromatic hydrogens). Gaussian only provides the shifts and no data about the intensities can be directly extracted from its results.

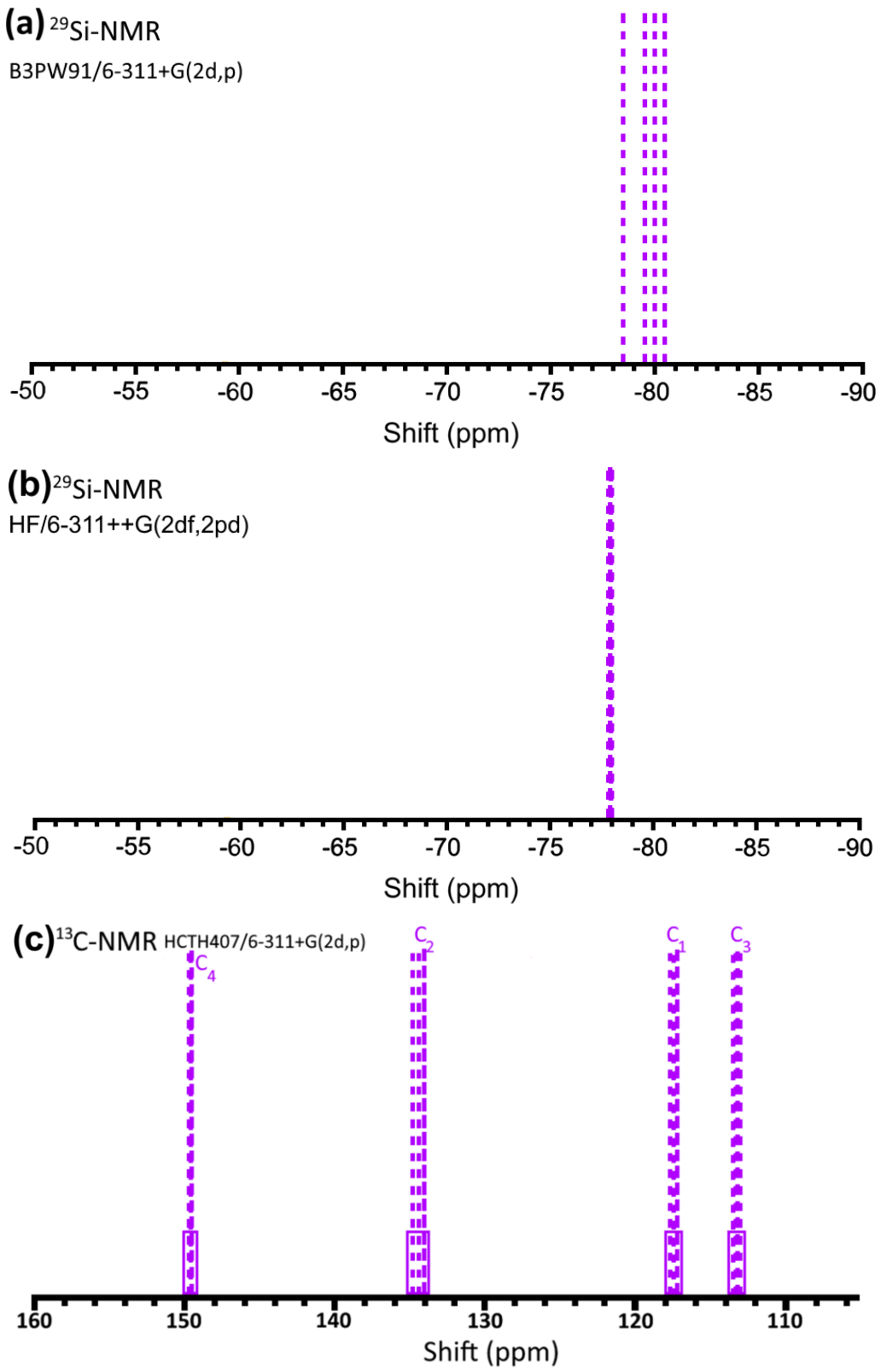

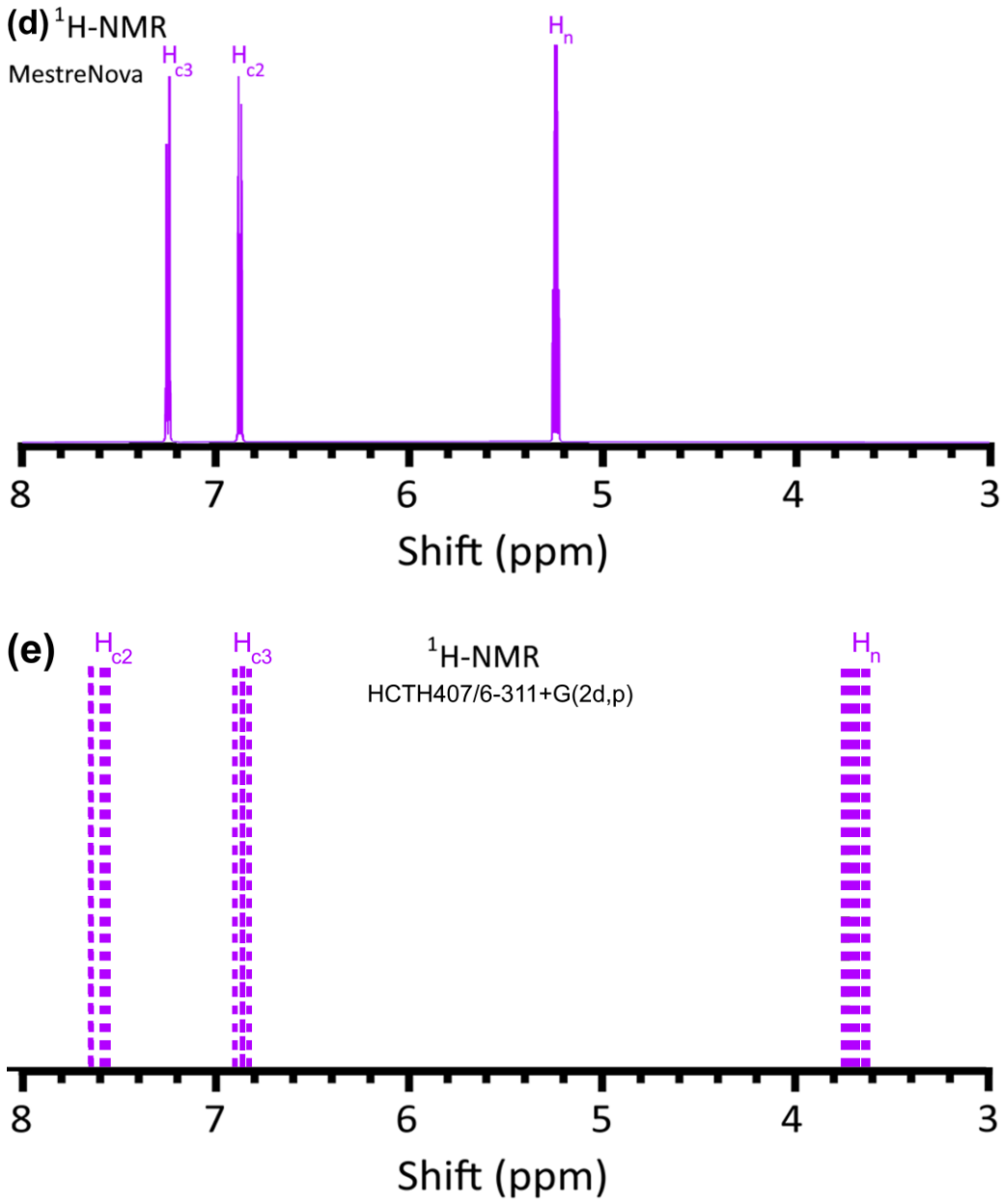

Figure 57. Reproducibility of the predicted spectra for (a-b) ^{29}Si-NMR (c) ^{13}C-NMR and (d-e) ^{1}H-NMR using the optimized methods for four different 8-ring *para*-OAPS structures

b.4) Comparison of the three isomers

To compare all three isomers with the experimental spectra and account for the slight differences in geometries, the predicted shifts were averaged on the four different structures studied previously for each isomer.

b.4.1) The ^{29}Si-NMR predicted spectra for meta-OAPS, ortho-OAPS, and para-OAPS

Following the *meta*-OAPS tests (Section b.2.), the ^{29}Si-NMR spectra were predicted for all three isomers using both DFT at the B3PW91/6-311+G(2d,p) level of theory and the heavier HF/6-311++G(2df,2pd) approach. The average predicted spectra for *meta*-OAPS (orange), *para*-OAPS (purple) and *ortho*-OAPS (green) are compared in Figure 58 to the experimental (a) commercial, (b) controlled and (c) pure *meta*-OAPS and *para*-OAPS of Lee et al.[107] The *x*-axis scale was zoomed to the -75 to -82 ppm range to better distinguish the differences.

For the B3PW91/6-311+G(2d,p) method, the average predicted shits of the *ortho* and *meta* isomer differ by less than 0.2 ppm, which suggests an overlap. This could explain why there are similar experimental peaks in (a) and (b), whereas there should be no *ortho* isomer in the latter. However, the predicted shift of the *para* isomer is on the right side of both other isomers, unlike the order of the intensities in the commercial OAPS (which should have less *para* and more *meta* isomer), the controlled OAPS (which should have more *para* and less *meta* isomer), as well the pure samples of Lee et al. Although, there is a much better agreement for B3PW91/6-311+G(2d,p) than for the other DFT predictions tested (Figures 48 and 51), it does not seem to be able to properly reproduce the isomer differences.

Using a different method can produce different results.[204] Indeed, HF/6-311++G(2df,2pd) shows not only slightly different shifts but also a different order for the shifts. The *para* peak is now on the left side of the *meta*, which is more consistent with both experimental spectra. The *ortho* peak is displaced towards higher values and it is difficult to assign it to a specific part of the commercial *ortho*-containing spectra. However, there is not any clear *ortho* signature in any of the experimental spectra (Figure 42), and as such, HF/6-311++G(2df,2pd) probably provides a better prediction than B3PW91/6-311+G(2d,p).

It is difficult to get fully satisfactory results from the ^{29}Si-NMR prediction methods tested here, which could be due to the fact that the peaks all fall within a very restricted ppm range. It is also difficult to explain why the main experimental peak of Lee et al. for the pure *para* isomer (c) does not clearly appear neither in the commercial (a) nor in the controlled (b) samples, especially considering that the latter should have a significant amount of *para* isomer. So there are still issues in both the predicted and experimental shifts.

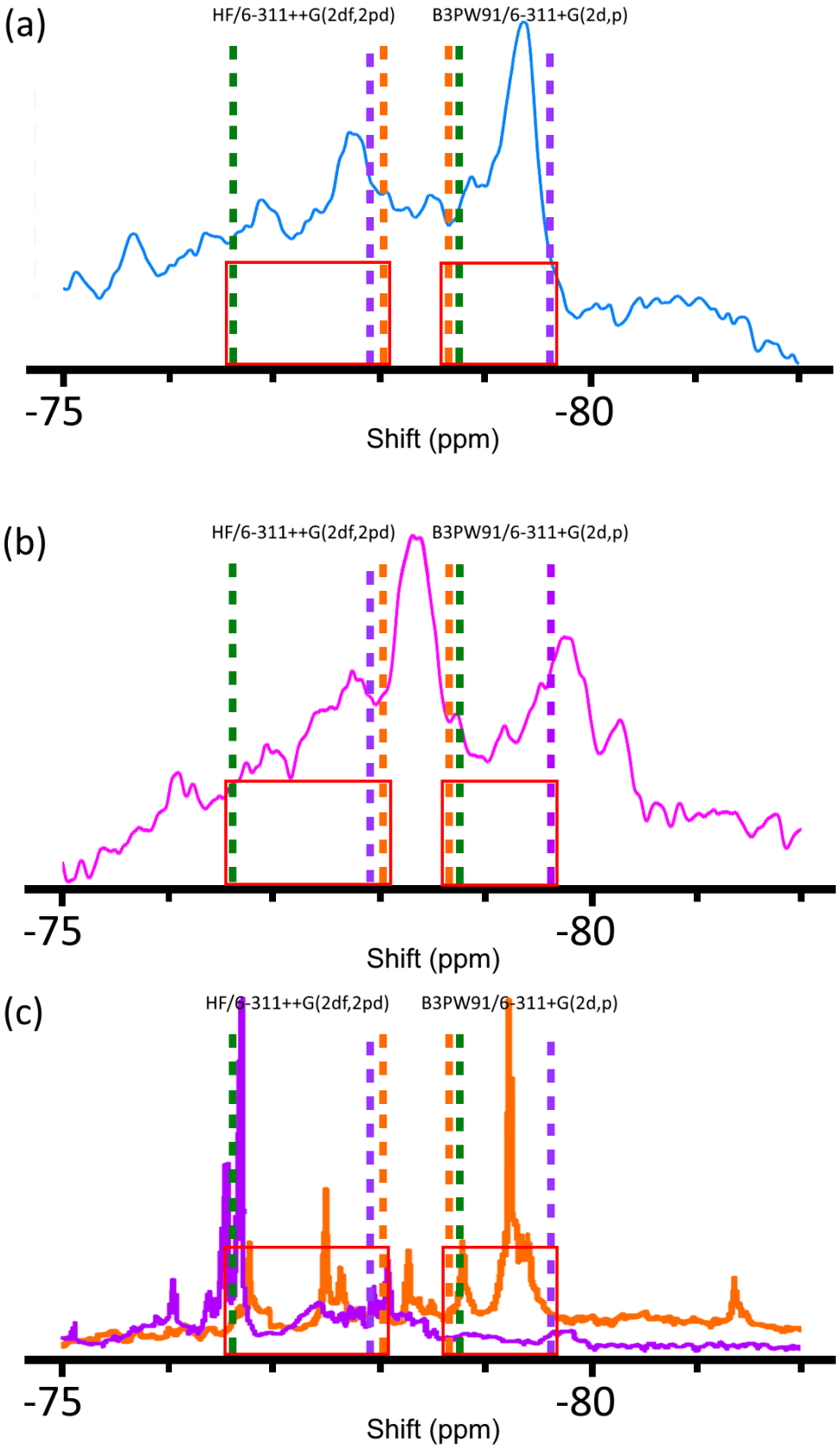

Figure 58. The experimental ^{29}Si-NMR spectra of (a) the commercial OAPS (blue line) (b) the controlled OAPS (pink line) and (c) the pure *meta* (orange line) and *para* (purple line) isomers of Lee et al.[107] compared to the predicted shifts by Gaussian (dashed lines) with B3PW91/6-311+G(2d,p) and HF/6-311++G(2df,2pd) for the there OAPS isomers.

b.4.2) The ^{13}C-NMR predicted spectra for meta-OAPS, ortho-OAPS, and para-OAPS

The average ^{13}C-NMR spectra were predicted for all three isomers using DFT at the HCTH407/6-311+G(2d,p) level of theory. They are compared in Figure 59 to those of the experimental (a) commercial and (b) controlled samples. As before, the predicted peaks are identified by their colours with orange representing the *meta* isomer, green representing the *ortho* isomer and purple representing the *para* isomer.

In Figure 59(a), the predicted *ortho* green shift at 111.5 ppm (P) matches a weak experimental peak for the commercial OAPS sample. A similar match can be observed for two *para* purple shifts at 117.5 ppm (K) and 149.5 ppm (B). The *meta* orange shift at 130.5 ppm (G) and the *ortho* green shift at 131.5 ppm (F) are close to two medium-intensity experimental peaks. Both *meta* orange shifts at 120.5 ppm (J) and 121 ppm (I) are adjacent to stronger experimental peaks. The overlap at 134.5 ppm (*ortho* green in D and *para* purple in E) is close to the experimental peak at 136 ppm. The *meta* orange shift at 127.8 ppm (H) is within less than 1 ppm from the sharpest experimental peak at 129 ppm. This good compatibility between the various peaks indicates that the HCTH407/6-311+G(2d,p) level of theory seems to produce rather accurate ^{13}C-NMR predictions for the commercial OAPS. In addition, the same number of experimental and predicted shifts confirms that all three isomers are present in this sample.

Figure 59(b) shows that each predicted *meta* or *para* shift is also very close to an adjacent experimental peak in the controlled OAPS sample. The predicted B and C shifts are next to weak experimental signals at 151 ppm and 148 ppm, respectively. The same compatibility can be observed for the G, H, I, J, K and L predicted shifts with adjacent experimental signals. Two *para* shifts, E and O, are compatible with the main experimental peaks at 135 ppm and 113 ppm respectively. As expected, there are only ten peaks in the experimental spectrum. This confirms the absence of the *ortho* isomer in the controlled sample, whereas there are sixteen peaks in (a) for the commercial OAPS.

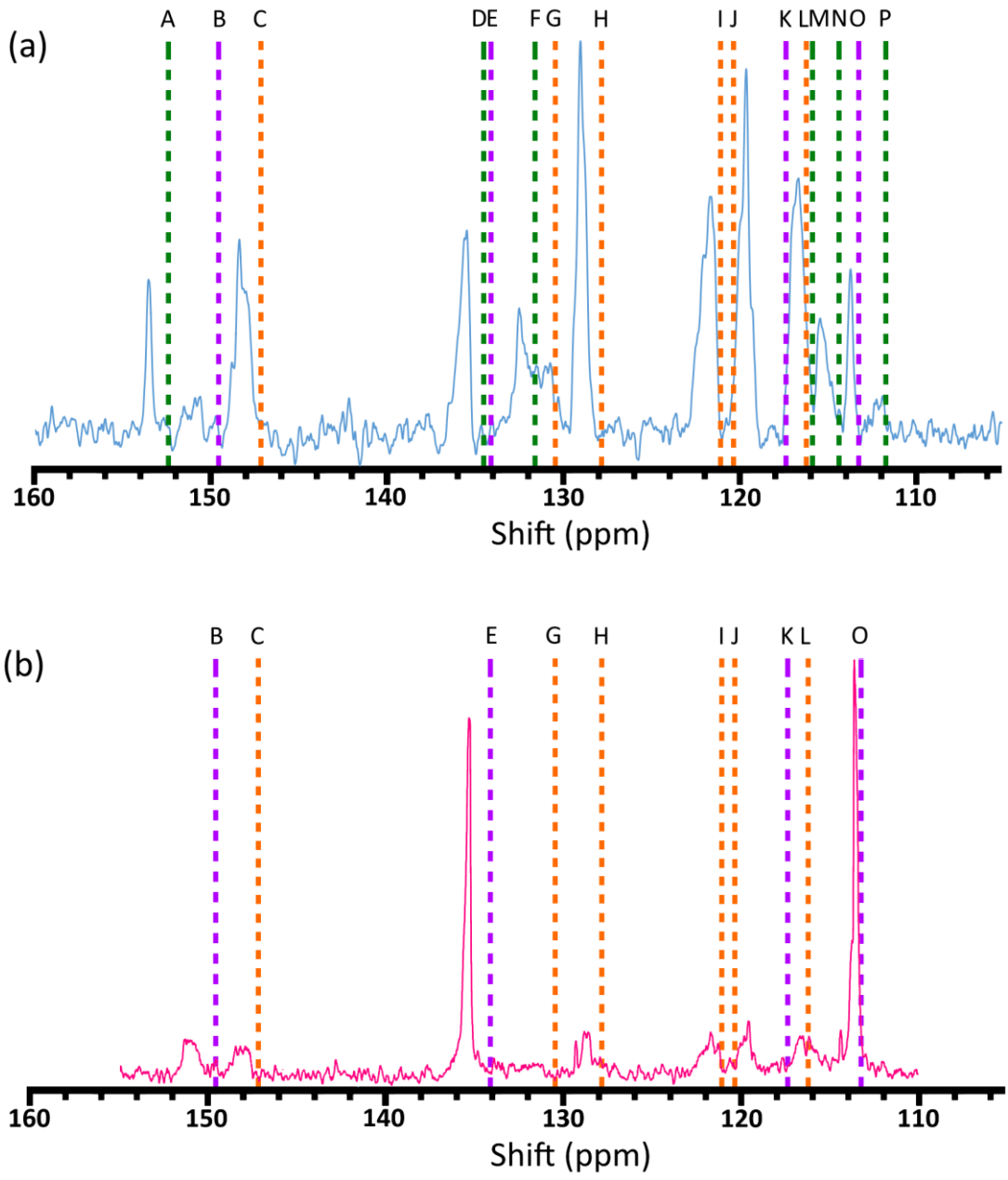

Figure 59. The experimental ^{13}C-NMR spectra of (a) the commercial OAPS (blue line) and (b) the controlled OAPS (pink line) compared with the predicted shifts by Gaussian (dashed lines) at the HCTH407/6-311+G(2d,p) level of theory for the three OAPS isomers.

Tables 16 and 17 give the precise chemical shift values for each peak attributed to each specific carbon of each isomer (Figures 47 and 55) in the commercial and controlled OAPS samples, respectively. They also report in each case the absolute errors e_i between the experimental and predicted shifts. The mean absolute error (MAE) and root mean rectangle error (RMSE) can be calculated from:[205]

$$\text{MAE} = \frac{1}{n}\sum_{i=1}^{n}|e_i| \tag{8}$$

$$\text{RMSE} = \sqrt{\frac{1}{n}\sum_{i=1}^{n}e_i^2} \tag{9}$$

where n is the number of shifts.

For the commercial sample (Table 16), the MAE and RMSE are 0.80 ppm and 0.90 ppm, respectively. For the controlled sample (Table 17), the MAE and RMSE are 0.80 ppm and 0.95 ppm. These RMSE values are much smaller than the values of 1.89 ppm reported by Abil et al.[183] and 4.46 ppm reported by Zhang et al.[206] for a large variety of small molecules without any silicon atoms. Such small errors indicate that HCTH407/6-311+G(2d,p) is indeed pretty accurate in predicting the experimental ^{13}C-NMR chemical shifts for OAPS. In addition, the number of peaks confirms the presence (Table 16) and absence (Table 17) of the *ortho* isomer in the respective experimental samples.

Table 16. Comparison between the predicted δ_{calc} and experimental δ_{exp} ^{13}C NMR shifts in ppm along with their absolute error e_i in ppm for each peak identified in the commercial OAPS sample (Figure 59(a)).

C-Type	δ_{calc}	δ_{exp}	$\lvert e_i \rvert$	Identification	Isomer type
C_1	130.45	130.70	0.25	G	meta
C_2	120.36	119.55	0.81	J	meta
C_3	147.13	148.34	1.21	C	meta
C_4	116.30	116.64	0.34	L	meta
C_5	127.82	128.97	1.15	H	meta
C_6	121.11	121.60	0.49	I	meta
C_1	111.75	111.78	0.03	P	ortho
C_2	152.41	153.53	1.12	A	ortho
C_3	114.40	115.28	0.88	N	ortho
C_4	131.59	132.45	0.86	F	ortho
C_5	115.90	115.28	0.62	M	ortho
C_6	134.53	135.54	1.01	D	ortho
C_1	117.42	116.64	0.78	K	para
C_2	134.09	135.54	1.45	E	para
C_3	113.28	113.60	0.32	O	para
C_4	149.57	151.00	1.43	B	para

Table 17. Same as Table 16 but for in the controlled OAPS sample (Figure 59(b)).

C-Type	δ_{calc}	δ_{exp}	$\|e_i\|$	Identification	Isomer type
C_1	130.45	129.28	1.17	G	meta
C_2	120.36	119.74	0.62	J	meta
C_3	147.13	147.71	0.58	C	meta
C_4	116.30	116.13	0.17	L	meta
C_5	127.82	128.20	0.38	H	meta
C_6	121.11	121.51	0.40	I	meta
C_1	117.42	116.13	1.29	K	para
C_2	134.09	135.35	1.26	E	para
C_3	113.28	113.59	0.31	O	para
C_4	149.57	151.36	1.79	B	para

The calculated shielding tensors and experimental chemical shifts can be related by using a linear relationship described with a linear equation $\delta_{calc\text{-}scaled} = a\delta_{calc} + b$ which cancels systemic errors (a and b are slope and intercept, $\delta_{calc\text{-}scaled}$ is the scaling calculated chemical shifts close to the experimental chemical shifts, and δ_{calc} is calculated shielding tensors).[183, 198, 207] Figure 60 shows the linear correlation[183] between the δ_{calc} and δ_{exp} ^{13}C-NMR shifts for the commercial OAPS (Table 16), which can be fitted by:

$$\delta_{calc\text{-}scaled} = 1.04\ \delta_{calc} - 4.36 \qquad (10)$$

The slope is close to 1 and the correlation is very good (R = 0.9992).

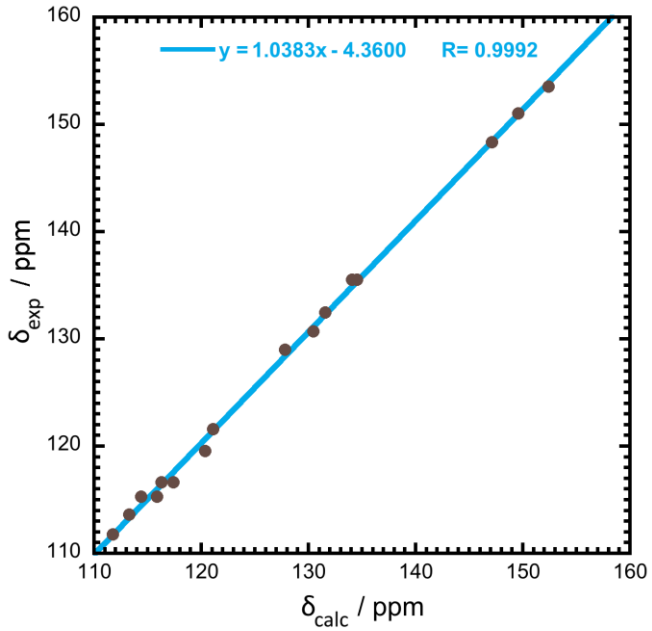

Figure 60. Linear correlation between the δ_{calc} and δ_{exp} for the ^{13}C-NMR shifts in the commercial OAPS

Equation 10 can be used to scale the δ_{calc} originating from Gaussian in order for them to be even closer to the experimental δ_{exp}. These scaled predicted shifts $\delta_{calc\text{-}scaled}$ are reported in Table 18 for the commercial OAPS. They decrease the MAE and RMSE to 0.44 ppm and 0.54 ppm, respectively. Such a correlation can thus further improve the chemical shifts predicted at the HCTH407/6-311+G(2d,p) level of theory for OAPS.

Table 18. Comparison between the predicted scaled $\delta_{calc\text{-}scaled}$ and experimental δ_{exp} ^{13}C NMR shifts in ppm along with their absolute error e_i in ppm for each peak identified in the commercial OAPS sample (Figure 59(a)).

C Type	$\delta_{calc\text{-}scaled}$	δ_{exp}	$\lvert e_i \rvert$	Identification	Isomer type
C_1	131.09	130.70	0.39	G	meta
C_2	120.61	119.55	1.06	J	meta
C_3	148.41	148.34	0.07	C	meta
C_4	116.39	116.64	0.25	L	meta
C_5	128.36	128.97	0.61	H	meta
C_6	121.39	121.60	0.21	I	meta
C_1	111.67	111.78	0.11	P	ortho
C_2	153.89	153.53	0.36	A	ortho
C_3	114.42	115.28	0.86	N	ortho
C_4	132.27	132.45	0.18	F	ortho
C_5	115.98	115.28	0.70	M	ortho
C_6	135.32	135.54	0.22	D	ortho
C_1	117.56	116.64	0.92	K	para
C_2	134.87	135.54	0.67	E	para
C_3	113.26	113.60	0.34	O	para
C_4	150.94	151.00	0.06	B	para

Figure 61 shows likewise the very good linear correlation (R = 0.9983) between the δ_{exp} and δ_{calc} ^{13}C-NMR shifts for the controlled OAPS (Table 17), which can be fitted by:

$$\delta_{calc\text{-}scaled} = 1.05\ \delta_{calc} - 5.85 \qquad (11)$$

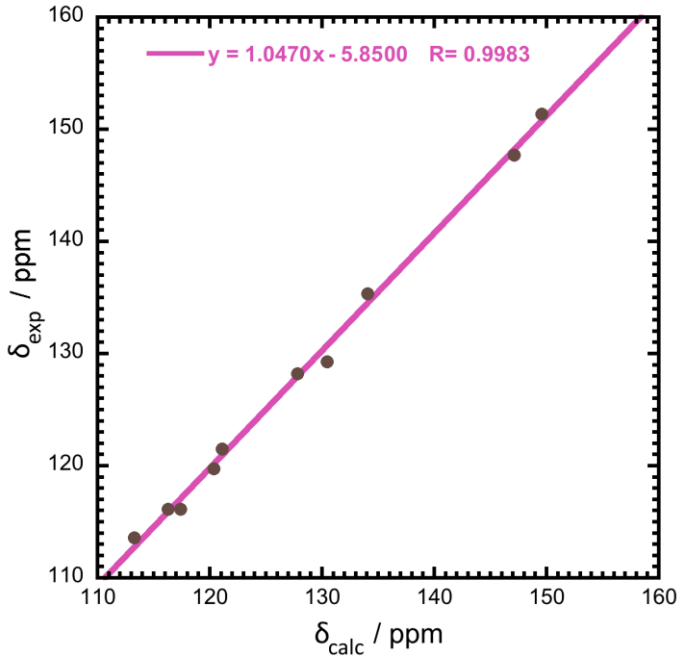

Figure 61. Linear correlation between the δ_{calc} and δ_{exp} for the ^{13}C-NMR shifts in the controlled OAPS

As for Figure 60, the slope of the linear correlation in Figure 61 is close to 1, which confirms the accuracy of the predicted ^{13}C-NMR shifts for both types of OAPS. The $\delta_{calc\text{-}scaled}$ obtained from applying Equation 11 are reported in Table 19 for the controlled OAPS. The MAE and RMSE decrease to 0.66 ppm and 0.75 ppm, respectively.

Table 19. Comparison between the predicted scaled $\delta_{calc\text{-}scaled}$ and experimental δ_{exp} ^{13}C NMR shifts in ppm along with their absolute error e_i in ppm for each peak identified in the controlled OAPS sample (Figure 59(b)).

C-Type	$\delta_{calc\text{-}scaled}$	δ_{exp}	$\lvert e_i \rvert$	Identification	Isomer type
C_1	130.73	129.28	1.45	G	meta
C_2	120.17	119.74	0.43	J	meta
C_3	148.19	147.71	0.48	C	meta
C_4	115.91	116.13	0.22	L	meta
C_5	127.98	128.20	0.22	H	meta
C_6	120.95	121.51	0.56	I	meta
C_1	117.09	116.13	0.96	K	para
C_2	134.54	135.35	0.81	E	para
C_3	112.76	113.59	0.83	O	para
C_4	150.75	151.36	0.61	B	para

These analyses confirm that Gaussian at the HCTH407/6-311+G(2d,p) level of theory is able to predict very accurately the ^{13}C-NMR shifts for all OAPS isomers, regardless of

whether there are three isomers (commercial sample) or only two isomers (controlled sample).

b.4.3) The ^{1}H-NMR predicted spectra for meta-OAPS, ortho-OAPS, and para-OAPS

The ^{1}H-NMR spectra were predicted for all three isomers using both MestreNova and Gaussian at the HCTH407/6-311+G(2d,p) level of theory. They are compared to those of the experimental (a) commercial and (b) controlled samples in Figure 62 for MestreNova and in Figure 63 for Gaussian. The letters used to identify the predicted peaks for the aromatic hydrogens are those of their adjacent aromatic carbons (Tables 18-19). The amine hydrogens connected to the nitrogen are referred to by the name of their isomer.

For the aromatic hydrogens of the commercial sample (left regions of Figures 62(a) and 63(a)), ten slightly overestimated shifts are predicted by both MestreNova and Gaussian, with four of them overlapping. As a result, only eight peaks are observable from 6.7 ppm to 7.9 ppm, in agreement with the eight observable experimental shifts (red rectangles). However, it is worth noting that the relative order of these peaks is somewhat different between MestreNova and Gaussian, which means that both codes do not assign the same peaks to the same isomer. For the amine hydrogens (right regions of Figures 62(a) and 63(a)), three MestreNova shifts are predicted in the range 4.9-5.5 ppm, *i.e.* close to the three experimental peaks. This is compatible with the presence of the *ortho* isomer in addition to the *meta* and *para* isomers in the commercial sample. Gaussian also predicts three separate shifts albeit in an underestimated range, i.e. 3.5-4.5 ppm. Unlike the aromatic hydrogens, both predicted sets of amine hydrogen shifts are in the same relative order.

The situation is similar for the predicted amine hydrogen shifts (right regions of Figures 62(b) and 63(b)), where the experimental peak related to the *ortho* isomer disappears. For the aromatic hydrogens (left regions of Figures 62(b) and 63(b)), the predicted shifts are again slightly displaced towards higher values and their identification differs according to the code used. There are six of them, which relate to the six observable experimental shifts for the *meta* and *para* isomers (red rectangles).

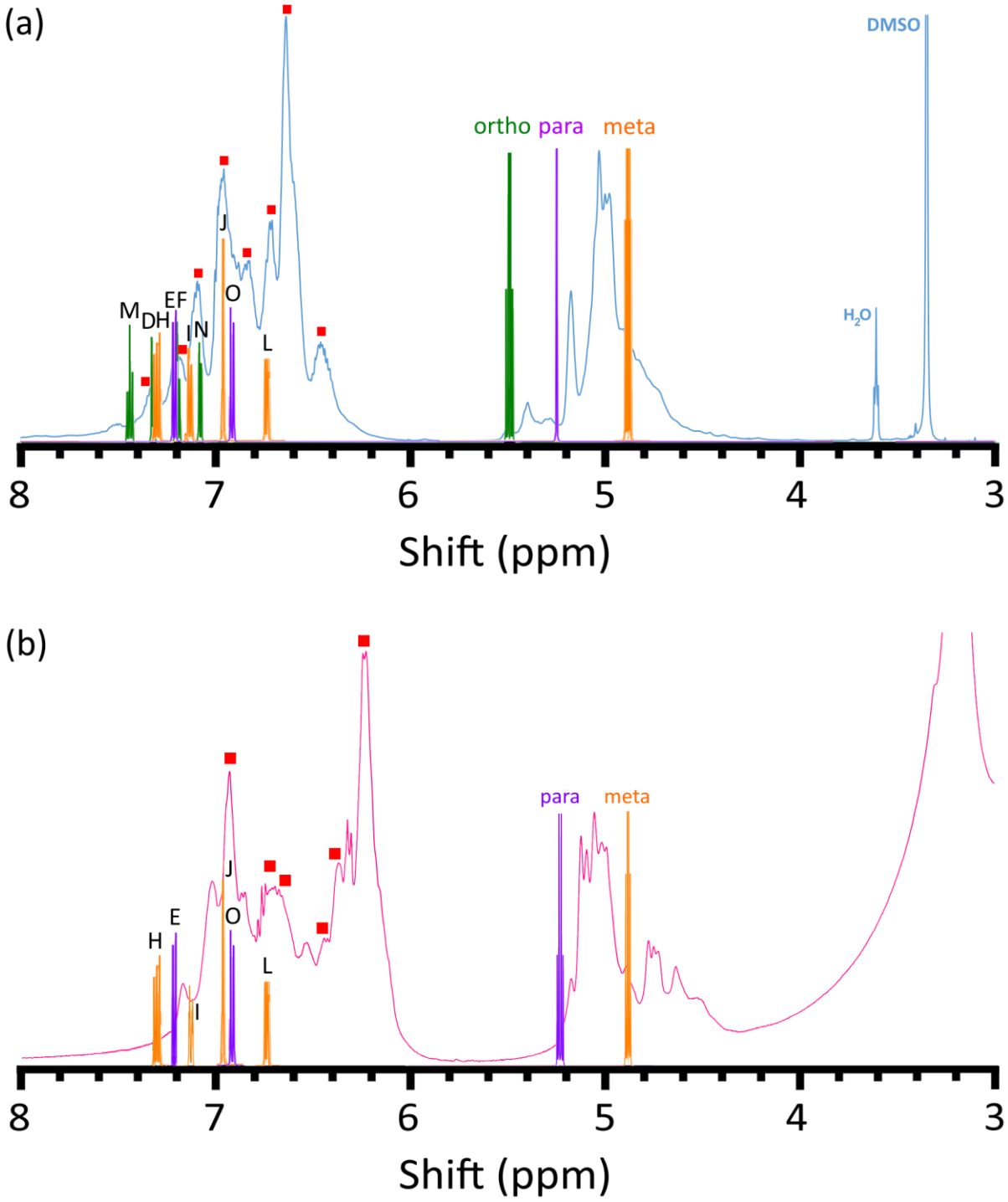

Figure 62. The experimental ^{1}H-NMR spectra of (a) the commercial OAPS (blue line) and (b) the controlled OAPS (pink line) compared with the predicted shifts by MestreNova (orange, green and purple lines) for the three isomers.

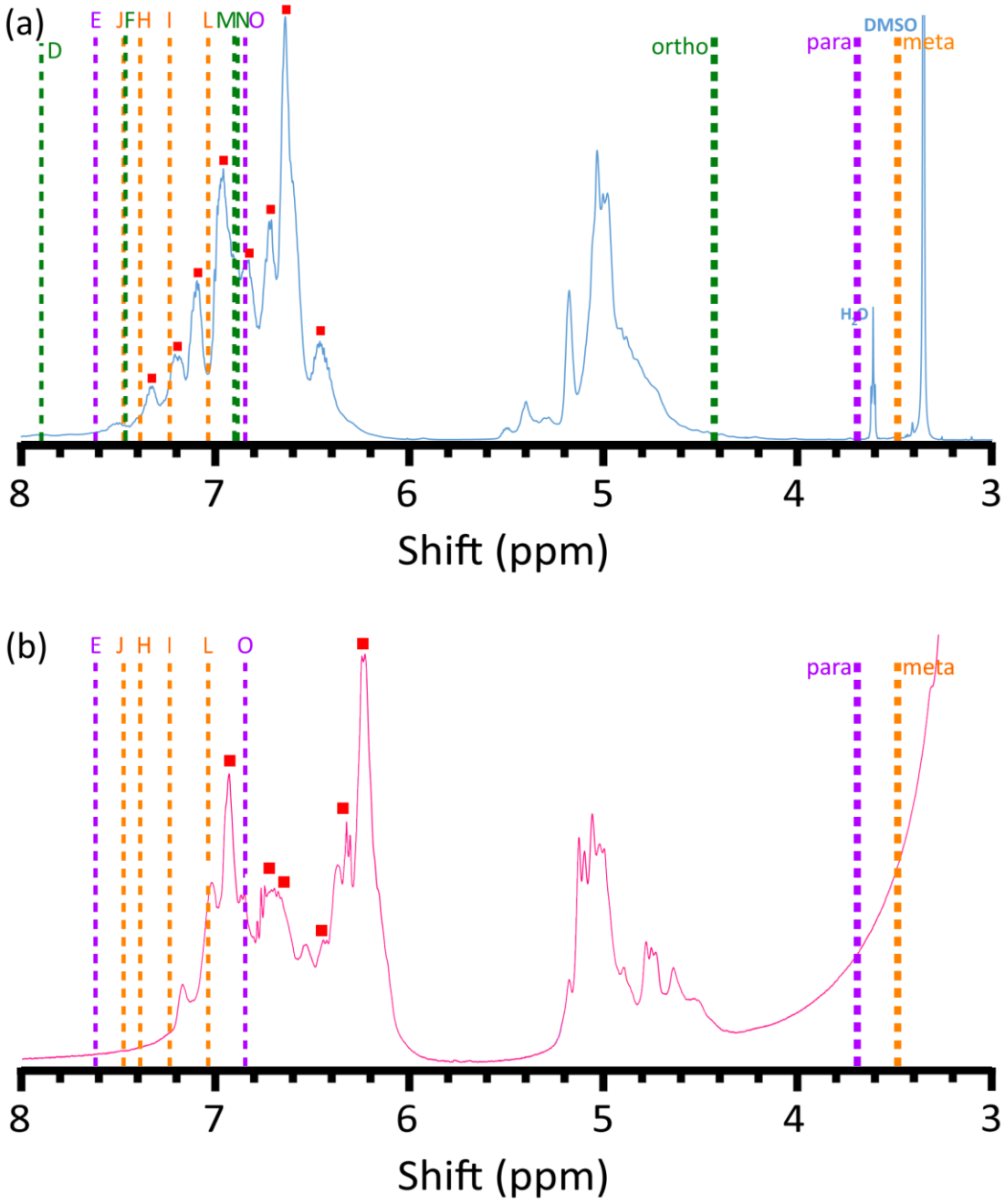

Figure 63. Same as Figure 62 but for the Gaussian-predicted shifts at the HCTH407/6-311+G(2d,p) level of theory.

Tables 20 and 21 report the absolute errors e_i between the experimental δ_{exp} and the MestreNova-predicted δ_{calc} ^{1}H-NMR shifts in both the commercial and controlled OAPS samples. The same analyses carried out with the Gaussian predictions at the HCTH407/6-311+G(2d,p) level of theory are provided in Tables 22 and 23.

The MestreNova-predicted MAE and RMSE for the ^{1}H-NMR shifts of the commercial OAPS (Table 20) are 0.16 ppm and 0.18 ppm, respectively. If the amine

hydrogens are removed from the calculations, the aromatic hydrogens MAE and RMSE are 0.18 ppm and 0.19 ppm. The MAE and RSME for the controlled OAPS (Table 21) are 0.39 ppm and 0.42 ppm when all hydrogens are taken into account, and 0.47 ppm for both parameters when only the aromatic hydrogens are considered.

The corresponding Gaussian-predicted MAE and RMSE for all hydrogens in the commercial OAPS (Table 22) are 0.60 ppm and 0.74 ppm, respectively. Those related to the aromatic hydrogens are 0.37 ppm and 0.38 ppm. The MAE and RMSE for the controlled OAPS (Table 23) are 0.85 ppm and 0.90 ppm, whereas they decrease to 0.69 and 0.70 after removing the amine shifts. The fact that the MAE and RMSE are close to each other indicates that the errors are not scattered.

Table 20. The predicted δ_{calc} by MestreNova and experimental δ_{exp} ^{1}H NMR shifts in ppm along with their absolute error e_i in ppm for each peak identified in the commercial OAPS sample (Figure 62(a))

H-Type	δ_{calc}	δ_{exp}	$\lvert e_i \rvert$	Identification	Isomer type
H_{C2}	6.96	6.71	0.25	J	meta
H_{C4}	6.74	6.46	0.28	L	meta
H_{C5}	7.30	7.21	0.09	H	meta
H_{C6}	7.13	6.95	0.18	I	meta
H_n	4.88	5.09	0.21	meta	meta
H_{C3}	7.08	6.84	0.24	N	ortho
H_{C4}	7.19	7.09	0.10	F	ortho
H_{C5}	7.43	7.32	0.11	M	ortho
H_{C6}	7.31	7.21	0.10	D	ortho
H_n	5.49	5.40	0.09	ortho	ortho
H_{C2}	7.25	7.09	0.16	E	para
H_{C3}	6.87	6.63	0.24	O	para
H_n	5.24	5.18	0.06	para	para

Table 21. Same as Table 20 but for the controlled OAPS sample (Figure 62(b)).

H-Type	δ_{calc}	δ_{exp}	$\lvert e_i \rvert$	Identification	Isomer type
H_{C2}	6.96	6.45	0.51	J	meta
H_{C4}	6.74	6.23	0.51	L	meta
H_{C5}	7.30	6.93	0.37	H	meta
H_{C6}	7.13	6.70	0.43	I	meta
H_n	4.88	4.78	0.10	meta	meta

H_{C2}	7.25	6.75	0.50	E	para
H_{C3}	6.87	6.37	0.50	O	para
H_n	5.25	5.06	0.19	para	para

Table 22. The δ_{calc} by Gaussian at the HCTH407/6-311+G(2d,p) level of theory and δ_{exp} ^{1}H NMR shifts in ppm along with their e_i in ppm for each peak identified in the commercial OAPS sample (Figure 63(a)).

H-Type	δ_{calc}	δ_{exp}	$\lvert e_i \rvert$	Identification	Isomer type
H_{C2}	7.44	7.09	0.35	J	meta
H_{C4}	7.04	6.72	0.32	L	meta
H_{C5}	7.39	6.96	0.43	H	meta
H_{C6}	7.25	6.84	0.41	I	meta
H_n	3.48	5.03	1.55	meta	meta
H_{C3}	6.88	6.64	0.24	N	ortho
H_{C4}	7.46	7.09	0.37	F	ortho
H_{C5}	6.90	6.64	0.26	M	ortho
H_{C6}	7.89	7.32	0.57	D	ortho
H_n	4.43	5.40	0.97	ortho	ortho
H_{C2}	7.62	7.21	0.41	E	para
H_{C3}	6.90	6.46	0.44	O	para
H_n	3.69	5.18	1.49	para	para

Table 23. Same as Table 22 but for the controlled OAPS sample (Figure 63(b))

H-Type	δ_{calc}	δ_{exp}	$\lvert e_i \rvert$	Identification	Isomer type
H_{C2}	7.44	6.75	0.69	J	meta
H_{C4}	7.04	6.37	0.67	L	meta
H_{C5}	7.39	6.70	0.69	H	meta
H_{C6}	7.25	6.45	0.80	I	meta
H_n	3.48	4.78	1.30	meta	meta
H_{C2}	7.62	6.93	0.69	E	para
H_{C3}	6.86	6.23	0.63	O	para
H_n	3.69	5.06	1.37	para	para

Figures 64 and 65 illustrate the linear correlations for the commercial OAPS between the δ_{exp} and the δ_{calc} for the ^{1}H-NMR shifts predicted by both MestRenova (Table 20) and Gaussian (Table 22), respectively while taking into account either (a) all hydrogens or (b) only the aromatic hydrogens. All cases are well correlated (R > 0.97) with the slopes being

slightly different depending on the prediction method used and on whether the amine ^{1}H-NMR shifts are included or excluded.

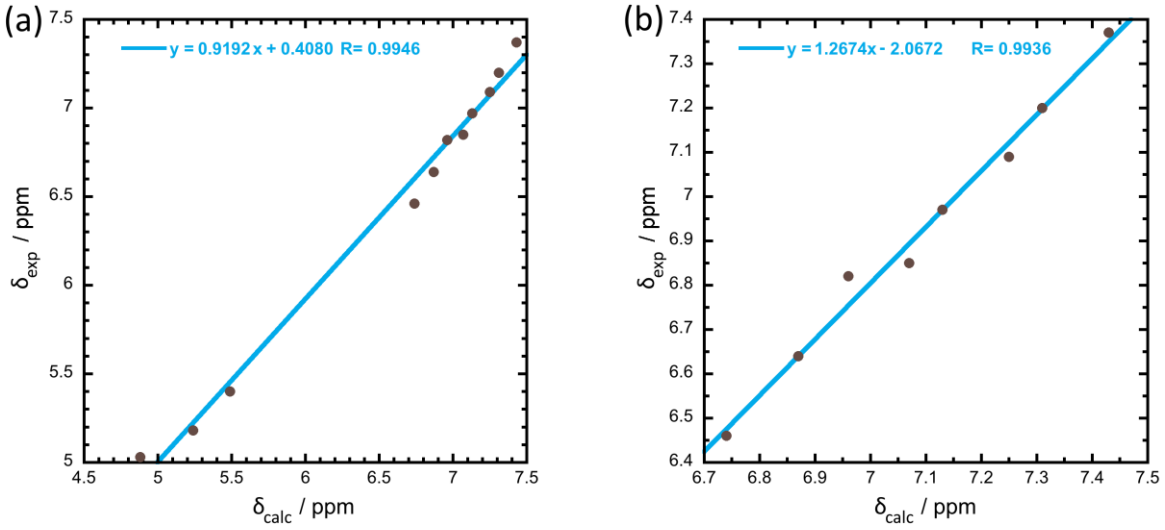

Figure 64. Linear correlation between the MestreNova-predicted δ_{calc} and the δ_{exp} ^{1}H-NMR shifts taking into account either (a) all hydrogens or (b) only the aromatic hydrogens in the commercial OAPS.

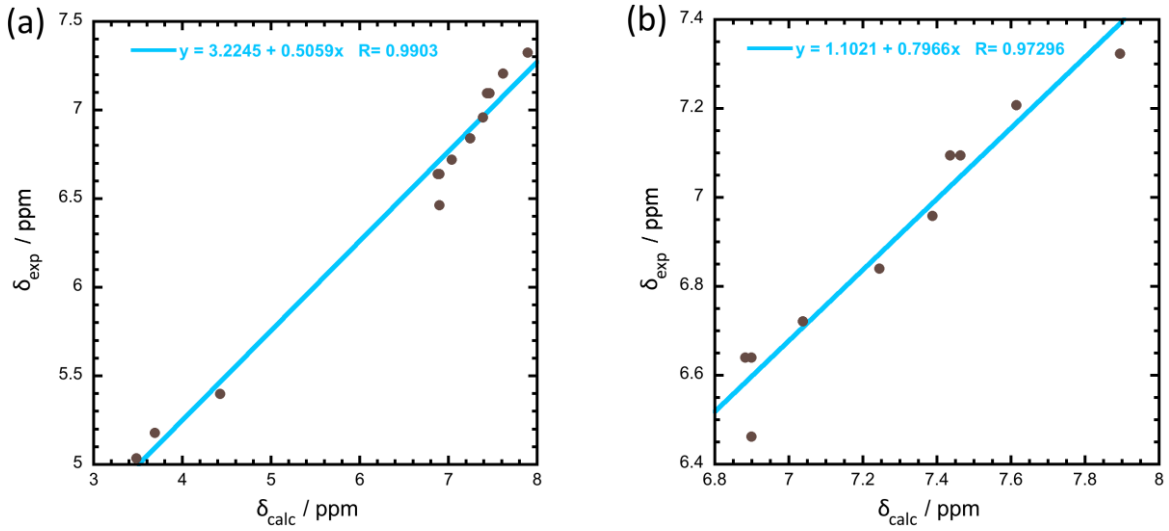

Figure 65. Same as Figure 64 but for the Gaussian-predicted shifts at the HCTH407/6-311+G(2d,p) level of theory.

As before, the scaled predicted shifts $\delta_{calc\text{-}scaled}$ were obtained for the commercial OAPS from the correlations. However, in this case, both types of approaches were investigated, i.e. either while including all hydrogens (Figures 64(a) and 65(a)) or the aromatic hydrogens only (Figures 64(b) and 65(b)). The latter is expected to be more precise than the former due to the problems related to the amine predictions.

The MestRenova-predicted $\delta_{calc\text{-}scaled}$ are reported in Tables 24-25. Compared to the unscaled predictions, the MAE and RMSE fall by 50% to 0.08 ppm and 0.09 ppm, respectively, for all hydrogens (Table 24). Ignoring the amine shifts (Table 25) further reduces the MAE and RMSE to 0.03 ppm.

Table 24. The scaled MestreNova-predicted $\delta_{calc\text{-}scaled}$ and experimental δ_{exp} ^{1}H NMR shifts in ppm along with their absolute error e_i in ppm for each hydrogen peak identified in the commercial OAPS (Figure 64(a)).

H-Type	$\delta_{calc\text{-}scaled}$	δ_{exp}	$\lvert e_i \rvert$	Identification	Isomer type
H_{C2}	6.81	6.71	0.10	J	meta
H_{C4}	6.60	6.46	0.14	L	meta
H_{C5}	7.12	7.21	0.09	H	meta
H_{C6}	6.96	6.95	0.01	I	meta
H_n	4.89	5.09	0.20	meta	meta
H_{C3}	6.92	6.84	0.08	N	ortho
H_{C4}	7.02	7.09	0.07	F	ortho
H_{C5}	7.24	7.32	0.08	M	ortho
H_{C6}	7.13	7.21	0.08	D	ortho
H_n	5.45	5.40	0.05	ortho	ortho
H_{C2}	7.07	7.09	0.02	E	para
H_{C3}	6.72	6.63	0.09	O	para
H_n	5.22	5.18	0.04	para	para

Table 25. Same as Table 24 but for each aromatic hydrogen peak identified in the commercial OAPS sample (Figure 64(b)).

H-Type	$\delta_{calc\text{-}scaled}$	δ_{exp}	$\lvert e_i \rvert$	Identification	Isomer type
H_{C2}	6.75	6.71	0.04	J	meta
H_{C4}	6.48	6.46	0.02	L	meta
H_{C5}	7.18	7.21	0.03	H	meta
H_{C6}	6.97	6.95	0.02	I	meta
H_{C3}	6.91	6.84	0.08	N	ortho
H_{C4}	7.05	7.09	0.02	F	ortho
H_{C5}	7.35	7.32	0.03	M	ortho
H_{C6}	7.20	7.21	0.01	D	ortho
H_{C2}	7.12	7.09	0.03	E	para
H_{C3}	6.64	6.63	0.01	O	para

The corresponding Gaussian-predicted $\delta_{calc\text{-}scaled}$ are reported in Tables 26-27. The full MAE and RMSE fall to 0.09 ppm and 0.10 ppm (Table 26), whereas ignoring the amine hydrogen shifts reduces them to 0.05 ppm and 0.06 ppm, respectively (Table 27). Such correlations can thus be used to achieve more accurate ^{1}H-NMR shifts by either prediction method.

Table 26. The scaled Gaussian-predicted $\delta_{calc\text{-}scaled}$ and experimental δ_{exp} ^{1}H NMR shifts in ppm along with their absolute error e_i in ppm for each hydrogen peak identified in the commercial OAPS (Figure 65(a)).

H-Type	$\delta_{calc\text{-}scaled}$	δ_{exp}	$\lvert e_i \rvert$	Identification	Isomer type
H_{C2}	6.99	7.09	0.10	J	meta
H_{C4}	6.78	6.72	0.06	L	meta
H_{C5}	6.96	6.96	0.00	H	meta
H_{C6}	6.89	6.84	0.05	I	meta
H_n	4.99	5.03	0.04	meta	meta
H_{C3}	6.71	6.64	0.07	N	ortho
H_{C4}	7.00	7.09	0.09	F	ortho
H_{C5}	6.71	6.64	0.07	M	ortho
H_{C6}	7.22	7.32	0.10	D	ortho
H_n	5.46	5.40	0.06	ortho	ortho
H_{C2}	7.08	7.21	0.13	E	para
H_{C3}	6.71	6.46	0.25	O	para
H_n	5.09	5.18	0.09	para	para

Table 27. Same as Table 26 but for each aromatic hydrogen peak identified in the commercial OAPS sample (Figure 65(b)).

H-Type	$\delta_{calc\text{-}scaled}$	δ_{exp}	$\lvert e_i \rvert$	Identification	Isomer type
H_{C2}	7.03	7.09	0.06	J	meta
H_{C4}	6.71	6.72	0.01	L	meta
H_{C5}	6.99	6.96	0.03	H	meta
H_{C6}	6.87	6.84	0.03	I	meta
H_{C3}	6.58	6.64	0.06	N	ortho
H_{C4}	7.05	7.09	0.04	F	ortho
H_{C5}	6.60	6.64	0.04	M	ortho
H_{C6}	7.39	7.32	0.07	D	ortho
H_{C2}	7.17	7.21	0.04	E	para
H_{C3}	6.60	6.46	0.14	O	para

Figures 66 for MestreNova (Table 21) and 67 for Gaussian (Table 23) both show that the amine hydrogen ^{1}H-NMR shifts also change the slope of the linear correlations in the controlled OAPS sample with (a) including for all hydrogens and (b) including only for the aromatic hydrogens. The R is more than 0.97 in all cases, which is still good.

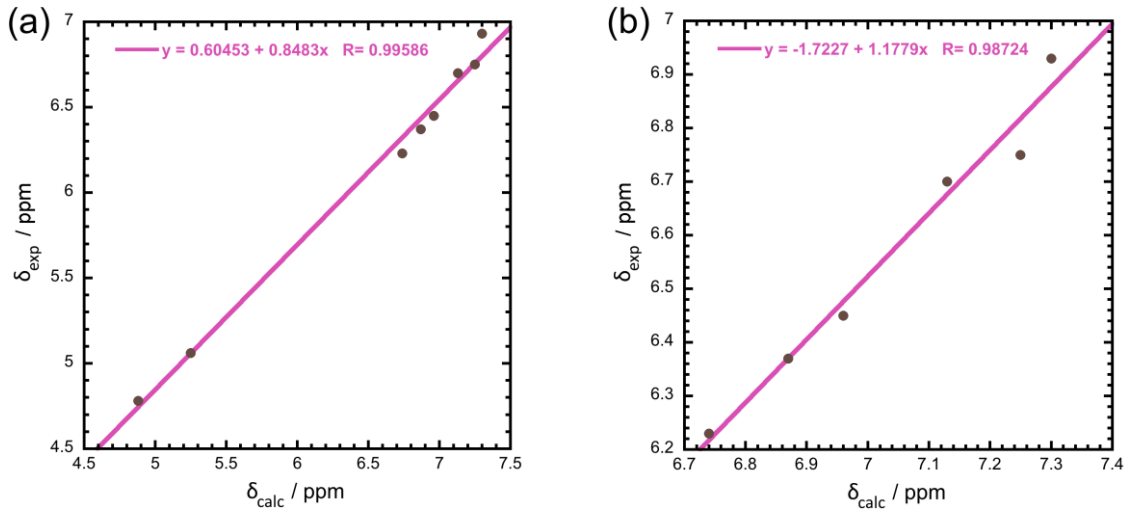

Figure 66. Linear correlation between the MestreNova-predicted δ_{calc} and the δ_{exp} ^{1}H-NMR shifts taking into account either (a) all hydrogens or (b) only the aromatic hydrogens in the controlled OAPS.

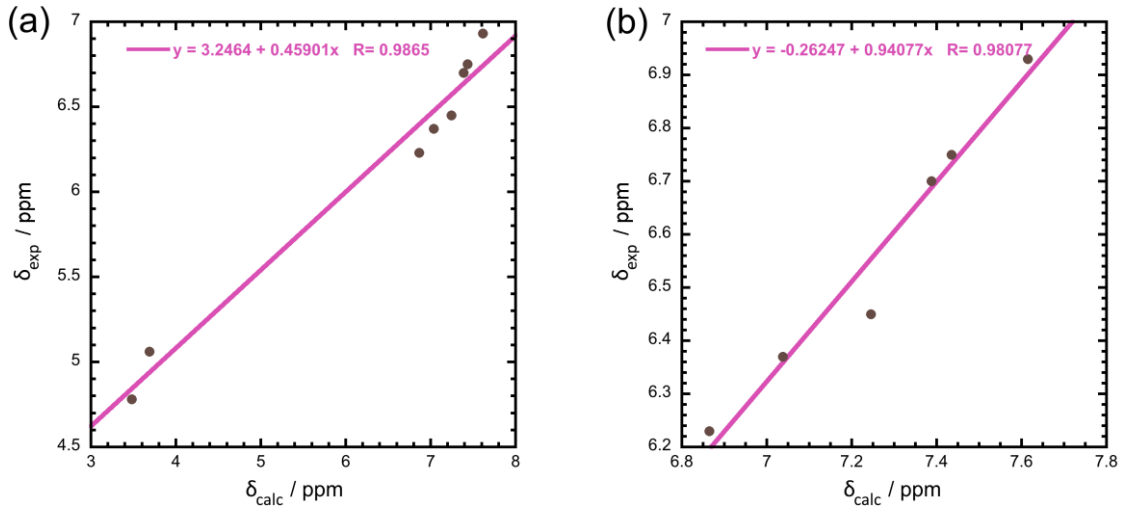

Figure 67. Same as Figure 65 but for the Gaussian-predicted shifts at the HCTH407/6-311+G(2d,p) level of theory.

The scaled predicted shifts $\delta_{calc\text{-}scaled}$ for the controlled OAPS were again calculated by using the correlations for either all hydrogens (Figures 66(a) and 67(a)) or only for the aromatic hydrogens (Figures 66(b) and 67(b)).

The MestRenova-predicted $\delta_{calc\text{-}scaled}$ are reported in Tables 28-29. Compared to the unscaled predictions, the full MAE and RMSE are reduced to 0.05 ppm and 0.07 ppm, respectively (Table 28), and to 0.03 ppm and 0.04 ppm after subtracting the amine shifts (Table 29).

Table 28. The scaled MestreNova-predicted $\delta_{calc\text{-}scaled}$ and experimental δ_{exp} ^{1}H NMR shifts in ppm along with their absolute error e_i in ppm for each hydrogen peak identified in the controlled OAPS (Figure 66(a)).

H-Type	$\delta_{calc\text{-}scaled}$	δ_{exp}	$\lvert e_i \rvert$	Identification	Isomer type
H_{C2}	6.51	6.45	0.06	J	meta
H_{C4}	6.32	6.23	0.09	L	meta
H_{C5}	6.80	6.93	0.13	H	meta
H_{C6}	6.65	6.7	0.05	I	meta
H_n	4.74	4.78	0.04	meta	meta
H_{C2}	6.75	6.75	0.00	E	para
H_{C3}	6.43	6.37	0.06	O	para
H_n	5.06	5.06	0.00	para	para

Table 29. Same as Table 28 but for each aromatic hydrogen peak identified in the controlled OAPS sample (Figure 66(b)).

H-Type	$\delta_{calc\text{-}scaled}$	δ_{exp}	$\lvert e_i \rvert$	Identification	Isomer type
H_{C2}	6.48	6.45	0.03	J	meta
H_{C4}	6.22	6.23	0.01	L	meta
H_{C5}	6.88	6.93	0.05	H	meta
H_{C6}	6.68	6.7	0.02	I	meta
H_{C2}	6.82	6.75	0.07	E	para
H_{C3}	6.37	6.37	0.00	O	para

The corresponding Gaussian-predicted $\delta_{calc\text{-}scaled}$ are reported in Tables 30-31. The full MAE and RMSE both fall to 0.12 ppm (Table 30), while ignoring the amine hydrogens further reduce the MAE to 0.08 ppm (Table 31). This improvement in accuracy when the amine hydrogens are omitted shows that precise values for the OAPS aromatic hydrogens shifts can be obtained from both prediction methods when associated with the appropriate scaling.

Table 30. The scaled Gaussian-predicted $\delta_{calc\text{-}scaled}$ and experimental δ_{exp} ^{1}H NMR shifts in ppm along with their absolute error e_i in ppm for each hydrogen peak identified in the controlled OAPS (Figure 67(a)).

H-Type	$\delta_{calc\text{-}scaled}$	δ_{exp}	$\lvert e_i \rvert$	Identification	Isomer type
H_{C2}	6.66	6.75	0.09	J	meta
H_{C4}	6.48	6.37	0.11	L	meta
H_{C5}	6.64	6.70	0.06	H	meta
H_{C6}	6.57	6.45	0.12	I	meta
H_n	4.84	4.78	0.06	meta	meta
H_{C2}	6.74	6.93	0.19	E	para
H_{C3}	6.40	6.23	0.17	O	para
H_n	4.94	5.06	0.12	para	para

Table 31. Same as Table 30 but for each aromatic hydrogen peak identified in the controlled OAPS sample (Figure 67(b)).

H-Type	$\delta_{calc\text{-}scaled}$	δ_{exp}	$\lvert e_i \rvert$	Identification	Isomer type
H_{C2}	6.73	6.75	0.02	J	meta
H_{C4}	6.36	6.37	0.01	L	meta
H_{C5}	6.55	6.70	0.15	H	meta
H_{C6}	6.69	6.45	0.24	I	meta
H_{C2}	6.90	6.93	0.03	E	para
H_{C3}	6.20	6.23	0.03	O	para

Despite the slight displacements between predicted and experimental peaks, both MestreNova and Gaussian at the HCTH407/6-311+G(2d,p) level of the theory seem to be able to provide results that are compatible with the experimental ^{1}H-NMR OAPS shifts. Such results can even be quantitatively improved using the scaling factors displayed in Figures 64-67, especially when the amine hydrogen predictions are omitted.

However, it remains unclear why the relative order of the predicted aromatic hydrogens peaks differ, *i.e.* the identification of each peak as belonging to a specific isomer depends on the prediction method used. Since it was not possible to differentiate both methods using the 1D-NMR experimental spectra, it was attempted to predict the 2D-NMR spectra with each of them.

b.4.4) 2D-NMR predictions

The ^{13}C-NMR $\delta_{calc\text{-}scaled}$ shifts (Section b.4.2.) for both types of OAPS were combined with their respective aromatic ^{1}H-NMR $\delta_{calc\text{-}scaled}$ shifts (Section b.4.3.) in Figure 68 to predict 2D-NMR spectra comparable to the available experimental HSQC spectra (Figure 45). (a) and (b) show the predictions by MestreNova and Gaussian, respectively, for the commercial OAPS, while (c) and (d) are the corresponding predictions for the controlled OAPS.

In the predicted 2D-NMR spectrum of the commercial OAPS with MestreNova (Figure 68(a)), some peaks can easily be assigned. The G, P and K shifts on the ^{13}C-NMR axis are related to the *meta*, *ortho*, and *para* aromatic carbons connected to the silicons in the OAPS cages. Similarly, the C, A and B shifts correspond to the carbons connected to the amine nitrogens. The other ^{13}C-NMR shifts are connected to the aromatic hydrogens and their cross-points can be compared to the experimental HSQC spectrum. However, it is clear that the predicted cross-points are scattered and far from the experimental spectrum (for example M and N).

The situation improves significantly for the predicted 2D-NMR spectrum of the commercial OAPS with Gaussian (Figure 68(b)). The G, P, K, C, A and B shifts on the ^{13}C-NMR axis can again be assigned to the carbons linked either to the OAPS cage silicons or to the amine nitrogens. As far as the cross-points are concerned, the *ortho* D, *para* E, *ortho* F and *meta* H shifts correspond very well to experimental contour lines. The other cross-points are slightly more displaced because of the differences between predicted and experimental peaks. The *meta* L peak seems to be the furthest from its corresponding contour line, which could be due to an underestimation in the ^{13}C-NMR spectrum. But the Gaussian-predicted cross-points still reproduce rather well the ten contour points of the experimental HSQC spectrum, i.e. the prediction is much better than for MestreNova in (a).

In the predicted 2D-NMR spectrum of the controlled OAPS with MestreNova (Figure 68(c)), the G, K, B and C shifts on the ^{13}C-NMR axis are related to the carbons connected either to the cage silicons or to the amine nitrogens. For the carbons connected to aromatic hydrogens, the black rectangles suggest that the two sharpest ^{13}C-NMR peaks, which correspond to large contour cross-points, can be assigned to the *para* isomer. On the other hand, the H, I, J and L shifts can be assigned to the *meta* isomer. However, as for (a), the predicted shifts for the aromatic hydrogens lead to cross-points that are displaced with respect

to the experimental signals, even if there is a better agreement than for the commercial OAPS.

The situation for the predicted 2D-NMR spectrum of the controlled OAPS improves once again with Gaussian (Figure 68(d)). The assignment of each peak to a specific isomer is similar to MestreNova but the cross-points are much closer to the experimental adjacent contour point. The black rectangles confirm that the sharp ^{13}C-NMR peaks correspond to the *para* isomer.

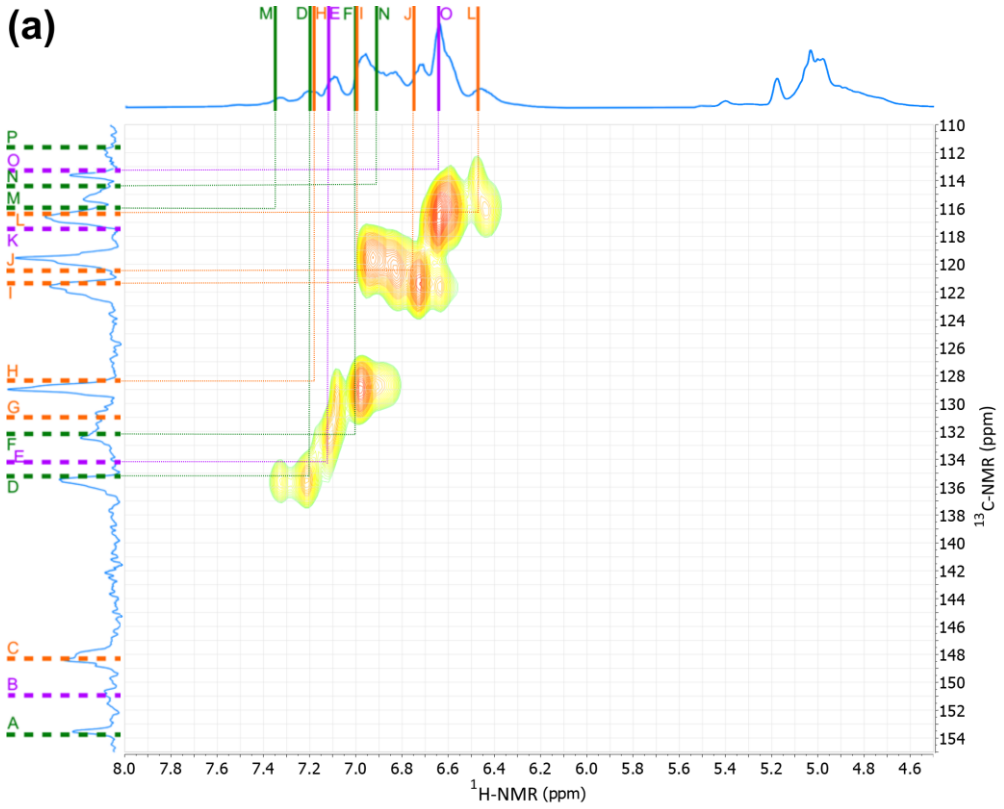
(a)
M D H E F I N J O L
P O N M K J I H G F E D C B A
8.0 7.8 7.6 7.4 7.2 7.0 6.8 6.6 6.4 6.2 6.0 5.8 5.6 5.4 5.2 5.0 4.8 4.6
1H-NMR (ppm)
110 112 114 116 118 120 122 124 126 128 130 132 134 136 138 140 142 144 146 148 150 152 154
13C-NMR (ppm)

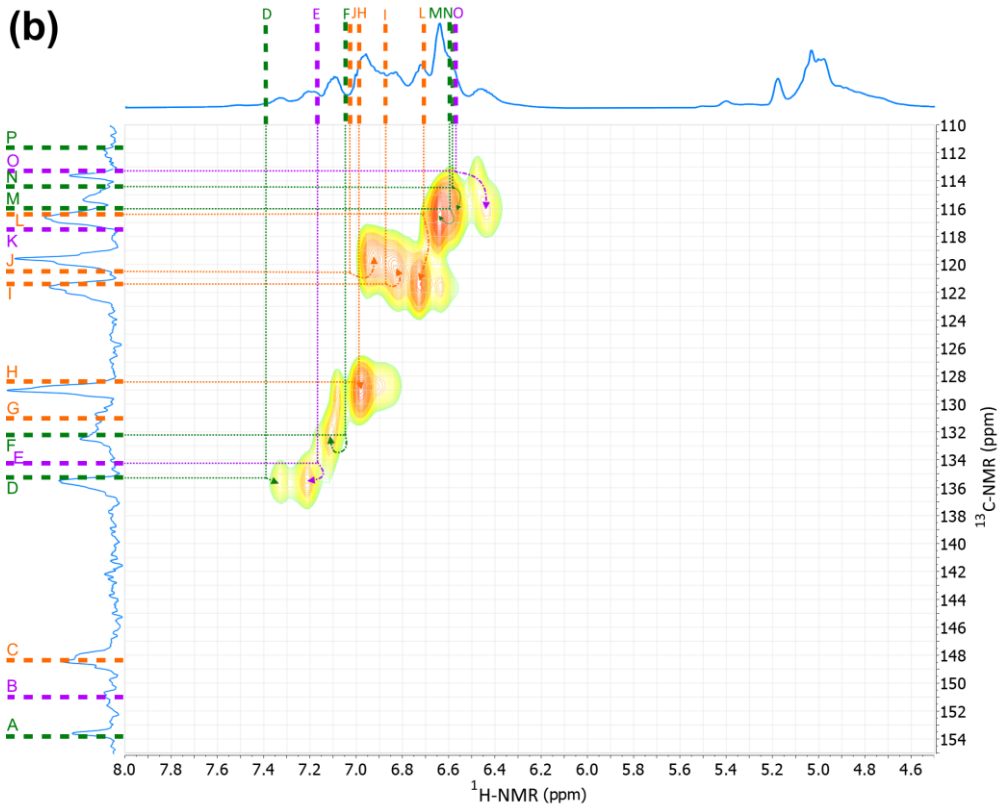
(b)
D E F J H I L M N O
P O N M K J I H G F E D C B A
8.0 7.8 7.6 7.4 7.2 7.0 6.8 6.6 6.4 6.2 6.0 5.8 5.6 5.4 5.2 5.0 4.8 4.6
1H-NMR (ppm)
110 112 114 116 118 120 122 124 126 128 130 132 134 136 138 140 142 144 146 148 150 152 154
13C-NMR (ppm)

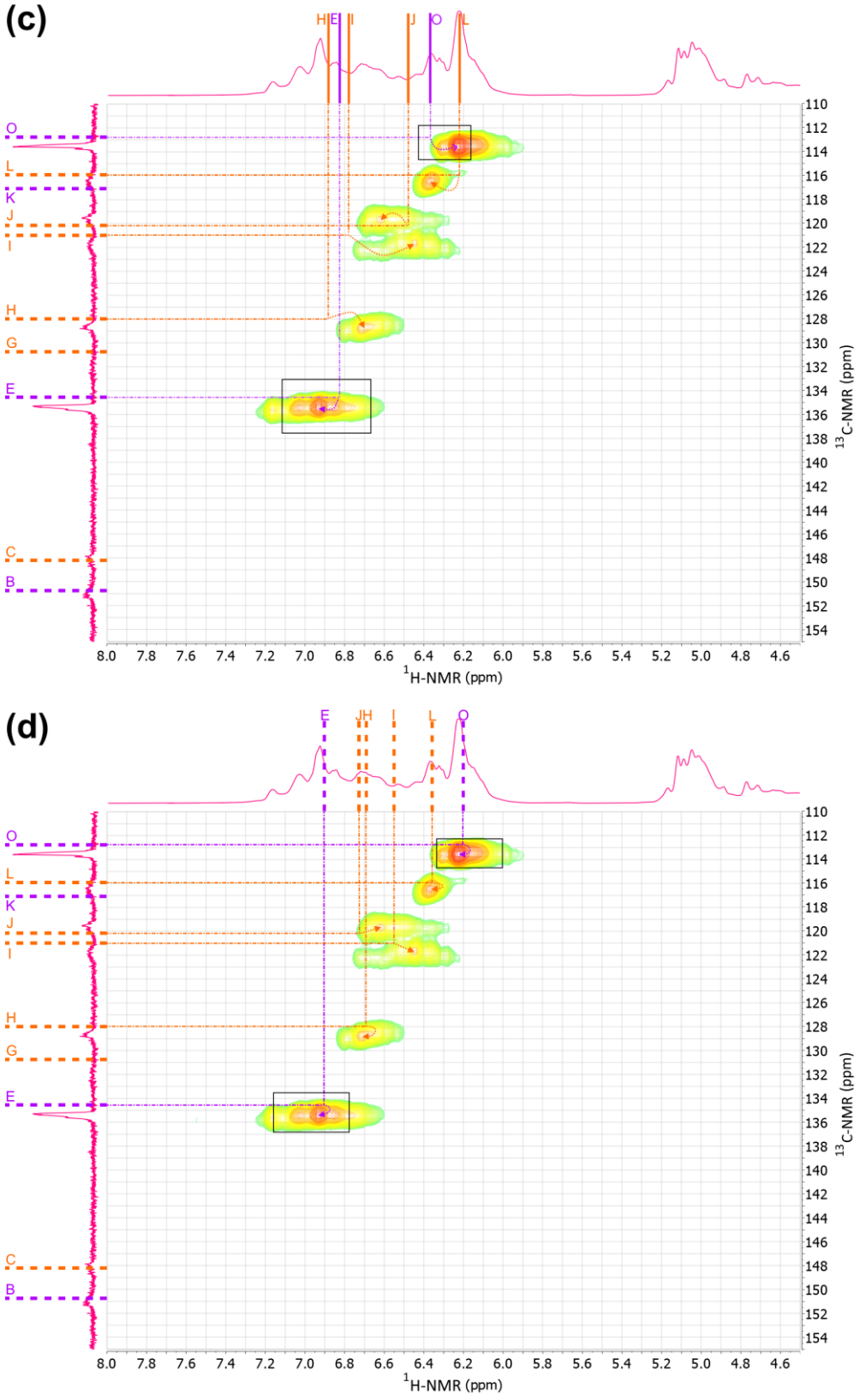

Figure 68. The experimental HSQC spectrum for the commercial (blue) and controlled (pink) OAPS compared to the $\delta_{calc\text{-}scaled}$ for the ^{13}C-NMR shifts (*y*-axis) and the ^{1}H-NMR shifts (*x*-axis) predicted by (a and c) MestreNova and (b and d) Gaussian at the HCTH407/6-311+G(2d,p) level of theory. The colours for the isomers are orange for *meta*, green for *ortho* and purple for *para*.

While Section b.4.3. showed that it was difficult to unambiguously assess the quality of the MestreNova and Gaussian predictions for ^{1}H-NMR using the 1D spectra only, the 2D-NMR predictions prove that the DFT calculations are much better at predicting accurate chemical shifts for ^{1}H-NMR than MestreNova.

Consequently, the final isomer assignment for each peak is that predicted by Gaussian at the HCTH407/6-311+G(2d,p) level of theory. It is summarized in Table 32.

Table 32. The Gaussian-predicted $\delta_{calc\text{-}scaled}$ compared to the δ_{exp} for the ^{1}H NMR and ^{13}C-NMR chemical shifts in ppm for each aromatic carbon and hydrogen peaks identified in the commercial and controlled OAPS samples and the assignment of each signal to a specific isomer (Tables 18, 19, 27, 31).

H and C Type	Commercial $\delta_{calc\text{-}scaled}$	Commercial δ_{exp}	Controlled $\delta_{calc\text{-}scaled}$	Controlled δ_{exp}	Identification	Isomer type
C_1	131.09	130.70	130.73	129.28	G	meta
H_{C2} - C_2	7.03-120.61	7.09-119.55	6.73-120.17	6.75-119.74	J	meta
C_3	148.41	148.34	148.19	147.71	C	meta
H_{C4} - C_4	6.71-116.39	6.72-116.64	6.36-115.91	6.37-116.13	L	meta
H_{C5} - C_5	6.99-128.36	6.96-128.97	6.55-127.98	6.70-128.20	H	meta
H_{C6} - C_6	6.87-121.39	6.84-121.60	6.69-120.95	6.45-121.51	I	meta
C_1	111.67	111.78	-	-	P	ortho
C_2	153.89	153.53	-	-	A	ortho
H_{C3} - C_3	6.58-114.42	6.64-115.28	-	-	N	ortho
H_{C4} - C_4	7.05-132.27	7.09-132.45	-	-	F	ortho
H_{C5} - C_5	6.60-115.98	6.64-115.28	-	-	M	ortho
H_{C6} - C_6	7.39-135.32	7.32-135.54	-	-	D	ortho
C_1	117.56	116.64	117.09	116.13	K	para
H_{C2} - C_2	7.17-134.87	7.21-135.54	6.90-134.54	6.93-135.35	E	para
H_{C3} - C_3	6.60-113.26	6.46-113.60	6.20-112.76	6.23-113.59	O	para
C_4	150.94	151.00	150.75	151.36	B	para

V. Hybrid membranes based on OAPS

1) *Fabrication of polyOAPS-imide membranes*

Following the extensive characterization of OAPS on its own, the commercial OAPS produced by Gelest and the 6FDA dianhydride (4,4′-(hexafluoroisopropylidene) diphthalic anhydride, Figure 7) produced by Sigma-Aldrich were selected as the monomers to fabricate new hybrid polyOAPS-imide membranes aimed at being more resistant to high temperatures and pressures than the initial polyPOSS-imides.

The fabrication procedure was based on the previous polyPOSS-imide work (Figure 12),[4] and its three steps are schematically shown for OAPS in Figure 69. It is expected that the hypercrosslinked structures will be somewhat dependent on the OAPS isomer.[208-209] We note that an OAPS cage could potentially carry several different isomers for the aminophenyl arms but as these are not able to be distinguished experimentally, the isomers are not specified in the schemes.

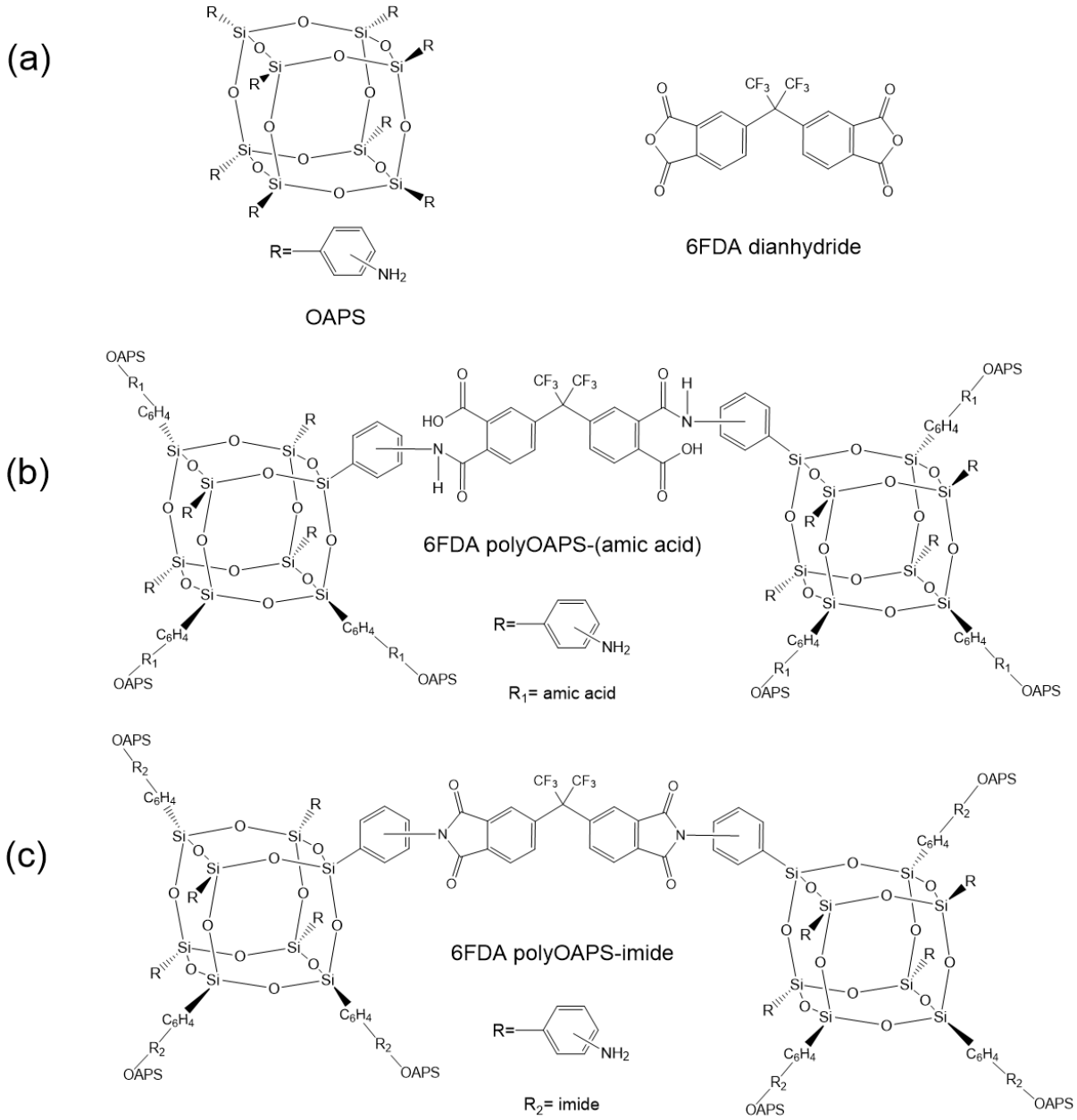

Figure 69. Chemical structures of (a) the OAPS and the 6FDA dianhydride monomers, (b) the interfacial polycondensation step leading to a 6FDA polyOAPS-(amic acid) network with an average connectivity of 4, and (c) the imidization step leading to the final 6FDA polyOAPS-imide network.

As for the polyPOSS-imides, 6FDA-based polyOAPS-imide membranes were produced through interfacial polycondensation between an organic phase containing the 6FDA dianhydride in toluene, and an aqueous phase containing OAPS in a mixture of DMSO/water with a ratio of 3/2 v/v. Solutions of 0.1% w/v 6FDA in toluene and 2.5% w/v OAPS in DMSO were first prepared separately. OAPS cannot be dissolved in water but, as explained in Section III, DMSO is soluble with toluene. As such, water was added in a

second step to the OAPS/DMSO solution in order to reach a 3/2 DMSO/water ratio and create two separate phases between the 6FDA-containing and OAPS-containing solutions.

α-alumina disks were chosen as the main mechanical supports for the membranes. In order to add a layer with smaller pores, a thin layer of γ-alumina (3 μm) was deposited on each α-alumina support by dip coating (Figure 70). Since the formation of the γ-alumina layer is very sensitive to dust, the coating procedure was performed in a cleanroom. A solution of $Al(OH)Ac_2$/polyvinyl alcohol (PVA) was first prepared. Then, the support was contacted for a few seconds to get completely coated with the alumina solution. The coated support was later displaced into a high-temperature (HT) oven and heated up to 650°C to undergo calcination.

Figure 70 summarizes the whole membrane fabrication procedure. Following the modification of the alumina support:

- The support was fixed in a Buchner funnel and the OAPS solution in DMSO/water was poured on it. After 20 minutes, the excess solution was poured out, and a rubber roller was rolled on the surface of the support to remove the droplets. A very thin layer of the OAPS solution remained on the surface of the support.
- The 6FDA solution in toluene was then added to start the polycondensation reaction. A new thin layer of hypercrosslinked polyOAPS-(amic acid) network (Figure 69(b)) was immediately formed. In this reaction, the limiting reactant is OAPS and the excessive one is 6FDA. After 13 minutes, the 6FDA solution was poured out and the support was taken out of the Buchner funnel. It was left in a vacuum oven for 48 hours at 50°C in order to evaporate the solvents.
- The polyOAPS-(amic acid) membrane on its support was subsequently transferred into the HT oven to perform the imidization, i.e. the transition from the amic acid to the imide form for 6FDA (Figure 69(c)). The step-by-step annealing program was as follows with a ramp rate of 5 °C/min to prevent any shrinkage of the membrane: 3 hours up to 100 °C, 3 hours up to 150 °C, 3 hours up to 200 °C, 2 hours up to 250 °C, 2 hours up to 300 °C. It was finally cooled for 3 hours to get back to ambient temperature. As can be seen in Figure 70, the final 6FDA polyOAPS-imide membrane is brown.

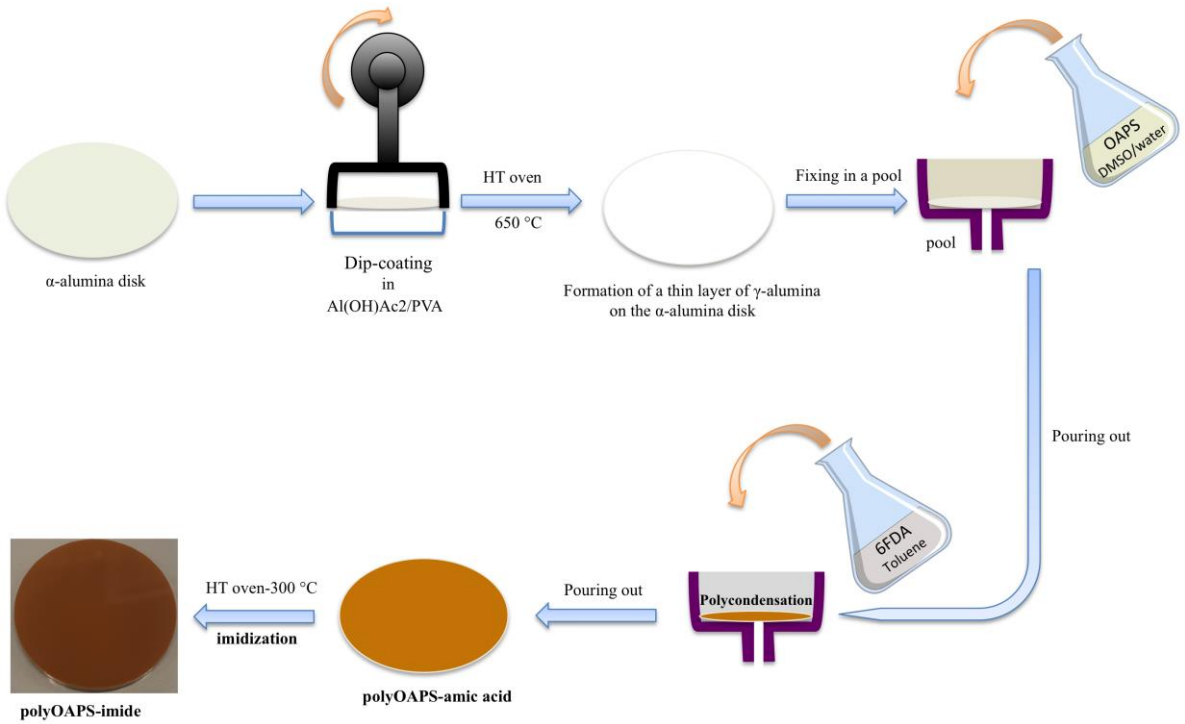

Figure 70. The fabrication procedure of an hypercrosslinked 6FDA-based polyOAPS-imide membrane.

2) *TGA analysis of the membranes*

Thermal gravimetric analyses (TGA) were carried out using an STA 449 F3 Jupiter (NETZSCH). Following the interfacial polycondensation, 15 mg of free-standing polyOAPS-(amic acid) membrane was transferred inside an aluminium pan and was warmed up under a nitrogen atmosphere (stream of 50 ml min^{-1}) with a heating rate of 10 °C/min. As shown in Figure 71, a first weight loss occurs at 150-300°C, indicating the imidization step and the production of water. The second weight loss at ~400°C shows the start of the degradation process for the organic part. The sample reaches an almost constant mass at ~650 °C, and the weight loss continues up to 1100 °C at a gentle slope related to the degradation of the inorganic part.

Simulation studies on the thermomechanical characteristics of the new polyOAPS-imide membranes at 400°C show that the *ortho* isomer provides a better resistance for the 6FDA polyOAPS-imide membranes than the *meta* and *para* isomers.[208] However, in all cases, the polyOAPS-imide membranes remain thermally superior to the polyPOSS-imides membranes, which degrade experimentally before 350°C.[31] Following imidization,

polyOAPS-imide networks can thus tolerate very high temperatures, which is crucial for the separation of hot gases.

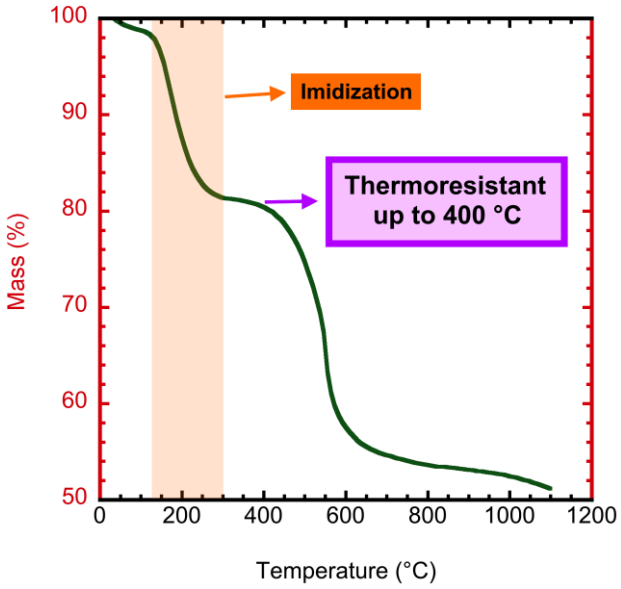

Figure 71. TGA analysis of a 6FDA polyOAPS-(amic acid) membrane

3) *IR spectroscopy characterization of the membranes*

The ATR-IR Perkin Elmer Paragon 1000 PC was used to compare the IR spectra for OAPS, 6FDA polyOAPS-(amic acid), and 6FDA polyOAPS-imide (Figure 72) in order to follow the various stages of the preparation procedure. (a) shows the whole IR spectra while (b) specifically displays the 1000-2000 cm^{-1} range for clarity.

The Si-O-Si band, which can be observed at 1100 cm^{-1} in all three spectra, is due to the OAPS cages. The polyOAPS-(amic acid) presents two typical amide bands at 1590 and 1650 cm^{-1}, corresponding to the N-H bending and the C=O stretching, respectively as well as a small shoulder at 1715 cm^{-1} indicating the presence of the carboxylic acid functional group. Following the thermal treatment, the aforementioned peaks should disappear due to the imidization process. Indeed, the amic acid bands are no anymore clearly observable in the polyOAPS-imide spectrum, thus showing that imidization is efficient. However, small bands corresponding to the N-H bending can still be observed for the polyOAPS-imide. This is probably due to unreacted NH_2 groups on the OAPS cage. This is not unexpected as it is difficult for steric reasons to have all eight arms of the inorganic precursor reacting with a dianhydride (Figure 69), and as such, some of the initial amine groups remain present in the

final network. The two new bands at 1720 and 1780 cm^{-1} in the polyOAPS-imide spectrum can be attributed to the imide C=O symmetric and asymmetric stretching modes, respectively. The band at 1270 cm^{-1} is the C-F stretching of the 6FDA organic bridge, which is present in both the polyOAPS-(amic acid) and polyOAPS-imide but is absent in the inorganic OAPS precursor.

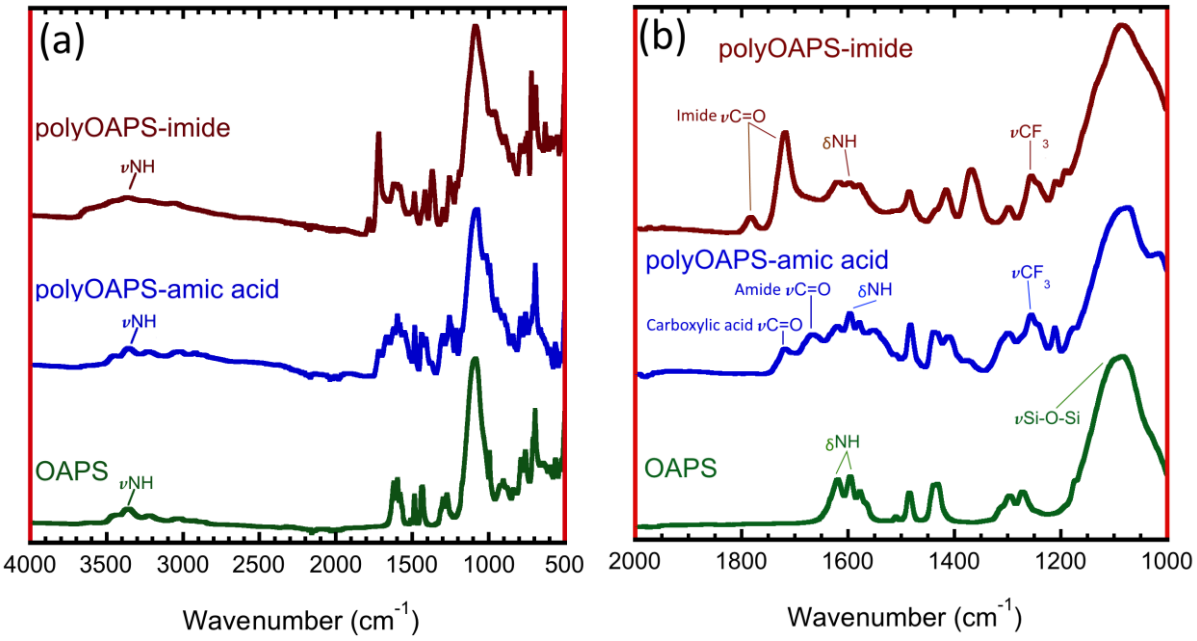

Figure 72. IR spectra of the OAPS, 6FDA polyOAPS-(amic acid), and 6FDA polyOAPS-imide.

Figure 72 thus confirms that the final product is indeed basically a polyOAPS-imide membrane.

4) *Permeance and gas selectivity of the new membranes*

An automatic single-gas permeation set-up was used in a dead-end mode at a trans-membrane pressure of 2 bar and at five different temperatures (50, 100, 150, 200, and 250 °C) in order to measure the permeance of the new membranes. He, H_2, N_2, CO_2 and CH_4 were tested as pure feeds, and the permeance results were averaged over three membranes each. In the following Figures (Figs. 73-75), results related to the new 6FDA polyOAPS-imide membranes will be presented on (a) the left while those related to the initial 6FDA polyPOSS-imides for the same temperature range will be displayed on (b) the right for comparison.

Figure 73 shows the permeances as a function of the kinetic diameter for the different gases. The polyOAPS-imide membranes based on 6FDA are able to maintain their

permeation characteristics at temperatures at least up to 250 °C (a). This is much higher than for conventional polymers which suffer from a performance loss at elevated temperatures. As expected for glassy polymers, the permeance tends to decrease with the increase in the gas kinetic diameter.[4, 210] Compared to the polyPOSS-imides (b), the gas permeances in polyOAPS-imide membranes are a bit lower for He and H_2, similar for CO_2 and generally larger for N_2 and CH_4. The latter is probably related to the larger amount of free volume in the OAPS-based membranes, which allows for larger penetrants to permeate better. However, it should also be noted that permeances are not normalized to the membrane thicknesses. These are expected to be close but slight differences could affect the results.

For all gases except for CO_2, the permeance increases with the temperature in the order $CH_4 > N_2 > H_2 \approx$ He for both polyOAPS-imide and polyPOSS-imide matrices, indicating that the diffusion of the larger penetrants (CH_4 and N_2) is thermally improved to a greater extent than that of the smaller ones. The differences in free volumes between both types of membranes, i.e. polyOAPS-imides >> polyPOSS-imides,[208-209] lead to more differences for the latter as a function of the temperature. Indeed, polyPOSS-imides are able to provide significantly more diffuse jumps for the larger penetrants at high temperatures with respect to those at ambient temperatures.[210] On the other hand, diffusion in polyOAPS-imides is easier both at ambient and high temperatures.

The differences as a function of temperature are less marked for CO_2 because of its higher solubility at low temperatures. The affinity toward CO_2 results from the trifluoromethyl and the imide groups, which confirms that the gas molecules diffuse through the organic part of the network.[4, 209, 211] At higher temperatures, the CO_2 diffusivity increases while its solubility decreases, thus counteracting the influence of temperature.[4] The selectivity of CO_2 over the other gases thus decreases as a function of temperature. Both types of membranes show close permeances for CO_2, which confirms that the 6FDA organic linker is more important than the inorganic precursor for the transport of this penetrant.

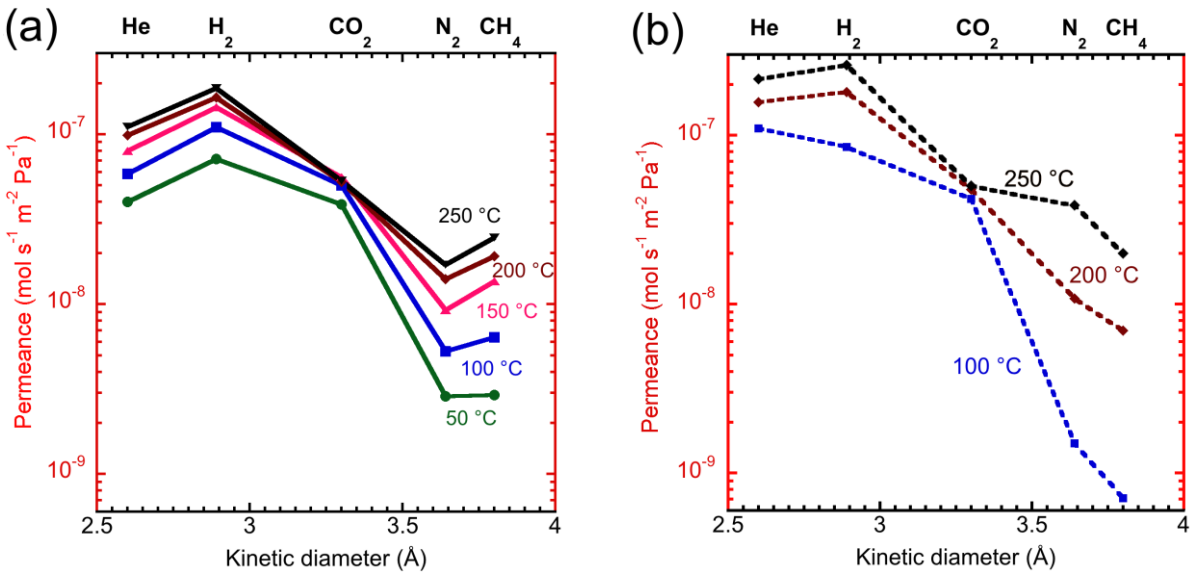

Figure 73. Gas permeances of (a) the new polyOAPS-imides and (b) the polyPOSS-imides at 2 bar.[4]

Figure 74 compares the Arrhenius plots of the permeances in both types of membranes on a logarithmic scale as a function of $R^{-1}T^{-1}$ (lower *x*-axis). The temperature is also provided in °C on the top *x*-axis for clarity. They show that the gas permeance is thermally activated. The activation energies were obtained from nonlinear fits of the temperature-dependent permeation data. They decrease in the order $CH_4 > N_2 > He \approx H_2 > CO_2$ for the polyOAPS-imides (a). It is the same as for the initial polyPOSS-imides,[4] except for H_2 which is slightly larger than for He (b). The linear trends in the Arrhenius plots indicate that the activation energies of the sorption and diffusion are not severely affected by the temperature.[210] This is unlike the chain-rearrangement-induced permeability loss in conventional polymeric membranes at high temperatures.[4, 212-213]

Activation energies are associated both with the penetrant size and with the molecular nature of the membrane. The larger penetrants generally exhibit larger activation energies in polymer membranes (except for CO_2 due to its high solubility).[210] A high activation energy results from a great resistance within the polymer matrix for the penetrant to perform a diffusive jump.[210] On the other hand, lower activation energies are associated with fewer energy barriers for gas permeation. As noted above, molecular motions generated at higher temperatures create larger gaps between the chains, which have more impact on the larger penetrants since they encounter more severe diffusive resistance at ambient temperatures.[210] The effect of temperature on the CO_2 permeance is low, and as a result, its activation energy is low in both types of membranes. For all other gases, the activation energies are higher in the polyPOSS-imide membranes (b). This is especially striking for CH_4 and N_2, where they

are more than twice the activation energies in the polyOAPS-imides (a). According to molecular modelling screening investigations,[209] polyOAPS-imides have open structures resulting from the high free volume generated by the intrinsic planarity and rigidity of the phenyl rings, and as such a high sorption capacity. PolyPOSS-imides are much more compact, thus providing more efficient barriers at low temperatures.

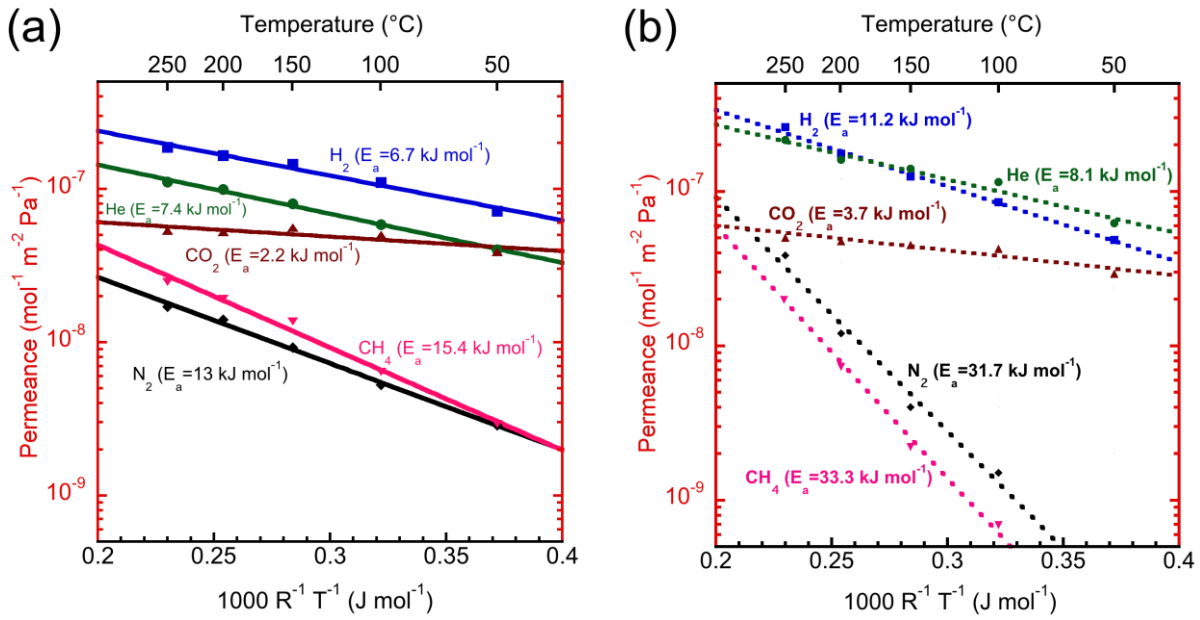

Figure 74. Arrhenius plots of gas permeances for He, H_2, CO_2, N_2 and CH_4 for (a) the new polyOAPS-imides and (b) the polyPOSS-imides at 2 bar.[4]

Figure 75 compares the ideal permselectivity of the gas pairs under study, i.e. H_2/CO_2, CO_2/CH_4, H_2/CH_4, CO_2/N_2, He/CO_2, He/CH_4 and H_2/N_2 as a function of temperature in both types of membranes. Regardless of the more open structures in the new polyOAPS-imides (a), which decrease the selectivities with respect to the more gas-sieving polyPOSS-imides (b), the gas selectivities are still satisfactorily maintained at high temperatures due to the rigidity of the hypercrosslinked polyOAPS-imide networks. Indeed, the molecular simulations[209] confirm the superior mechanical stabilities of polyOAPS-imides over polyPOSS-imides, while molecular motions still allow for the diffusion of the gas molecules.[4]

Most of the selectivities over both membranes decrease as a function of the temperature due to the different gas activation energies. They vary more dramatically for the polyPOSS-imide membranes (b), because of their higher activation energies. On the other hand, the He/CO_2 and H_2/CO_2 selectivities increase with temperature due to the higher activation energies of He and H_2 over CO_2. The polyOAPS-imide membranes are able to

preserve gas selectivities of ~10 for H_2/CH_4 and H_2/N_2 up to 250°C which shows their interest in gas separations at high temperatures.

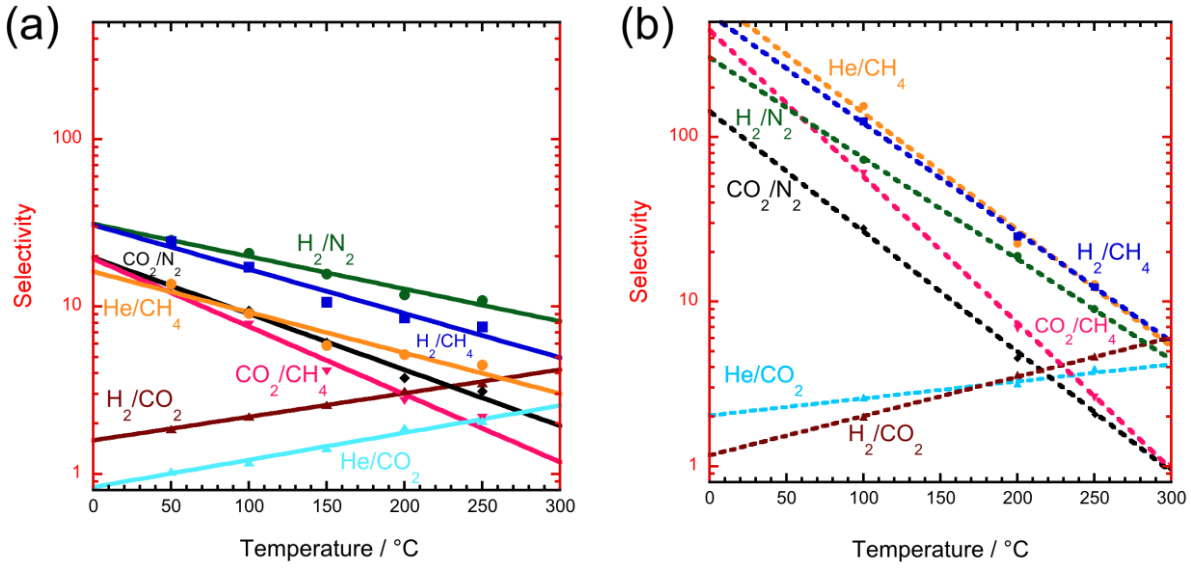

Figure 75. Permselectivities for (a) the new polyOAPS-imides and (b) the polyPOSS-imides at 2 bar.[4]

The permeation studies show that the polyPOSS-imide membranes have higher selectivities at temperatures below 300°C (b). But the trendlines suggest that the scenario can be reversed at higher temperatures than 300°C (a). While polyPOSS-imides will eventually degrade below 350°C, polyOAPS-imides will remain active under such harsh conditions, particularly for H_2/CO_2, He/CO_2 as well as H_2/N_2 to some extent.

This can be interesting as H_2 separation is a critical step in hydrocarbon fuel processing.[214] Helium is also important as it is used as an inert gas in welding, a carrier gas in scientific equipment and so on.[215-216]

5) ***Morphology of the new polyOAPS-imide membrane***

Figure 76 shows the surfaces on the scales of (a) 1 µm and (b) 200 nm as well as the cross-sections on the scales of (c) 1 µm and (d) 200 nm of a 6FDA polyOAPS-imide membrane studied by Field Emission Scanning Electron Microscopy (FE-SEM) with a ZEISS Gemini FE-SEM 500 apparatus.

Figures 76(a-b) confirm that the polyOAPS-imide surfaces are intact without any cracks a the corresponding scales. The polycondensation reaction thus results in dense layers

with no pores and defects. Figures 76(c-d) show the cross-sections of the polyOAPS-imide membranes with their three layers. The lowest layer is the α-alumina with sintered grains. The middle layer is the γ-alumina with a thickness of ~3.5 μm (c). γ-alumina has a uniform morphology, indicating that the sol-gel process was properly performed. The top layer is the polyOAPS-imide membrane and its thickness can be evaluated as being ~45 nm (d). Such low thicknesses along with intact surfaces confirm the high efficiency of the membrane preparation procedure via interfacial polymerization followed by imidization.

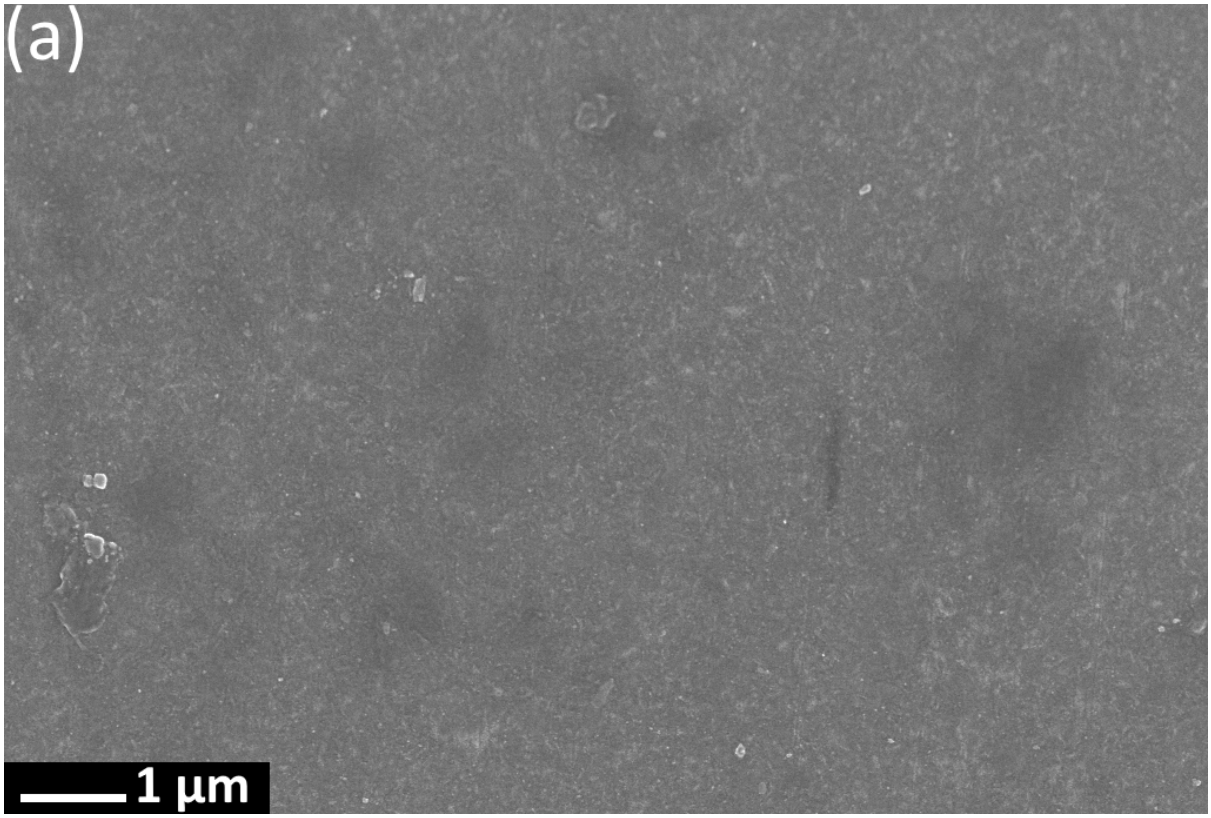

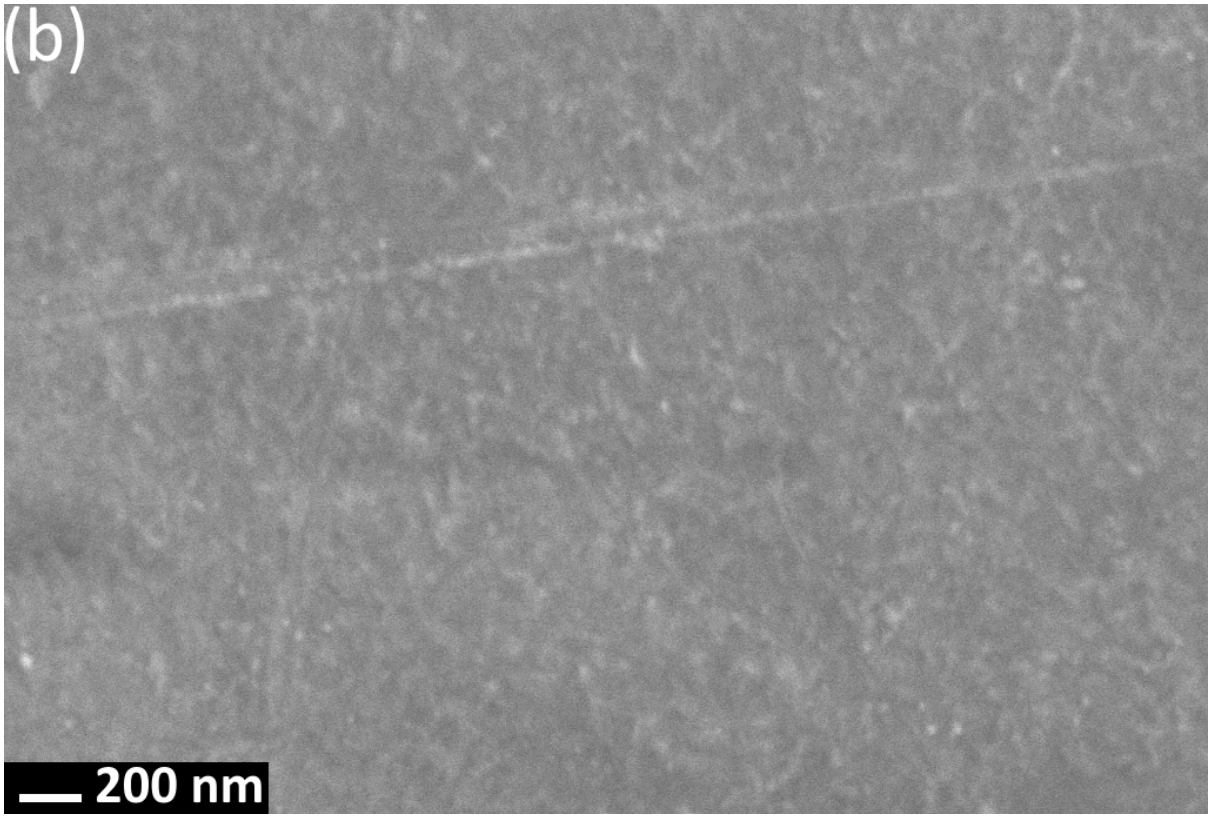
(b)
200 nm

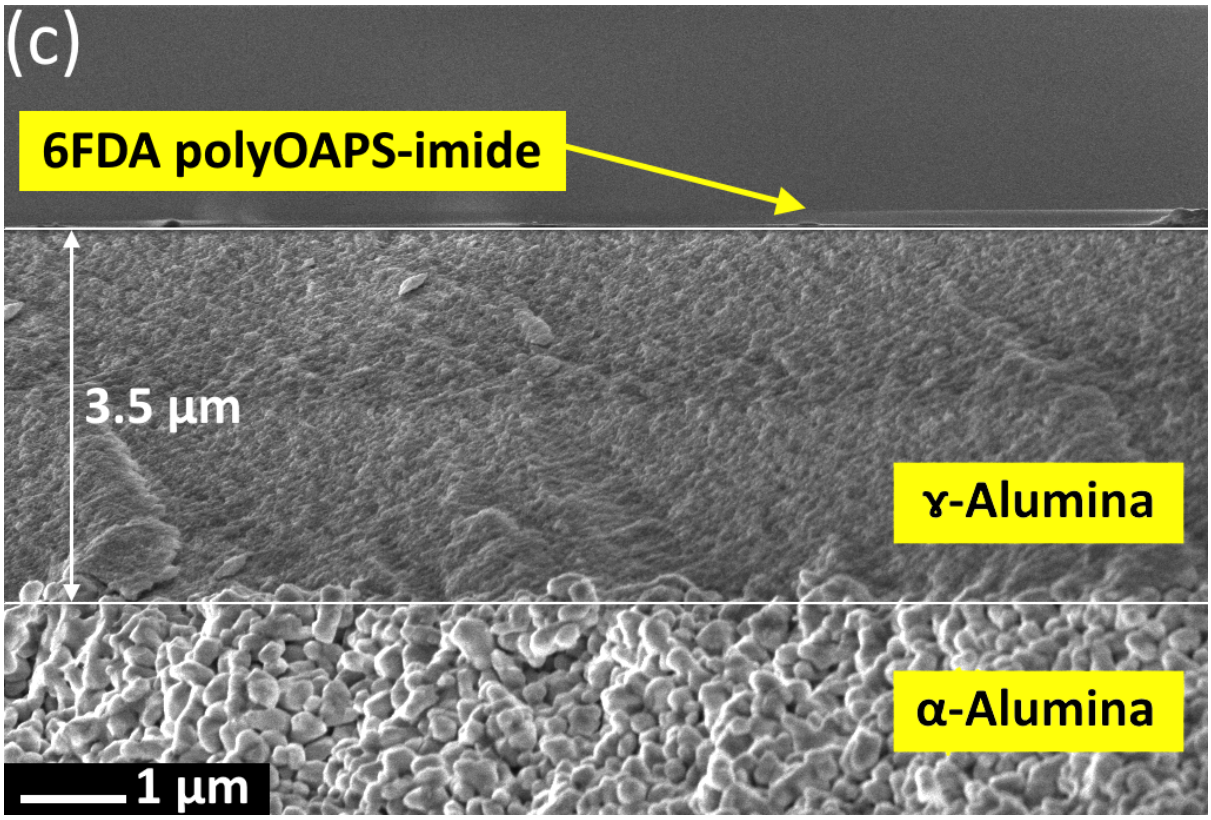
(c)
6FDA polyOAPS-imide
3.5 µm
ɣ-Alumina
α-Alumina
1 µm

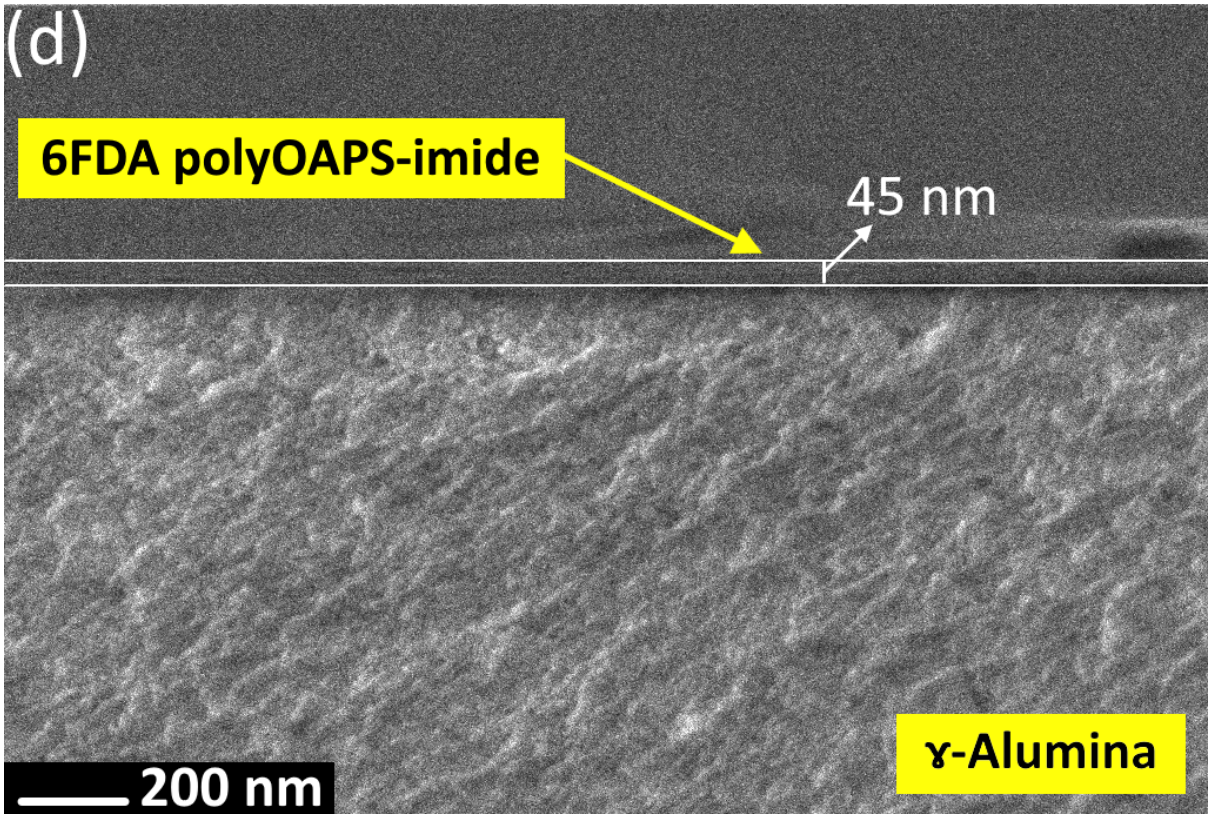

Figure 76. The surface (a and b) and cross-section (c and d) of a 6FDA polyOAPS-imide membrane at different scales.

FE-SEM can be combined with Energy Dispersive Spectroscopy (EDS) to probe the elements contained in the sample under study. Figure 77 displays the EDS spectrum of the same 6FDA polyOAPS-imide membrane characterized by FE-SEM in Figure 76. The presence of Si and N results from the OAPS inorganic precursor while F and C are related to the organic 6FDA links. O has the largest peak as it is present in the membrane and both two alumina layers. The Al peak also results from the alumina layers. There is a weak Na peak which probably corresponds to impurities.

The EDS spectrum thus confirms the presence of the appropriate atoms in the polyOAPS-imide membranes. However, it was not possible to extract an unambiguous quantitative assignment because of the small size of the C peak, which is probably related to technical problems.

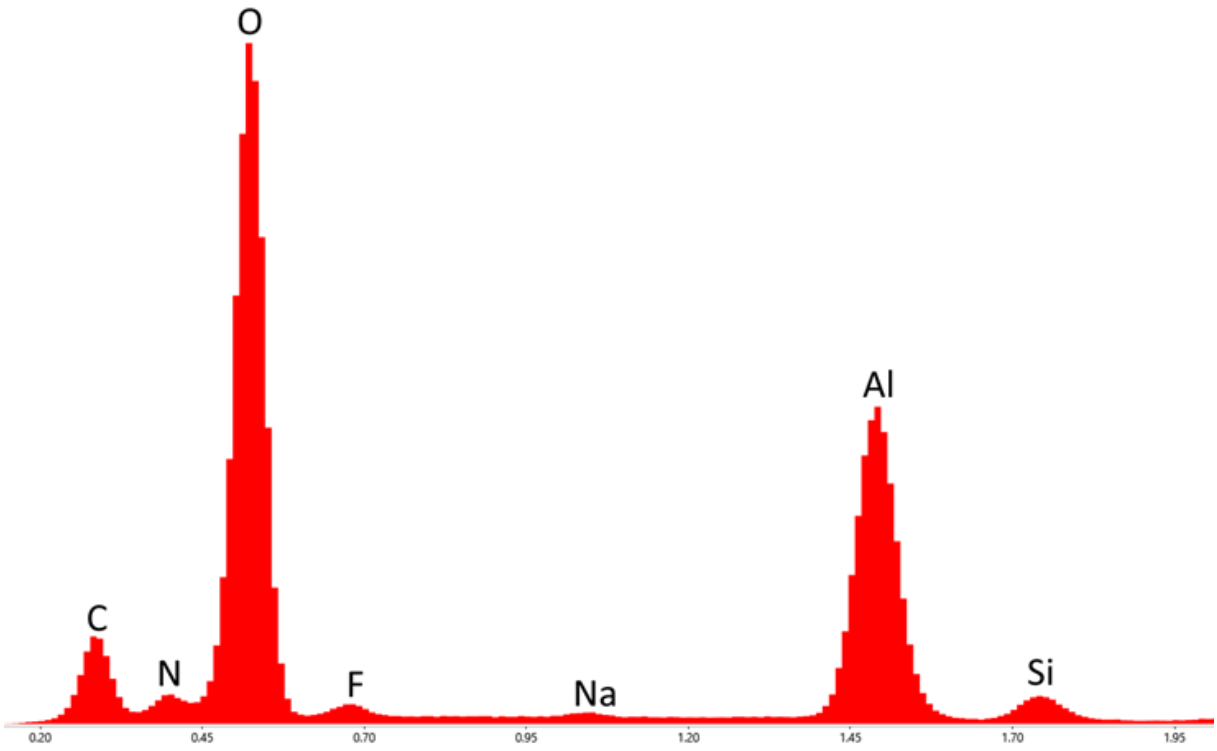

Figure 77. EDS spectrum of a 6FDA polyOAPS-imide membrane.

The morphology analyses confirm the intact structures of the polyOAPS-imide membranes, i.e. they are thin and can be selective. The intermediate γ-alumina layer forms a uniform structure, which preserves the hybrid membrane very well.

VI. Force-field development for OAPS

To investigate the molecular scale of polyOAPS-imide networks, the *gmq* program[217] was used by researchers at LEPMI, USMB, to carry out molecular modelling simulations of OAPS, imides and polyOAPS-imide networks.[208-209] *gmq* is principally designed for molecular dynamics (MD) simulations of dense materials with periodic boundary conditions in three dimensions.[217] This program has displayed its performance in numerous papers published in the literature previously.[30-31, 218-224]

Before generating the model networks, a specific force-field had to be developed for OAPS on its own. MD simulations are based on the forces applied to every atom, and the force-field describes the potential energy contribution of all other atoms. In *gmq*, a basic force-field includes bends, torsions, out-of-plane, van der Waals and electrostatic interactions as well as special -CH_3, -CH_2-, X-Y-H_2, -CH and linear triatomic constraints.[225] Each atom interacts with the others via either bonded or non-bonded potentials and the total potential energy U_{pot} is as in Equation 12.[10, 217]

$$U_{pot} = \sum U_{bonded} + \sum U_{non-bonded} \tag{12}$$

The bending, torsional and out-of-plane potentials contribute to the bonded potentials, *i.e.* those involving closely-connected atoms (Equation 13):

$$\sum U_{bonded} = \sum_{\theta} U_{bend}(\theta) + \sum_{\tau} U_{tors}(\tau) + \sum_{i-sp2} U_{oop}(i) \tag{13}$$

where θ, τ, and *i*-sp^2 are the bending angles, the dihedral angles, and i the atoms with sp^2 hybridization respectively (Figure 78).

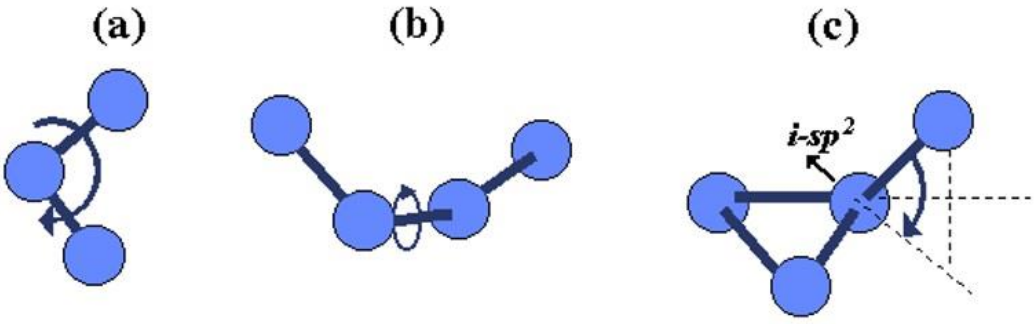

Figure 78. The bonding interactions: (a) bending, (b) torsion, and (c) out-of-plane

The bond distances b_0 are kept constant by rigid constraints in order to use a time step of 10^{-15} s and ensure equipartition of the energy (Equation 14):

$$\left|r_{ij}\right|^2 - b_0^2 = 0 \tag{14}$$

The bending potential keeps the bending angles θ defined by atoms *i*-*j*-*k* close to their equilibrium values (Equations 15 and 16):

$$U_{bend}(\theta) = \frac{1}{2} k_\theta (\cos\theta - \cos\theta_0)^2 \tag{15}$$

$$\cos\theta = \frac{(r_{ij} \bullet r_{kj})}{\left|r_{ij}\right|\left|r_{kj}\right|} \tag{16}$$

where k_θ is a constant indicating the flexibility of the angle and θ_0 is the equilibrium bending angle.

The torsional potential energy around the *j*-*k* bond in an (*i*, *j*, *k*, *l*) atom quadruplet is described as in Equations 17 and 18:

$$U_{tors}(\tau) = \sum_{n=0}^{6} a_n \cos^n \tau \tag{17}$$

$$\cos\tau = \frac{(r_{ij} \times r_{jk}) \bullet (r_{jk} \times r_{kl})}{\left|r_{ij} \times r_{jk}\right| \bullet \left|r_{jk} \times r_{kl}\right|} \tag{18}$$

where the a_n are the coefficients of a polynomial of order *n*. For this term, two different possibilities may occur. If the atoms separated by more than three bonds are defined as being non-bonded, Equation 17 represents the entire torsional energy. But if the atoms separated by more than two bonds are defined as being non-bonded, a part of torsional energy is described by Equation 17 while the non-bonded interactions between the end atoms of the torsion quadruplet, *i* and *l*, form the rest.

The out-of-plane potential is used to restrict the movement of a central trivalent atom *i* connected directly to three atoms *j*, *k* and *l* on a plane (Equation 19):

$$U_{oop}(i) = \frac{1}{2} k_{oop} s^2 \tag{19}$$

where s is the perpendicular distance of atom i from the plane of atoms j, k, and l, and k_{oop} is the force constant. s can be calculated through Equation 20:

$$s = r_{ji} \bullet \frac{(r_{jk} \times r_{jl})}{\left| r_{jk} \times r_{jl} \right|} \tag{20}$$

The non-bonded potentials include the Van der Waals interactions and the electrostatic interactions resulting from the charges on the atoms (Equation 21):

$$\sum U_{non-bonded} = \sum_{(i,j)nb} U_{vdw}(r) + \sum_{(i,j)nb} U_{coul}(r) \tag{21}$$

Different forms of Van der Waals (*vdw*) potentials are available in *gmq*, but the Lennard-Jones (LJ) 12-6 potential is mostly used (Equation 22):

$$U_{LJ}(\left| r_{ij} \right|) = 4\varepsilon \left(\left(\frac{\sigma}{r_{ij}} \right)^{12} - \left(\frac{\sigma}{r_{ij}} \right)^{6} \right) \tag{22}$$

where ε is the well depth of the LJ potential and σ is the distance at which the potential is zero. The $(1/r_{ij})^{12}$ term describes the Pauli repulsions at short distances while $(1/r_{ij})^{6}$ accounting for the attractions between the atoms at longer distances.

For unlike-atom pairs, the cross-terms are calculated via standard combination rules[226-228] (Equations 23 and 24):

$$\sigma_{(i,j)} = \frac{\sigma_{(i,i)} + \sigma_{(j,j)}}{2} \tag{23}$$

$$\varepsilon_{(i,j)} = \sqrt{(\varepsilon_{(i,i)} \times \varepsilon_{(j,j)})} \tag{24}$$

The electrostatic interactions between charged particles are described by the Coulombic potential (Equation 25):

$$U_{coul}\left(\left|r_{ij}\right|\right)=\frac{q_i q_j}{\left(4\pi\varepsilon_0\left|r_{ij}\right|\right)} \quad (25)$$

where q_i and q_j represent the partial charges on the atoms and ε_0 is the vacuum permittivity. The Ewald summation approach is used to calculate electrostatic interactions in periodic systems.[229]

The Hyperchem program[203] was used to build the primary OAPS molecular structures. The output of Hyperchem is a **.ent* file containing the coordinates and the connectivities of the atoms. In each *ent* file, the atom names were replaced with the atom-type numbers defined for *gmq*. Table 33 shows the atom labels and atom-types needed to describe OAPS. The atom-types that are not given have been used elsewhere for MD simulations of aliphatic-based polyPOSS-imides.[26, 30-31] Since OAPS had not been modelled in the former works, some specific atom-types (32 for Car3 and 33 for Hcar3) were added.

Table 33. Atom labels and atom types used for modelling OAPS with *gmq*

Atom label	Atom type	Description
Si	1	Silicon in cage
O	2	Oxygen in cage
Npri	4	The nitrogen of the primary amine
Hnpri	24	The hydrogen of the primary amine
Car3	32	Aromatic carbon of the aminophenyl ring
Hcar3	33	The hydrogen of the aminophenyl ring

To obtain accurate force-field parameters, i.e. the equilibrium bond distances, the equilibrium bending angles, the partial charges as well as the optimized coordinates for OAPS starting structures, the **.ent* files were converted to input files to carry out DFT optimizations with Gaussian at the B3LYP/6-31G(d,p) level of theory. As mentioned before, this basis set is a good compromise between time and accurate energy minimisation.[149] The VMD software[230] was used for the visualization of the atomic structures. Figure 79 shows optimized *meta*-OAPS, *ortho*-OAPS and *para*-OAPS molecular structures.

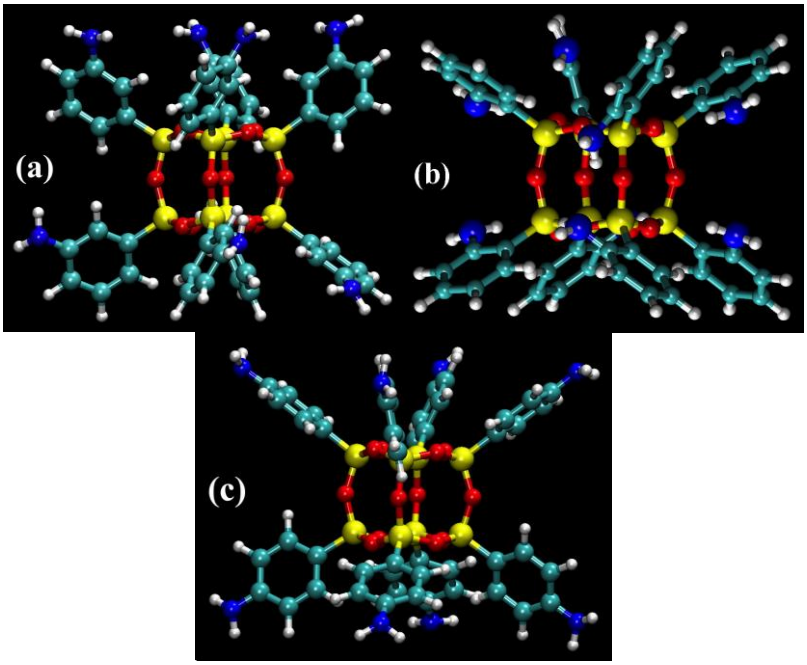

Figure 79. Optimized structures for the (a) *meta*, (b) *ortho*, and (c) *para* isomers of OAPS shown with VMD.[230]

The optimized partial charges (Equation 25) for each separate OAPS isomer extracted from the Gaussian outputs are given in Figure 80. The sum of the charges must be equal to zero for each structure.

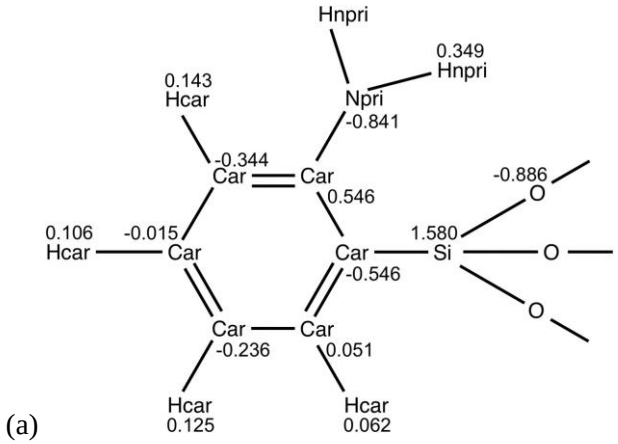

(a)

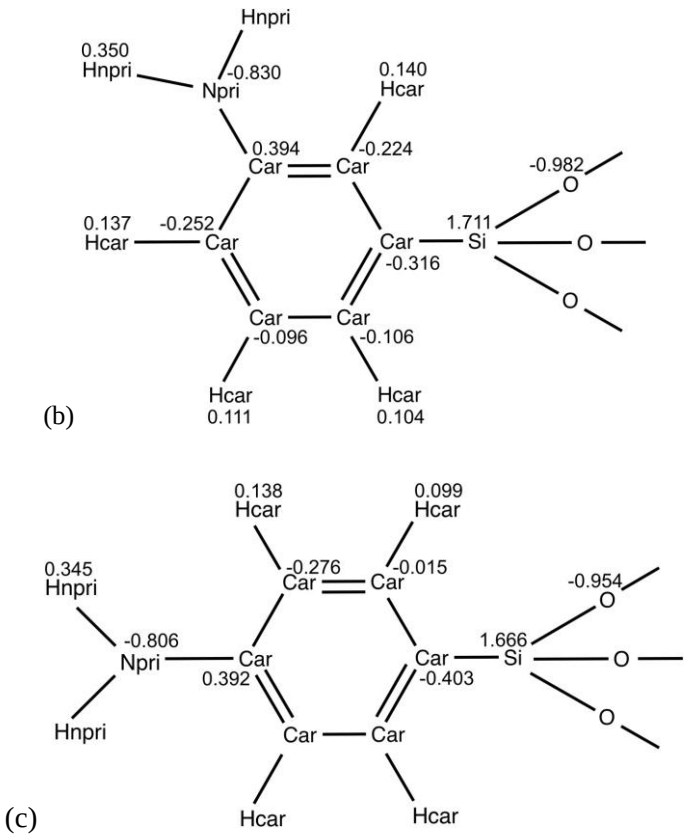

Figure 80. Individual charge distributions in the (a) *ortho*, (b) *meta*, and (c) *para* isomers of OAPS

In Figure 80, the charges of each isomer were calculated individually due to the different charge distributions. But to be able to simulate both individual isomers and mixtures of *ortho*, *meta*, and *para* isomers, it is crucial to have the same charges on the cage Si and O atoms. So after averaging the charges of Si and O, the other charges were adapted again to ensure total charge neutrality. The resulting final charge distributions are given in Figure 81.

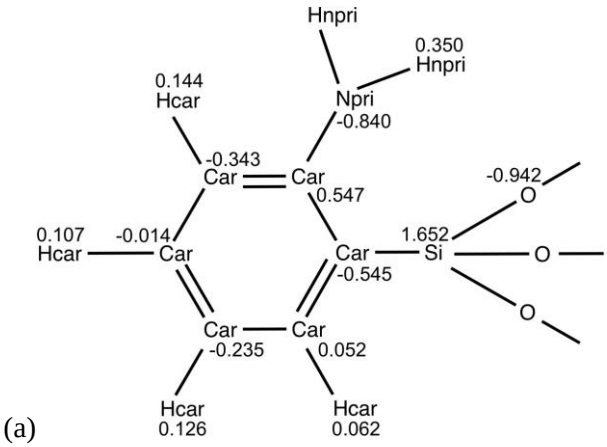

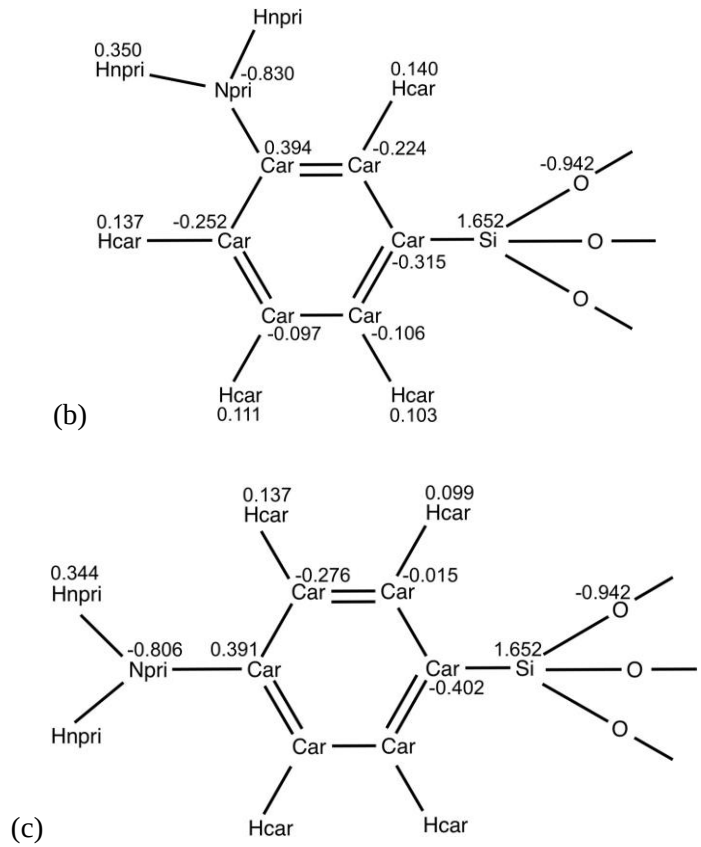

Figure 81. Final charge distributions in the (a) *ortho*, (b) *meta*, and (c) *para* isomers of OAPS

The equilibrium bond lengths (Equation 14) and bending angles (Equation 15) are other parameters, which can be extracted from the Gaussian-optimized structures over all three isomers. Table 34 shows the equilibrium bond lengths for OAPS.

Table 34. Bond types in OAPS and their equilibrium lengths

Bond type	b_0 / Å
Si-O	1.65
Si-Car	1.85
Car-Car	1.40
Car-Hcar	1.08
Car-Npri	1.39
Npri-Hnpri	1.01

The equilibrium bending angles extracted from Gaussian and their respective constants k_θ adapted from the TRIPOS force-field are given in Table 35.[231-234] Table 36 indicates the dihedral types with the coefficients of the polynomial a_0, a_1, a_2 and a_3 (Equation

17). Table 37 shows the out-of-plane parameters (Equation 19) and Table 38 the van der Waals parameters (Equation 22). All parameters that were not extracted from the optimized Gaussian outputs were adapted from the literature.[231]

Table 35. Bond-angle types in OAPS, equilibrium angles and their constants

Bond-angle type	θ_0 / deg	k_θ / kJ mol^{-1}
O-Si-O	109.0	-
Si-O-Si	148.8	-
O-Si-Car	109.9	477.8
Si-Car-Car	120.9	879.1
Car-Car-Car	120.0	879.1
Car-Car-Hcar	120.1	879.1
Car-Car-Npri	120.6	1465.1
Car-Npri-Hnpri	115.4	constrained
Hnpri-Npri-Hnpri	112.2	constrained

Table 36. Dihedral types in OAPS and their polynomial constants

Dihedral type	a_0 / kJ mol^{-1}	a_1 / kJ mol^{-1}	a_2 / kJ mol^{-1}	a_3 / kJ mol^{-1}
-Si-Car-	-0.135	0	0	0.480 (a_6 used instead of a_3)
-Car-Npri-	11.380	0	-11.380	0
-Car-Car-	16.736	0	-16.736	0

Table 37. Out-of-plane types in OAPS and their force constants

Out-of-plane atom	k_{oop} / kg.s^{-2}
Car-Si-Car-Car	667
Car-Car-Car-Hcar	667
Car-Npri-Car-Car	667

Table 38. Non-bonded atom pairs in OAPS and Van der Waals parameters

Like-atom pair i...i	σ_{ii} / Å	ε_{ii}/k_B / K
Si...Si	3.385	294.38
O...O	2.955	102.15
Npri...Npri	2.762	47.81
Car...Car	3.029	53.84
Hnpri...Hnpri	2.673	21.14
Hcar...Hcar	2.673	21.14

This force-field was used by the molecular modelling team at LEPMI, USMB, to carry out separate MD simulations of the three OAPS isomers in the bulk state at room temperature. These OAPS simulation boxes were combined with different dianhydride-containing boxes (6FDA, PMDA and ODPA) in order to create model networks for a large number of different polyOAPS-imide hyper-cross-linked networks both at room and at high temperatures.[208-209]

VII. Conclusions

The gas separation process by dense polymer-based membranes is a promising alternative to the cryogenic distillation or adsorption separation processes due to its much lower energy costs. But this is difficult under harsh conditions since most polymers tend to lose their structural integrity at high temperatures. Hybrid ultrathin membranes based on inorganic POSS cross-linked with organic imides are able to improve the thermomechanical resistance while preserving the gas separation properties. These can perform under tougher operating conditions than conventional polymers, but the aliphatic arms of the POSS precursors have been shown to be prone to thermal degradation above 300°C.

This work aims to attain more thermally-stable hybrid membranes based on a related inorganic siloxane-based cage, octa(aminophenyl)silsesquioxane (OAPS), which replaces the aliphatic arm of the initial POSS with a phenyl arm. The difficulty with using OAPS is that it has three different isomers depending on the *meta*, *ortho*, and *para* position of the amine group with respect to the phenyl group. An extensive literature search showed that the isomer ratios were not clearly defined and that several synthesis routes gave different results. This is problematic as molecular modelling suggests that the nature of the isomer will strongly affect the resistance and selectivities of the resulting membranes.

Experimental characterizations were carried out both for a commercial OAPS containing all three isomers and for a controlled OAPS containing only the *para* and *meta* isomers. This included picnometry, which showed that the densities of the commercial and controlled OAPS samples were close, i.e. respectively 1.39 g/cm^3 and 1.37 g/cm^3. IR, as well as ^{29}Si, ^{13}C and ^{1}H-NMR spectra, were also obtained for both types of OAPS. To better identify the isomers, the experimental results were compared to predictions of the IR and NMR spectra by quantum mechanical methods such as DFT with Gaussian and by machine-learning methods such as MestreNova.

IR predictions allowed for the identification of the various modes of vibrations and assigned some of the experimental peaks to specific isomers. The 1-D and 2-D NMR predictions were more difficult to carry out as the results were found to be highly dependent on the method and the level of theory used. Despite not being able to reproduce the experimental ^{29}Si-NMR shifts to a fully satisfactory level, the Gaussian-predicted shifts at the HCTH407/6-311+(2d,p) level of theory were consistent with the experimental ^{13}C-NMR and

^{1}H-NMR shifts. MestreNova was also tested for the prediction of the ^{1}H-NMR shifts but did not give accurate results when compared with the 2-D HSQC OAPS experimental spectra. On the other hand, the Gaussian-predicted shifts were found to be well compatible with the contour clouds of the 2-D NMR spectra for both the commercial OAPS (3 isomers) and the controlled OAPS (2 isomers). Within this context, quantum mechanical methods are clearly superior to machine-learning methods, despite being computationally much more expensive. As a result, each peak in the ^{13}C-NMR and ^{1}H-NMR OAPS spectra could be assigned to a specific isomer using the Gaussian predictions.

OAPS was then used as the inorganic precursor along with the organic 6FDA dianhydride to make new hybrid membranes with increased thermoresistance. The fabrication procedure was similar to that developed for the initial polyPOSS-imides, i.e. it combined interfacial polycondensation with imidization. The IR analyses assessed the extent of imidization and the TGA analyses proved that the new polyOAPS-imide membranes could preserve their structures up to 400°C. FE-SEM showed that these membranes had intact surfaces and thicknesses of ~45 nm, while the thickness of the intermediate γ-alumina was ~3.5 μm. Additional EDS analyses confirmed the presence of the appropriate elements. The new polyOAPS-imide membranes were found to preserve gas selectivities of ~10 for H_2/CH_4 and H_2/N_2 at 250°C while the selectivities increased as a function of temperature for He/CO_2 and H_2/CO_2. The apparatus could only test the permeation characteristics of the new membranes up to 250°C, but since the new membranes preserve their structure up to 400°C, it is likely that the permeation trends are valid at higher temperatures.

In parallel, a force-field was developed to carry out molecular dynamics simulations of the three OAPS isomers in order to characterize their differences at the atomic level. Different force-field parameters such as partial charges, bond length, and bond angles were extracted from the DFT calculations. They were used in another work to create model polyOAPS-imides in order to complement the experimental characterizations.

PolyOAPS-imide membranes thus appear as promising materials for gas separation under harsh conditions. The IR and NMR spectra for OAPS can help identify which isomers are present in the inorganic precursor. However, the membrane fabrication procedure such as the reaction time and the thermal treatment should be tested to a better extent in order to ensure reproducibility.

VIII. Annexes and References:

Annexe 1

How to extract IR results from Gaussian

This tutorial describes how to get the IR data from Gaussian for an optimized structure. *metaOAPS-IR* is used here as an example.

1. An input file of the optimized structure should be fed to Gaussian with the following IR (frequency) command: *freq b3lyp/6-31G(d,p)*

The geometry optimization and IR commands can be carried out in one single run using:
opt freq b3lyp/6-31G(d,p)

The level of theory for both the optimization and frequency calculations must be the same and the basis sets (here *b3lyp/6-31G(d,p)*) can be chosen based on the accuracy needed. The Gaussian output is a file called *metaOAPS-IR.log.*

2. Avogadro is a freely-available software very useful to analyze the IR frequencies calculated by Gaussian. It works as described below:

* First open Avogadro

* Open the *log* file by clicking on the *metaOAPS-IR.log* file.

* A table on the right side shows the frequencies and the absolute intensities. Click on "*Show Spectra…*". This displays the IR spectrum with the same wavenumbers as the Gaussian *log* file but with normalized intensities. Avogadro sets the highest intensity peak (here, 1137.48 cm^{-1}) to 100 and renormalizes the other intensities.

* "Animation" under the right table allows the user to identify the vibrations corresponding to each wavenumber. Close the "Spectra visualization" and click on one of the wavenumbers in the right table, then click on "Start Animation" to observe the type of vibration corresponding to the selected wavenumber.

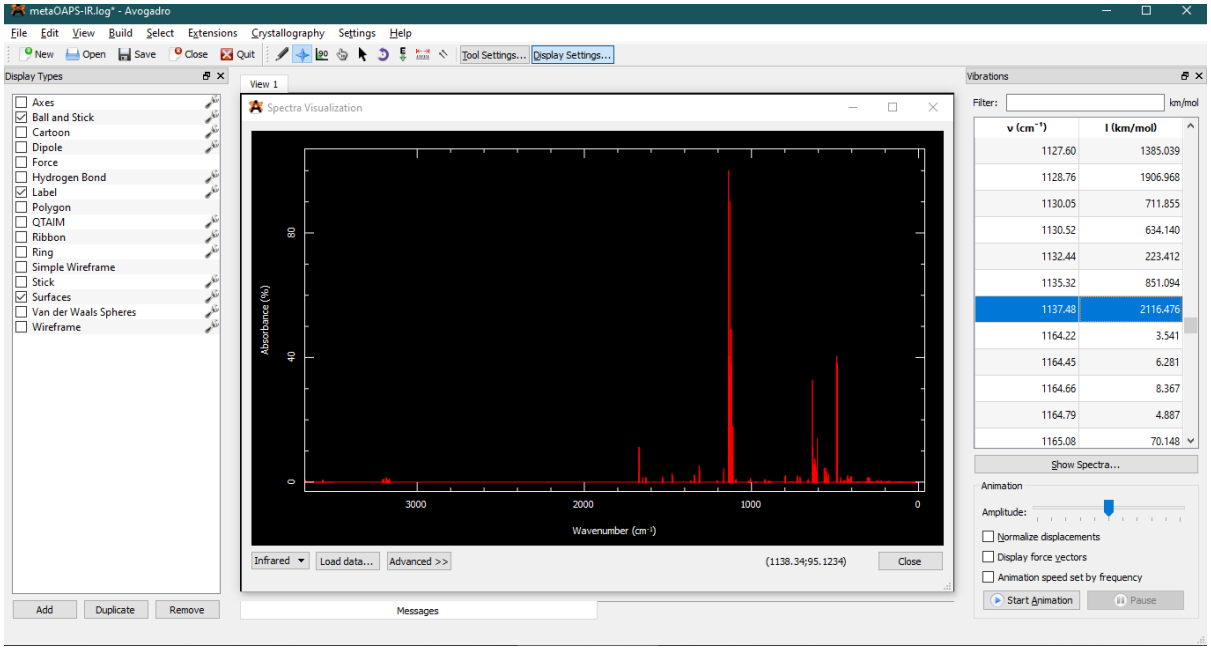

* Click on “Show Spectra…” then on “Advanced” to see the possible functions. In the “Appearance” tab, the background and spectra colour can be changed. The spectra can be exported with the desired size using the “Export image” tab. The width of the peaks is adjustable with the “Gaussian width” in the “Infrared Spectra Setting” tab. A *.tsv* version of the data can be exported with “Export data” to plot them with Excel.

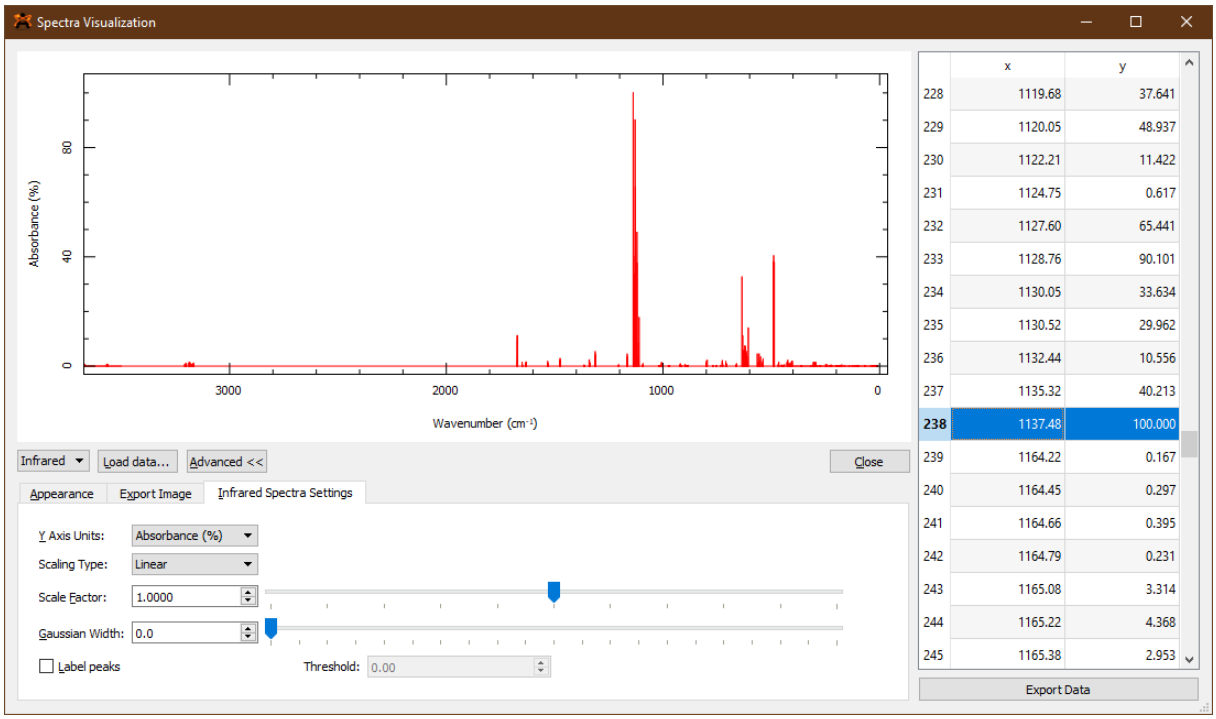

3. An alternative way to extract the frequencies and their intensities is to open the Gaussian *log* file using text editors. Open *metaOAPS-IR.log* and search “Frequencies” and “IR Inten”, which indicate the wavenumber and their corresponding intensities, respectively. It should be noted that the intensity is not normalized with respect to the highest one as in Avogadro.

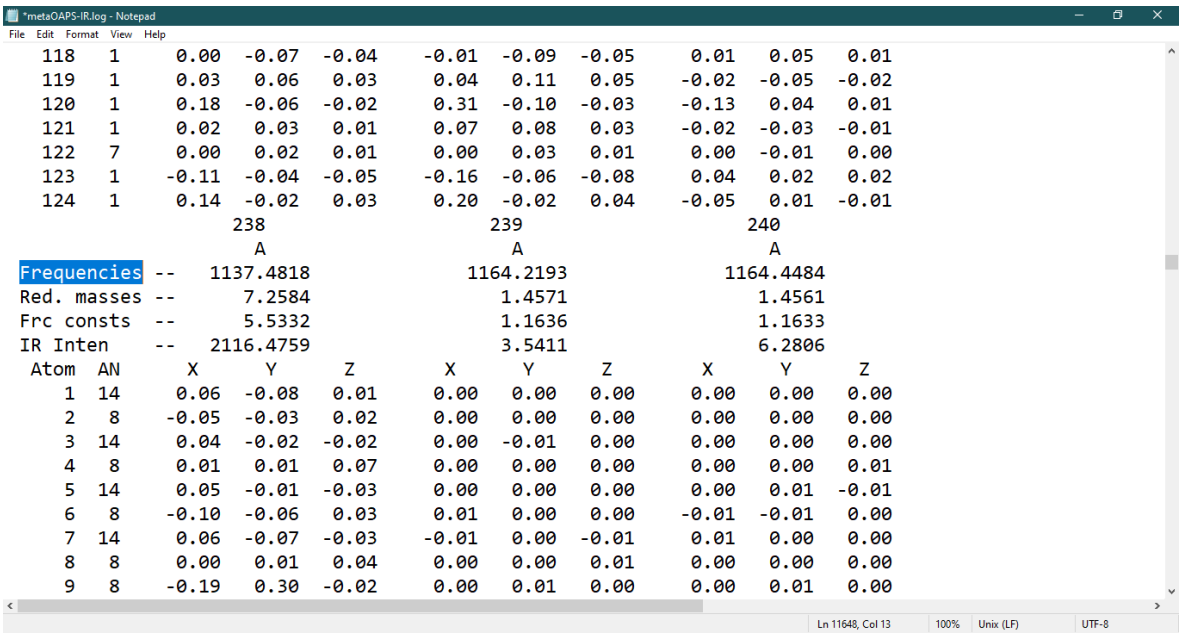

* The frequencies and their corresponding absolute intensities can then be found one by one by continuing to search for “Frequencies”.

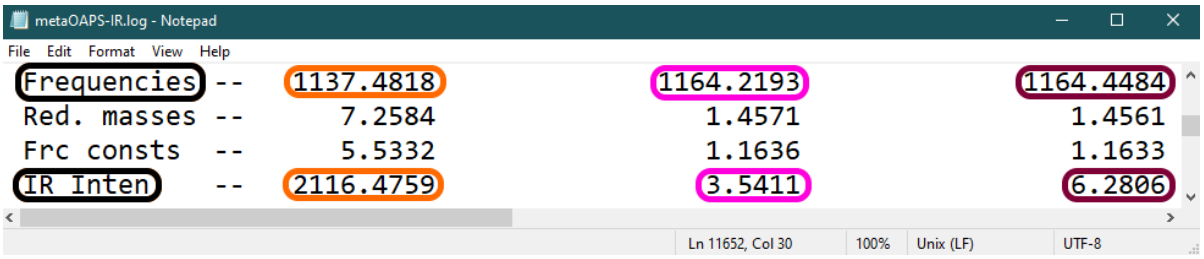

Annexe 2

How to extract NMR shifts from Gaussian

This tutorial first describes how to get the Gaussian NMR data for the TMS (trimethylsilane) reference, and then for an arbitrary structure such as *meta*-ONPS.

1. An input file of the optimized TMS is fed to Gaussian using the following command:

nmr=(giao) B3LYP/6-31G(d,p) scrf=(solvent=dmso)

The geometry optimization and NMR commands can also be carried out in one single run:
Write at the start of the file: *B3LYP/6-31G(d,p) Opt Density=Current Pop=MK,*
then: *the atomic coordinates*
at the end: *nmr=(giao) B3LYP/6-31G(d,p) scrf=(solvent=dmso)*

The basis set (here, *B3LYP/6-31G(d,p)*) can be chosen depending on the accuracy needed. The Gaussian output is a file called *TMS.log*

2. Avogadro is a freely-available software very useful to analyze the NMR shifts calculated by Gaussian. It works as described below:

* First open Avogadro

* Open the *log* file by clicking on the *TMS.log* file

* Make sure that the options such as "Tool settings…" and "Display settings…" are activated in the top bar. Then their menus can appear in the window.

* If the atom numbers do not appear on the atoms, click on the  icon in the “Label“ row. A small window appears, as in the following Figure.

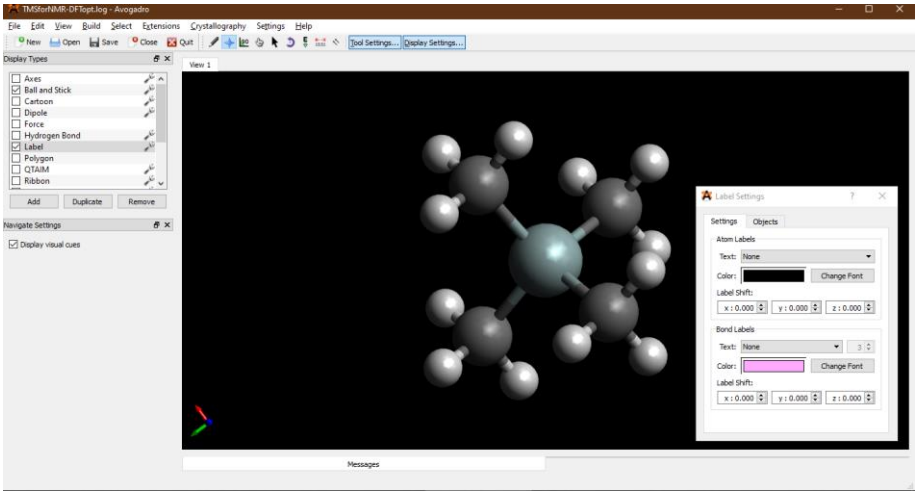

* The “Atom number” can be selected from the “Text” menu:

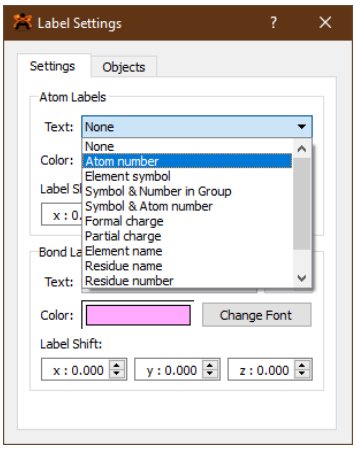

* Click on the "Extensions" menu and "Spectra" to get the chemical shielding values in ppm.

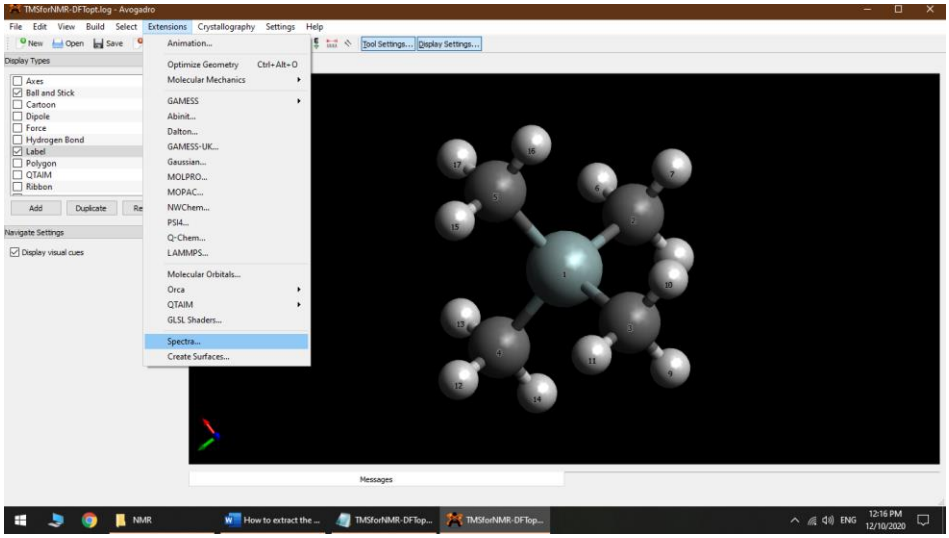

* A new window opens. Click on “Advanced” and “NMR spectra settings” respectively. Since TMS itself is the reference, make sure that the values of “Reference” and “Gaussian width” are zero. As can be seen below, the default “Nucleus” is Si and its chemical shielding is given

on the right side, i.e. 412.39 ppm. This is the reference for ^{29}Si-NMR at the B3LYP/6-31G(d,p) level of theory. It is also possible to see the shielding value on the red peak by checking the box “Label Peaks”, which is on the same row as “Nucleus”.

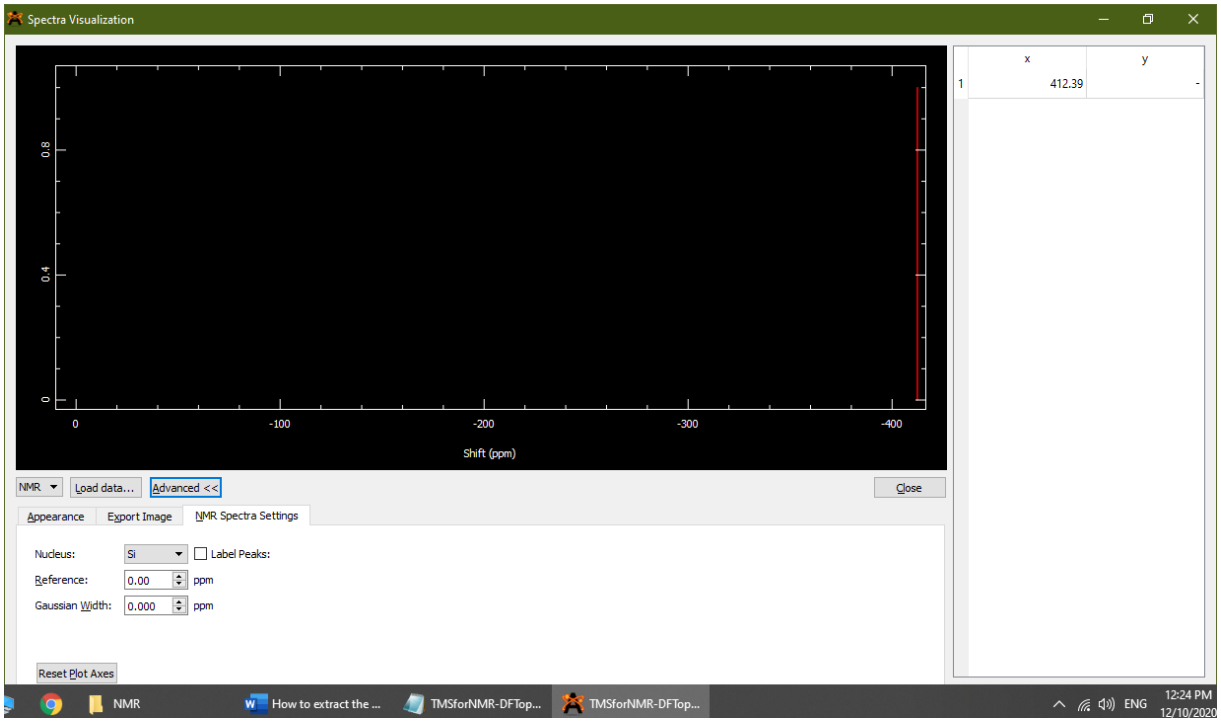

* By changing the “Nucleus” value to C, the chemical shielding values of the TMS carbons will appear on the right side. It is possible to zoom in on the peaks by using the mouse. Since in a single-point structure, the charge distribution and bond lengths can be slightly different (even for atoms with the same chemical environments), the chemical shielding values for the same atoms must be averaged. The average of the four values that appear in the Figure is 192.29 ppm and it can be used as the reference for ^{13}C-NMR at the B3LYP/6-31G(d,p) level of theory.

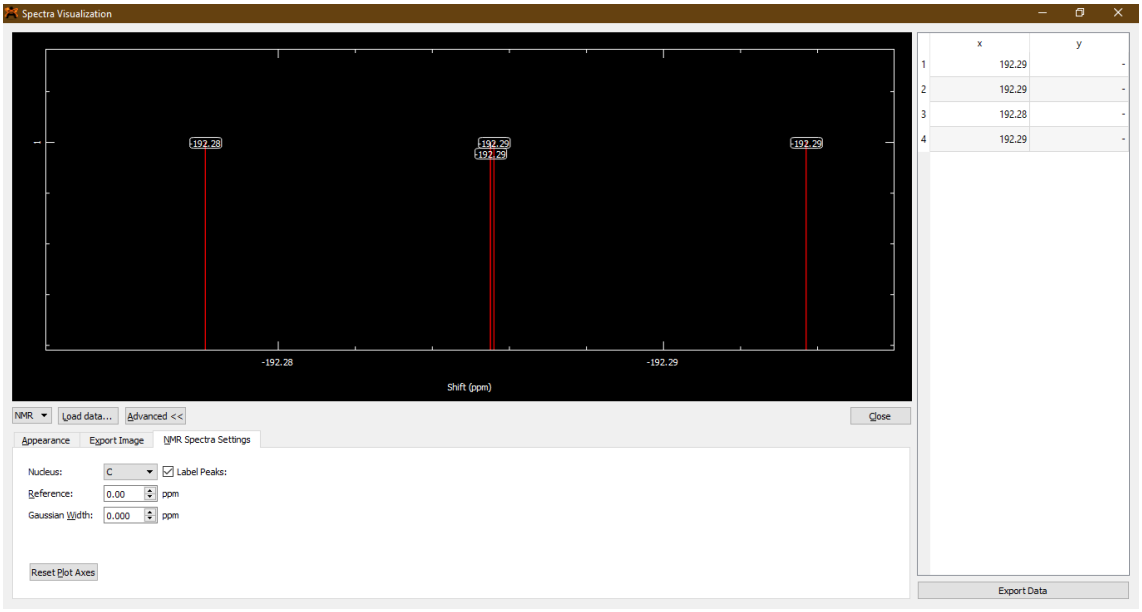

* All hydrogens in TMS have the same chemical environments and their average chemical shielding is 31.72 ppm. It is necessary to mention that the numbers in the table on the right side are not the atom numbers but the order of the hydrogens' chemical shieldings based on the atom numbers. For example, number 1 shows the chemical shielding for the hydrogen with the lowest atom number, which is the hydrogen with atom number 6. Number 6 shows the chemical shielding for the hydrogen with the sixth-highest atom number, which is the hydrogen with atom number 10. It is possible to find the order of the atoms by using either Avogadro or the input structure.

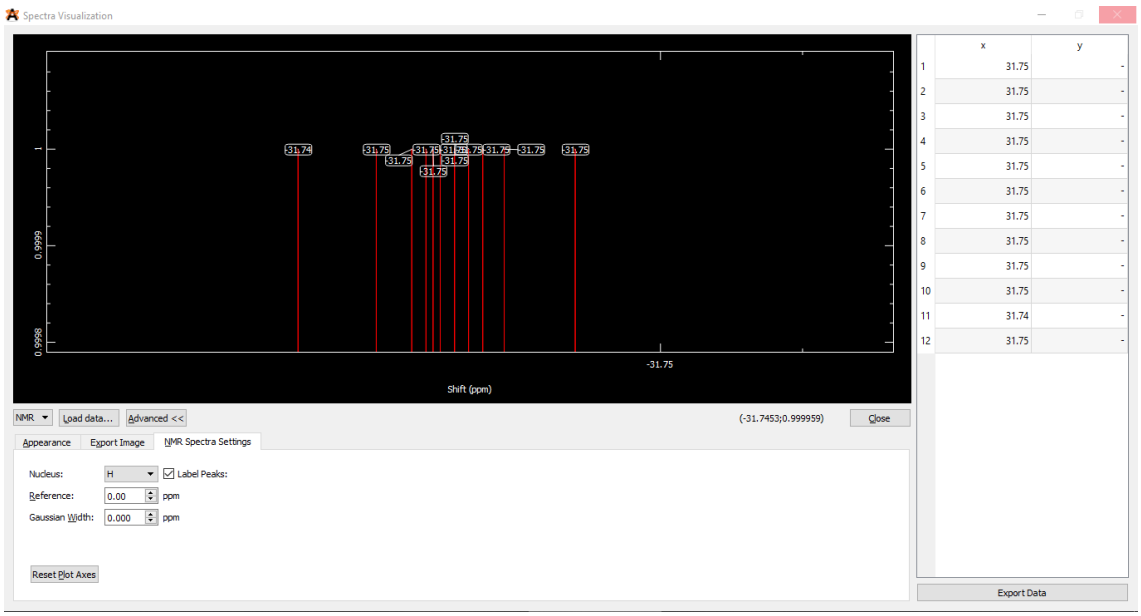

3. An alternative way to extract the chemical shielding is to open the log files using text editors. Open the TMS log file and search "Isotropic", as indicated in the Figure below:

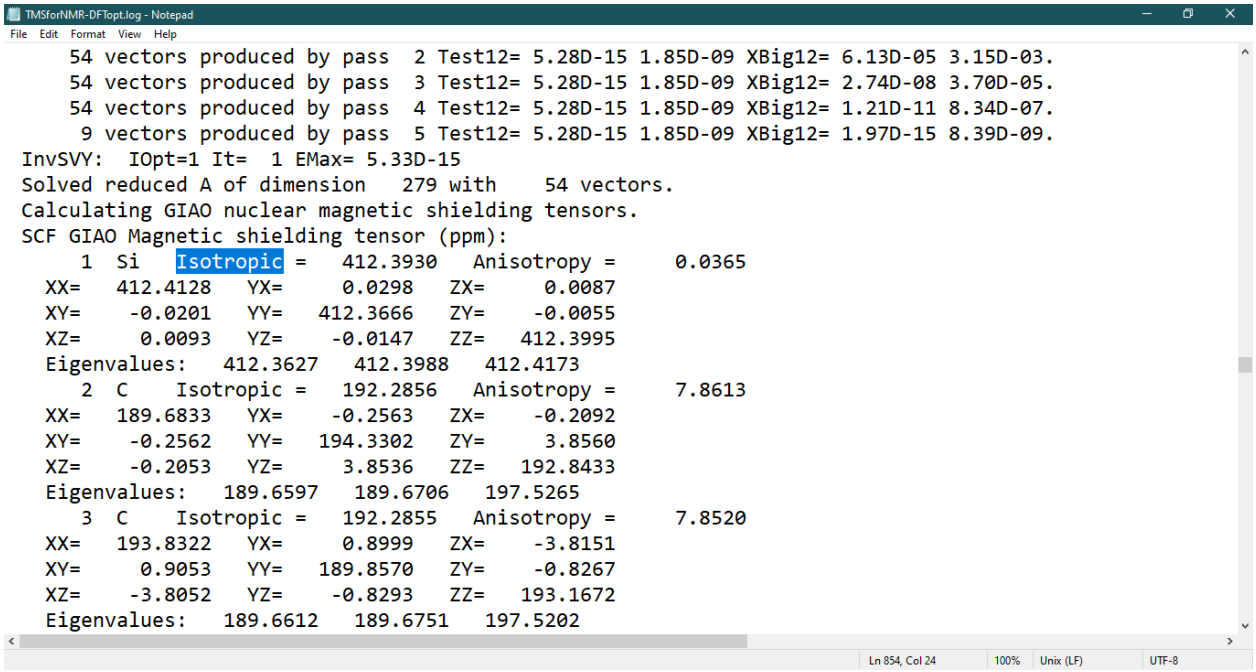

The value for atom number 1, 412.3930 ppm, is the chemical shielding for the Si atom in TMS at the B3LYP/6-31G(d,p) level of theory. The atom numbers 2, 3, 4, and 5 give the chemical shielding values for the four carbons of TMS and should be averaged to calculate the chemical shielding for C in TMS. In that example, the reference chemical shielding values for Si, C, and H were 412.39 ppm, 192.29 ppm, and 31.72 ppm respectively.

After extracting the chemical shielding values for Si, C, and H, the chemical shifts can be obtained from:

$$\delta = \sigma_{iso} - \sigma$$

where δ is the chemical shift, σ is the chemical shielding value of the target, and σ_{iso} is the isotropic value or chemical shielding for the standard reference used in the NMR.

4. The level of theory for both the reference (TMS) and the structure under study must be the same. For example, if the structure is studied with the HF/6-31G* level of theory, the same level (HF/6-31G*) must be applied for TMS.

5. To calculate the chemical shifts of a non-reference structure such as *meta*-ONPS:
   - Open *meta*-ONPS.log with Avogadro and display the atom numbers using "Label" and  Then, click on "Extensions"/"Spectra".
   - Click on "Advanced", then NMR Spectra Settings.
   - Select Si as the nucleus.

- **Now type 412.39 in the Reference box. This is the reference obtained from TMS.**
- Upon typing the reference, the chemical shifts appear in the graphical window. The table on the right still shows the chemical shielding values (ex: 473.79 ppm), while the plot displays the corresponding chemical shifts (-60.4 ppm), i.e. the difference in shielding values between the sample and reference atoms (see Equation above). It would be preferable if Avogadro could display directly the chemical shifts in the table, but this is not the case right now.
- By zooming in on the spectrum, it is possible to see the exact values of the chemical shifts.
- Since all the Si atoms have the same chemical environment in *meta*-ONPS, the average ^{29}Si-NMR chemical shifts for the eight Si with the level of theory understudy is -60.77 ppm.

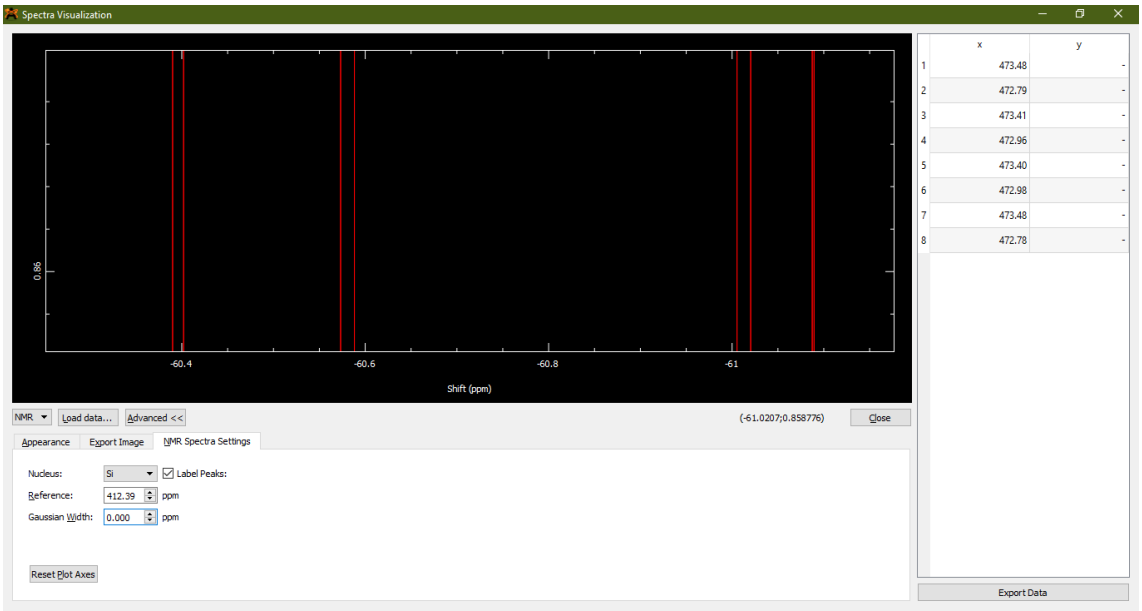

- In order to observe the chemical shifts for Carbon, the Nucleus should be changed to C and the reference shielding for C, i.e. 192.29 ppm, should be inserted into the Reference box.

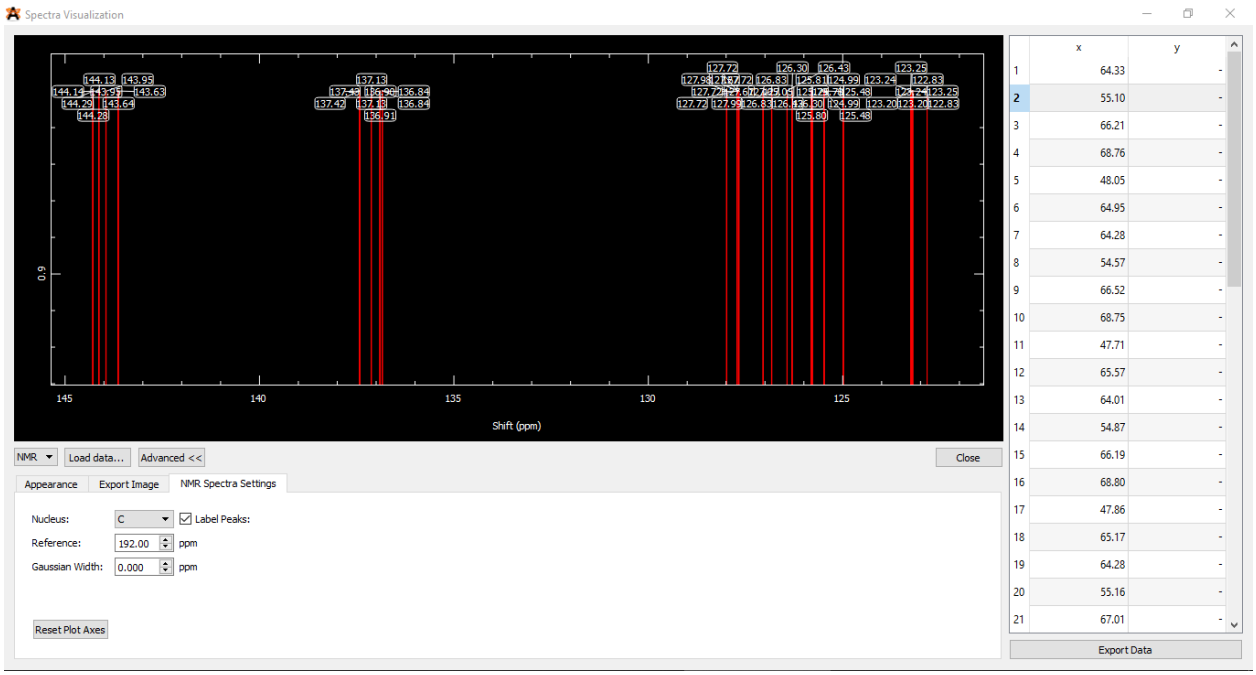

As can be seen, the shifts are very close to each other and the table on the right side does not include the atom numbers. It is possible to see better by zooming on the spectrum.

6. An alternative is to study the Gaussian *log* file directly along with the structure opened by Avogadro, which provides the atom numbers:

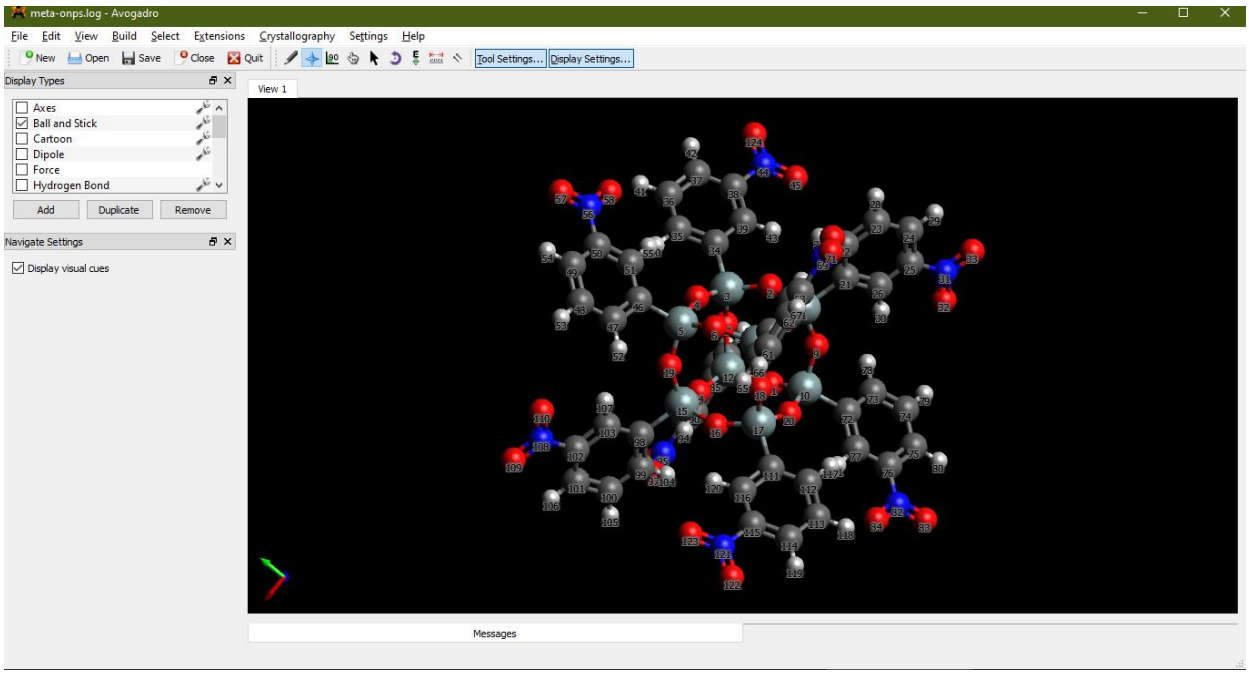

or by using directly a drawn Figure:

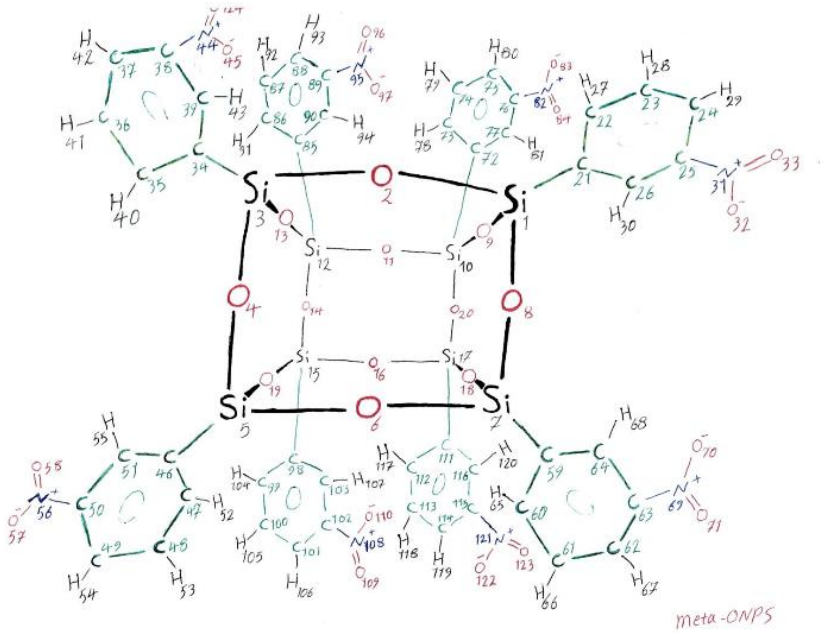

For example, there are eight carbons connected to the Si atoms, all of which have the same chemical environment. Their atom numbers are: 21, 34, 46, 59, 72, 85, 98 and 111. It is then possible to find their corresponding chemical shielding values in the Gaussian *log* file:

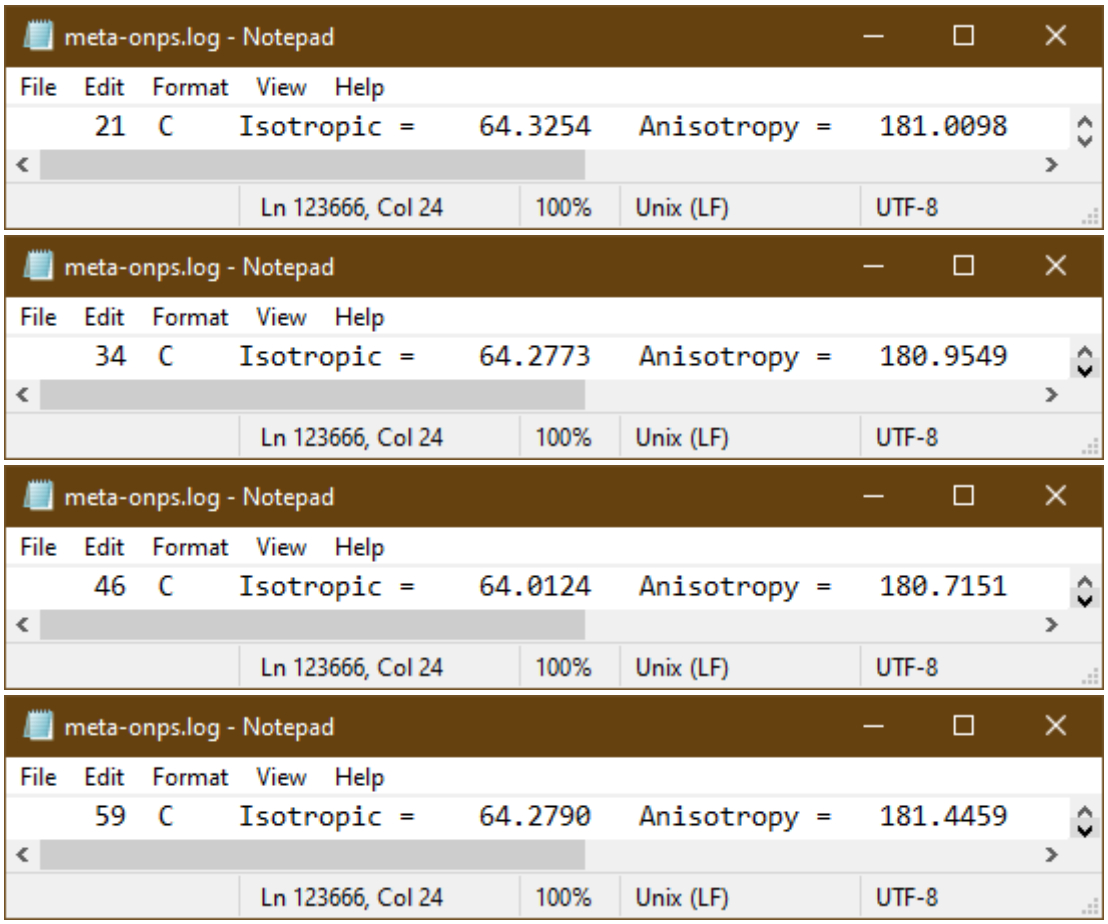

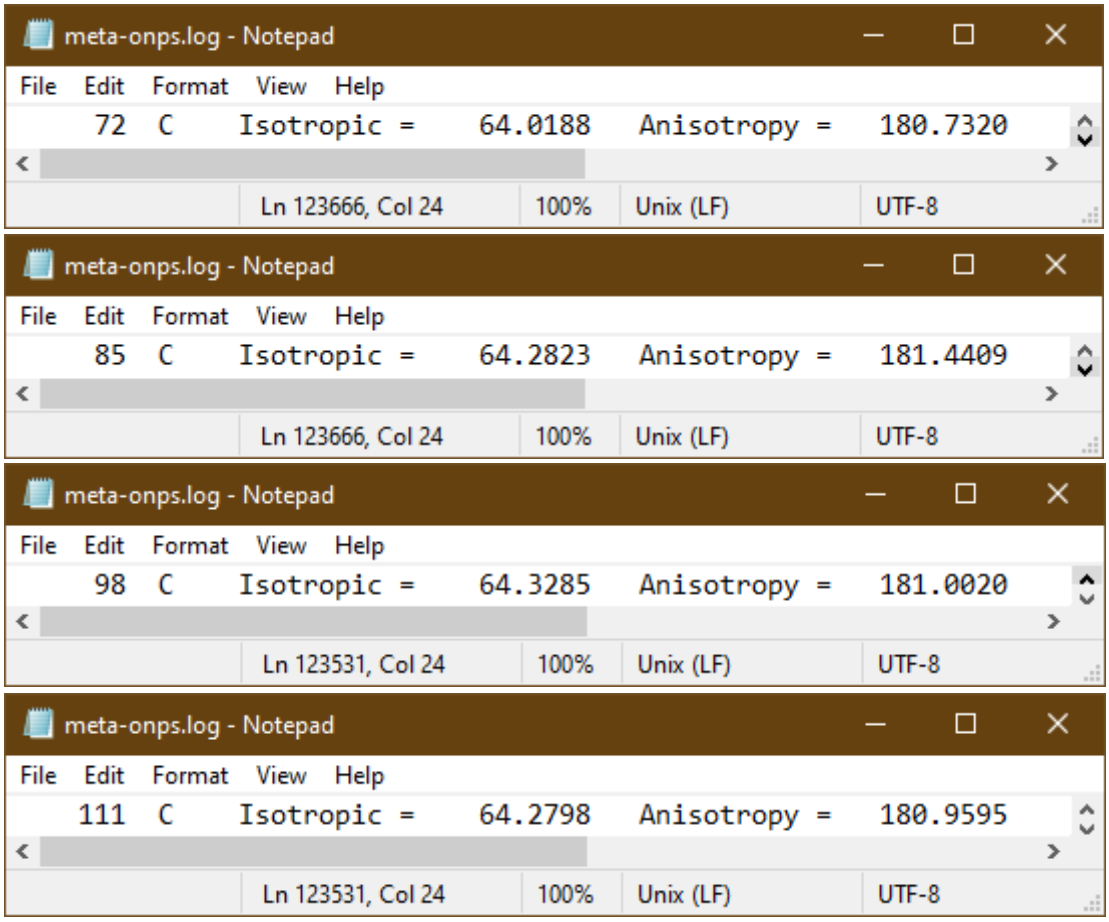

The average shielding value of the carbons connected to the silicons is 64.23 ppm. According to the reference chemical shielding which is 192.29 ppm, the average chemical **shift** of the carbons connected to the silicons is thus: 192.29 - 64.23 = **128.06 ppm**. The chemical shifts of the other atoms can be calculated according to the same procedure.

GaussView is another software prepared to visualize the chemical shielding values calculated by Gaussian. It is not free, but it is probably improved with respect to Avogadro.

References

1. Gielen, D.; Boshell, F.; Saygin, D.; Bazilian, M. D.; Wagner, N.; Gorini, R., The role of renewable energy in the global energy transformation. *Energy Strategy Reviews* **2019,** *24*, 38-50.
2. Project., G. C., Supplemental data of Global Carbon Budget 2020 (Version 1.0). **2020**.
3. Carapellucci, R.; Milazzo, A., Membrane systems for CO_2 capture and their integration with gas turbine plants. *Proceedings of the Institution of Mechanical Engineers, Part A: Journal of Power and Energy* **2003,** *217* (5), 505-517.
4. Raaijmakers, M. J.; Hempenius, M. A.; Schön, P. M.; Vancso, G. J.; Nijmeijer, A.; Wessling, M.; Benes, N. E., Sieving of hot gases by hyper-cross-linked nanoscale-hybrid membranes. *Journal of the American Chemical Society* **2013,** *136* (1), 330-335.
5. Calle, M.; Doherty, C. M.; Hill, A. J.; Lee, Y. M., Cross-linked thermally rearranged poly (benzoxazole-co-imide) membranes for gas separation. *Macromolecules* **2013,** *46* (20), 8179-8189.
6. Calle, M.; Lozano, A. E.; Lee, Y. M., Formation of thermally rearranged (TR) polybenzoxazoles: Effect of synthesis routes and polymer form. *European Polymer Journal* **2012,** *48* (7), 1313-1322.
7. Joseph, W.; Abed, J.; Mercier, R.; Mcgrath, J. E., Synthesis and characterization of fluorinated polybenzoxazoles via solution cyclization techniques. *Polymer* **1994,** *35* (23), 5046-5050.
8. Kim, S.; Han, S. H.; Lee, Y. M., Thermally rearranged (TR) polybenzoxazole hollow fiber membranes for CO_2 capture. *Journal of membrane science* **2012,** *403*, 169-178.
9. Ismail, A. F.; Khulbe, K. C.; Matsuura, T., Gas separation membranes. *Switzerland: Springer* **2015**.
10. Pandiyan, S. A molecular-level understanding of CO_2 permeability in polymer membranes. Université de Savoie, 2009.
11. Scott, K.; Hughes, R., *Industrial membrane separation technology*. Springer Science & Business Media: 2012.
12. Everett, D., Manual of symbols and terminology for physicochemical quantities and units, appendix II: Definitions, terminology and symbols in colloid and surface chemistry. *Pure and Applied Chemistry* **1972,** *31* (4), 577-638.
13. McNaught, A.; Wilkinson, A., IUPAC. *Compendium of Chemical Terminology, 2nd ed.(the" Gold Book")* **1997,** *2*.
14. Everett, D. H., Manual of symbols and terminology for physicochemical quantities and units, appendix II: Definitions, terminology and symbols in colloid and surface chemistry. *Pure and Applied Chemistry* **1972,** *31* (4), 577-638.
15. Burwell Jr, R. L., Manual of symbols and terminology for physicochemical quantities and units—appendix II heterogeneous catalysis. In *Advances in Catalysis*, Elsevier: 1977; Vol. 26, pp 351-392.
16. Srikanth, G., Membrane Separation Processes. *Technology and Business Opportunities, Water Conditioning & Purification, pp1-4* **2008**.
17. Vinh-Thang, H.; Kaliaguine, S., Predictive models for mixed-matrix membrane performance: a review. *Chemical reviews* **2013,** *113* (7), 4980-5028.
18. Souza, V.; Quadri, M., Organic-inorganic hybrid membranes in separation processes: a 10-year review. *Brazilian Journal of Chemical Engineering* **2013,** *30* (4), 683-700.
19. Chauhan, R.; Panday, P., Membrane for gas separation. *Prog. Polym. Sci* **2001,** *26*, 853-893.
20. Burdyny, T.; Struchtrup, H., Hybrid membrane/cryogenic separation of oxygen from air for use in the oxy-fuel process. *Energy* **2010,** *35* (5), 1884-1897.
21. Zhu, Y.; Liu, X.; Zhou, Z. In *Optimization of cryogenic air separation distillation columns*, 2006 6th World Congress on Intelligent Control and Automation, IEEE: 2006; pp 7702-7705.
22. Allen, J.; Stover, D., Making oxygen on the moon. *Popular Science* **1995,** *247* (2), 23-23.
23. Meriläinen, A.; Seppälä, A.; Kauranen, P., Minimizing specific energy consumption of oxygen enrichment in polymeric hollow fiber membrane modules. *Applied energy* **2012,** *94*, 285-294.
24. Changela, M.; McKee, R.; Heshan, H.; Pathak, V.; Quinlan, M.; Strickland, J., Evaluation of Natural Gas Process Technology. *LW August* **1996,** *7*.
25. Scholes, C. A.; Stevens, G. W.; Kentish, S. E., Membrane gas separation applications in natural gas processing. *Fuel* **2012,** *96*, 15-28.
26. Brown, D.; Neyertz, S.; Raaijmakers, M. J.; Benes, N. E., Sorption and permeation of gases in hyper-cross-linked hybrid poly (POSS-imide) networks: An in silico study. *Journal of membrane science* **2019,** *577*, 113-128.
27. Vanherck, K.; Koeckelberghs, G.; Vankelecom, I. F., Crosslinking polyimides for membrane applications: a review. *Progress in polymer science* **2013,** *38* (6), 874-896.
28. Rezakazemi, M.; Sadrzadeh, M.; Matsuura, T., Thermally stable polymers for advanced high-performance gas separation membranes. *Progress in Energy and Combustion Science* **2018,** *66*, 1-41.
29. Raaijmakers, M. J.; Ogieglo, W.; Wiese, M.; Wessling, M.; Nijmeijer, A.; Benes, N. E., Sorption behavior of compressed CO_2 and CH_4 on ultrathin hybrid poly (POSS-imide) layers. *ACS applied materials & interfaces* **2015,** *7* (48), 26977-26988.
30. Neyertz, S.; Brown, D.; Raaijmakers, M. J.; Benes, N. E., A molecular characterization of hyper-cross-linked hybrid polyPOSS-imide networks. *Computational materials science* **2016,** *117*, 338-353.
31. Neyertz, S.; Brown, D.; Raaijmakers, M. J.; Benes, N. E., The influence of the dianhydride precursor in hyper-cross-linked hybrid polyPOSS-imide networks. *Physical Chemistry Chemical Physics* **2016,** *18* (41), 28688-28703.
32. Neyertz, S., Gas transport in dense polymeric membranes, molecular dynamics simulations. *Encyclopedia of Membrane Science and Technology* **2013**, 1-21.
33. Karplus, M.; Petsko, G. A., Molecular dynamics simulations in biology. *Nature* **1990,** *347* (6294), 631.
34. Critchley, J.; Knight, G.; Wright, W. W., *Heat-resistant polymers: technologically useful materials*. Springer Science & Business Media: 2013.
35. Ravve, A., *Principles of polymer chemistry*. Springer Science & Business Media: 2013.
36. Huheey, J.; Cottrell, T., The strengths of chemical bonds. Butterworths, London: 1958.

37. Arnold Jr., C., Stability of high-temperature polymers. *Journal of Polymer Science: Macromolecular Reviews* **1979,** *14* (1), 265-378.
38. Mark, J. E., *Physical properties of polymers handbook*. Springer: 2007; Vol. 1076.
39. Wright, W., The development of heat resistant organic polymers. In *The degradation and stabilisation of polymers*, Applied Science Publishers Ltd London: 1975; p 43.
40. Gilleo, K.; Ongley, P., Pros and cons of thermoplastic and thermoset polymer adhesives in microelectronic assembly applications. *Microelectronics international* **1999,** *16* (2), 34-38.
41. Abadie, M. J., *High performance polymers-polyimides based-from chemistry to applications*. 2012.
42. Guo, Q., *Thermosets: structure, properties, and applications*. Woodhead Publishing: 2017.
43. Karimi-Varzaneh, H. A.; Carbone, P.; Müller-Plathe, F., Hydrogen bonding and dynamic crossover in Polyamide-66: a molecular dynamics simulation study. *Macromolecules* **2008,** *41* (19), 7211-7218.
44. Skreiberg, A.; Skreiberg, Ø.; Sandquist, J.; Sørum, L., TGA and macro-TGA characterisation of biomass fuels and fuel mixtures. *Fuel* **2011,** *90* (6), 2182-2197.
45. Réjasse, F.; Rapaud, O.; Léchelle, J.; Trolliard, G.; Khodja, H.; Masson, O.; Martin, G.; Maitre, A., Novel insight into the chemical analysis of light elements in oxycarbides. *Acta Materialia* **2018,** *157*, 11-20.
46. Wang, X. S.; Li, X. G.; Yan, D., Isothermal gravimetric analysis of poly (trimethylene terephthalate). *Journal of applied polymer science* **2002,** *84* (8), 1600-1608.
47. Cassidy, P. E., History of heat-resistant polymers. *Journal of Macromolecular Science—Chemistry* **1981,** *15* (7), 1435-1460.
48. Kemmish, D. J., *Practical guide to high performance engineering plastics*. Smithers Rapra: 2011.
49. Lee, J. S.; Wantink, K. L., Catheter Shaft and Method of Forming Same. Google Patents: 2014.
50. Kyriacos, D., High-temperature engineering thermoplastics. In *Brydson's Plastics Materials*, Elsevier: 2017; pp 545-615.
51. Bashford, D., Polyethersulphones (PES). In *Thermoplastics*, Springer: 1997; pp 464-468.
52. Utracki, L., Present and future trends in polymer blends technology. *International Polymer Processing* **1987,** *2* (1), 3-12.
53. Bashford, D., Polyetheretherketone (PEEK). In *Thermoplastics*, Springer: 1997; pp 445-447.
54. Eveloy, V.; Rodgers, P.; Diana, A., Performance investigation of thermally enhanced polymer composite materials for microelectronics cooling. *Microelectronics Journal* **2015,** *46* (12), 1216-1224.
55. VIVES, V. C.; Dix, J.; Brady, D., Polyphenylene sulfide (PPS) in harsh environments. ACS Publications: 1983.
56. Sadrzadeh, M.; Bhattacharjee, S., Rational design of phase inversion membranes by tailoring thermodynamics and kinetics of casting solution using polymer additives. *Journal of membrane science* **2013,** *441*, 31-44.
57. Miller-Chou, B. A.; Koenig, J. L., A review of polymer dissolution. *Progress in Polymer Science* **2003,** *28* (8), 1223-1270.
58. Dawsey, T.; McCormick, C. L., The lithium chloride/dimethylacetamide solvent for cellulose: a literature review. *Journal of Macromolecular Science—Reviews in Macromolecular Chemistry and Physics* **1990,** *30* (3-4), 405-440.
59. Striegel, A., Theory and applications of DMAc/LiCl in the analysis of polysaccharides. *Carbohydrate polymers* **1997,** *34* (4), 267-274.
60. Scott, K., *Handbook of industrial membranes*. Elsevier: 1995.
61. Sroog, C., Polyimides. *Progress in Polymer Science* **1991,** *16* (4), 561-694.
62. Spiliopoulos, I. K.; Mikroyannidis, J. A.; Tsivgoulis, G. M., Rigid-Rod Polyamides and Polyimides Derived from 4, 3 ‘‘-Diamino-2 ‘, 6 ‘-diphenyl-or Di (4-biphenylyl)-p-terphenyl and 4-Amino-4 ‘‘-carboxy-2 ‘, 6 ‘-diphenyl-p-terphenyl. *Macromolecules* **1998,** *31* (2), 522-529.
63. Freeman, B.; Yampolskii, Y.; Pinnau, I., *Materials science of membranes for gas and vapor separation*. John Wiley & Sons: 2006.
64. Liaw, D. J.; Liaw, B. Y. In *Synthesis and properties of polyamides derived from 1, 4‐bis (4‐aminophenoxy)‐2‐tert‐butylbenzene*, Macromolecular Symposia, Wiley Online Library: 1997; pp 343-348.
65. Liaw, D.-J.; Liaw, B.-Y.; Li, L.-J.; Sillion, B.; Mercier, R.; Thiria, R.; Sekiguchi, H., Synthesis and characterization of new soluble polyimides from 3, 3 ‘, 4, 4 ‘-benzhydrol tetracarboxylic dianhydride and various diamines. *Chemistry of materials* **1998,** *10* (3), 734-739.
66. Sun, X.; Yang, Y.-K.; Lu, F., Synthesis and properties of ionic, rigid-rod, and thermally stable polyimides containing bipyridinium triflates. *Macromolecules* **1998,** *31* (13), 4291-4296.
67. Kasashima, Y.; Kumada, H.; Yamamoto, K.; Akutsu, F.; Naruchi, K.; Miura, M., Preparation and properties of polyamides and polyimides from 4, 4″ -diamino-o-terphenyl. *Polymer* **1995,** *36* (3), 645-650.
68. Ballauff, M.; Schmidt, G. F., Rigid rod polymers with flexible side chains, 2. Observation of a novel type of layered mesophase. *Die Makromolekulare Chemie, Rapid Communications* **1987,** *8* (2), 93-97.
69. Kaneda, T.; Katsura, T.; Nakagawa, K.; Makino, H.; Horio, M., High‐strength‐high‐modulus polyimide fibers II. Spinning and properties of fibers. *Journal of applied polymer science* **1986,** *32* (1), 3151-3176.
70. Liaw, D.-J.; Liaw, B.-Y.; Hsu, P.-N.; Hwang, C.-Y., Synthesis and Characterization of New Highly Organosoluble Poly (ether imide) s Bearing a Noncoplanar 2, 2 ‘-Dimethyl-4, 4 ‘-biphenyl Unit and Kink Diphenylmethylene Linkage. *Chemistry of materials* **2001,** *13* (5), 1811-1816.
71. Glatz, F. P.; Mülhaupt, R., Syntheses and properties of soluble poly (arylene thioether imide) s and the corresponding poly (arylene sulfone imide) s. *Polymer Bulletin* **1993,** *31* (2), 137-143.
72. Sen, S. K.; Dasgupta, B.; Banerjee, S., Effect of introduction of heterocyclic moieties into polymer backbone on gas transport properties of fluorinated poly (ether imide) membranes. *Journal of Membrane Science* **2009,** *343* (1-2), 97-103.

73. Kim, T.; Koros, W.; Husk, G.; O'Brien, K. C., Relationship between gas separation properties and chemical structure in a series of aromatic polyimides. *Journal of Membrane Science* **1988,** *37* (1), 45-62.
74. Coleman, M.; Koros, W., Isomeric polyimides based on fluorinated dianhydrides and diamines for gas separation applications. *Journal of Membrane Science* **1990,** *50* (3), 285-297.
75. Yamamoto, H.; Mi, Y.; Stern, S.; St. Clair, A., Structure/permeability relationships of polyimide membranes. II. *Journal of Polymer Science Part B: Polymer Physics* **1990,** *28* (12), 2291-2304.
76. Stern, S.; Mi, Y.; Yamamoto, H.; Clair, A. K. S., Structure/permeability relationships of polyimide membranes. Applications to the separation of gas mixtures. *Journal of Polymer Science Part B: Polymer Physics* **1989,** *27* (9), 1887-1909.
77. Tanaka, K.; Kita, H.; Okano, M.; Okamoto, K.-i., Permeability and permselectivity of gases in fluorinated and non-fluorinated polyimides. *Polymer* **1992,** *33* (3), 585-592.
78. Walker, D. R.; Koros, W. J., Transport characterization of a polypyrrolone for gas separations. *Journal of membrane science* **1991,** *55* (1-2), 99-117.
79. Sen, S. K.; Banerjee, S., Gas transport properties of fluorinated poly (ether imide) films containing phthalimidine moiety in the main chain. *Journal of Membrane Science* **2010,** *350* (1-2), 53-61.
80. Al-Masri, M.; Kricheldorf, H. R.; Fritsch, D., New polyimides for gas separation. 1. polyimides derived from substituted terphenylenes and 4, 4 '-(Hexafluoroisopropylidene) diphthalic anhydride. *Macromolecules* **1999,** *32* (23), 7853-7858.
81. Mi, Y.; Stern, S.; Trohalaki, S., Dependence of the gas permeability of some polyimide isomers on their intrasegmental mobility. *Journal of membrane science* **1993,** *77* (1), 41-48.
82. Peter, J.; Khalyavina, A.; Kříž, J.; Bleha, M., Synthesis and gas transport properties of ODPA–TAP–ODA hyperbranched polyimides with various comonomer ratios. *European polymer journal* **2009,** *45* (6), 1716-1727.
83. Yamamoto, H.; Mi, Y.; Stern, S.; St. Clair, A. K., Structure/permeability relationships of polyimide membranes. II. *Journal of Polymer Science Part B: Polymer Physics* **1990,** *28* (12), 2291-2304.
84. Garg, P.; Singh, R.; Choudhary, V., Selective polydimethylsiloxane/polyimide blended IPN pervaporation membrane for methanol/toluene azeotrope separation. *Separation and purification technology* **2011,** *76* (3), 407-418.
85. Lin, L.; Wang, A.; Dong, M.; Zhang, Y.; He, B.; Li, H., Sulfur removal from fuel using zeolites/polyimide mixed matrix membrane adsorbents. *Journal of Hazardous materials* **2012,** *203*, 204-212.
86. Tsai, M.-H.; Huang, S.-L.; Chen, P.-J.; Chiang, P.-C.; Chen, D.-S.; Lu, H.-H.; Chiu, W.-M.; Chen, J.-C.; Lu, H.-T., Characteristics and properties of polyimide/vanadium oxide hybrid membranes. *Desalination* **2008,** *233* (1-3), 232-238.
87. Cordes, D. B.; Lickiss, P. D.; Rataboul, F., Recent developments in the chemistry of cubic polyhedral oligosilsesquioxanes. *Chemical reviews* **2010,** *110* (4), 2081-2173.
88. Hill, A. F.; Fink, M. J., *Advances in Organometallic Chemistry*. Academic Press: 2008.
89. Hybrid Plastics. Available at http://www.hybridplastics.com.
90. Rios-Dominguez, H.; Ruiz-Trevino, F.; Contreras-Reyes, R.; Gonzalez-Montiel, A., Syntheses and evaluation of gas transport properties in polystyrene–POSS membranes. *Journal of membrane science* **2006,** *271* (1-2), 94-100.
91. Reddy, B. S.; Gnanasekaran, D., Structure-gas transport property relationships of poly (dimethylsiloxane-urethane) nanocomposite membranes. In *Advances in Nanocomposites–Synthesis, Characterization and Industrial Applications*, Intech–Publishing Croatia: 2011; pp 195-226.
92. Zhang, D.; Liu, Y.; Shi, Y.; Huang, G., Effect of polyhedral oligomeric silsesquioxane (POSS) on crystallization behaviors of POSS/polydimethylsiloxane rubber nanocomposites. *RSC Advances* **2014,** *4* (12), 6275-6283.
93. Yang, D.; Zhang, W.; Yao, R.; Jiang, B., Thermal stability enhancement mechanism of poly (dimethylsiloxane) composite by incorporating octavinyl polyhedral oligomeric silsesquioxanes. *Polymer degradation and stability* **2013,** *98* (1), 109-114.
94. Rezakazemi, M.; Vatani, A.; Mohammadi, T., Synthesis and gas transport properties of crosslinked poly (dimethylsiloxane) nanocomposite membranes using octatrimethylsiloxy POSS nanoparticles. *Journal of Natural Gas Science and Engineering* **2016,** *30*, 10-18.
95. Rahman, M. M.; Filiz, V.; Shishatskiy, S.; Abetz, C.; Neumann, S.; Bolmer, S.; Khan, M. M.; Abetz, V., PEBAX® with PEG functionalized POSS as nanocomposite membranes for CO_2 separation. *Journal of Membrane Science* **2013,** *437*, 286-297.
96. Iyer, P.; Iyer, G.; Coleman, M., Gas transport properties of polyimide–POSS nanocomposites. *Journal of Membrane Science* **2010,** *358* (1-2), 26-32.
97. Li, Y.; Chung, T.-S., Molecular-level mixed matrix membranes comprising Pebax® and POSS for hydrogen purification via preferential CO_2 removal. *international journal of hydrogen energy* **2010,** *35* (19), 10560-10568.
98. Dasgupta, B.; Sen, S. K.; Banerjee, S., Aminoethylaminopropylisobutyl POSS—Polyimide nanocomposite membranes and their gas transport properties. *Materials Science and Engineering: B* **2010,** *168* (1-3), 30-35.
99. Raaijmakers, M. J.; Kappert, E. J.; Nijmeijer, A.; Benes, N. E., Thermal imidization kinetics of ultrathin films of hybrid poly (POSS-imide) s. *Macromolecules* **2015,** *48* (9), 3031-3039.
100. Raaijmakers, M. J.; Wessling, M.; Nijmeijer, A.; Benes, N. E., Hybrid polyhedral oligomeric silsesquioxanes–imides with tailored intercage spacing for sieving of hot gases. *Chemistry of materials* **2014,** *26* (12), 3660-3664.
101. Laine, R. M.; Roll, M. F., Polyhedral phenylsilsesquioxanes. *Macromolecules* **2011,** *44* (5), 1073-1109.
102. Brown, J. F.; Vogt, L. H.; Prescott, P. I., Preparation and characterization of the lower equilibrated phenylsilsesquioxanes. *Journal of the American Chemical Society* **1964,** *86* (6), 1120-1125.
103. Brown Jr, J. F., The polycondensation of phenylsilanetriol. *Journal of the American Chemical Society* **1965,** *87* (19), 4317-4324.
104. Asuncion, M. Z.; Laine, R. M., Silsesquioxane barrier materials. *Macromolecules* **2007,** *40* (3), 555-562.

105. Olsson, K.; C, G., On octa-(arylsilsesquioxanes),(ArSi) 8O12. 1. phenyl, 4-tolyl, and 1-naphthyl compounds. *Arkiv for Kemi* **1961,** *17* (6), 529-&.
106. Tamaki, R.; Tanaka, Y.; Asuncion, M. Z.; Choi, J.; Laine, R. M., Octa (aminophenyl) silsesquioxane as a nanoconstruction site. *Journal of the American Chemical Society* **2001,** *123* (49), 12416-12417.
107. Lee, A.; Haddad, T. S.; Schwab, J. J.; An, Y. Z. *Molecular Structure Analysis of Aminophenyl Silsesquioxane (Preprint)*; MICHIGAN STATE UNIV EAST LANSING DEPT OF CHEMICAL ENGINEERING AND MATERIALS …: 2006.
108. Applied research, technology and innovation (SINTEF). Available at https://www.sintef.no/en/this-is-sintef/.
109. Gelest Inc. Available at https://www.gelest.com/.
110. Li, F.; Li, Y.; Chung, T.-S.; Kawi, S., Facilitated transport by hybrid POSS®–Matrimid®–Zn^{2+} nanocomposite membranes for the separation of natural gas. *Journal of Membrane Science* **2010,** *356* (1-2), 14-21.
111. Tamaki, R.; Choi, J.; Laine, R. M., A polyimide nanocomposite from octa (aminophenyl) silsesquioxane. *Chemistry of materials* **2003,** *15* (3), 793-797.
112. Choi, J.; Tamaki, R.; Kim, S. G.; Laine, R. M., Organic/inorganic imide nanocomposites from aminophenylsilsesquioxanes. *Chemistry of materials* **2003,** *15* (17), 3365-3375.
113. Zhang, J.; Xu, R. W.; Yu, D. S., A novel and facile method for the synthesis of octa (aminophenyl) silsesquioxane and its nanocomposites with bismaleimide‐diamine resin. *Journal of applied polymer science* **2007,** *103* (2), 1004-1010.
114. Kute, V.; Banerjee, S., Novel semi‐fluorinated poly (ether imide) s derived from 4‐(p‐aminophenoxy)‐3‐trifluoromethyl‐4′‐aminobiphenyl. *Macromolecular Chemistry and Physics* **2003,** *204* (17), 2105-2112.
115. Solvents Miscibility Chart. Available at https://scharlab.com/tabla-reactivos-mezclabilidad.php.
116. Pavia, D. L.; Lampman, G. M.; Kriz, G. S.; Vyvyan, J. A., *Introduction to spectroscopy*. Cengage Learning: 2008.
117. Huang, F.; Rong, Z.; Shen, X.; Huang, F.; Du, L.; Li, Z., Organic/inorganic hybrid bismaleimide resin with octa (aminophenyl) silsesquioxane. *Polymer Engineering & Science* **2008,** *48* (5), 1022-1028.
118. Abraham, R. J.; Mobli, M., *Modelling ^{1}H NMR spectra of organic compounds: theory, applications and NMR prediction software*. John Wiley & Sons: 2008.
119. Kim, S.; Choi, J.; Tamaki, R.; Laine, R. M., Synthesis of amino-containing oligophenylsilsesquioxanes. *Polymer* **2005,** *46* (12), 4514-4524.
120. Takahashi, K.; Sulaiman, S.; Katzenstein, J. M.; Snoblen, S.; Laine, R. M., New Aminophenylsilsesquioxanes—Synthesis, Properties, and Epoxy Nanocomposites. *Australian journal of chemistry* **2006,** *59* (8), 564-570.
121. Sulaiman, S. Synthesis and characterization of polyfunctional Polyhedral Silsesquioxane Cages. University of Michigan, 2011.
122. Huang, J.-c.; He, C.-b.; Xiao, Y.; Mya, K. Y.; Dai, J.; Siow, Y. P., Polyimide/POSS nanocomposites: interfacial interaction, thermal properties and mechanical properties. *Polymer* **2003,** *44* (16), 4491-4499.
123. Ni, Y.; Zheng, S., A novel photocrosslinkable polyhedral oligomeric silsesquioxane and its nanocomposites with poly (vinyl cinnamate). *Chemistry of Materials* **2004,** *16* (24), 5141-5148.
124. Waseda, Y.; Matsubara, E.; Shinoda, K., *X-ray diffraction crystallography: introduction, examples and solved problems*. Springer Science & Business Media: 2011.
125. Balke, S.; Hamielec, A.; LeClair, B.; Pearce, S., Gel permeation chromatography. *Industrial & Engineering Chemistry Product Research and Development* **1969,** *8* (1), 54-57.
126. Nagendiran, S.; Dinakaran, K.; Chandramohan, A.; Alagar, M.; Hamerton, I., Synthesis and characterization of organosoluble radiation‐resistant composite materials from octa (maleimidophenyl) silsesquioxane and aryldiamines. *Polymers for Advanced Technologies* **2018,** *29* (4), 1261-1270.
127. MesreNova Mestrelab Research. Available at https://mestrelab.com/.
128. M. J. Frisch, G. W. T., H. B. Schlegel, G. E. Scuseria, M. A. Robb, J. R. Cheeseman, G. Scalmani, V. Barone, G. A. Petersson, H. Nakatsuji, X. Li, M. Caricato, A. Marenich, J. Bloino, B. G. Janesko, R. Gomperts, B. Mennucci, H. P. Hratchian, J. V. Ortiz, A. F. Izmaylov, J. L. Sonnenberg, D. Williams-Young, F. Ding, F. Lipparini, F. Egidi, J. Goings, B. Peng, A. Petrone, T. Henderson, D. Ranasinghe, V. G. Zakrzewski, J. Gao, N. Rega, G. Zheng, W. Liang, M. Hada, M. Ehara, K. Toyota, R. Fukuda, J. Hasegawa, M. Ishida, T. Nakajima, Y. Honda, O. Kitao, H. Nakai, T. Vreven, K. Throssell, J. A. Montgomery, Jr., J. E. Peralta, F. Ogliaro, M. Bearpark, J. J. Heyd, E. Brothers, K. N. Kudin, V. N. Staroverov, T. Keith, R. Kobayashi, J. Normand, K. Raghavachari, A. Rendell, J. C. Burant, S. S. Iyengar, J. Tomasi, M. Cossi, J. M. Millam, M. Klene, C. Adamo, R. Cammi, J. W. Ochterski, R. L. Martin, K. Morokuma, O. Farkas, J. B. Foresman, and D. J. Fox *Gaussian 09, Revision A.02*, Gaussian, Inc., Wallingford CT: 2016.
129. AccuPyc II 1340, by Micromeritics Instrument Corp. Available at https://www.micromeritics.com/Product-Showcase/AccuPyc-II-1340.aspx.
130. Band, Y. B.; Avishai, Y., 15 - Density Functional Theory. In *Quantum Mechanics with Applications to Nanotechnology and Information Science*, Band, Y. B.; Avishai, Y., Eds. Academic Press: Amsterdam, 2013; pp 871-889.
131. Hanwell, M. D.; Curtis, D. E.; Lonie, D. C.; Vandermeersch, T.; Zurek, E.; Hutchison, G. R., Avogadro: an advanced semantic chemical editor, visualization, and analysis platform. *Journal of cheminformatics* **2012,** *4* (1), 17.
132. Avogadro: an open-source molecular builder and visualization tool. Version 1.20. Available http://avogadro.cc/.
133. Christiansen, O., Vibrational structure theory: new vibrational wave function methods for calculation of anharmonic vibrational energies and vibrational contributions to molecular properties. *Physical Chemistry Chemical Physics* **2007,** *9* (23), 2942-2953.
134. Rippers, Y. QM MM calculations on the membrane bound hydrogenase from Ralstonia eutropha. Technische Universität Berlin, 2015.
135. Parr, R. G., Density functional theory of atoms and molecules. In *Horizons of quantum chemistry*, Springer: 1980; pp 5-15.

136. Dirac, P. A. In *Note on exchange phenomena in the Thomas atom*, Mathematical proceedings of the Cambridge philosophical society, Cambridge University Press: 1930; pp 376-385.
137. Perdew, J. P.; Burke, K.; Ernzerhof, M., Generalized gradient approximation made simple. *Physical review letters* **1996,** *77* (18), 3865.
138. Lee, C.; Yang, W.; Parr, R. G., Development of the Colle-Salvetti correlation-energy formula into a functional of the electron density. *Physical review B* **1988,** *37* (2), 785.
139. Becke, A. D., A new mixing of Hartree–Fock and local density‐functional theories. *The Journal of chemical physics* **1993,** *98* (2), 1372-1377.
140. Harb, Z., Atieh. Theoretical determination of NMR parameters of metabolites and proteins
Détermination théorique des paramètres RMN de métabolites et protéines. Université Claude Bernard - Lyon I, 2011.
141. Guzzo, M.; Gatti, M.; Reining, L. Exchange and correlation effects in the electronic properties of transition metal oxides: the example of NiO. Master's thesis, Universitadegli studi di Milano-Bicocca, 2008.
142. Orbital Polarization Terms in Basis Sets. 2020.
143. Ditchfield, R.; Hehre, W. J.; Pople, J. A., Self‐consistent molecular‐orbital methods. IX. An extended Gaussian‐type basis for molecular‐orbital studies of organic molecules. *The Journal of Chemical Physics* **1971,** *54* (2), 724-728.
144. Hehre, W. J., *A guide to molecular mechanics and quantum chemical calculations*. Wavefunction Irvine, CA: 2003; Vol. 2.
145. Gaussian Basis Sets. 2020.
146. Wodrich, M. D.; Corminboeuf, C.; Schleyer, P. v. R., Systematic errors in computed alkane energies using B3LYP and other popular DFT functionals. *Organic letters* **2006,** *8* (17), 3631-3634.
147. Jensen, F., Basis set convergence of nuclear magnetic shielding constants calculated by density functional methods. *Journal of chemical theory and computation* **2008,** *4* (5), 719-727.
148. Schaffer, C. L.; Thomson, K. T., Density functional theory investigation into structure and reactivity of prenucleation silica species. *The Journal of Physical Chemistry C* **2008,** *112* (33), 12653-12662.
149. Hassan, H. B., Density Function Theory B3LYP/6-31G** Calculation of Geometry Optimization and Energies of Donor-Bridge-Acceptor Molecular System. *Int. J. Curr. Eng. Sci. Res.* **2014,** *4*, 2342-2345.
150. Ibrahim, M.; Koglin, E., Vibrational spectroscopic study of acetate group. *Acta Chimica Slovenica* **2004,** *51* (3), 453-460.
151. Ibrahim, M.; Koglin, E., Spectroscopic study of polyaniline emeraldine base: modelling approach. *Acta Chim Slov* **2005,** *52* (2), 159-63.
152. Castellá-Ventura, M.; Kassab, E., Comparative semiempirical and ab initio study of the harmonic vibrational frequencies of aniline—I. The ground state. *Spectrochimica Acta Part A: Molecular Spectroscopy* **1994,** *50* (1), 69-86.
153. Iriarte, A. G.; Cutin, E. H.; Della Védova, C. O., Infrared and Raman spectra of 2-chloro-2, 2-difluoroacetamide ($ClF_2CC(O)NH_2$). *Journal of molecular structure* **2006,** *800* (1-3), 154-157.
154. Gundersen, S.; Samdal, S.; Seip, R.; Shorokhov, D. J.; Strand, T. G., The molecular structure, conformation, potential to internal rotation and force field of 2, 2, 2-trifluoroacetamide as studied by gas electron diffraction and quantum chemical calculations. *Journal of molecular structure* **1998,** *445* (1-3), 229-242.
155. Samdal, S.; Seip, R., The molecular structure, conformation, potential to internal rotation and force field of 2, 2, 2-trichloroacetamide as studied by gas electron diffraction and quantum chemical calculations. *Journal of molecular structure* **1997,** *413*, 423-439.
156. Rai, A. K.; Kumar, S.; Rai, A., Infrared, Raman spectra and DFT calculations of chlorine substituted anilines. *Vibrational spectroscopy* **2006,** *42* (2), 397-402.
157. Krishnan, P. S. G.; He, C., Octa (maleimido phenyl) silsesquioxane copolymers. *Journal of Polymer Science Part A: Polymer Chemistry* **2005,** *43* (12), 2483-2494.
158. Derome, A. E., *Modern NMR techniques for chemistry research*. Elsevier: 2013.
159. Pegg, D. T.; Doddrell, D. M.; Bendall, M. R., Proton‐polarization transfer enhancement of a heteronuclear spin multiplet with preservation of phase coherency and relative component intensities. *The Journal of Chemical Physics* **1982,** *77* (6), 2745-2752.
160. Aue, W.; Bartholdi, E.; Ernst, R. R., Two‐dimensional spectroscopy. Application to nuclear magnetic resonance. *The Journal of Chemical Physics* **1976,** *64* (5), 2229-2246.
161. Balci, M., *Basic ^{1}H-and ^{13}C-NMR spectroscopy*. Elsevier: 2005.
162. Bremser, W., HOSE—a novel substructure code. *Analytica Chimica Acta* **1978,** *103* (4), 355-365.
163. London, F., Théorie quantique des courants interatomiques dans les combinaisons aromatiques. **1937**.
164. Ditchfield, R., Self-consistent perturbation theory of diamagnetism: I. A gauge-invariant LCAO method for NMR chemical shifts. *Molecular Physics* **1974,** *27* (4), 789-807.
165. Wolinski, K.; Hinton, J. F.; Pulay, P., Efficient implementation of the gauge-independent atomic orbital method for NMR chemical shift calculations. *Journal of the American Chemical Society* **1990,** *112* (23), 8251-8260.
166. Bashford, D. SCRF: Self-Consistent Reaction Field. Available at https://www.scm.com/doc/ADF/Input/SCRF.html.
167. Mennucci, B.; Cances, E.; Tomasi, J., Evaluation of solvent effects in isotropic and anisotropic dielectrics and in ionic solutions with a unified integral equation method: theoretical bases, computational implementation, and numerical applications. *The Journal of Physical Chemistry B* **1997,** *101* (49), 10506-10517.
168. Miertus, S.; Tomasi, J., Approximate evaluations of the electrostatic free energy and internal energy changes in solution processes. *Chemical physics* **1982,** *65* (2), 239-245.

169. Miertuš, S.; Scrocco, E.; Tomasi, J., Electrostatic interaction of a solute with a continuum. A direct utilizaion of AB initio molecular potentials for the prevision of solvent effects. *Chemical Physics* **1981,** *55* (1), 117-129.
170. Pascual‐ahuir, J.-L.; Silla, E.; Tunon, I., GEPOL: An improved description of molecular surfaces. III. A new algorithm for the computation of a solvent‐excluding surface. *Journal of Computational Chemistry* **1994,** *15* (10), 1127-1138.
171. Mennucci, B.; Tomasi, J., Continuum solvation models: A new approach to the problem of solute's charge distribution and cavity boundaries. *The Journal of chemical physics* **1997,** *106* (12), 5151-5158.
172. Cossi, M.; Barone, V.; Cammi, R.; Tomasi, J., Ab initio study of solvated molecules: a new implementation of the polarizable continuum model. *Chemical Physics Letters* **1996,** *255* (4-6), 327-335.
173. Barone, V.; Cossi, M.; Tomasi, J., A new definition of cavities for the computation of solvation free energies by the polarizable continuum model. *The Journal of chemical physics* **1997,** *107* (8), 3210-3221.
174. Cances, E.; Mennucci, B.; Tomasi, J., A new integral equation formalism for the polarizable continuum model: Theoretical background and applications to isotropic and anisotropic dielectrics. *The Journal of chemical physics* **1997,** *107* (8), 3032-3041.
175. Lipparini, F.; Scalmani, G.; Mennucci, B.; Cancès, E.; Caricato, M.; Frisch, M. J., A variational formulation of the polarizable continuum model. *The Journal of chemical physics* **2010,** *133* (1), 014106.
176. Caricato, M., Absorption and emission spectra of solvated molecules with the EOM–CCSD–PCM method. *Journal of chemical theory and computation* **2012,** *8* (11), 4494-4502.
177. Cammi, R., Coupled‐cluster theories for the polarizable continuum model. II. Analytical gradients for excited states of molecular solutes by the equation of motion coupled‐cluster method. *International Journal of Quantum Chemistry* **2010,** *110* (15), 3040-3052.
178. Scalmani, G.; Frisch, M. J., Continuous surface charge polarizable continuum models of solvation. I. General formalism. *The Journal of chemical physics* **2010,** *132* (11), 114110.
179. Tomasi, J.; Mennucci, B.; Cances, E., The IEF version of the PCM solvation method: an overview of a new method addressed to study molecular solutes at the QM ab initio level. *Journal of Molecular Structure: THEOCHEM* **1999,** *464* (1-3), 211-226.
180. Öztürk, N.; Özdemir, T.; Alpaslan, Y. B.; Gokce, H.; Alpaslan, G., Experimental (FT-IR, Raman and NMR) and theoretical (B3LYP, B3PW91, M06-2X and CAM-B3LYP) analyses of p-tert-butylphenyl salicylate. *Bilge International Journal of Science and Technology Research* **2018,** *2* (1), 56-73.
181. Costa, F. L. P.; de Albuquerque, A. C. F.; dos Santos Jr, F. M.; de Amorim, M. B., GIAO‐HDFT scaling factor for ^{13}C NMR chemical shifts calculation. *Journal of Physical Organic Chemistry* **2010,** *23* (10), 972-977.
182. Du, V. A.; Stipicic, G. N.; Schubert, U., ^{29}Si NMR Shielding Calculations Employing Density Functional Theory, Focussing on Hypervalent Silicon Compounds. Wiley Online Library: 2011.
183. Aliev, A. E.; Courtier-Murias, D.; Zhou, S., Scaling factors for carbon NMR chemical shifts obtained from DFT B3LYP calculations. *Journal of Molecular Structure: THEOCHEM* **2009,** *893* (1-3), 1-5.
184. AA, R.; Godarzian, A., ^{29}Si NMR chemical shift calculation for silicate species by Gaussian software. *Journal of the Physical Society of Japan* **2005,** *74* (5), 1609-1620.
185. Avcı, D.; Bahçeli, S.; Tamer, Ö.; Atalay, Y., Comparative study of DFT/B3LYP, B3PW91, and HSEH1PBE methods applied to molecular structures and spectroscopic and electronic properties of flufenpyr and amipizone. *Canadian Journal of Chemistry* **2015,** *93* (10), 1147-1156.
186. Perdew, J., Proceedings of the 21st Annual International Symposium on the Electronic Structure of Solids, Dresden, 1991. **1991**.
187. Boese, A. D.; Handy, N. C., A new parametrization of exchange–correlation generalized gradient approximation functionals. *The Journal of Chemical Physics* **2001,** *114* (13), 5497-5503.
188. Hamprecht, F. A.; Cohen, A. J.; Tozer, D. J.; Handy, N. C., Development and assessment of new exchange-correlation functionals. *The Journal of chemical physics* **1998,** *109* (15), 6264-6271.
189. Krivdin, L. B., Computational protocols for calculating ^{13}C NMR chemical shifts. *Progress in nuclear magnetic resonance spectroscopy* **2019,** *112*, 103-156.
190. Wolff, S.; Ziegler, T., Calculation of DFT-GIAO NMR shifts with the inclusion of spin-orbit coupling. *The Journal of chemical physics* **1998,** *109* (3), 895-905.
191. Bagley, A. C.; AbuNada, I.; Yin, J.; DeVore, T. C., Investigations of NMR chemical shifts using DFT-B3LYP-GIAO calculations. In *NMR Spectroscopy in the Undergraduate Curriculum: Upper-Level Courses and Across the Curriculum Volume 3*, ACS Publications: 2016; pp 67-77.
192. Rani, A. U.; Sundaraganesan, N.; Kurt, M.; Cinar, M.; Karabacak, M., FT-IR, FT-Raman, NMR spectra and DFT calculations on 4-chloro-N-methylaniline. *Spectrochimica Acta Part A: Molecular and Biomolecular Spectroscopy* **2010,** *75* (5), 1523-1529.
193. Baaden, M.; Granger, P.; Strich, A., Dependence of NMR isotropic shift averages and nuclear shielding tensors on the internal rotation of the functional group X about the CX bond in seven simple vinylic derivatives H_2C= CH-X. *Molecular Physics* **2000,** *98* (6), 329-342.
194. Diaz, M.; Jaballas, J.; Arias, J.; Lee, H.; Onak, T., ^{13}C NMR Studies on carboranes and derivatives: experimental/calculational correlations. *Journal of the American Chemical Society* **1996,** *118* (18), 4405-4410.
195. Willoughby, P. H.; Jansma, M. J.; Hoye, T. R., A guide to small-molecule structure assignment through computation of (^{1}H and ^{13}C) NMR chemical shifts. *Nature protocols* **2014,** *9* (3), 643-660.
196. Hill, D. E.; Vasdev, N.; Holland, J. P., Evaluating the accuracy of density functional theory for calculating ^{1}H and ^{13}C NMR chemical shifts in drug molecules. *Computational and Theoretical Chemistry* **2015,** *1051*, 161-172.

197. Pierens, G. K.; Venkatachalam, T.; Reutens, D. C., NMR and DFT investigations of structure of colchicine in various solvents including density functional theory calculations. *Scientific reports* **2017,** *7* (1), 1-9.
198. Li, J.; Liu, J.-K.; Wang, W.-X., GIAO ^{13}C NMR Calculation with Sorted Training Sets Improves Accuracy and Reliability for Structural Assignation. *The Journal of Organic Chemistry* **2020,** *85* (17), 11350-11358.
199. Jensen, F., *Introduction to computational chemistry*. John wiley & sons: 2017.
200. Bahgat, K.; Fraihat, S., Normal coordinate analysis, molecular structure, vibrational, electronic spectra and NMR investigation of 4-Amino-3-phenyl-^{1}H-1, 2, 4-triazole-5 (4H)-thione by ab initio HF and DFT method. *Spectrochimica Acta Part A: Molecular and Biomolecular Spectroscopy* **2015,** *135*, 1145-1155.
201. Da Silva, H. C.; De Almeida, W. B., Theoretical calculations of ^{1}H NMR chemical shifts for nitrogenated compounds in chloroform solution. *Chemical Physics* **2020,** *528*, 110479.
202. Benzi, C.; Crescenzi, O.; Pavone, M.; Barone, V., Reliable NMR chemical shifts for molecules in solution by methods rooted in density functional theory. *Magnetic Resonance in Chemistry* **2004,** *42* (S1), S57-S67.
203. Hyperchem(TM) Hyperchem Inc. Available at http://www.hypercubeusa.com/.
204. Zhang, C.; Patschinski, P.; Stephenson, D. S.; Panisch, R.; Wender, J. H.; Holthausen, M. C.; Zipse, H., The calculation of ^{29}Si NMR chemical shifts of tetracoordinated silicon compounds in the gas phase and in solution. *Physical Chemistry Chemical Physics* **2014,** *16* (31), 16642-16650.
205. Chai, T.; Draxler, R. R., Root mean square error (RMSE) or mean absolute error (MAE)? – Arguments against avoiding RMSE in the literature. *Geosci. Model Dev.* **2014,** *7* (3), 1247-1250.
206. Zhang, Y.; Wu, A.; Xu, X.; Yan, Y., Geometric dependence of the B3LYP-predicted magnetic shieldings and chemical shifts. *The Journal of Physical Chemistry A* **2007,** *111* (38), 9431-9437.
207. Lodewyk, M. W.; Siebert, M. R.; Tantillo, D. J., Computational prediction of ^{1}H and ^{13}C chemical shifts: a useful tool for natural product, mechanistic, and synthetic organic chemistry. *Chemical Reviews* **2012,** *112* (3), 1839-1862.
208. Neyertz, S.; Salimi, S.; Radmanesh, F.; Benes, N. E.; Brown, D., High-temperature molecular screening of hybrid polyOAPS-imide networks based on octa (aminophenyl) silsesquioxane for increased thermomechanical resistance. *Physical Chemistry Chemical Physics* **2021,** *23* (19), 11438-11454.
209. Neyertz, S.; Brown, D.; Salimi, S.; Radmanesh, F.; Benes, N. E., Molecular characterization of polyOAPS-imide isomer hyper-cross-linked membranes: Free-volume morphologies and sorption isotherms for CH_4 and CO_2. *Journal of Membrane Science* **2021**, 119531.
210. Zimmerman, C. M.; Koros, W. J., Polypyrrolones for membrane gas separations. II. Activation energies and heats of sorption. *Journal of Polymer Science Part B: Polymer Physics* **1999,** *37* (12), 1251-1265.
211. Neyertz, S.; Gopalan, P.; Brachet, P.; Kristiansen, A.; Männle, F.; Brown, D., Oxygen transport in amino-functionalized polyhedral oligomeric silsesquioxanes (POSS). *Soft Materials* **2014,** *12* (1), 113-123.
212. Han, S.; Lee, Y., Recent high performance polymer membranes for CO_2 separation. In *Membrane engineering for the treatment of gases*, 2011; pp 84-124.
213. Han, S. H.; Kwon, H. J.; Kim, K. Y.; Seong, J. G.; Park, C. H.; Kim, S.; Doherty, C. M.; Thornton, A. W.; Hill, A. J.; Lozano, A. E., Tuning microcavities in thermally rearranged polymer membranes for CO_2 capture. *Physical chemistry chemical physics* **2012,** *14* (13), 4365-4373.
214. Li, X.; Singh, R. P.; Dudeck, K. W.; Berchtold, K. A.; Benicewicz, B. C., Influence of polybenzimidazole main chain structure on H_2/CO_2 separation at elevated temperatures. *Journal of Membrane Science* **2014,** *461*, 59-68.
215. Clarke, R.; Nuttall, W.; Glowacki, B., Endangered helium: Bursting the myth. *Chem. Eng* **2013,** *870*, 32-36.
216. Scholes, C. A.; Ghosh, U. K., Review of membranes for helium separation and purification. *Membranes* **2017,** *7* (1), 9.
217. Brown, D., The gmq User Manual. 5 ed.; 2013. Available at http://www.lmops.univ-savoie.fr/brown/gmq.html.
218. Neyertz, S.; Brown, D., The effect of structural isomerism on carbon dioxide sorption and plasticization at the interface of a glassy polymer membrane. *Journal of membrane science* **2014,** *460*, 213-228.
219. Neyertz, S.; Brown, D., Nanosecond-time-scale reversibility of dilation induced by carbon dioxide sorption in glassy polymer membranes. *Journal of Membrane Science* **2016,** *520*, 385-399.
220. Neyertz, S.; Brown, D., Air Sorption and Separation by Polymer Films at the Molecular Level. *Macromolecules* **2018,** *51* (18), 7077-7092.
221. Tanis, I.; Brown, D.; Neyertz, S.; Heck, R.; Mercier, R.; Vaidya, M.; Ballaguet, J.-P., A comparison of pure and mixed-gas permeation of nitrogen and methane in 6FDA-based polyimides as studied by molecular dynamics simulations. *Computational Materials Science* **2018,** *141*, 243-253.
222. Pandiyan, S.; Brown, D.; van der Vegt, N. F.; Neyertz, S., Atomistic models of three fluorinated polyimides in the amorphous state. *Journal of Polymer Science Part B: Polymer Physics* **2009,** *47* (12), 1166-1180.
223. Neyertz, S.; Brown, D.; Pandiyan, S.; van der Vegt, N. F., Carbon dioxide diffusion and plasticization in fluorinated polyimides. *Macromolecules* **2010,** *43* (18), 7813-7827.
224. Pandiyan, S.; Brown, D.; Neyertz, S.; van der Vegt, N. F., Carbon dioxide solubility in three fluorinated polyimides studied by molecular dynamics simulations. *Macromolecules* **2010,** *43* (5), 2605-2621.
225. Hammonds, K. D.; Ryckaert, J.-P., On the convergence of the SHAKE algorithm. *Computer Physics Communications* **1991,** *62* (2-3), 336-351.
226. Lorentz, H., Ueber die Anwendung des Satzes vom Virial in der kinetischen Theorie der Gase. *Annalen der physik* **1881,** *248* (1), 127-136.
227. Berthelot, D., Sur le mélange des gaz. *Compt. Rendus* **1898,** *126*, 1703-1706.
228. Allen, M., Tildesley. DJ Computer simulation of liquids. Oxford: clarendon Press: 1987.
229. Ewald, P. P., *Annal of Physics* **1921,** *64*, 235-287.
230. Humphrey, W., Dalke, A. and Schulten, K., VMD - Visual Molecular Dynamics. *J. Molec. Graphics* **1996,** *14*, 33-38.

231. Clark, M.; Cramer III, R. D.; Van Opdenbosch, N., Validation of the general purpose Tripos 5.2 force field. *Journal of Computational Chemistry* **1989,** *10* (8), 982-1012.
232. Li, H.-C.; Lee, C.-Y.; McCabe, C.; Striolo, A.; Neurock, M., Ab initio analysis of the structural properties of alkyl-substituted polyhedral oligomeric silsesquioxanes. *The Journal of Physical Chemistry A* **2007,** *111* (18), 3577-3584.
233. Striolo, A.; McCabe, C.; Cummings, P. T., Effective interactions between polyhedral oligomeric sislesquioxanes dissolved in normal hexadecane from molecular simulation. *Macromolecules* **2005,** *38* (21), 8950-8959.
234. Yani, Y.; Lamm, M. H., Molecular dynamics simulation of mixed matrix nanocomposites containing polyimide and polyhedral oligomeric silsesquioxane (POSS). *Polymer* **2009,** *50* (5), 1324-1332.